

Orthogonal Bichromophoric Systems: From Null Exciton Coupling to Symmetry-Breaking Charge Separation

A thesis submitted for the degree of

Doctor of Philosophy

in

Chemistry

by

Ebin Sebastian



Indian Institute of Science Education and Research
Thiruvananthapuram (IISER TVM),
Thiruvananthapuram – 695551
Kerala, India

July 2022

Declaration

I hereby declare that the Ph. D. thesis entitled “**Orthogonal Bichromophoric Systems: From Null Exciton Coupling to Symmetry-Breaking Charge Separation**” is an independent work carried out by me at the School of Chemistry, Indian Institute of Science Education and Research Thiruvananthapuram (IISER TVM), under the supervision of **Prof. Mahesh Hariharan** and it has not been submitted anywhere else for any other degree, diploma or title. In keeping with the general practice of reporting the scientific observations, due acknowledgements have been made wherever the work described is based on the findings of other investigators.

Place: IISER Thiruvananthapuram

Ebin Sebastian

Date: 21-10-2022

This is to certify that the work embodied in the thesis entitled “**Orthogonal Bichromophoric Systems: From Null Exciton Coupling to Symmetry-Breaking Charge Separation**” has been carried out by **Ebin Sebastian (PHD172005)** under my supervision at the School of Chemistry, Indian Institute of Science Education and Research Thiruvananthapuram (IISER TVM) and the same has not been submitted elsewhere for a degree.

Place: IISER Thiruvananthapuram

Prof. Mahesh Hariharan

Date: 21-10-2022

(Thesis Supervisor)

This thesis is dedicated

To

My beloved family

Teachers

And

Friends

Acknowledgements

Understanding the thesis dissertation marks the end of a long, eventful, and exciting Ph.D. research life at IISER TVM. What is left behind is a beautiful memory of people who came across my life at different times and made their impact in molding my personal and professional life, I would like to acknowledge them for their help along the way.

First and foremost, I am extremely grateful to my mentor and supervisor, Prof. Mahesh Hariharan, for his invaluable advice, unconditional support, patience, and providing a state-of-the-art research facility during my Ph.D. study. His immense knowledge and plentiful experience have encouraged me throughout my academic research and daily life. I am incredibly grateful to him for encouraging me to think independently and motivating me to pursue my research interests. I could not have imagined having a better mentor and advisor for my Ph.D. research.

I would like to express my sincere gratitude to Prof. J. N. Moorthy and Prof. V. Ramakrishnan, present and former Directors of IISER TVM, for providing excellent infrastructure and research facilities at IISER TVM. I thank the present and former heads of school of chemistry for the research facilities at CIL, IISER TVM. I am deeply grateful to my thesis doctoral committee members, Dr. Reji Varghese and Dr. V. Sivaranjana Reddy, for their insightful comments, support, guidance, and encouragement. I would like to offer my special thanks to Prof. K. George Thomas and Dr. Adithya Lakshmana for providing extensive help and support during my Ph. D. program. I thank all faculty members of the school of chemistry at IISER TVM for their support and motivation to widen my research perspectives.

I am deeply obliged to all past and present Hariharan group members: Dr. Shinaj K. R., Dr. Ajith R. M., Dr. Kalaivanan N., Dr. Abbey M. P., Dr. Nanditha G. N., Mr. Nagaraj K., Dr. Remya R., Ms. Devika S. Ms. Athira T. J., Dr. Arun T., Ms. Amalu M., Ms. Lijina M. P., Dr. Mahesh G., Ms. Swathi Krishna P. E., Dr. Bappa G., Mr. Aniruddha M., Ms. Kavya V., Mr. Jibin S., Mr. Philip D. M., Ms. Gopika G., Ms. Ishamol S., Mr. Vinayak B., Mr. Amal K. H., Mr. Niyas M. A., Ms. Ambili R. V., Ms. Hridya P., Mr. Vishnu V. K., Ms. Meera M., Mr. Alfy B., Mr. Deepu G., Mr. Krishna P., Mr. Jeswin S., Ms. Akshaya N., Ms. Keerthy P. S., Mr. Vivek V. K., D. Mr. Akhilesh K. U., Ms. Hruidya C. B., Mr. Sohan D. J., Mr. Dillep P. S., and Ms. Pallavi P. D. for the unconditional support, care, motivation and help during my Ph. D. work. I want to give a special mention to Dr. Abbey M. P., Dr. Sandeep K., and Dr. Kalaivanan N. for being incredible mentors, backing me with stimulating discussions and enlightening me on the introductory lessons of research. I want to offer my special thanks to BS-MS students, Mr.

Amal K. H., Ms. Hridya P., Mr. Alfy B., and Mr. Jeswin S., for their contribution to the works in the present thesis.

Special thanks to several people who have made my research life at IISER TVM more enjoyable, especially Dr. Sandeep K. and Dr. Baiju. P., Dr. Shinaj K. R., Dr. Feba T. P., Ms. Shamna M., Dr. Shine K. A. Dr. Murali G., Dr. Atchimnaidu, S., Dr. Perumal, D., Dr. Nthiyanandan K., Mr. Sujith M., Mr. Ajaykumar M. P., Mr. Manoj B., Mr. Sanoop M. S., Dr. Hemna F., Dr. Elizabeth M. T., Dr. Swathi, Dr. Reshma M., Dr. Swathi V. C., Mr. Vishnu E. K., Mr. Livin P., Ms. Aiswarya E., Ms. Merin V., Dr. T. Shyamala, Dr. Vignesh A., Dr. Hema S., Ms. Arthi R., Dr. Rishika R., Dr. Arun D., Mr. Shyamkumar V. H., Mr. Akhil D., Mr. Cijil R., Mr. Bichu S., Mr. Anook Nazer E.A., Ms. S. Arya G., Ms. Anjana J., Mr. Sulfikarali T., Mr. Ajay J., Ms. Aathira E., Dr. Ramkumar K., Dr. Raju C., Dr. Deepti S., Dr. Selvakumar B., Dr. Jobha A. J., Dr. Parvathy J., Dr. Dhanya S.R., Mr. Muhammed Shafeek O. M., Mr. Akash S., Ms. Aparna R. K., Ms. Keerthana, Ms. Meera J., Ms. Anju B. S., Ms. Shourya G., Mr. Aditesh M., Mr. Tuhin S., Ms. Kalyanakrishnan A. V., Mr. Jayakrishnan K. R., Ms. Fathima P., Mr. Anto J., Ms. Gayathri K and Mr. Blesson S., I thank Ms. Varsha M. (wife of Prof. Mahesh Hariharan) for her care, support, and words of inspiration during my research journey at IISER TVM.

I am grateful to Mr. Alex P. A. for single-crystal X-ray diffraction measurements and structure solving, Mr. Adarsh B. for NMR measurements, Mr. Nibith K. for the elemental, GC-MS, and IR analyses, Mr. Kiran for MALDI-TOF mass analysis, Mr. Pradeep K. G., Ms. Athira S. and Mr. Prem K. for HRMS mass analyses. I would also like to thank all the teaching and nonteaching (library, IT, purchase, finance, stores, and mess) staff of IISER TVM for their help and support. I also thank the technical support from Laser Spectra Services, Bangalore. I thank the University Grants Commission (UGC), the Government of India, and IISER TVM for the financial assistance.

I take this opportunity to express my sincere gratitude to all my teachers at Sree Sankara College, Kalady, for the motivation and encouragement. I would also like to thank all my friends at Sree Sankara College, Kalady (M. G. University) and Government Higher Secondary School, Puliyanam, for their help and support, especially Mr. Edwin T., Mr. Amal T., Mr. Amal V., Mr. Arun T., Mr. Sarun J., Ms. Chinju J., Ms. Navya J., Ms. Anu J., Ms. Kukku B., Mr. Melbin J., Mr. Anil K., Ms. Geethu D., Ms. Jisha P., and Mr. George J. I want to offer my special thanks to all the members of Kandam Cricket League (KCL), Dr. Ranjith P., Dr. Ben J., Mr. Varun M. K., Mr. Akhil A., Mr. Jeswin J., Mr. Navaneeth K., Mr. Sujith M., Mr. Ajaykumar M. P., Mr.

Sanoop M. S., Mr. Vishnu E. Mr. Blesson S., Mr. Akash S., Mr. Anook Nazer E.A., Mr. Livin P., and Mr. Rishith R., for making all weekends memorable and for the love, support, and care.

Lastly, I would like to thank my family: parents (Ms. Jenny S., and Mr. Sebastian M. C.), brothers (Mr. Albin S., Mr. Anson V., and Mr. Nibson V.), and wife, for their unconditional love, support, and care. Especially, I would like to thank my wife, Ms. Saniya Gracious, for showing faith in me and for being patient, understanding, and helping me complete the dissertation on time.

- Ebin Sebastian

Preface

The molecular coalition of chromophoric materials in photosynthetic organisms and optoelectronic devices play a vital role in ensuring a high degree of solar energy harvesting, energy transport, charge separation, and energy conversion. Specifically, in the photosynthetic complexes, impinging solar photons are transferred to the reaction center through coherent exciton transport. The symmetry-breaking charge separation process (SB-CS), which triggers the sequential electron transfer, converts electronic excitation energy to chemical energy at the reaction center. The comprehensive understanding of the photophysical processes (exciton formation, energy transfer, and charge separation) in molecular dimers and their precise dependence on the spatial arrangement, π -overlap, and intermolecular distances are essential for the design of efficient and robust artificial solar energy conversion systems. Chapter 1 will introduce two fundamental concepts of photophysics, molecular exciton theory and symmetry-breaking charge separation (SB-CS). Kasha's molecular exciton theory based on the long-range Coulombic coupling accounts for coherent exciton coupling among the co-facial, parallel transition dipoles (H-aggregate), and staggered transition dipoles (J-aggregate). Interestingly, Kasha postulates a null excitonic splitting in orthogonally stacked molecular, which was lacking an experimental signature for decades. Later, Spano and co-workers introduced short-range charge transfer mediated coupling, which depends on orbital interaction among the monomeric units.

The generation of electron-hole radical pair at the active layer of organic photovoltaics through symmetry-breaking charge-separation (SB-CS) has a crucial role in enhancing open-circuit voltage (V_{oc}) and thereby increasing power conversion efficiency. Since the SB-CS materials achieve intramolecular charge separation with a negligible energetic driving force and decelerated charge recombination rate, SB-CS has been subjected to extensive experimental and theoretical studies. Chapter 1 assesses the fundamentals of photosynthetic reaction centers, especially the 'special pair', and discusses how covalent control over the geometric arrangement, surrounding dielectric medium, and substitutions on multichromophoric perylene-dimide architecture affect the energy landscape of SB-CS and

charge recombination (CR). We systematically summarise the kinetically favored undesirable radiative and non-radiative deactivation channels of SB-CS and CR processes on diverse chromophoric arrangements.

The concept of exciton coupling in molecular aggregates has gathered immense attention recently due to its imperative role in tailoring the optical properties and electronic communication of the π -conjugated chromophoric assembly. Though vital for advanced optoelectronic and photovoltaic applications, the ideal Greek cross-dipole ($\alpha=90^\circ$) stacked chromophore in a crystalline state remains elusive. In Chapter 2, we will discuss the first crystalline evidence for null exciton coupling in an ideal Greek cross-dipole (+)-assembly that affords monomer-like optical properties and an exceptional charge-filtering (selective hole transport) effect. The 1,7-dibromoperylene-3,4,9,10-tetracarboxylic tetrabutylester (**PTE-Br₂**) crystallize in a novel Greek cross (+) assembly, which exhibits monomer-like fluorescence excitation, emission spectra and fluorescence lifetime and quantum yield measurement in the crystalline state. Monomeric optical characteristics of crystalline **PTE-Br₂** as compared to monomeric **PTE-Br₂** in chloroform solution advocate the null exciton splitting in Greek cross assembly. In contrast, cross assembly of **PTE** (X-type, $\alpha=70.2^\circ$) and J-type stacking of **PTE-Br₄** ($\alpha=0^\circ$, $\theta=90^\circ$) in crystalline state display excitonic splitting in the energy levels and render perturbed photophysical properties. Using the semi-classical Marcus theory, the charge-transfer rates calculation of **PTE-Br_{0,2,4}** shows a selective hole transport phenomenon in the Greek cross(+)- stacked **PTE-Br₂**. The molecular assembly exhibiting a selective charge transfer property can be employed as a hole and electron transport layer of organic solar cell. So, the precise rotational angle-dependent optical and charge transfer properties of **PTE-Br₂** can result in the rational design of optoelectronic materials.

The comprehensive understanding of the structure-property relationships in molecular architectures has enabled the development of photosynthetic mimics and photovoltaics devices. In chapter 3, we discuss the null exciton coupling assisted highly efficient photoinduced symmetry-breaking charge separation (SB-CS) in a Greek cross (+)-oriented spiro-conjugated perylenediimide dimer (**Sp-PDI₂**) via hole transfer. The absorption and emission spectra of **Sp-PDI₂** in toluene resemble **Ref-PDI**, which indicates the null excitonic coupling in a side-to-side orthogonal arranged PDI dimer. Theoretical calculations have reinstated the infrequent manifestation of null exciton splitting in **Sp-PDI₂**. Negligible contribution of long-range Coulombic and short-range charge-transfer coupling render null exciton splitting spectroscopic signature in **Sp-PDI₂**. The orthogonal arranged **Sp-PDI₂** possesses a selective hole-transfer

coupling, facilitating the ultrafast symmetry-breaking charge-separation (SB-CS) in polar solvents, which is characterized by femtosecond transient absorption spectroscopy measurement. The significant electronic coupling (hole transfer coupling) and minimum activation energy barrier of **Sp-PDI₂** accelerated the SB-CS formation and dissociation of null exciton. Fascinatingly, the rate of charge recombination (CR) decelerated in **Sp-PDI₂** due the Marcus inverted region effect (driving force of CR is larger than the total reorganization energy for CR). As a result, the ratio of SB-CS rate over CR rates of Sp-PDI₂ shows an unprecedentedly high value of 2647 in acetonitrile, the highest value reported in multichromophoric PDI architectures. The current study integrates the two fundamental concepts of photophysics, null exciton coupling and symmetry-breaking charge separation, and provides experimental evidence for the role of selective charge filtering effect in governing efficient SB-CS.

The manifestation of structural defects and concomitant exciton trap states in the multichromophoric architectures hamper exciton and charge transport across photovoltaic devices, reducing the photon-to-current conversion efficiency. Developing robust organic materials exhibiting optimized charge separation and charge recombination dynamics is pivotal for the advancement of organic photovoltaics. Chapter 4 demonstrates unprecedented excimer formation in the relaxed excited-state geometry of bichromophoric systems impeding the lifetime of symmetry-broken charge-separated states. we map the excited-state conformational changes of **SC-SPDI₂** and **SC-NPDI₂** liable for populating the distinct excited-state potential energy surface depending on the surrounding dielectric environment. The conformational flexibility of near-orthogonal **SC-SPDI₂** and **SC-NPDI₂** bichromophoric systems trigger structural relaxation in the excited-state resulting in a π -stacked foldamer structure. Temperature-dependent photoluminescence measurements and quantum chemical calculation have rationalized the excimer nature of the foldamer conformation. **SC-SPDI₂** and **SC-NPDI₂** undergo ultrafast structural relaxation with a lifetime of 11.3 ps and 23.6 ps, respectively, leading to a stable excimer state population in toluene. The near-orthogonal arranged **SC-SPDI₂** and **SC-NPDI₂** possess effective electronic communication facilitating the ultrafast dissociation of delocalized Frenkel excitons (FE) and evolution of thermodynamically feasible symmetry-breaking charge separation (SB-CS) state in polar solvents. The rate constant of SB-CS in polar solvents is many-fold higher than that of unrelaxed excimer formation in toluene. The transformation of SB-CS to charge transfer enhanced excimer state due to efficient configuration mixing between stabilized SB-CS and FE states in the foldamer conformation could reduce the power conversion efficiency. The present investigation highlights the necessity of conformational control in suppressing undesired deactivation channels to achieve

prolonged SB-CS and provides fundamental insights into photofunctional materials' design principles.

Contents

List of Figures

List of Tables

List of Schemes

1. Introduction to Molecular Exciton Theory and Symmetry-Breaking Charge Separation

| | |
|---|----|
| 1.1. Introduction..... | 1 |
| 1.2. Origin of Exciton Theory..... | 4 |
| 1.3. Exciton Theory; Kasha Model and Beyond..... | 7 |
| 1.3.1. The magic angle stacked PDI aggregates..... | 8 |
| 1.3.2. Null aggregate in Folda-Dimers PDI..... | 9 |
| 1.4. Symmetry-Breaking Charge Separation (SB-CS) in Molecular Constructs for Efficient Light Energy Conversion..... | 10 |
| 1.4.1. SB-CS in organic photovoltaics..... | 13 |
| 1.4.2. Kinetics of SB-CS processes..... | 14 |
| 1.4.3. Thermodynamics of SB-CS..... | 15 |
| 1.4.4. SB-CS in photosynthetic reaction centers..... | 17 |
| 1.5. Photoinduced SB-CS in multichromophoric PDI architectures..... | 18 |
| 1.5.1. Linearly arranged PDI dimers..... | 18 |
| 1.5.2. Slip-stacked PDI dimers..... | 21 |
| 1.5.3. Cofacially arranged PDI dimers..... | 21 |
| 1.5.4. SB-CS in triangularly arranged PDI trimer..... | 27 |
| 1.5.5. SB-CS in angularly arranged PDI dimers..... | 29 |
| 1.6. Aim and Objectives of the Thesis..... | 34 |
| 1.7. References..... | 35 |

2. Null Exciton Splitting in Chromophoric Greek Cross (+)-Aggregate

| | |
|--|----|
| 2.1. Introduction..... | 43 |
| 2.2. Result and Discussion..... | 45 |
| 2.2.1. Synthesis and single-crystal structure..... | 45 |
| 2.2.2. Crystal close packing analysis..... | 46 |
| 2.2.3. QTAIM, Hirshfeld Surface, and SAPT(0) analysis..... | 49 |
| 2.2.4. Optical Properties..... | 51 |
| 2.2.5. Charge transport analysis..... | 54 |

| | |
|--|-----|
| 2.3. Conclusion..... | 58 |
| 2.4. Experimental Section..... | 60 |
| 2.5. Additional Tables..... | 62 |
| 2.6. Additional Figures..... | 70 |
| 2.7 Appendix..... | 76 |
| 2.8. Reference..... | 84 |
| 3. Null Exciton Coupled Chromophoric Dimer Exhibits Symmetry-Breaking Charge Separation | |
| 3.1. Introduction..... | 92 |
| 3.2. Result and Discussion..... | 94 |
| 3.2.1. Synthesis, Single-crystal Structure and Geometry Optimizations | 94 |
| 3.2.2. Optical Properties | 95 |
| 3.2.3. Theoretical Investigation. | 98 |
| 3.2.4. Energetics..... | 109 |
| 3.2.5. SB-CS dynamics..... | 109 |
| 3.2.6. Evaluation using electron transfer theory..... | 114 |
| 3.3. Conclusion..... | 119 |
| 3.4. Experimental Section..... | 121 |
| 3.5. Additional Tables..... | 124 |
| 3.6. Additional Figures..... | 128 |
| 3.7 Appendix..... | 136 |
| 3.8. Reference..... | 142 |
| 4. Symmetry-Broken Charge Separated State Hampered by Excimer Evolution: Impact of Excited-State Structural Evolution | |
| 4.1. Introduction..... | 152 |
| 4.2. Result and Discussion..... | 154 |
| 4.2.1. Synthesis, characterization, and geometry Optimizations..... | 154 |
| 4.2.2. Optical Properties..... | 156 |
| 4.2.3. Excited-state geometry optimizations and fragment-based analysis..... | 158 |
| 4.2.4. Solvent-dependent optical properties..... | 161 |
| 4.2.5. Energetics..... | 163 |
| 4.2.6. Excited-state population dynamics..... | 165 |
| 4.2.7. Interplay of FE and CT contribution on excimer state..... | 174 |
| 4.2.8. Time-resolved emission spectroscopy measurements..... | 175 |

| | |
|--|------------|
| 4.2.9. Temperature-dependent photoluminescence measurements..... | 177 |
| 4.3. Conclusion..... | 178 |
| 4.4. Experimental Section..... | 180 |
| 4.5. Additional Tables..... | 183 |
| 4.6. Additional Figures..... | 186 |
| 4.7 Appendix..... | 201 |
| 4.8. Reference..... | 203 |
| 5. List of Publications..... | 211 |
| 6. Workshops and Conferences..... | 213 |
| 7. Copyrights and Permissions | 215 |

List of Figures

| Figure | Title | Page |
|--------|--|------|
| 1.1 | Schematic depicting excitation energy transfer pathways in models where chromophores are arranged in a two-dimensional planar distribution. b) Energy collection in an antenna system is depicted as an energy funnel. Shorter wavelengths of light are absorbed by peripheral antenna complexes, followed by energy-transfer processes to the lower-energy pigments located closer to the reaction center. Adapted with permission from ref (3). Copyright (2017) American Chemical Society. | 2 |
| 1.2 | Energy transfer in the purple bacterial photosystem. B800 BChls of LH2 are shown in green, B850 BChls of LH2 and B875 BChls of LH1 are shown in alternating red and orange, and P870 BChls of the RC are shown in yellow. Lifetimes in picoseconds (ps) are given for the energy transfer events indicated by the arrows. Energy absorbed by antenna carotenoids is passed to neighboring BChls. Double-headed arrows indicate femtosecond (fs) energy migration within the B850 or B875 pigment rings (Adapted from ref (7)). | 3 |
| 1.3 | Exciton splitting in a naphthalene dimer. Adapted with permission from ref (17). (2004) The Royal Society. | 5 |
| 1.4 | Schematic representation of exciton splitting for a molecular dimer with various orientations of transition dipoles. | 6 |
| 1.5 | Schematic representation of the changes in absorption (blue) and fluorescence (red) spectra on the formation of H- and J-aggregates from cyanine dye monomers. Adapted with permission from ref (19). Copyright (2017) IOP Publishing, Ltd. | 6 |
| 1.6 | (a) t_h and (b) t_e within a π -stacked perylene dimer (3.5 \AA π -stacking distance) as a function of transverse displacement, evaluated from density functional theory (DFT) calculated energy level splittings. The DFT calculated (c) HOMO and (d) LUMO of perylene. (e) The product, $t_h t_e (\propto J_{CT})$, and (f) the unscreened Coulomb coupling as a function of transverse displacement, evaluated using time-dependent DFT calculated atomic transition charge densities. Red (blue) regions correspond to a J- (H-) type interaction. All DFT calculations use the B3LYP functional and cc-pVDZ basis. The sign convention for t_h and t_e based on symmetry operations under which the dimer transition dipole moment is symmetric. Adapted with permission from ref (22). Copyright (2017) American Chemical Society. | 8 |
| 1.7 | Single-crystal structure of mb-PBI. (a) Perspective view from the side of the core structure of mb-PBI. The angle θ indicates the slip angle of transition dipoles of adjacent molecules. (b) Morphology of the mb-PBI single-crystal. Adapted with permission from ref (20). Copyright (2018) American Chemical Society. | 9 |
| 1.8 | (a) Top view and (b) side view onto the geometry-optimized structures of Bis-PBI 3(S). (c) Absorption (solid blue lines, $c_0 = 10^{-5} \text{ M}$), normalized fluorescence (solid red lines, $c_0 = 10^{-7} \text{ M}$), and excitation spectra (green dashed lines, $c_0 = 10^{-7} \text{ M}$) of Bis-PBI 3(S) in TCE at room temperature. The wavelengths for excitation (λ_{ex}) and detection (λ_{em}) to obtain the fluorescence and excitation spectra, respectively, are | 10 |

| | | |
|------|---|----|
| | highlighted by arrows in the graphs. Insets: Samples of Ref-PBI and Bis-PBIs 3(S) under UV light ($\lambda = 365$ nm) and fluorescence quantum yields (Φ_{Fl}). Adapted with permission from ref (27). Copyright (2018) American Chemical Society. | |
| 1.9 | a) A simplified scheme of charge separation and electron transfer events in the purple bacterial reaction center, red arrows represent electron transfer pathways and the corresponding time constants. The green spheres in the middle of chlorins indicate the Mg atom in bacteriochlorophyll. P is a bacteriochlorophyll (BChl) dimer; B _A and B _B are monomeric BChls; H _A and H _B are bacteriopheophytins (BPhs); Q _A and Q _B are ubiquinones, and Fe is nonheme iron. b) Transient absorption spectra of biperylenylpropane in acetonitrile. c) A schematic representation of the simplest organic bilayer solar cell with proposed working principle based on sandwich configuration of conventional donor and an acceptor exhibiting symmetry-breaking charge separation. | 12 |
| 1.10 | Left: Energy level scheme pertaining to a photoinduced CS. Right: Free energy dependence of the CS rate constant calculated using Equation (6) (Eq. (5) predicts the same behaviour in the normal regime). Adapted with permission from ref (41). Copyright (2012) WILEY-VCH Verlag GmbH & Co. KGaA, Weinheim. | 16 |
| 1.11 | Geometry adopted by ‘special pairs’ in different reaction centers. | 17 |
| 1.12 | Structures of multichromophoric PDI systems exhibiting SB-CS discussed in chapter 1. | 19 |
| 1.13 | (a) Steady-state absorption (solid lines) and fluorescence (dotted lines) spectra of 5a in different solvents. Femtosecond transient absorption spectra of 5a in (b) THF and (d) CHCl ₃ . Insets show the decay profiles. (c) Energy state diagram of 5a depicting excimer-mediated SB-CS process. | 23 |
| 1.14 | (a) Optimized structures of 7 , 6a and 6b showing increasing interplanar distance. (b) Schematic potential energy diagrams for SB-CS in the dimers in CH ₂ Cl ₂ . Arrows are shown for 7 . | 26 |
| 1.15 | a) Normalized steady-state UV–vis absorption and (b) emission spectra of Ref-PDI (red) and trimer 8 (blue) in CH ₂ Cl ₂ . c) Schematic of symmetry-breaking charge separation in trimer 8 upon photoexcitation. d) (top) Femtosecond transient absorption spectra of molecule 8 showing the excited-state dynamics after photoexcitation. (bottom) Species-associated spectra reconstructed from global fits to the sequential A → B → ground state (GS) model, where A is singlet excited state (¹ *PDI) and B is the SB-CS state. | 28 |
| 1.16 | a-d) fs-TA spectra of 10 in toluene (TOL, a and b) and dimethylformamide (DMF, c and d) in short delay time (a and c) and long delay time (b and d). e) Simplified energy diagram showing relaxed-singlet state mediated symmetry-breaking charge separation in dimer 10 . | 30 |
| 2.1 | Dihedral angle (torsion angle) along the bay region (highlighted in light green) of PTE-Br₀ (a), PTE-Br₂ (b) and PTE-Br₄ (c), respectively. | 46 |
| 2.2 | Schematic representation of molecular structure (left) and the close-packing depicting weak intermolecular interactions (right) in a) PTE-Br₀ (C•••O, π - π), b) PTE-Br₂ (Br•••O, C•••Br), and c) PTE-Br₄ (π - π , C•••C) stacked dimers. Rotation angle (α) among the dimers with respect to their long molecular axis are 70.2° (PTE-Br₀); 90° (PTE-Br₂) and 0° (PTE-Br₄). | 48 |

| | | |
|------|---|-----|
| 2.3 | a) Columnar assembly of PTE-Br₂ along c-axis and b) two different dimers [concave (Dimer 1) and convex (Dimer 2) shaped] in the columnar stacking. | 49 |
| 2.4 | QTAIM electron density map depicting intermolecular interaction in crystalline PTE-Br₀ (a), PTE-Br₄ (b) and PTE-Br₂ (c[dimer 1] and d [dimer 2]). | 50 |
| 2.5 | Hirshfeld 2D fingerprint plot for crystalline PTE-Br₀ (a), PTE-Br₂ (b) and PTE-Br₄ (c). | 50 |
| 2.6 | Fluorescence excitation (solid), emission (broken) and time-resolved fluorescence decay profiles of PTE-Br₀ (a, d), PTE-Br₂ (b, e) and PTE-Br₄ (c, f) in dilute chloroform solution (brown) and crystalline state (black) | 51 |
| 2.7 | Time-resolved emission spectrum (TRES, $\lambda_{\text{ex}}=440$ nm) of crystalline PTE-Br₀ assembly (X-aggregate). | 53 |
| 2.8 | Evolution-associated spectra (EAS; A) and the relative population profiles (B) of the crystalline PTE-Br₀ assembly (X-aggregate). | 54 |
| 2.9 | a) Computed anisotropic mobility along the ac plane and b) schematic depiction of the charge-filtering (selective hole transfer (k_h)) phenomenon in PTE-Br₂ Greek cross (+)-aggregate. | 55 |
| 2.10 | HOMO and LUMO orbital geometries of PTE-Br₂ dimer. | 56 |
| 2.11 | Rotation angle (α) dependent ratio of charge transfer rates ($\frac{k_h}{k_e}$) of centroid matched PTE-Br₄ (A) and model derivative perylene (B). To remove the discrepancy arising from the large longitudinal and transverse molecular slips in PTE-Br₄ and perylene, the molecular dimers were manually adjusted via overlapping the centroids of the co-facial dimers and subsequently the rotation angle-dependent charge transfer rates were computed. | 57 |
| 2.12 | Rotation angle (α) dependent ratio of charge transfer rates ($\frac{k_h}{k_e}$) of centroid matched PTE-Br₄ (a) and model derivative perylene (b). To remove the discrepancy arising from the large longitudinal and transverse molecular slips in PTE-Br₄ and perylene, the molecular dimers were manually adjusted via overlapping the centroids of the co-facial dimers and subsequently the rotation angle-dependent charge transfer rates were computed. | 58 |
| 3.1 | Molecular structure of (a) PDI , (b) Ref-PDI , and (c) Sp-PDI₂ . (d & e) Single-crystal X-ray structure of Sp-PDI₂ . “R” represents 3-pentyl group. | 96 |
| 3.2 | Normalized absorption (solid black line) and emission spectra (solid red line) of Ref-PDI (top) and Sp-PDI₂ (bottom) in toluene at room temperature. | 97 |
| 3.3 | Transition dipole vectors (μ) of Sp-PDI₂ for (a) $S_0 \rightarrow S_1$ transition and (b) $S_0 \rightarrow S_2$ transition. (Transition dipole moment for $S_0 \rightarrow S_1$ and $S_0 \rightarrow S_2$ transition is the same and calculated as 7.79 D). | 99 |
| 3.4 | Schematic of the Sp-PDI₂ molecule with the P_z orbitals around the spiro-link showing (a) destructive interference between LUMOs and (b) constructive interference between HOMOs of PDI molecule. (c) Top: schematic of the LUMO-LUMO orbital interaction of PDI dimer responsible for the electron transfer integral in different rotational angles. Middle: the electron and hole transfer integrals as a function of the rotational angle between two orthogonally arranged PDI molecules. Bottom: schematic of the HOMO-HOMO orbital interaction of PDI dimer | 101 |

| | | |
|------|---|-----|
| | responsible for hole transfer integral in different rotational angles (representation of HOMO and LUMO molecular orbitals of PDI molecule is restricted to the Pz orbitals that are close enough to interact through space). | |
| 3.5 | The ground-state potential energy surface of Sp-PDI₂ computed at the wb97xd/def2svp level of theory in a vacuum. | 102 |
| 3.6 | (Top) Electron-hole correlation plots of Sp-PDI₂ for the S ₁ , S ₂ , S ₃ , and S ₄ states (fragment 1: PDI A, fragment 2: spiro-carbon, and fragment 3: PDI B). (Bottom) Distribution of hole (yellow) and electron (green) for first four excited states of Sp-PDI ₂ obtained from hole–electron isosurface analyses. | 103 |
| 3.7 | Energy level diagram of different singlet excited states of Sp-PDI₂ , depicting hole and electron transfer between neighboring PDI molecule and corresponding isosurface of hole (blue) and electron (yellow) distribution. | 104 |
| 3.8 | Variation of the modulus of Coulombic coupling $ J_{\text{Coul}} $ and charge-transfer coupling (J_{CT}) as a function of rotation angle (θ) between the perylenediimide monomers (for evaluating J_{CT} , $E_{\text{CT}} - E_{\text{S}_1} = 0.875$ eV was used as constant). | 105 |
| 3.9 | (a) Absorption and (b) emission spectra for Sp-PDI₂ in different solvents. (c) Fluorescence lifetime decay profile of Sp-PDI₂ in different solvents. | 106 |
| 3.10 | (a) Cyclic voltammetry data and (b) differential pulse voltammograms of Ref-PDI and Sp-PDI₂ in CH ₂ Cl ₂ . (Tetrabutylammonium hexafluorophosphate (0.1 M) as the supporting electrolyte, scan rate 200 mV s ⁻¹ . Fc/Fc ⁺ =ferrocene/ferrocenium couple.) | 108 |
| 3.11 | (Top) Femtosecond transient absorption spectra of Sp-PDI₂ in (a) toluene, (b) THF, and (c) ACN showing the excited-state dynamics after photoexcitation. (Middle) Species associated spectra reconstructed from target analysis of A → GS model for toluene, A ⇌ B → GS model for THF and A → B → GS model for ACN, respectively, where A is 1* Sp-PDI₂ , B is the SB-CS state and GS is the ground state ($\lambda_{\text{ex}}=440$ nm). (Bottom) Relative population profiles of the excited state are fitted by kinetic models. | 111 |
| 3.12 | Time-resolved emission spectra (TRES, $\lambda_{\text{ex}}=478$ nm) of Sp-PDI₂ in THF at room temperature. | 113 |
| 3.13 | (a) Decay associated spectra (DAS) and (b) the relative population profiles of the Sp-PDI₂ in THF. The orange (A) and green (B) colored spectrum and decay profiles correspond to CS→GS emission and LE→GS emission, where microenvironmental does not favour CS, respectively. | 114 |
| 3.14 | Schematic description of the internal reorganization energy calculation for (a) charge separation and (b) charge recombination processes. | 116 |
| 3.15 | Mechanism of symmetry-breaking charge separation, back charge transfer and charge recombination of Sp-PDI₂ in polar solvents. | 117 |
| 3.16 | Schematic potential energy diagrams for SB-CS of Sp-PDI₂ in different solvents. | 118 |
| 3.17 | (a) UV-vis absorption changes of Sp-PDI₂ upon the addition of cobaltocene (CoCp ₂) and (b) difference absorption spectra of Sp-PDI₂ obtained by subtracting ground state absorption from that of chemically reduced anions radicals. | 119 |

| | | |
|------|--|-----|
| 3.18 | (a) UV-vis absorption changes of Sp-PDI₂ upon the addition of antimony pentachloride (SbCl ₅) and (b) difference absorption spectra of Sp-PDI₂ obtained by subtracting ground state absorption from that of chemically oxidized cation radicals. | 119 |
| 4.1 | Molecular structure of monomeric SPDI and NPDI (a) and dimeric SC-SPDI₂ and SC-NPDI₂ (b). Optimized geometries of SC-SPDI₂ (c) and SC-NPDI₂ (d) with the corresponding dihedral angles between the monomeric planes. | 155 |
| 4.2 | Optimised structures of core annulated perylenediimide monomers a) SPDI and b) NPDI showing the in-plane bend in the perylene core. | 155 |
| 4.3 | Optimised structures of core annulated perylenediimide monomers a) SPDI and b) NPDI showing the C-S and C-N bond lengths. | 156 |
| 4.4 | Normalised absorption spectra of sulphur annulated (SPDI) and nitrogen annulated (NPDI) perylenediimide monomers compared to unsubstituted PDI. | 156 |
| 4.5 | Normalized UV-vis absorption, emission spectra (e) and fluorescence decay profile (f) of SC-SPDI₂ (Top) and SC-NPDI₂ (Bottom) in toluene at room temperature. | 157 |
| 4.6 | Excited-state structural relaxation of SC-SPDI₂ dimer upon photoexcitation. | 159 |
| 4.7 | Potential energy curve of the dimers a) SC-NPDI₂ and b) SC-SPDI₂ in the ground state with varying torsional angles. | 160 |
| 4.8 | Pictorial representation of the delocalized Frenkel exciton (left), charge resonance states (middle) of FC geometry, and excimer state (right) of relaxed foldamer structure of SC-SPDI₂ . a) Schematic representation of hole-electron distribution in the dimer, the rectangular box represents each fragment; dashed orange circles depict holes, and solid blue circles depict excited electrons. Hole-electron correlation plots (b) and corresponding isosurface of the hole (c, orange) and electron (d, blue) distribution of different excited-states of SC-SPDI₂ . The CT and PR values are given at the bottom to define the nature of excitations. | 161 |
| 4.9 | Solvent-dependent absorption and emission spectra of a) SC-NPDI₂ and b) SC-SPDI₂ | 162 |
| 4.10 | Solvent-dependent normalized emission spectra of a) SC-SPDI₂ and b) SC-NPDI₂ | 163 |
| 4.11 | Fluorescence decay profiles of a) SC-SPDI₂ and b) SC-NPDI₂ in different solvents. The fluorescence decay profile of SC-NPDI₂ in ACN is biexponentially fitted. The second component is assigned to scattering contribution as SC-NPDI₂ has very low fluorescence quantum yield in ACN (<0.1%). | 164 |
| 4.12 | (a, c) Cyclic voltammetry data and (b, d) differential pulse voltammograms of SC-SPDI₂ and SC-NPDI₂ in CH ₂ Cl ₂ . (Tetrabutylammonium hexafluorophosphate (0.1 M) as the supporting electrolyte, scan rate 100 mV s ⁻¹ . Fc/Fc ⁺ =ferrocene/ferrocenium couple). | 164 |
| 4.13 | Femtosecond transient absorption spectra (top), evolution associated spectra (EAS, middle) and population profiles (bottom) of SPDI in different solvents | 166 |
| 4.14 | Femtosecond transient absorption spectra (top), evolution associated spectra (EAS, middle) and population profiles (bottom) of NPDI in different solvents. | 166 |
| 4.15 | a) Femtosecond transient absorption contour maps (top) and spectra (bottom) of SC-SPDI₂ in toluene (TOL) showing the excited-state dynamics after photoexcitation at 470 nm. (b) Evolution associated difference spectra reconstructed from global | 167 |

| | | |
|------|---|-----|
| | analysis of $A \rightarrow B \rightarrow C \rightarrow D$ model, where FE is the Frenkel exciton/Singlet excited state; Ex^* is the unrelaxed excimer state; Ex is the relaxed excimer state. (c) Schematic representation of excited-state dynamics of SC-SPDI₂ in toluene at room temperature. | |
| 4.16 | Femtosecond transient absorption spectra (top), Evolution associated spectra (bottom) of SC-NPDI₂ in toluene. | 168 |
| 4.17 | (a) Femtosecond transient absorption contour maps (top) and spectra (bottom) of SC-SPDI₂ in acetonitrile (ACN) showing the excited-state dynamics after photoexcitation at 470 nm. (b) Evolution associated difference spectra reconstructed from global analysis of $A \rightarrow B \rightarrow C \rightarrow D$ model, where FE is the Frenkel exciton/Singlet excited state; SB-CS is the symmetry-breaking charge-separated state; Ex is the excimer state. (c) Schematic representative excited-state dynamics of SC-SPDI₂ in acetonitrile at room temperature. | 169 |
| 4.18 | Femtosecond transient absorption spectra (top), Evolution associated spectra (EAS, bottom) of SC-SPDI₂ in acetone. | 170 |
| 4.19 | Femtosecond transient absorption spectra (top), Evolution associated spectra (EAS, bottom) of SC-NPDI₂ in a) acetone and b) acetonitrile. | 171 |
| 4.20 | The potential energy diagram summarizes the excited-state dynamics of SC-SPDI₂ and SC-NPDI₂ undergoes structural relaxation in polar solvents (ACE and ACN) and non-polar solvent (TOL), where FE is the Frenkel exciton, Ex^* is the unrelaxed excimer state, Ex is the stable excimer state and SB-CS is the symmetry-breaking charge-separated state. The x-axis represents the reaction coordinate and E on the y-axis indicates the potential energy. | 172 |
| 4.21 | (Top) Nanosecond transient absorption spectra of SC-SPDI₂ in (a) TOL, (b) ACE and (c) ACN showing the excited-state dynamics after photoexcitation in N_2 atmosphere. (Bottom) Evolution-associated spectra were reconstructed from global analysis of the $A \rightarrow GS$ model in all solvents. | 173 |
| 4.22 | (Top) Nanosecond transient absorption spectra of SC-NPDI₂ in (a) TOL, (b) ACE and (c) ACN showing the excited-state dynamics after photoexcitation in N_2 atmosphere. (Bottom) Evolution associated spectra were reconstructed from global analysis of the $A \rightarrow GS$ model in all solvents. | 173 |
| 4.23 | Time-resolved emission spectra (TRES, $\lambda_{ex}=478$ nm) of SC-SPDI₂ in TOL, b) decay associated spectra (DAS), (c) the relative population profiles of SC-SPDI₂ in TOL and d) normalised decay associated spectra. The orange (A) and green (B) colored spectrum and decay profiles correspond to emission from the unrelaxed and relaxed excimer states. | 175 |
| 4.24 | a)Time-resolved emission spectra (TRES, $\lambda_{ex}=478$ nm) of SC-NPDI₂ in TOL, b) decay associated spectra (DAS), (c) the relative population profiles of SC-NPDI₂ in TOL and d) normalised decay associated spectra. The orange (A) and green (B) colored spectrum and decay profiles corresponds to emission from the unrelaxed and relaxed excimer states. | 176 |
| 4.25 | The temperature-dependent photoluminescence spectra of (a) SC-SPDI₂ and (b) SC-NPDI₂ in toluene. | 177 |
| 4.26 | Comparison of time-resolved emission spectra with steady-state emission spectra at different temperatures for a) SC-SPDI₂ and b) SC-NPDI₂ in TOL. | 178 |

List of Tables

| Table | Title | Page |
|-------|---|------|
| 1.1 | The effects of the different parameters on the SB-CS processes of multichromophoric PDI are discussed in chapter 1. | 32 |
| 2.1 | Crystallographic data and refinement parameters for PTE-Br_{0,2,4} crystal derivatives. | 47 |
| 2.2 | Relative % percentage intermolecular interactions between monomers of crystalline PTE-Br_{0,2,4} obtained from Hirshfeld analysis. | 50 |
| 2.3 | The interaction energies in selected dimers determined by SAPT(0)/jun-cc-pvdz calculations and SAPT(0) energy components for crystalline PTE-Br_{0,2,4} . | 51 |
| 2.4 | Photophysical properties of PTE-Br_{0,2,4} in monomeric (CHCl ₃). | 52 |
| 2.5 | Photophysical properties of PTE-Br_{0,2,4} in the crystalline state. | 53 |
| 2.6 | Charge transport properties (hole/electron reorganization energies and mobility) in PTE-Br_{0,2,4} assemblies. | 55 |
| 3.1 | UV/vis and fluorescence spectroscopic data of Ref-PDI and Sp-PDI₂ were measured in toluene at room temperature. | 98 |
| 3.2 | Experimentally and theoretically calculated excitonic coupling and hole/electron transfer integrals of Sp-PDI₂ . | 100 |
| 3.3 | Energy (ΔE), oscillator strength (f), mean position (POR), participation ratio (PR) of initial orbital (hole) and final orbital (electron) and charge transfer character (CT) of excited singlet states in Sp-PDI₂ . | 102 |
| 3.4 | Photophysical properties of Ref-PDI and Sp-PDI₂ in different solvents. | 107 |
| 3.5 | Summary of redox potentials and HOMO/LUMO calculations of Ref-PDI and Sp-PDI₂ (CH ₂ Cl ₂ , 298 K, $\epsilon_s = 8.93$). | 109 |
| 3.6 | Time constants (τ), rate constants (k), driving forces (ΔG), reorganization energy (λ) and activation barrier (ΔG^\ddagger) for symmetry-breaking charge-separation (SB-CS), back charge-transfer (BCT) and charge recombination (CR) in Sp-PDI₂ . | 112 |
| 3.7 | Computed energies of charge-separated state and ground state of Sp-PDI₂ by employing CDFT and DFT. | 116 |
| 4.1 | Photoluminescence Quantum Yield (ϕ_{Fl}) and Fluorescence Lifetime (τ_{Fl}) of SPDI , NPDI , SC-SPDI₂ , and SC-NPDI₂ . | 158 |
| 4.2 | Summary of redox potentials and HOMO/LUMO calculations of SC-SPDI₂ and SC-NPDI₂ (CH ₂ Cl ₂ , 298 K, $\epsilon_s = 8.93$). | 165 |
| 4.3 | Time constants for the different excited processes as observed from the fsTA measurements of SC-SPDI₂ and SC-NPDI₂ in different solvents. | 170 |

| | | |
|-----|--|-----|
| 4.4 | Driving forces (ΔG), Time Constants (τ), Rate Constants (k) for Symmetry-Breaking Charge Separation (SB-CS) of SC-SPDI₂ and SC-NPDI₂ in different solvents. | 172 |
|-----|--|-----|

List of Schemes

| Scheme | Title | Page |
|--------|--|------|
| 1.1 | Kinetic and thermodynamic profiles of photoinduced symmetry-breaking charge separation (SB-CS) and charge recombination (CR). LE represents the locally/singlet excited state of the PDI dimer. (k_{Fl} : rate constant of fluorescence emission k_{SB-CS} : rate constant of SB-CS; k_{CR} : rate constant for charge recombination; ΔG_{SB-CS} : free energy change for SB-CS; ΔG_{CR} : free energy change for CR. | 20 |
| 1.2 | Energy diagram of the photophysical pathway in PDI dimers leading to the formation of triplet exciton of the PDI by way of charge recombination (CR) through SOCT-ISC or RP-ISC mechanisms. | 27 |
| 2.1 | Exciton splitting diagram for a molecular dimer with staggered (J-aggregate), co-facial (H-aggregate), and Greek cross (+-aggregate) configurations. | 44 |
| 2.2 | The synthesis scheme of PTE-Br₀ and PTE-Br₂ | 45 |
| 2.3 | The synthesis scheme of PTE-Br₄ . | 46 |
| 3.1 | Showing the synthesis of PDI , Ref-PDI , and Sp-PDI₂ . | 95 |
| 4.1 | Showing the synthesis scheme for monomers (SPDI and NPDI) and dimers (SC-SPDI₂ and SC-NPDI₂). | 154 |

Chapter 1

Introduction to Molecular Exciton Theory and Symmetry-Breaking Charge Separation

1.1. Introduction

Sunlight is the most abundant energy source supporting life on earth, and effectively harvesting this vast energy resource may meet the world's rising energy demands. Over billions of years, nature has succeeded in perfectionating the energy and electron transfer processes in the photosynthesis complex for efficient energy transduction and chemical transformation (~100% efficiency).^{1,2} In natural photosynthesis, the excitation energy is captured by pigment molecular aggregates in the antenna complex of the photosystem (Figure 1.1). The temporarily stored excitation energy in pigment aggregate is further channeled to the reaction center (RC) photosystem (a pigment-protein complex embedded in a protein scaffold), where a stable charge-separated state across the membrane is created. Symmetry-breaking charge separation triggers a series of electron transfer events in the reaction center, coupled with the proton's translocation across the membrane. An electrochemical proton gradient is generated due to proton translocation used for ATP synthesis.^{3,4}

The light-harvesting (LH) complexes (or pigment-protein complexes) of the photosystem are involved in the initial processes such as i) absorption of sunlight by pigment aggregate, ii) ultrafast transfer of the excitation energy to a reaction center (RC). In photosynthetic plants, algae, and bacteria, the impressive structural diversity can be found in light-harvesting (LH) antennas, whereas reaction centers of photosynthesis organisms exhibit a slight variation in pigment-protein architectures. The photosynthetic unit of purple phototrophic bacteria comprises two pigment-protein complexes: The core complex (RC-LH1) and the peripheral complex (LH2).⁵ The reaction center (RC) of the purple bacteria photosystem is surrounded by a light-harvesting complex called LH1, together which forms the RC-LH1 complex. The RC-LH1 complex of the purple bacterial photosystem is surrounded by several LH2 complexes in a two-dimensional network.

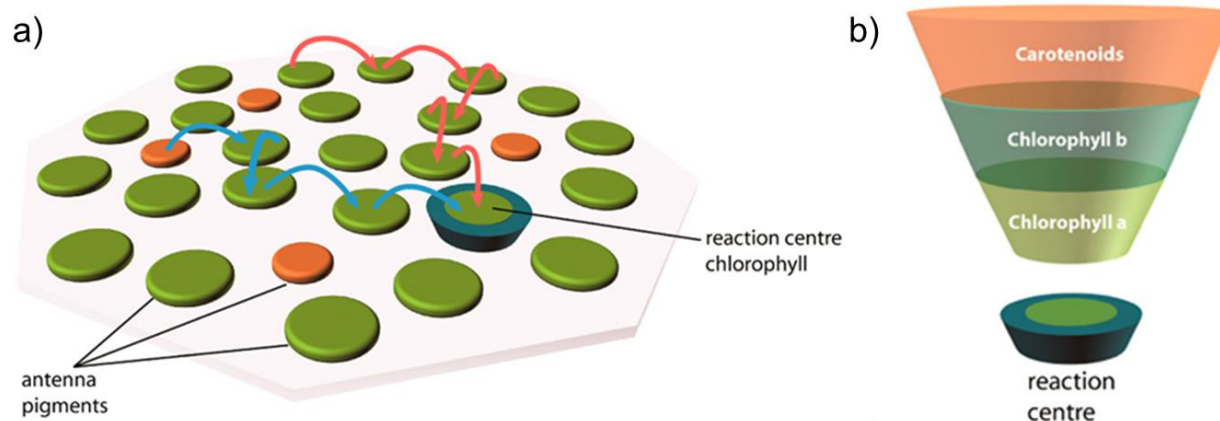


Figure 1.1: a) Schematic depicting excitation energy transfer pathways in models where chromophores are arranged in a two-dimensional planar distribution. b) Energy collection in an antenna system is depicted as an energy funnel. Shorter wavelengths of light are absorbed by peripheral antenna complexes, followed by energy-transfer processes to the lower-energy pigments located closer to the reaction center. Adapted with permission from ref (3). Copyright (2017) American Chemical Society.

The X-ray structure of the light-harvesting complex 2 (LH2) complexes from the purple non-sulfur photosynthetic bacterium *Rps. acidophila*, strain 10050 provides the pigment-protein arrangement in LH2.⁶ The LH2 complex features of 27 bacteriochlorophylls (BChl) pigment units which are arranged in two distinct circular rings (B800 and B850, Figure 1.2). These two pigment coalitions are generally known as B800 and B850, based on the absorption maximum at room temperature. The B800 ring of LH2 (green colored ring in Figure 1.2) comprises of well-separated 9 BChl pigments, whereas the B850 ring of LH2 (alternating red and orange colored ring in Figure 1.2) contains 18 strongly interacting BChl pigments. Though B800 and B850 pigment pools are made of identical BChl molecules, the difference in the absorption maximum of these two pigment aggregates (B800 and B850) arises from the difference in the intermolecular electronic interaction (excitonic coupling) between the monomer units of the two ring systems. In the B850 ring of LH2, the distance between the BChl pigment is less than 1 nm, which has resulted in strong excitonic coupling.

Upon absorption of a photon from sunlight, the excitation energy is quickly and efficiently transferred among the various LH2 complexes, which absorb at higher energies (800 and 850 nm). The downhill energy transfer cascade evolves when excitation energy is transferred from LH2 to

LH1 (LH1 absorbs at lower energy $\sim 870\text{--}880\text{ nm}$) and subsequently to the reaction center (RC), see Figure 1.2.⁷ Time-resolved spectroscopy measurement shows that the excitation energy is transferred within B800 and then to B850 take place on a picosecond time scale with a quantum efficiency. Further, the excitation energy is transferred to the neighboring B850 ring of another LH2 complex ($\sim 5\text{ ps}$) and finally to LH1 ($\sim 3\text{--}5\text{ ps}$). In the last step, the excitation energy is funneled to the reaction center from LH1 in the time constant of $30\text{--}40\text{ ps}$.⁸ One of the exciting aspects is that the light-harvesting complex of the purple bacterial photosystem shown in Figure 1.2 is made up of the same bacteriochlorophyll (BChl), which is stacked in a distinct arrangement with varying distance and relative position with respect to each other. By exploring the relative spatial orientation of the BChl pigments in the light-harvesting complex, thereby tuning the excitonic coupling among the BChl pigment, nature has perfectionated in efficient downhill energy flow in a photosynthetic organism.

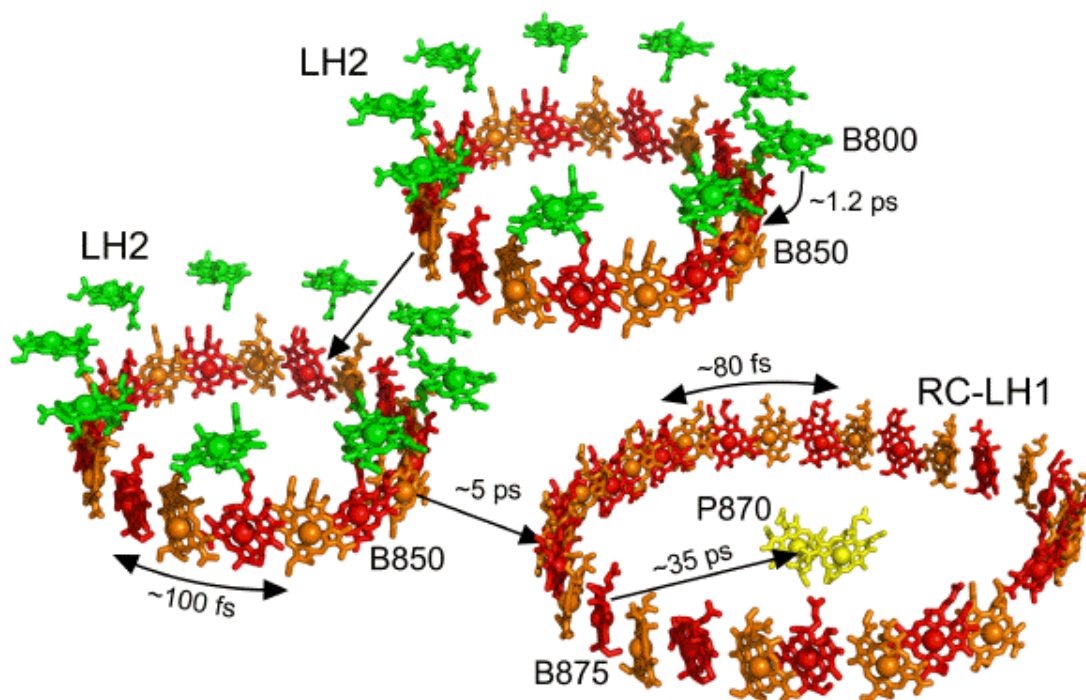


Figure 1.2: Energy transfer in the purple bacterial photosystem. B800 BChls of LH2 are shown in green, B850 BChls of LH2 and B875 BChls of LH1 are shown in alternating red and orange, and P870 BChls of the RC are shown in yellow. Lifetimes in picoseconds (ps) are given for the energy transfer events indicated by the arrows. Energy absorbed by antenna carotenoids is passed to neighboring BChls. Double-headed arrows indicate femtosecond (fs) energy migration within the B850 or B875 pigment rings (Adapted from ref (7)).

1.2. Origin of Exciton Theory

A comprehensive understanding of the structure-property relationships in molecular assembly is of prime importance to the design and development of advanced photovoltaics systems and artificial photosynthesis systems. The independent discovery of molecular aggregates in the 1930s by Scheibe and Jelley^{9,10} ignited considerable research from a fundamental to an applicational level.^{11–14} In their original studies, Scheibe and Jelley observed an unusual and exciting bathochromic shifted electronic absorption spectrum in a highly concentrated solution of 1,1'-diethyl-2,2'-cyanine, 1,1'-diethyl-2,2'-cyanine chloride (pseudocyanine, PIC). Later, Davydov¹⁵ proposed the exciton theory to understand the electronic excitation in molecular crystals. Based on Davydov's exciton theory, Kasha developed the molecular exciton theory, which correlates the photophysical properties and relative arrangement of excitonic coupled molecular systems^{11,16}, especially the electronic interaction of chromophores in photosynthetic antennae.¹⁷

When two or more chromophores are photoexcited, transition densities of the chromophores interact with each other and result in excitonic splitting. The excitonic coupling exchanges electronic excitation energy between molecules. At large inter-chromophoric separations, the excitonic coupling (J_{Coul}) arises from dipole-dipole interaction between transition dipole moments, and the excitation energy exchange is slow compared with relaxation processes. i.e., the excitation energy hops incoherently by the Förster energy transfer mechanism.^{17,18} When the magnitude of excitonic coupling is relatively large as compared to the reorganization energy, Coulombic interaction (J_{Coul}) modifies the stationary electronic states of the chromophoric system relative to the monomeric chromophores. According to the molecular exciton model, Coulombic interaction between chromophores in photosynthetic systems is weak, and the electronic state of the individual chromophoric unit is unchanged. An example of a molecular exciton interaction is shown in Figure 1.3. The left-hand side of the figure shows the naphthyl monomer molecular structure and electronic absorption spectrum. The molecular structure and electronic absorption spectrum of binorbornyl-bridged dinaphthyl molecules are shown on the right side of Figure 1.3. The strong excitonic coupled dinaphthyl dimer ($\sim 890\text{ cm}^{-1}$) results in the delocalization of excitation energy over both chromophores and energy splitting in the absorption band compared to the monomer naphthyl spectrum (Figure 1.3). The extent of exciton energy splitting is twice that of the Coulombic coupling (J_{Coul}).

According to Kasha's molecular exciton model, molecular assemblies are primarily classified into H-aggregates and J-aggregates. In H-aggregates (H denotes hypsochromic),

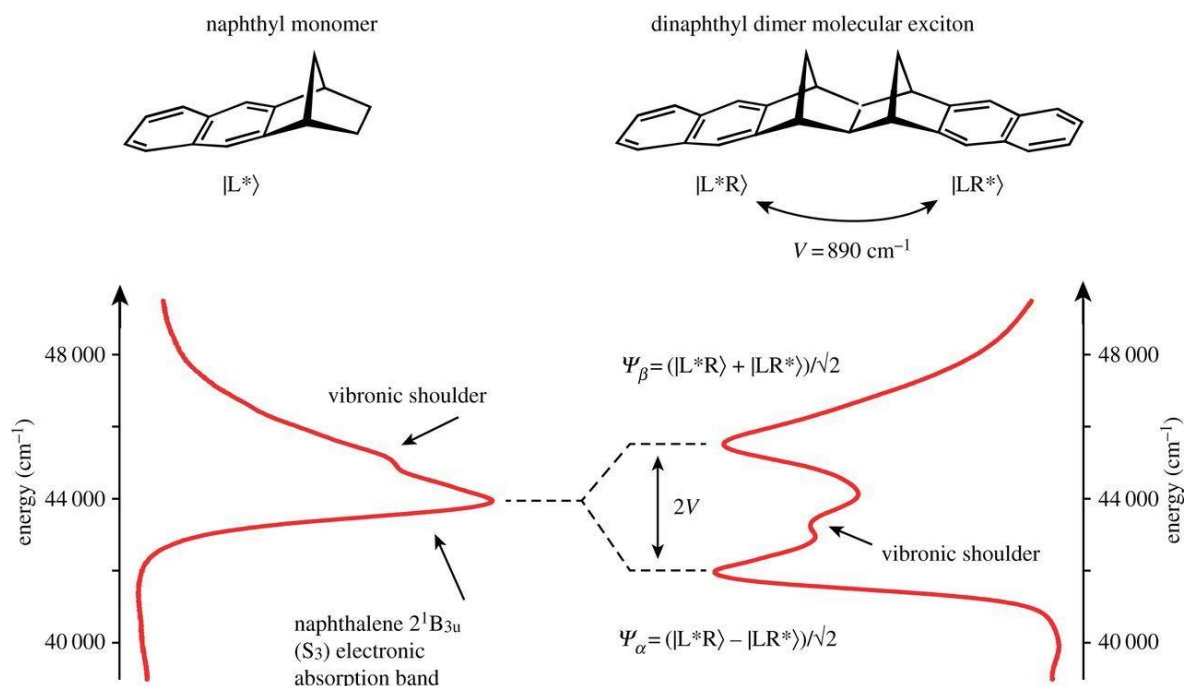


Figure 1.3: Exciton splitting in a naphthalene dimer. Adapted with permission from ref (17). Copyright (2004) The Royal Society.

chromophores are arranged in a sandwich association with Coulombic interaction between transition dipole moments resulting in energy splitting (Figure 1.4). The electronic transition to a lower energy level is forbidden due to the zero net transition dipole moment, whereas transition to a higher energy level is allowed in H-aggregates and results in a hypsochromic shifted (blue-shifted) absorption maximum and bathochromic shifted (red-shifted) fluorescence spectra compared to the monomer units.^{17,19} The optical properties of H-aggregates from cyanine dye monomers are shown in Figure 1.5.

Compared to monomers, J-aggregates (J, named after Jelley, one of the discoverer) exhibits red-shifted absorption and emission maximum due to the allowed transition to the lower energy level (Figure 1.4). In addition, the absorption and emission spectrum of J-aggregate shows a reduction in FWHM compared to the monomeric units. An example of optical properties of J-aggregate of cyanine dye is shown in Figure 1.4. Along with J and H-aggregates, Kasha predicted yet another unique class of cross dipole orientations having degenerate electronic states due to null Coulombic coupling (Figure 1.4). Parallely arranged molecular aggregates having transition dipoles with a slip angle of 54.7° known as the magic angle aggregate) are proposed to display monomer-like optical properties. (M-aggregate, Figure 1.4).²⁰ However, the Kasha dipole-dipole approximation fails to account for the observed photophysical properties of close-packed

chromophoric aggregate ($d \approx 3.5 \text{ \AA}$) due to the presence of orbital interaction among the chromophoric units.

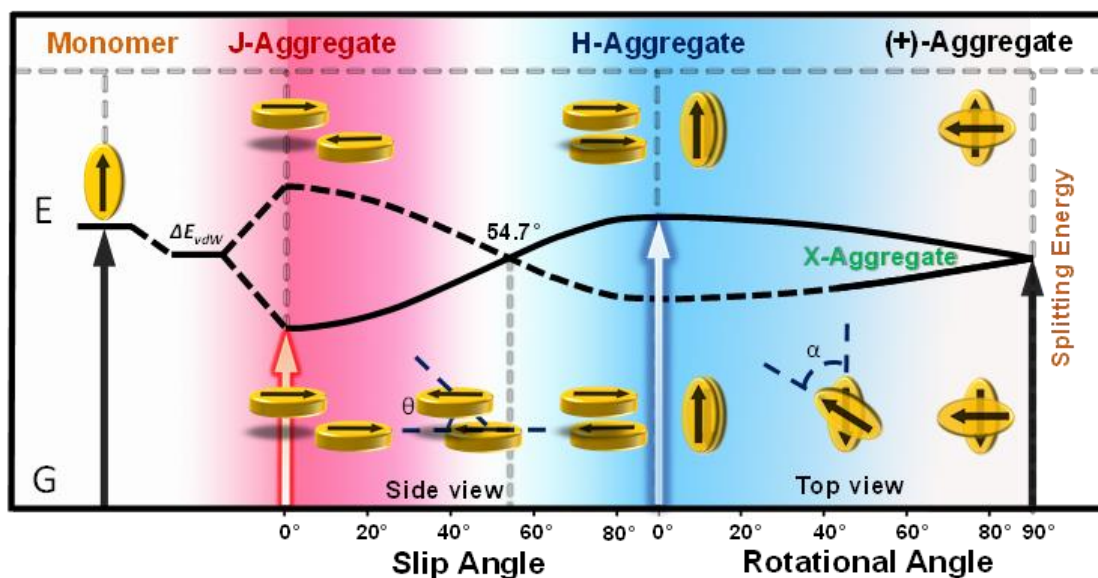


Figure 1.4: Schematic representation of exciton splitting for a molecular dimer with various orientations of transition dipoles.

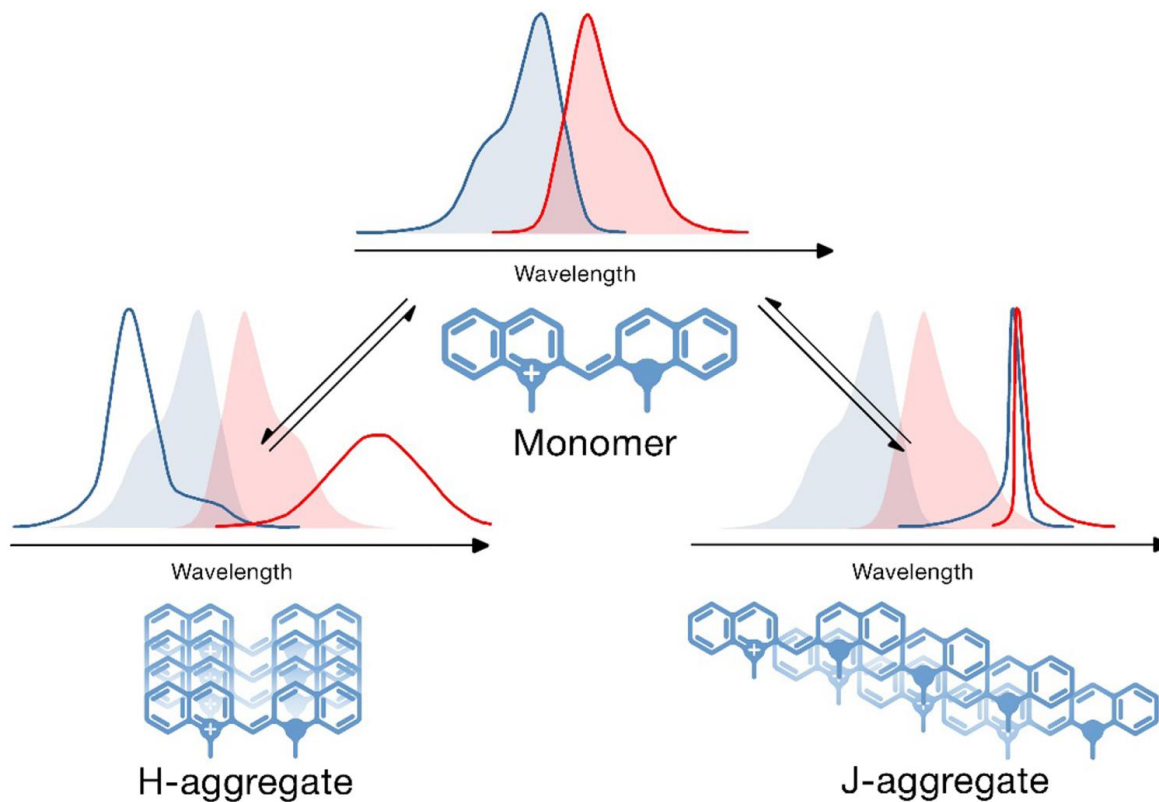


Figure 1.5: Schematic representation of the changes in absorption (blue) and fluorescence (red) spectra on the formation of H- and J-aggregates from cyanine dye monomers. Adapted with permission from ref (19). Copyright (2017) IOP Publishing, Ltd.

1.3. Exciton Theory; Kasha Model and Beyond

Spano and co-workers modified molecular exciton theory by introducing charge-transfer (CT) mediated coupling.^{21,22} In close-packed chromophore assembly with a shorter intermolecular distance ($d \approx 3.5 \text{ \AA}$), wave function overlap between the neighboring chromophore units results in a short-range charge transfer excitonic coupling (J_{CT}). As a result, net excitonic coupling and photophysical behavior of aggregate are defined by the interference of short-range CT and long-range Coulombic couplings.^{21,23}

The long-range Coulombic coupling originates from the interaction between two transition dipoles and can be represented using the ideal dipole approximation:^{24,25}

$$J_{Coul} = \frac{\mu^2 (1-3\cos^2\theta)}{4\pi\epsilon_0 R^3} \quad (\text{Eq 1})$$

where μ is the magnitude of the transition dipoles of the chromophores, R is the intermolecular distance, and θ is the slip angle. Conversely, molecular aggregates render a charge-transfer mediated exciton coupling (J_{CT}) originated from the orbital overlap between HOMOs and LUMOs of stacked chromophores.

$$J_{CT} = \frac{-2t_e t_h}{E_{CT} - E_{S_1}} \quad (\text{Eq 2})$$

Where t_e and t_h are electron and hole transfer coupling, depending on LUMO-LUMO and HOMO-HOMO interaction, respectively. E_{CT} and E_{S_1} are the energies of the virtual charge-transfer state and Frenkel exciton state, respectively. According to Eq 2, sign of J_{CT} depends on the signs of $t_e t_h$ and $E_{CT} - E_{S_1}$.

As a result, the net excitonic coupling in the close-packed chromophoric system is defined by the interference of charge-transfer and Coulombic couplings terms.

$$J_{Total} = J_{Coul} + J_{CT} \quad (\text{Eq 3})$$

The interplay between the J_{Coul} and J_{CT} render the photophysical behaviors of chromophoric assembly. While the hole and electron transfer integrals derived from wave function overlap between adjacent molecules and therefore diminish exponentially with molecular slip and distance.²² This sensitivity is depicted in Figure 1.6 for a perylene dimer.

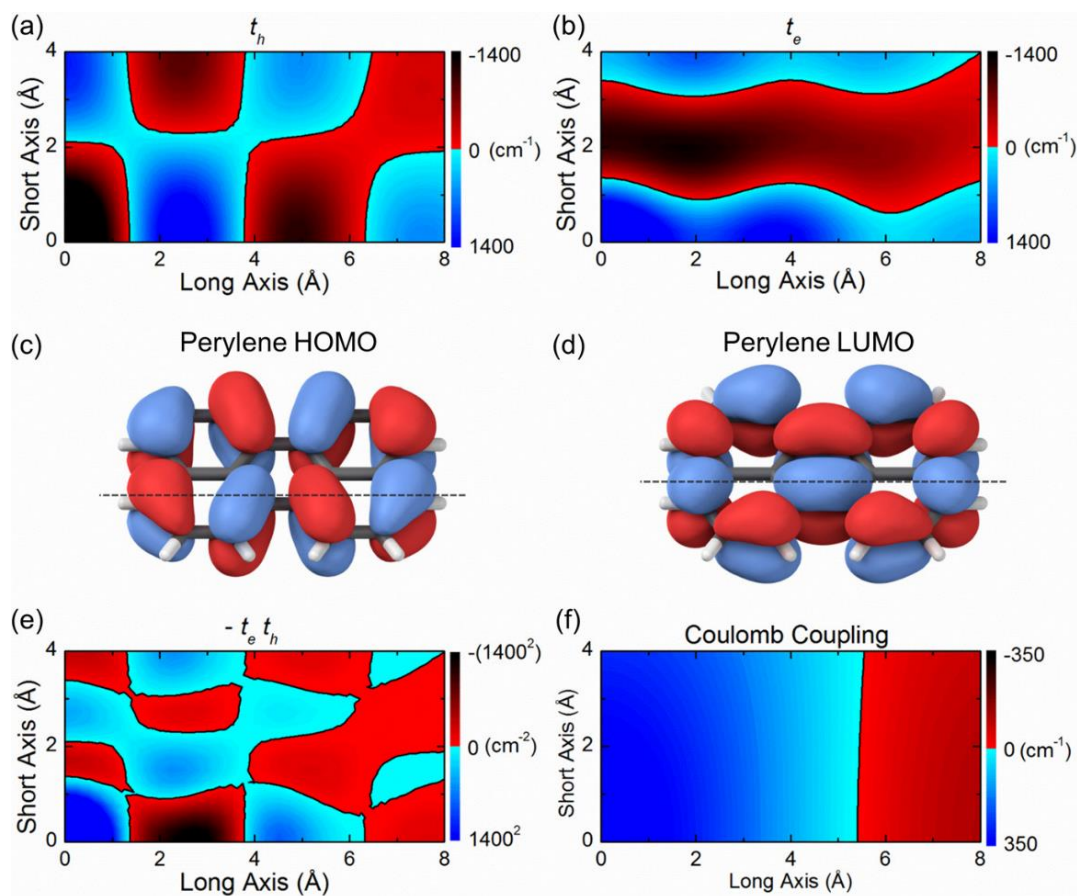


Figure 1.6: (a) t_h and (b) t_e within a π -stacked perylene dimer (3.5 \AA π -stacking distance) as a function of transverse displacement, evaluated from density functional theory (DFT) calculated energy level splittings. The DFT calculated (c) HOMO and (d) LUMO of perylene. (e) The product, $t_h t_e (\propto J_{CT})$, and (f) the unscreened Coulomb coupling as a function of transverse displacement, evaluated using time-dependent DFT calculated atomic transition charge densities. Red (blue) regions correspond to a J- (H-) type interaction. All DFT calculations use the B3LYP functional and cc-pVDZ basis. The sign convention for t_h and t_e based on symmetry operations under which the dimer transition dipole moment is symmetric. Adapted with permission from ref (22). Copyright (2017) American Chemical Society.

1.3.1. The magic angle stacked PDI aggregates. Researchers attempted to attain minimal excitonic coupling in organic chromophores through structural modifications and crystal engineering, which is supported by theoretical investigations.²⁶ The first experimental evidence for the Magic angle stacking, 54.7° slip-angled system, was unveiled by Xie and co-workers in a single crystal of N,N'-bis(4-methoxybenzyl)perylene-3,4,9,10-bis-(dicarboximide) (mb-PBI, Figure 1.7).²⁰ The magic angle stacked PDI aggregates exhibit marginal excitonic coupling due to the

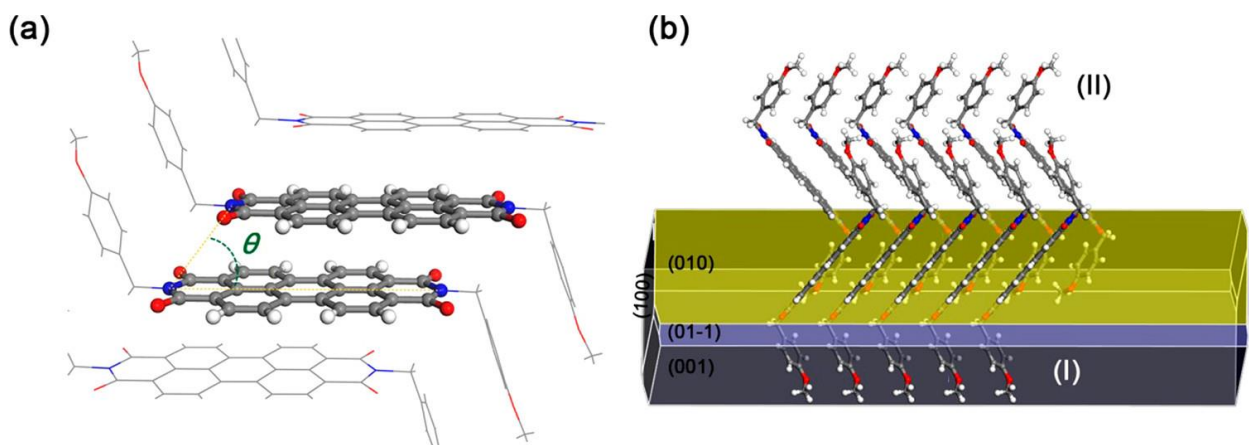


Figure 1.7: Single-crystal structure of mb-PBI. (a) Perspective view from the side of the core structure of mb-PBI. The angle θ indicates the slip angle of transition dipoles of adjacent molecules. (b) Morphology of the mb-PBI single-crystal. Adapted with permission from ref (20). Copyright (2018) American Chemical Society.

minimal long-range coupling allowing localization of Frenkel/CT mixing state with high fluorescence quantum yield in the solid-state. The importance of interference of Coulombic and CT-mediated couplings in defining total excitonic coupling was discussed by Spano and co-workers.²³

1.3.2. Null aggregate in Folda-Dimers PDI. In a closely arranged chromophoric assembly with small intermolecular distances, null excitonic coupled aggregates can be formed if the Coulombic and charge transfer mediated couplings have the same magnitude and opposite sign, i.e., destructive interference between Coulombic and charge transfer couplings. The perylenediimide foldamer reported by Würthner and co-workers demonstrated the first experimental evidence for the null exciton coupled aggregate originating from the interference of long-range Coulombic and short-range CT couplings (Figure 1.8). UV-Vis absorption and emission spectra of perylenediimide foldamer showed unchanged spectral features as that in the monomeric perylenediimide unit.²⁷ The calculated values of Coulombic ($+545 \text{ cm}^{-1}$) and charge transfer mediated couplings (-555 cm^{-1}) converged to a negligible net excitonic coupling (-10 cm^{-1}), rendering monomer-like optical behavior.

Engineering a minimal excitonic coupling through orthogonal stacking of chromophores having a rotational angle of 90° , remained as a challenge with several attempts reported over the past decades following the prediction of Kasha. Müllen and co-workers synthesized a zig-zag nanographene with D_{2h} symmetry possessing an angle of 90° between adjacent stacked molecules.²⁸ Along the line, the liquid crystals of triethyleneglycol substituted PDI reported by

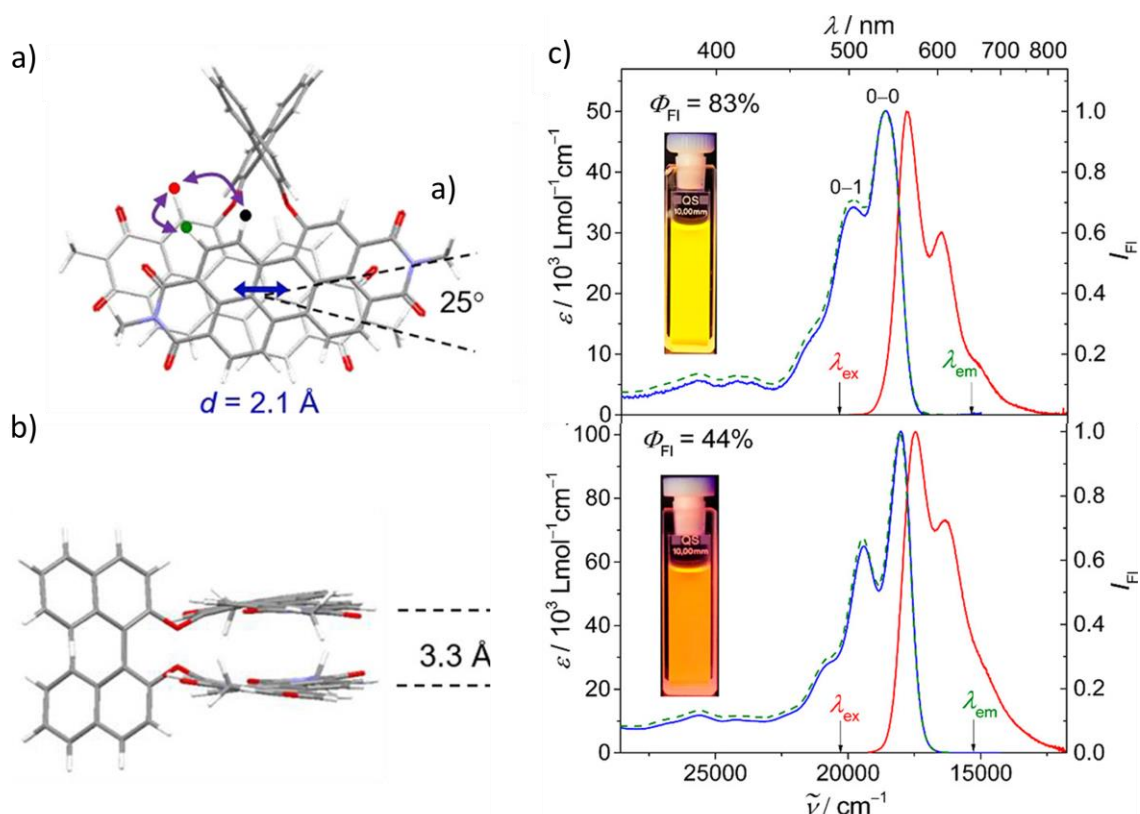


Figure 1.8: (a) Top view and (b) side view onto the geometry-optimized structures of Bis-PBI 3(S). (c) Absorption (solid blue lines, $c_0 = 10^{-5} \text{ M}$), normalized fluorescence (solid red lines, $c_0 = 10^{-7} \text{ M}$), and excitation spectra (green dashed lines, $c_0 = 10^{-7} \text{ M}$) of Bis-PBI 3(S) in TCE at room temperature. The wavelengths for excitation (λ_{ex}) and detection (λ_{em}) to obtain the fluorescence and excitation spectra, respectively, are highlighted by arrows in the graphs. Insets: Samples of Ref-PBI and Bis-PBI 3(S) under UV light ($\lambda = 365 \text{ nm}$) and fluorescence quantum yields (Φ_{FI}). Adapted with permission from ref (27). Copyright (2018) American Chemical Society.

Spieß and co-workers showed an orthogonal stacking of chromophores.²⁹ The cross dipole stacking with a rotational angle of 99.2° was reported in 2,5-bis(2-hydroxyethoxy)-1,4-bis(phenylethynyl)benzene.³⁰ The theoretical investigations devoted for the vanishing geometrical points of the exciton couplings gathered more fundamental understanding in the null aggregates photophysics.³¹

1.4. Symmetry-Breaking Charge Separation (SB-CS) in Molecular Constructs for Efficient Light Energy Conversion.

In photosynthetic bacteria, algae, and plants, the conversion of light energy into long-lived charge-separated species occurs in pigment-protein complexes called reaction centers (RCs).³² The

imbibing solar photons are harvested and the energy is transferred to weak excitonically coupled adjacent bacteriochlorophyll/chlorophylls via coherent exciton migration in the light-harvesting complex.³³ The energy of the harvested solar photon is further funneled into the reaction center-specific chlorophyll pairs ('special pair', P) through near-perfect quantum efficient energy transport. Finally, instead of transferring excitation energy to the neighboring pigment, these 'special pairs' (P) initiate the cascade of sequential electron transfer events in the reaction center by the symmetry-breaking charge-separation process (SB-CS).^{34,35}

The closely interacting bacteriochlorophyll/chlorophylls pair ('special pair', P) lies at the heart of the reaction center, where the highly reactive radical anion and cation are formed;³⁶ RCs of photosynthetic organism features pseudo- C_2 symmetric protein and pigment cofactors (dimeric pigment-protein complexes). Only one branch of cofactors is used for photon-driven charge separation; in the purple photosynthetic bacterial RC, the A branch is active, and charge separation takes place with near-unity quantum yield, and the B pathway is unused (Figure 1.9a).^{34,35} A series of ultrafast electron transfer reactions originate from the 'special pair', and each successive electron transfer step involves a decrease in the free energy and stabilization of reactive radical cation and anion by increasing the distance between them. All photosynthetic reaction centers namely purple photosynthetic bacteria, photosystem I, and photosystem II, exhibit similar primary reaction events.³⁷⁻³⁹ However, the presence of SB-CS suggested for green plant RC is still debated. The sequence of electron transfer events witnessed in the purple bacterial reaction center is shown in Figure 1.9a (PDB ID: 1M3X, Rhodospirillum rubrum). When the excitation energy reaches the reaction center, it is localized on the lowest excited state of 'special pair' (P). The time constants for sequential electron transfer from P* to H_A to Q_A to Q_B are 3 ps, 200 ps, and 200 μs, respectively, and the transfer of electrons from P* to H_A is thought to be via B_A (Figure 1.9a).³⁹

Inspired from nature's quantum efficient solar cell, the photosynthetic reaction center, which plays a crucial role in powering life processes by converting photon energy to chemical energy, scientists around the globe have made extensive experimental and theoretical exploration over the last few decades to recreate the primary charge separation process of photosynthesis. Polycyclic aromatic hydrocarbons (PAHs) and their derivatives exhibiting charge separation, energy transfer, singlet fission, and excimer formation are promising candidates for building photofunctional supramolecules.⁴⁰⁻⁴³ When the electronic communication between a pair of identical chromophores is not too strong and not too low, and their potentiometric bandgap is lower than the optical bandgap (E_{00}), photoexcitation of chromophoric pairs lead to excited state symmetry breaking charge-

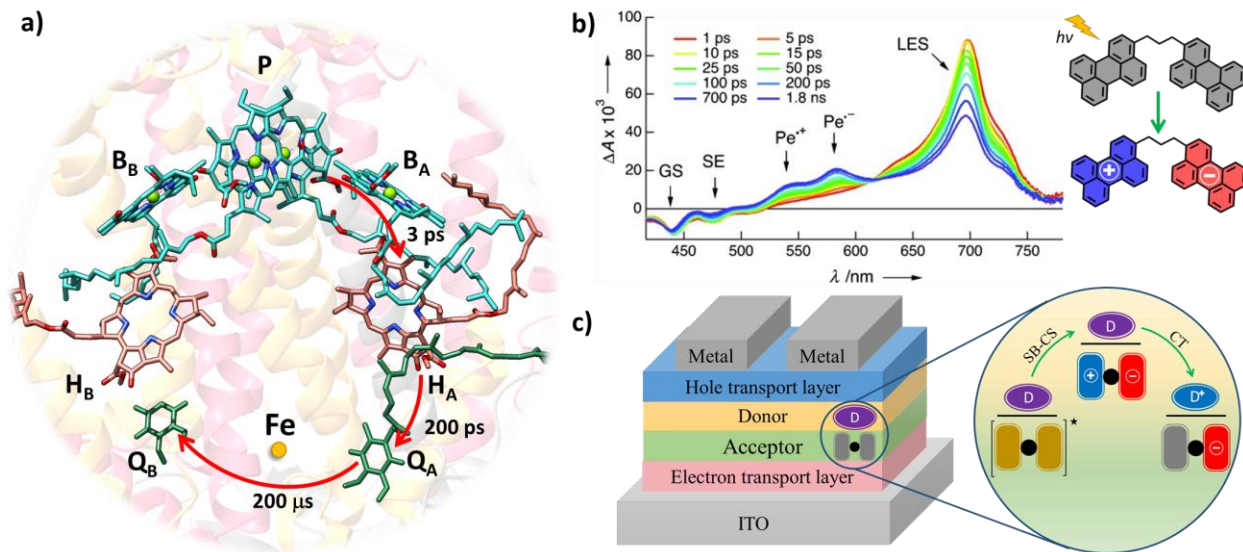
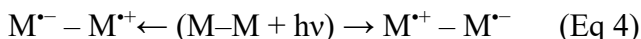


Figure 1.9: a) A simplified scheme of charge separation and electron transfer events in the purple bacterial reaction center, red arrows represent electron transfer pathways and the corresponding time constants. The green spheres in the middle of chlorins indicate the Mg atom in bacteriochlorophyll. P is a bacteriochlorophyll (BChl) dimer; B_A and B_B are monomeric BChls; H_A and H_B are bacteriopheophytins (BPhs); Q_A and Q_B are ubiquinones, and Fe is nonheme iron. b) Transient absorption spectra of biperylenylpropane in acetonitrile. c) A schematic representation of the simplest organic bilayer solar cell with proposed working principle based on sandwich configuration of conventional donor and an acceptor exhibiting symmetry-breaking charge separation.

separation (SB-CS) with the hole and electron localized on different chromophores,



Since the charge distribution among the identical chromophores is indistinguishable in SB-CS processes, this charge-separated state is known as the charge-resonance state.⁴¹ SB-CS in multichromophoric systems is analogous to exciton formation in silicon semiconductors where radical cation and anion are spatially separated easily due to low exciton binding energy (10-20 meV). In contrast, organic semiconductors have exciton binding energy of at least 100 meV, which leads to the formation of bound hole-electron pair, exciton.⁴⁴⁻⁴⁶ The SB-CS is well-explored in weakly coupled multichromophoric systems.⁴⁷⁻⁵³ Moreover, SB-CS processes in thin-film samples and polymers are an evolving topic of interest.⁵⁴ Intramolecular SB-CS between the perylene dimer covalently connected by propane linker in acetonitrile is shown in Figure 1.9b (GSB/GS: ground-state bleach, SE: stimulated emission, LE/LES: locally excited state, Pe^{•+}: perylene radical cation,

Pe⁻: perylene radical anion). The LE state formed upon photoexcitation eventually decays to form the charge-separated state of biperylenylpropane radical ion pair (Pe⁺ and Pe⁻). Notably, the totally symmetric excited state of the bimolecular dimer is effectively broken by the molecular vibration or fluctuation of the surrounding dielectric medium. Vauthey has presented a comprehensive account of fundamental concepts of SB-CS in multichromophoric donor-acceptor-based systems.¹⁷ The molecular architectures that can attain a prolonged charge-separated state by ultrafast charge separation and decelerate back charge transfer or charge recombination are indispensable for the effective functioning of photovoltaics and artificial photosynthesis.

1.4.1. SB-CS in organic photovoltaics. Organic photovoltaics (OPVs) is a rapidly emerging renewable energy source, with a reported power conversion efficiency of ~18%.⁵⁵ The working principle of OPVs is similar to that of nature's energy-conversion systems, wherein sunlight absorption, exciton formation, charge separation, and charge-carrier transport are the fundamental processes.^{56,57} The availability of different color absorbing materials and their ability to make efficient, transparent photovoltaic devices have attracted the commercial solar device market.⁵⁷ The efficiency of photovoltaics based on organic materials (OPV) is often limited by energetic and structural disorders.^{57,58} Measured open-circuit voltage (V_{oc}) of the organic solar cells is usually lower than those of inorganic solar cells. The lower V_{oc} magnitude is attributed to the large energy difference between the optical band gap and charge separated (CS) state, i.e., V_{oc} is directly related to the CT energies.⁵⁸ A prerequisite to achieve increased V_{oc} without compromising other important device parameters (short circuit current, J_{SC} or fill factor, FF) is lowering the driving force of charge-separation.⁵⁹ The energy loss during the charge-separated state formation (energy loss between the exciton and charge-separated state) is <100 mV for SB-CS, in contrast to the value of ~500 mV or more for charge separation in the donor-acceptor systems.⁶⁰ As a result, augmentation in the open-circuit voltage of OPV can be achieved by employing organic SB-CS materials as an active layer.⁶¹ Figure 1.9c shows the simplest structure of an organic bilayer solar cell with a superposition of a conventional donor and an acceptor exhibiting SB-CS. An excited localized singlet state is created upon photoexcitation, transforming into a charge-separated state through SB-CS. Finally, the donor (D) transfers an electron to the SB-CS acceptor (Figure 1.9c).

Thompson and co-workers successfully employed zinc chlorodipyrrin, (bis(dodecachloro-5-mesityldipyrrinato) zinc, ZCl) as an acceptor, which undergoes SB-CS at the donor/acceptor interface of the bilayered solar cell.⁶¹ The tetraphenyldibenzoperyflanthrene (DBP, donor)/ZCl (acceptor) bilayered cells exhibit higher open-circuit voltages of 1.33 V as compared to the

analogous (DBP)/C₆₀-based devices ($V_{oc} = 0.88$ V). Fourier-transform photocurrent spectroscopic and electroluminescence measurements have demonstrated that charge-separated state energies of DBP/C₆₀-based organic photovoltaic device amounts to 1.45 ± 0.05 eV, which is lower than CS state energy of 1.70 ± 0.05 eV in DBP/ZCl cell. A substantial increase in V_{oc} of the OPV devices observed when ZCl is employed as an acceptor (exhibits SB-CS) instead of the conventional acceptor (C₆₀), suggested an efficient and promising strategy to enhance the power conversion efficiency of OPV.

Perylene-3,4,9,10-bis(dicarboximide), PDI derivatives are a well-known class of visible-light absorbing organic chromophores exhibiting high fluorescence quantum yield and significant molar extinction coefficients. PDI derivatives have wide application in various organic electronics because of their robustness, appreciable electron-accepting behavior, high charge-carrier mobility, excellent thermal and photochemical stability.^{62,63} The optical properties and redox potentials of the PDI chromophores can be fine-tuned by careful substitution at the perylene core, whereas the imide substitution of PDI has only negligible influence.⁶⁴ By virtue of the stable radical cation and anion formation of PDI with strong transient absorption spectroscopic signatures, low internal reorganization energy ($\lambda_v = 0.25$ eV) and a highly conjugated flat molecular skeleton that facilitates electronic communication between neighboring molecules, SB-CS have been well explored in PDI-based multichromophoric systems.^{53,54,65,66} PDI is considered as a versatile chromophore that provides an opportunity to tailor different covalently linked multichromophoric arrangements through a simple bay and imide region substitution using diverse linkers or spacers (linkers or spacers are molecular entities that bridges two or more chromophores at the desired interchromophoric distance and relative spatial orientation). The researchers designed and synthesized various PDI assemblies and investigated their photophysics in light of these potential features.

1.4.2. Kinetics of SB-CS processes. Since SB-CS is considered to be a case of the electron transfer process, understanding of electron transfer theory can be used to describe SB-CS and charge recombination (CR) dynamics. The rate constant for SB-CS and CR can be estimated using the well-known classical Marcus formula;⁶⁷

$$k = \frac{2\pi}{\hbar} \frac{V^2}{\sqrt{4\pi\lambda k_b T}} \exp\left(-\frac{(\Delta G + \lambda)^2}{4\lambda k_b T}\right) \quad \text{only if } -\Delta G \leq \lambda \quad (\text{Eq 5})$$

Here, V indicates the electronic coupling matrix element between diabatic initial and final states; λ is the total energy required to distort the equilibrium geometry of the reactant state to the product

state, which is a measure of the electron-vibration coupling and is composed of solvation (λ_s) and vibrational (λ_v) components; ΔG is the free energy change between the equilibrium reactant and product states; k_b is Boltzmann constant; T is the temperature, and \hbar is the reduced Planck's constant. According to Eq. 5, the rate constant of charge separation principally depends on the Gibbs free energy change (ΔG), reorganization energy (λ), and electronic coupling (V). The most profound feature of the Marcus equation for charge transfer is the inverted region effect (Figure 1.10); the rate of electron/hole transfer will be slowed down given that the Gibbs free energy changes are more significant than the total reorganization energy (λ).^{68,69} However, the classical Marcus equation neglected the nuclear quantum effects, which could be playing a predominant role in the inverted regime ($-\Delta G > \lambda$). As a result, the classical Marcus theory is no longer valid when $-\Delta G > \lambda$.

The Marcus–Jortner–Levich (MJL) theory accounts for quantum effect in the charge transfer processes, described by Eq. 6, which overcomes the limitations of the classical Marcus model by separating the solvent reorganization energy (λ_s), from the solute reorganization energy (λ_v), and by incorporating the vibronic coupling between reactant and product state,⁷⁰

$$k = \frac{2\pi}{\hbar} \frac{V^2}{\sqrt{4\pi\lambda_s k_b T}} \sum_{n=0}^{\infty} \frac{e^{-S} S^n}{n!} \exp\left(-\frac{(\Delta G + \lambda_s + n\hbar\omega_{eff})^2}{4\lambda_s k_b T}\right) \quad (\text{Eq 6})$$

Here, S indicates the Huang-Rhys parameter, with $S = \frac{\lambda_v}{\hbar\omega_{eff}}$. $\hbar\omega_{eff}$ is the single effective vibrational mode that describes all the intramolecular modes. Eq. 6 accounts for the possible formation of the products in a vibrational excited state.

1.4.3. Thermodynamics of SB-CS. The thermodynamics of SB-CS and CR were estimated using the Weller formulation.^{71,72}

$$\Delta G_{CS} = e[E_{ox} - E_{red}] - E_{00} + C + S \quad (\text{Eq 7})$$

$$C = \frac{-e^2}{4\pi\epsilon_0} \left(\frac{1}{\epsilon_s r_{AD}}\right) \quad (\text{Eq 8})$$

$$S = \frac{e^2}{8\pi\epsilon_0} \left(\frac{1}{r_D} + \frac{1}{r_A}\right) \left(\frac{1}{\epsilon_s} - \frac{1}{\epsilon_{sp}}\right) \quad (\text{Eq 9})$$

$$\Delta G_{CR} = -(E_{00} + \Delta G_{CS}) \quad (\text{Eq 10})$$

where ΔG_{CS} and ΔG_{CR} are the free energy change of CS and CR, respectively, e is the electronic

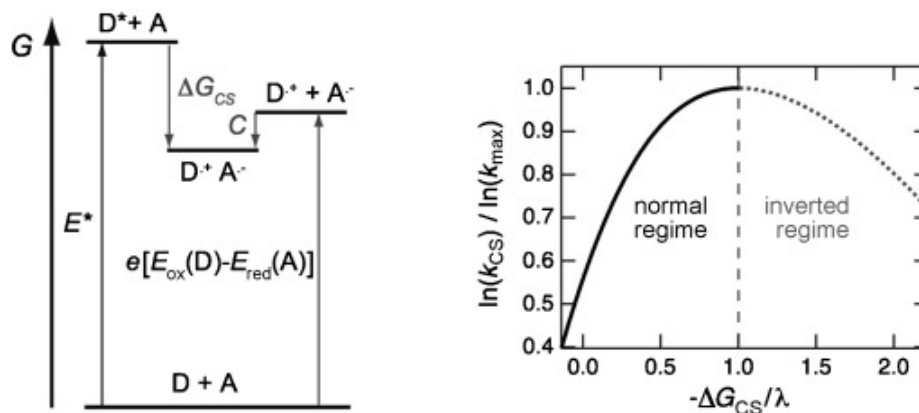


Figure 1.10: Left: Energy level scheme pertaining to a photoinduced CS. Right: Free energy dependence of the CS rate constant calculated using Equation (6) (Eq. (5) predicts the same behaviour in the normal regime). Adapted with permission from ref (41). Copyright (2012) WILEY-VCH Verlag GmbH & Co. KGaA, Weinheim.

charge, E_{ox} and E_{red} are the half-wave potential for one-electron oxidation and reduction of the donor and acceptor, respectively, E_{00} is the energy of the singlet excited state (the precursor of SB-CS), C and S are the Coulombic interactions between the two ions and their solvation energies, respectively, ϵ_S is the static dielectric constant of the solvent, ϵ_{sp} is the static dielectric constant of the solvent used for electrochemical measurements, r_{DA} is the center-to-center distance between donor and acceptor, and r_D and r_A are the ionic radii of the donor and acceptor, respectively. The intramolecular CS and CR are the two vital interfacial processes of organic solar cells, whereas the competition with other radiative and non-radiative decay channels directly influences the power conversion efficiency (PCE).

For the effectiveness of charge-separated state, CS has to be activationless ($-\Delta G \approx \lambda$) and hole-electron recombination should be in the inverted region ($-\Delta G > \lambda$).^{67,73} Predicting and tuning the rate constant of these two fundamental processes (rate constants of CS and CR, k_{CS} and k_{CR} , respectively) is the initial step to achieve charge generation efficiency at the interface and model the design of new materials. k_{CS}/k_{CR} is a paramount index for efficiently converting harvested light energy into a charge-separated state.⁷⁴ The chapter 1 discusses i) How the relative intermolecular arrangement of the chromophoric dimer/trimer affects the rate constant of CS and CR? ii) What are the radiative and non-radiative decay channels that compete with CS and CR in different configurations? iii) The role of rigidity of molecular skeleton and frontier molecular orbital interaction in rendering the charge separation. iv) How the substitution of electron-donating group on the parent molecular dimers influence the free energy change of charge separation? v) The effect

of change in solvent polarizability on the rate constant of SB-CS and charge recombination. vi) What are the different parameters that have to be considered while designing an efficient artificial 'special pair'?

1.4.4. SB-CS in photosynthetic reaction centers. We begin by establishing the relationship between efficient charge separation in different 'special pairs' of photosynthetic organisms and the significant contribution of charge-transfer (CT) mediated coupling to the total excitonic coupling.⁷⁵ Charge-transfer coupling (short-range) is governed by the electron and hole transfer integral derived from the frontier molecular orbital interactions, i.e., overlap between the highest occupied molecular orbitals (HOMOs) for hole transfer integral and lowest unoccupied molecular orbitals (LUMOs) for electron transfer integral. Nature has elegantly engineered 'special pairs' of different reaction centers resulting in a slip stacked arrangement of chlorophylls or bacteriochlorophylls with different spatial orientations (Figure 1.11). The strongly coupled dimers, 'special pairs', of the reaction center exhibit diverse net excitonic coupling in different photosynthetic organisms, purple photosynthetic bacteria (bRC, 500-1000 cm^{-1}), photosystem I (PSI, $\sim 300 \text{ cm}^{-1}$), and photosystem II (PSII, 85-150 cm^{-1}).⁷⁵ Though the strength of interaction varies in different 'special pairs', nature has preferred short-range (CT) coupling as a significant contributor to the total excitonic coupling over long-range Coulombic coupling (80 % in PSI and 70 % in bRC) to sink low-energy light quanta from the light-harvesting complex. Molecular orbital wavefunction overlap (hole and electron transfer coupling) between identical chlorophylls or bacteriochlorophylls facilitate the ultrafast formation of a symmetry-breaking charge-separated state by transfer of hole or electron. The extent of orbital overlap varies by the change in relative orientation of pair of chlorophylls or bacteriochlorophylls.

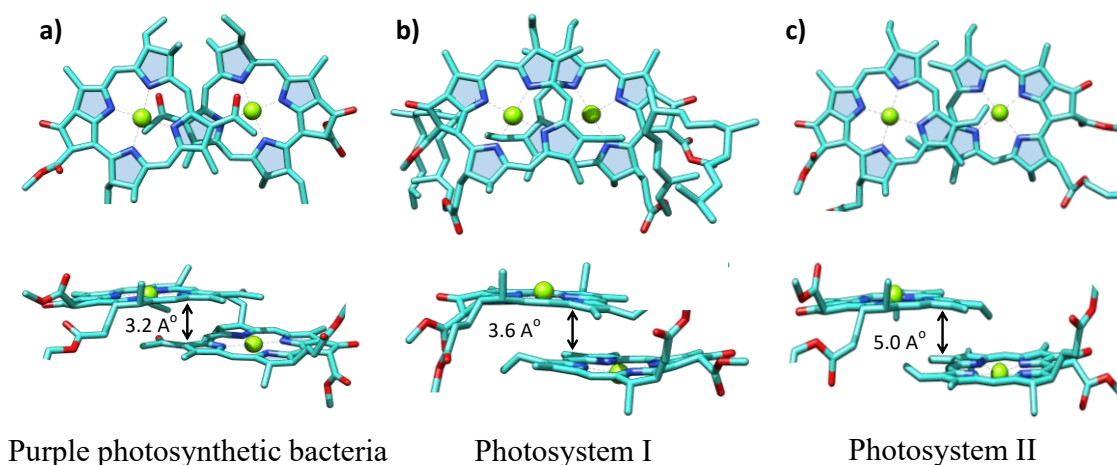


Figure 1.11: Geometry adopted by 'special pairs' in different reaction centers.

1.5. Photoinduced SB-CS in multichromophoric PDI architectures

1.5.1. Linearly arranged PDI dimers. Motivation acquired from nature's engineering marvel of the photosynthetic machinery, Wasielewski and co-workers have elegantly demonstrated the first example of SB-CS in head-to-tail arranged 1,7-bispyrrolidineyl-perylenediimide dimer (denoted as **1** in Figure 1.12, x = pyrrolidine).⁶² The ground-state structure of **1** resembles 9,9'-bianthryl, the most studied bichromophoric molecule with SB-CS properties, in which two anthracenes are connected in an edge-to-edge configuration mutually perpendicular to each other.^{49,76} The optimized structure of dimer **1** exhibits a center-to-center distance of 12.7 Å between the two PDI chromophores and a dihedral angle of 84°. The ground-state electronic absorption spectrum of dimer **1** shows a red-shifted spectral feature with an increased intensity ratio of the 0–0 and 0–1 absorption band (A_{0-0}/A_{0-1}) to the reference molecule (ref-PDI), indicating the weak J-type excitonic coupling. The linearly arranged PDI dimer **1** does not exhibit SB-CS in toluene (dielectric constant, $\epsilon = 2.38$), which could be due to the positive Gibbs free energy change for charge separation, hence, the rate constant of charge separation processes (k_{SB-CS}) may be much lower than rate constant of fluorescence emission (k_{Fl}). Whereas, in 2-methyl tetrahydrofuran (MTHF, $\epsilon = 6.97$), dimer **1** exhibits charge separation ($\tau_{SB-CS} = 55$ ps) and fast recombination ($\tau_{CR} = 99$ ps). The relative ratio of the rates for charge separation over charge recombination (k_{SB-CS}/k_{CR}) of dimer **1** amounts to 1.8. The solvent-dependent CS phenomena indeed represent the effect of surrounding solvent dielectric constant (ϵ) in facilitating SB-CS. Adams and co-workers probed SB-CS properties of an analogous non-substituted perylenediimide dimer (denoted as **2** in Figure 1.12) in DMF ($\epsilon = 38.3$). The dimer **2a** ($n = 0$) exhibits charge separation of lifetime $\tau_{SB-CS} = 113.25$ ps followed by hole-electron recombination ($\tau_{CR} = 316.45$ ps) and k_{SB-CS}/k_{CR} was found to be 2.79.⁷⁷

The UV-Vis absorption spectrum of pyrrolidine bay substituted PDI dimer **1** shows a massive red-shifted absorption maximum ($\lambda_{max}^{Abs} \sim 704$ nm) when compared to the non-substituted PDI ($\lambda_{max}^{Abs} \sim 520$ nm); as a result, optical band gap (E_{00}) is reduced in dimer **1** compared to dimer **2a**.^{62,64} Similarly, pyrrolidine substitution decreases the electrochemical bandgap of dimer **1**. The decrease in the k_{SB-CS}/k_{CR} ratio and accelerated charge separation rates of dimer **1** in a moderately polar solvent (toluene) compared to **2a** in a high polar solvent (MTHF) could have originated from the difference in Gibbs free energy change for CS and CR ($\Delta G_{CR} = -(E_{00} + \Delta G_{SB-CS})$). These examples showcase that substitution of the electron-donating group on the bay region of PDI

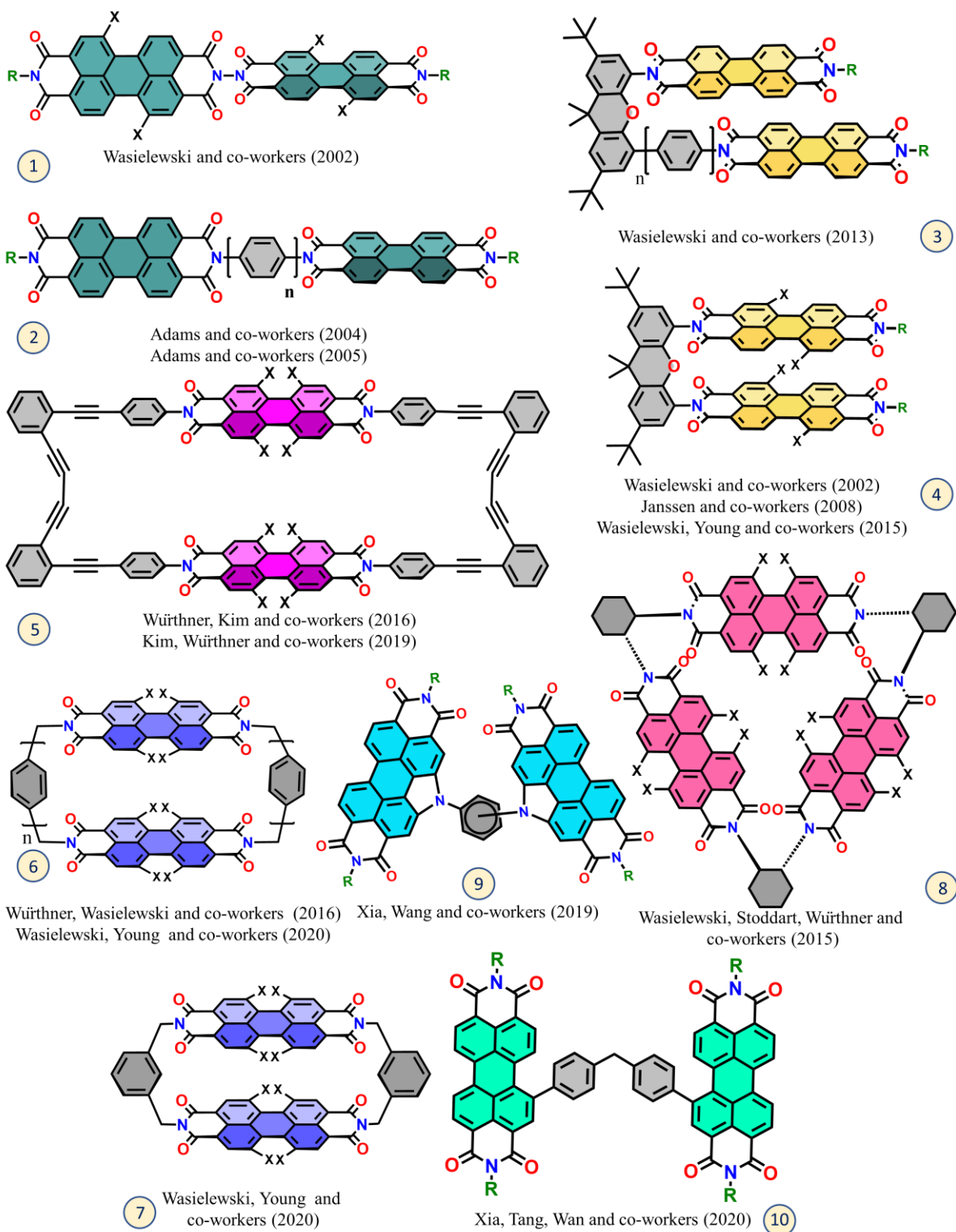


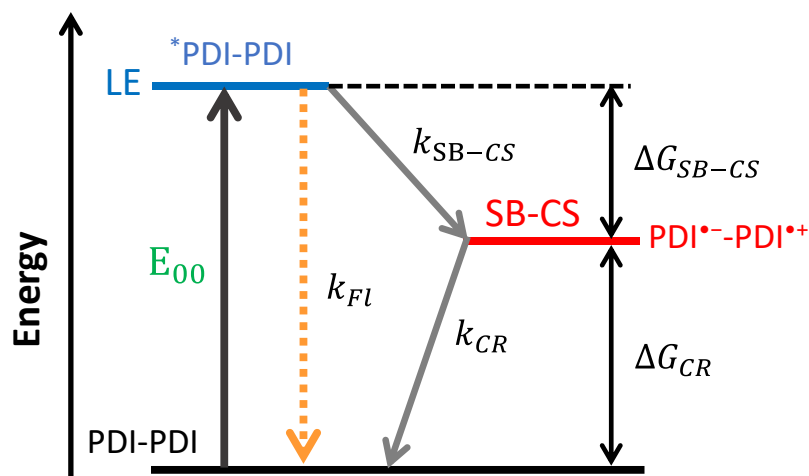
Figure 1.12: Structures of multichromophoric PDI systems exhibiting SB-CS discussed in chapter 1.

perturbs the optical and electrochemical bandgap of parent molecular dimer; consequently, Gibbs free energy change of the reaction gets affected, which could modify the rate constant of CS and

CR. Kinetic and thermodynamic profiles of photoinduced SB-CS and CR are shown in Scheme 1.1.

Adams and co-workers systematically investigated SB-CS in a series of PDI molecules connected through an oligo-1,4-phenylene bridge (denoted as **2** in Figure 1.12) to comprehend the distance-dependent charge-transport properties using time-resolved emission spectroscopy (TRES) and standard electron-transfer theories.⁶⁵ Photoexcitation of the dimers **2a**, **2b** ($n=0, 2$, respectively) populates singlet excited state (*PDI-PDI) with excitation energy localized on one of the PDI chromophores. The initially populated excited singlet state decays to a charge-separated state via SB-CS ($\text{PDI}^{\cdot-}\text{-PDI}^{\cdot+}$) in competition with radiative decay of the excited state to the ground state by fluorescence emission. When the distance between the PDI units increases from 12.9 Å (**2a**) to 21.6 Å (**2b**), the electronic coupling matrix element between reactant and product state decreases ($V = 97 \text{ cm}^{-1}$ for **2a** and 51 cm^{-1} for **2b**). As a result, the rate constant of charge separation reduces, $k_{\text{SB-CS}} = (59.8 \text{ ps})^{-1}$ and $(291.5 \text{ ps})^{-1}$ for **2a** and **2b**, respectively, and fluorescence quantum yield increases, $\Phi_{\text{FL}} = 0.73$ for **2a** and $\Phi_{\text{FL}} = 0.80$ for **2b**. The rate of charge recombination of **2a** and **2b** was found to be $k_{\text{CR}} = (2.26 \text{ ns})^{-1}$ and $(1.22 \text{ ns})^{-1}$, respectively, and the relative ratio, $k_{\text{SB-CS}}/k_{\text{CR}}$, of **2a** and **2b** amounts to 37.8 and 4.2 in DMF, respectively.

This example clearly shows the distance dependency of symmetry-breaking charge separation. An effective electronic coupling (V) between a locally excited (LE) state and SB-CS



Scheme 1.1: Kinetic and thermodynamic profiles of photoinduced symmetry-breaking charge separation (SB-CS) and charge recombination (CR). LE represents the locally/singlet excited state of the PDI dimer. (k_{FL} : rate constant of fluorescence emission; $k_{\text{SB-CS}}$: rate constant of SB-CS; k_{CR} : rate constant for charge recombination; $\Delta G_{\text{SB-CS}}$: free energy change for SB-CS; ΔG_{CR} : free energy change for CR.

state (wavefunction overlap between frontier molecular orbitals) is necessary for efficient charge separation to compete and win against the other decay processes such as fluorescence and non-fluorescence decay to the ground state. As a result, the approach of building organic bilayered solar cells by employing edge-to-edge arranged multichromophoric architecture is limiting the efficient solar energy conversion endeavor. It should be noted that in order to achieve near-unity quantum yield of SB-CS state, the rate constant of SB-CS processes (k_{SB-CS}) must be tenfold more than the rate constant of other competing deactivation pathways.

1.5.2. Slip-stacked PDI dimers. Wasielewski and co-workers designed and synthesized a covalently coupled slip-stacked PDI dimer (denoted as **3** in Figure 1.12) with a linear offset between PDI molecules.⁷⁸ The cofacial PDI molecules are linked to xanthene (Xan) through the phenyl bridge. The PDI dimer exhibit a slip of 4.3 Å incorporating one phenyl group into Xan (**3a**; n=1) and a slip of 7.9 Å incorporating two phenyl groups into Xan (**3b**; n = 2). Though these slip stacked conformations markedly resemble the ‘special pair’ arrangement of photosynthetic organisms,⁷⁵ spectroscopic signatures corresponding to the SB-CS phenomena were not observed for this molecule due to the formation of Xan^{•+}-PDI^{•-} charge-separated and excimer-like states.⁷⁸ However, tuning the energetics of the parent chromophoric dimer by substituting an electron-donating group or utilizing an inert spacer or linker may enable us to access an intramolecular charge-separated state. The particular work exemplifies that when employing photophysical active linkers to stitch chromophores, the charge-separated state formed between the linker and parent molecule competes with the desired end product (SB-CS state) and reduces the efficiency of CS state formation.

1.5.3. Cofacially arranged PDI dimers. Wasielewski and co-workers have developed a sandwich configuration of PDI dimer (denoted as **4** in Figure 1.12) by linking pyrrolidine core substituted PDI chromophores to xanthene through the 4-position.⁶² Geometry optimized structure of dimer **4a** (x = pyrrolidine) shows two PDI molecules oriented in a nearly cofacial arrangement with an interplanar distance of average 3.7 Å. Sandwich arranged PDI molecules are excitonically coupled in dimer **4a**, and the resultant ground-state absorption spectrum shows a blue-shifted absorption maximum with a significant decrease in the A_{0-0}/A_{0-1} compared to the ref-PDI (characteristic features of H-type excitonic coupling). The cofacial stacked dimer **4a** exhibits SB-CS in a low polar solvent (toluene), which is in sharp contrast to the linear analog dimer **1** (CS of **1** is switched off in toluene). The dimer **4a** displays ultrafast charge separation ($\tau_{SB-CS} = 0.52$ ps) and retarded charge recombination $\tau_{CR} = 222$ ps), and the relative ratio, k_{SB-CS}/k_{CR} , of **4a** amounts

to 426.9 in toluene. Whereas in 2-methyltetrahydrofuran (MTHF), rate constants of charge separation and recombination are accelerated ($\tau_{SB-CS} = 0.33$ ps and $\tau_{CR} = 38$ ps) and k_{SB-CS}/k_{CR} of **4a** is found to be 115. This particular example highlights the concept that engineering the relative orientation of chromophores in molecular dimers enables us to tune the excited-state processes in the same dielectric environment by regulating electronic communication and optical bandgap. The rate constant of charge separation in symmetric pair of molecular dimers is decided by the Gibbs free energy change of the reaction and electronic coupling matrix element between the initial and final state.

Later, similar sandwich arranged PDI dimers (denoted as **4** in Figure 1.12), core substituted PDI dimer (**4b**, x = 3,5-di-*t*-butylphenoxy), and bare PDI dimer (**4c**, x = hydrogen), were reported by Wasielewski and co-workers, and Janssen and co-workers.^{48,79–81} In contrast, 3,5-di-*t*-butylphenoxy-substituted (**4b**) and unsubstituted dimers (**4c**) do not show any characteristic excited state spectral signature of charge separation (PDI⁺-PDI⁻) between two PDI chromophores; instead, upon photoexcitation **4b** and **4c** in toluene shows excimer-like emission and triplet formation. SB-CS processes of **4a** in toluene is aided by the electron-donating pyrrolidine substituent that lowers the energy of CS state below the initially populated locally excited singlet state. When the energetics favour, cofacial or sandwich arranged chromophoric dimers show efficient charge separation and long-lived charge-separated state than the linearly arranged chromophoric analogue due to the enhanced frontier molecular orbital interaction of two monomeric PDI units, which enhances required hole/electron transfer coupling for ultrafast charge separation.

However, SB-CS in sandwich-like molecular architecture faces a bottleneck named excimer formation. The first example of excimer mediated intramolecular charge separation in a rigid cofacial arranged PDI dimer (denoted as **5** in Figure 1.12) tethered by two phenylene-butadiynylene was elucidated by Würthner, Kim, and co-workers.⁸² The optimized geometry of **5a** (x = hydrogen) revealed a rigid face-to-face arrangement with a PDI–PDI interplanar distance (d) of 3.24 Å (less than that of **4a**; d = 3.7 Å) with a 28.6° rotational displacement. According to Kasha's molecular exciton theory, electronic transition to the lower exciton is forbidden in the sandwich-arranged molecular dimer (H-type aggregate). Compared to the ref-PDI, bichromophoric system **5a** shows an electronic absorption spectrum with 0–1 vibronic band having higher intensity than the 0–0 band, indicating strong H-type excitonic coupling. The fluorescence spectra of **5a** in different solvents (chloroform, dichloromethane, and THF) show distinct spectral features suggesting the presence of an excimer state (Figure 1.13). In THF, broad and red-shifted excimer-like bands are

observed, the hallmark of excimer state, whereas in chlorinated solvents, the superimposed monomer-like bands onto the excimer band are noticeable. The observation infers that the excited-state dynamics of **5a** vary with solvents. The fluorescence quantum yield (Φ_{FL}) of **5a** in chlorinated solvents is 10-fold lower than THF, suggesting effective non-radiative channels of **5a** in chlorinated solvents. Femtosecond transient absorption (fs-TA) measurements of **5a** in different solvents unambiguously confirm to the excimer-mediated charge separation (Figures 1.13b and 1.13d). The fs-TA spectra of **5a** in THF (Figure 1.13b) shows positive excited-state absorption (ESA) band at ~ 600 nm assigned as a long-lived excimer state, which decays with a lifetime of 16 ns. However, fs-TA of **5a** in CHCl_3 shows (Figure 1.13d) a broad and featureless ESA band upon photoexcitation with an average lifetime of 36 ps (assigned as an excimer state). The excimer state of **5a** gradually decays with the evolution of a new spectral species, ESA red-shifted to 690 nm and a new band at 970 nm, assigned as a charge-separated state ($\tau_{CR} = 1.1$ ns). The coexistence of PDI radical anion (ESA ~ 690 nm) and cation (ESA ~ 970 nm) bands confirm to the SB-CS between the two PDI moieties in **5a** (in CHCl_3). The ratio of rates, k_{SB-CS}/k_{CR} , of **5a** amount to 30.5. The intermediate exciton trap state, excimer, lowers the rate of the charge-separated state generation; subsequently, CS efficiency diminishes, and excitation energy loss as a form of emission originates from the

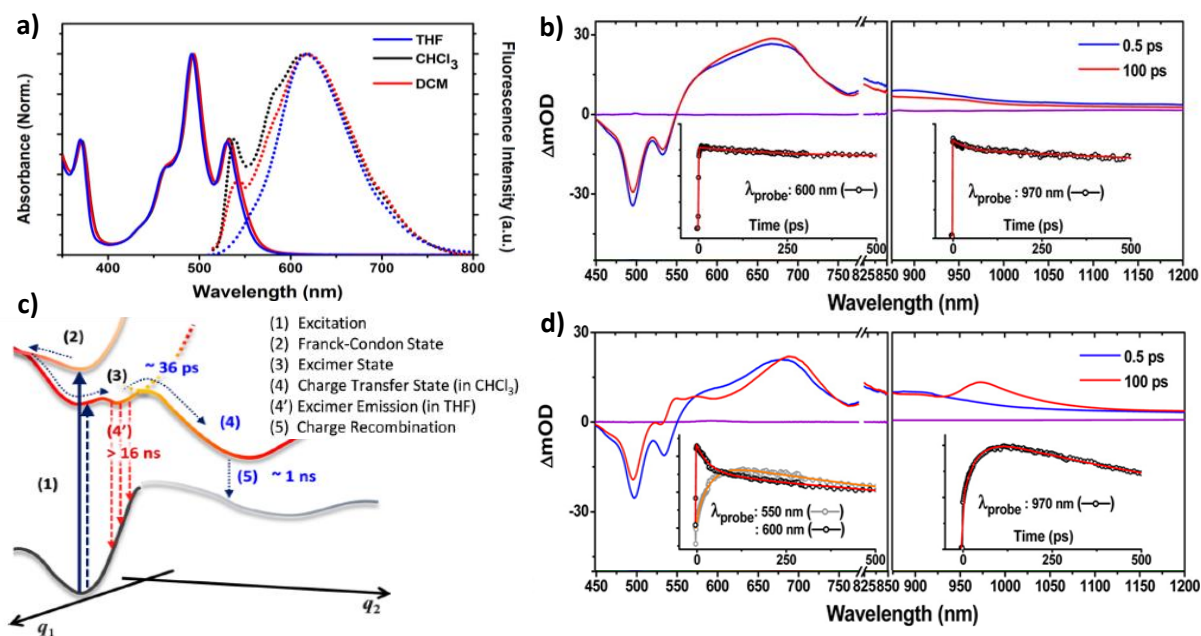


Figure 1.13: (a) Steady-state absorption (solid lines) and fluorescence (dotted lines) spectra of **5a** in different solvents. Femtosecond transient absorption spectra of **5a** in (b) THF and (d) CHCl_3 . Insets show the decay profiles. (c) Energy state diagram of **5a** depicting excimer-mediated SB-CS process.

excimer state. Figure 1.13c depicts the excimer-mediated SB-CS processes in dimer **5a**. The solvent modulated CT resonance enhancement in the excimer state of a cofacially stacked 4-tert-butyl-phenoxy bay substituted PDI dimer **5b** (x = 4-tert-butyl-phenoxy) in a rigid cyclophane were reported by Kim, Würthner and co-workers. The CT resonance-enhanced excimer state can be evolved through incomplete SB-CS from the relaxed excimer state with the assistance of a high dielectric environment.⁵⁹

Excimer state formation in cofacial PDI dimers is widely accepted as configurational mixing of the Frenkel exciton ($FE, |MM\rangle_{FE}^* = |M_1^*M_2\rangle + |M_1M_2^*\rangle$) and charge-transfer ($CT, |MM\rangle_{CT}^* = |M_1^+M_2^-\rangle|M_1^-M_2^+\rangle$) resonance states. i.e., superposition of the singlet excited charge resonance states.⁸³⁻⁸⁵

$$|MM_{EX}^*\rangle = \alpha (|MM\rangle_{FE}^*) + \beta (|MM\rangle_{CT}^*) \quad (Eq. 11)$$

According to Eq. 11, the characteristics of the excimer state depend on the relative contribution of each eigenstate (α and β), which is determined by distance and relative orientation between the chromophore and dielectric medium of the surrounding environment. Excimer acts as an exciton trap, and the occurrence of excimer state in organic semiconductor materials hinders the exciton diffusion to heterojunction interface to generate electron/hole pair by CS. As a result, the quantum yield of the desired CS process and device performance may reduce when the rate of excimer formation is faster than charge separation processes.^{83,86} However, mixing Frenkel excited singlet state and CT state may not always form the classic excimer; instead, it imparts CT character to the excited state without the fingerprint feature of an excimer state that is termed as “excimer-like state”.^{41,87} The excited-state transient absorption spectra of chromophoric excimers are typically present as broadened, featureless absorptions in the visible region that resemble the singlet excited-state transient absorption.

Würthner, Wasielewski, and co-workers have classically laid out the basic concepts for eliminating intermediate parasitic pathway, excimer state, in the charge-separation processes of cofacial PDI dimer (denoted as **6** in Figure 1.12) by tuning the distance between the chromophoric dimer.⁸⁸ The interplanar distance between the two PDI chromophores of dimer **6a** (n = 1 and x = 4-(tert-butyl) phenol) was calculated to be $\sim 7\text{\AA}$ which is approximately double the distance in dimers **4** and **5**. The UV-Vis absorption spectrum of **6a** shows an unperturbed absorption maximum at 582 nm, with a slight decrease in the A_{0-0}/A_{0-1} intensity ratio than ref-PDI in CH_2Cl_2 , indicating the weak excitonic coupling between the two PDI chromophores. Ten-fold fluorescence quenching

of **6a** in CH₂Cl₂ compared to ref-PDI directs the presence of a non-radiative deactivation process in the dimer. The charge separation (CS) occurs in ~161 ps in CH₂Cl₂ followed by charge recombination (CR, τ_{CR} = 8.90 ns) to triplet manifold of PDI (³*PDI, 27% singlet oxygen generation). The rate constant of CS in dimer **6a** were decelerated when compared to cofacially arranged molecules **4** and **5** due to reduced charge transfer coupling (*V*) and thermodynamic driving force for charge transfer (ΔG_{CS}) at longer distances and k_{SB-CS}/k_{CR} of **6a** is reported as 55.3. The interplanar separation (*d*) between the monomeric units is the crucial factor for tuning the rate constant of charge separation, as the electronic coupling matrix element (*V*) decreases exponentially with an increase in the distance. According to Weller equation (Eq.7), the distance dependence of ΔG_{CS} arises entirely from Coulomb term (*C*), which accounts Coulombic interaction between the radical ion pairs (when dimers exhibit identical optical and electrochemical band gaps in the same dielectric environment). The charge recombination of radical cation and anion of PDI molecule caused the generation of a significant amount of PDI triplet state, which could be an indirect consequence of cofacial arranged **PDI** dimer. The rivalry between charge recombination to ground state and triplet manifold population accelerated the decay of charge-separated state, resulting in the diminishing of much required long-lived charge separation.^{58,89}

Yet another attempt by Wasielewski, Young, and co-workers, the distance-dependent rate constant of SB-CS has been presented in cofacial stacked PDI dimers (denoted as **6** and **7** in Figure 1.14), with p-xylylene (**6a**; *n* = 1), 4,4'-diylidimethane-1,1'-biphenyl (**6b**; *n* = 2), and m-xylylene (**7**) spacers, (*x* = 4-(tert-butyl)phenol).⁹⁰ The interchromophoric distance is systematically varied from ~6.4, ~7.3, and ~10.8 Å for dimers **7**, **6a**, and **6b**, respectively, by maintaining the sandwich arrangement of the chromophoric dimers (Figure 1.14a). UV-Vis absorption spectra shows an increase in A_{0-0}/A_{0-1} as the distance between the PDIs increases, indicating the weakening of excitonic coupling between the PDIs. Global analysis of fs-TA data of each dimer in toluene does not show any spectral fingerprint of the PDI triplet manifold. In CH₂Cl₂, SB-CS is more energetically feasible and all the cyclophanes (**7**, **6a**, and **6b**) exhibit photoinduced SB-CS. Following Marcus theory, the rate constant of charge separation decreases as the electronic coupling and Gibbs free energy change for CS decrease, i.e., τ_{SB-CS} = 22 ps and 184 ps for dimer **7** and **6a**, respectively. Consequently, rate of charge separation competes with fluorescence decay and as the distance increases and fluorescence quantum yield increases (Φ_{FL} = 0.06, 0.18, and 0.85 for dimer **7**, **6a**, and **6b**, respectively), charge separation efficiency lowered. Potential energy surface showing change in the charge transfer coupling matrix element (*V*) and Gibbs free energy

change of SB-CS processes when the distance among the PDI chromophores increases are presented in the figure 1.14b. The rate constant of charge recombination for dimer **7** was observed as $k_{CR} = (7.3 \text{ ns})^{-1}$, and the k_{SB-CS}/k_{CR} of dimer **7** is reported as 331.8. In addition, charge recombination populates triplet manifold and triplet state decays with a lifetime of $\tau_T = 680 \text{ ns}$, 742 ns and 47.2 ns for **7**, **6a**, and **6b**, respectively. This particular example reinforces that when the charge transfer coupling (or orbital interaction) reduces, the rate constant of charge separation gradually decreases and competes with the rate constant of fluorescence emission processes. Schematic representation of energy levels of PDI dimers (**6a**, **6b** and **7**) shows triplet exciton generation via SB-CS processes in Scheme 1.2. Direct excitation of PDI dimers populated a locally excited state (LE), followed by the formation of the SB-CS state and its decay to form a triplet exciton state, which is accessible only in the polar solvent.

Triplet population through a polar transition state is well known in the literature either via spin-orbit charge-transfer intersystem crossing (SOCT-ISC) or radical pair intersystem crossing

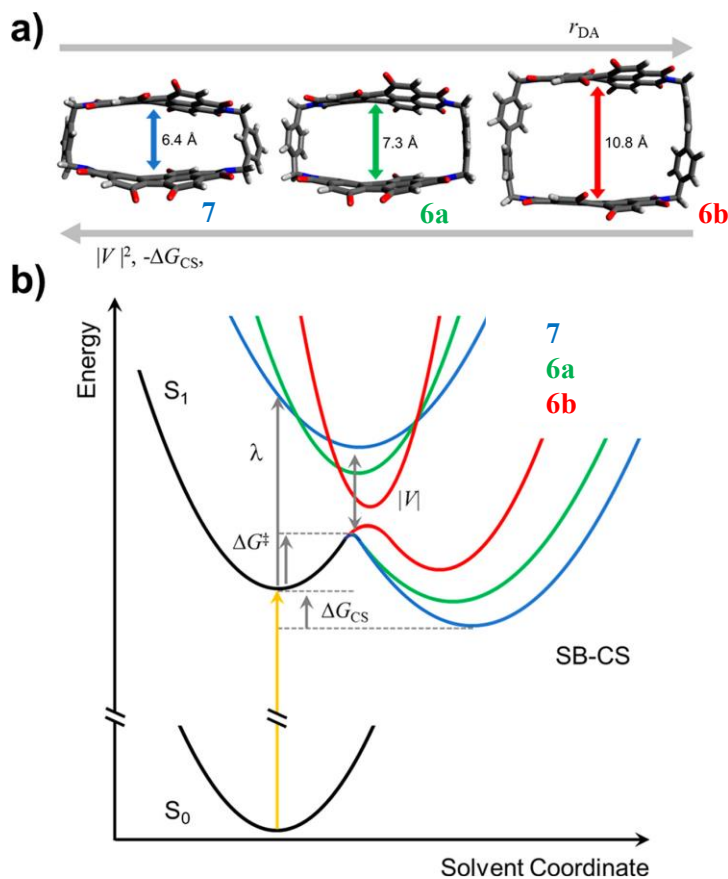
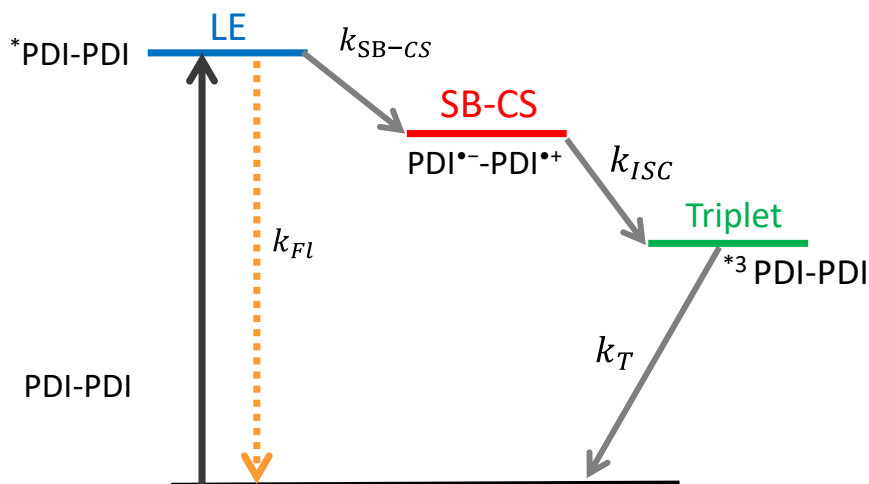


Figure 1.14: (a) Optimized structures of **7**, **6a**, and **6b** showing increasing interplanar distance. (b) Schematic potential energy diagrams for SB-CS in the dimers in CH_2Cl_2 . Arrows are shown for **7**.



Scheme 1.2: Energy diagram of the photophysical pathway in PDI dimers leading to the formation of triplet exciton of the PDI by way of charge recombination (CR) through SOCT-ISC or RP-ISC mechanisms.

(RP-ISC) mechanisms.^{89,91} A significant loss channel of the CS state in organic photovoltaics (OPV) is the recombination of charges to the triplet state. An organic semiconductor with a triplet manifold coupled to the charge-separated state has limited lifetime of charge separation; as a result, the efficiency of OPV may go down. The natural selection of magnesium (Mg) in bacteriochlorophyll or chlorophyll pair of reaction centers can be rationalized by weak spin-orbit coupling of Mg. In comparison, heavier atoms such as platinum (Pt) and palladium (Pd) induce large spin-orbit coupling due to the heavy atom effect that could promote the triplet population.⁷⁵ Triplet manifold formation via charge separation has been subjected to extensive study because CS state serves as a source of generating free electrons and holes, which further migrate towards electrodes to produce photocurrent. The open-circuit voltage of the organic solar cell gets reduced if the charge recombination promotes triplet exciton generation.^{58,92} In addition, the triplet state energy of PDIs is sufficient to generate very active singlet oxygen by the triplet energy transfer mechanism, which may damage the active layer of organic solar cells and result in low performance.⁹² The hole-electron recombination to the triplet exciton can be minimized by optimizing the precise arrangement of multichromophoric systems.

1.5.4. SB-CS in triangularly arranged PDI trimer. The SB-CS in a tailor-made PDI-based molecular triangle (denoted as **8** in Figure 1.12, x = phenoxy) was presented by Wasielewski, Stoddart, Würthner, and co-workers.⁶⁶ The rigid triangular architecture was synthesized by covalently linking the 1,6,7,12-tetra (4-phenoxy)-perylene-3,4:9,10-tetracarboxylic dianhydride

with (R, R)-trans-1,2-cyclohexanediamine. The steady-state UV–Vis absorption spectrum of trimer **8** (Figure 1.15a) shows a decrease in the A_{0-0}/A_{0-1} and unperturbed absorption maximum when compared to ref-PDI in CH_2Cl_2 , indicating weak excitonic coupling between the PDIs in trimer **8**. The fluorescence experiments of trimer **8** show (Figure 1.15b) the absence of features corresponding to red-shifted and long-lived excimer-like emission, ruling out the possibility of an emissive excimer state. Notably, significant quenching of fluorescence in trimer **8** when compared to ref-PDI is consistent with the effective non-radiative decay process such as SB-CS. Depending on the rate of charge-transfer, energetically degenerate four symmetry-broken ion-pair states have been generated from the initially populated Frenkel exciton state (S_1 , Figure 1.15c). The fs-TA measurement demonstrated the excited-state dynamics of trimer **8** (Figure 1.15d) in CH_2Cl_2 . The singlet excited state of trimer **8** (ESA at 705, 951, and 1028 nm; Figure 1.15d) undergoes ultrafast decay to a new transient absorption band characterized by positive features in the visible and near-IR region (ESA at ~ 473 , 619, 780, 969, and 1077 nm) corresponding to PDI radical cation (ESA ~ 473 and 619 nm) and anion (ESA ~ 780 , 969, and 1077 nm). The elegant design provides adequate electronic communication for ultrafast charge separation ($\tau_{\text{SB-CS}} = 12.0$ ps) and prevents π - π

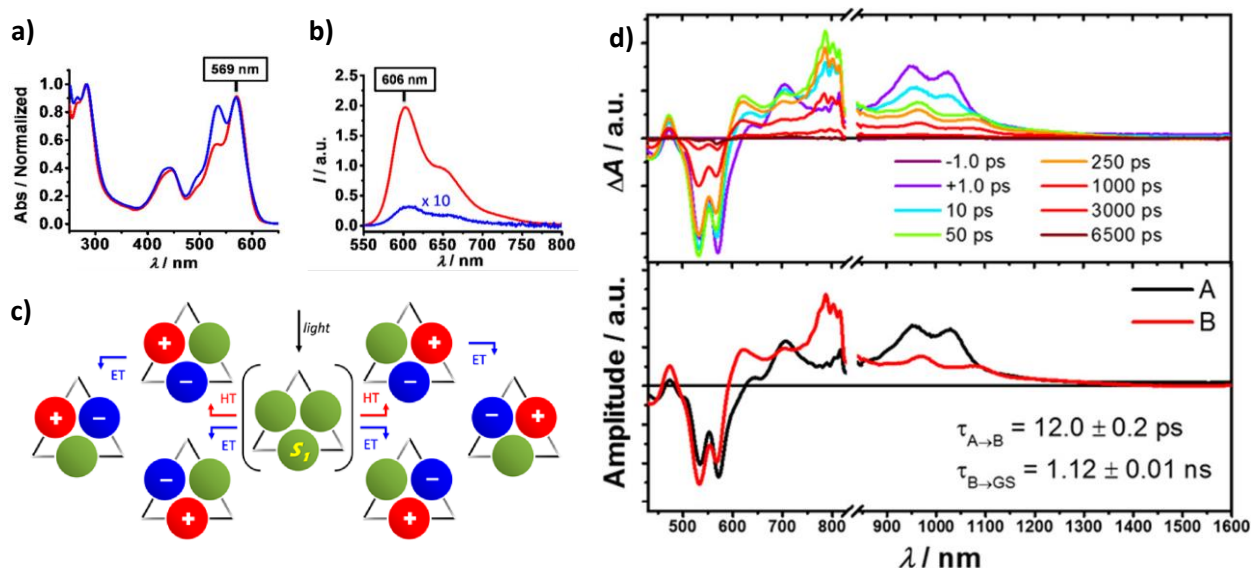


Figure 1.15: a) Normalized steady-state UV–vis absorption and (b) emission spectra of Ref-PDI (red) and trimer **8** (blue) in CH_2Cl_2 . c) Schematic of symmetry-breaking charge separation in trimer **8** upon photoexcitation. d) (top) Femtosecond transient absorption spectra of molecule **8** showing the excited-state dynamics after photoexcitation. (bottom) Species-associated spectra reconstructed from global fits to the sequential $A \rightarrow B \rightarrow$ ground state (GS) model, where A is singlet excited state ($^1\text{*PDI}$) and B is the SB-CS state.

stacking and concomitant excimer formation, exciton trap, in CH₂Cl₂. The decay of the charge-separated state to the ground state occurs with a rate constant of $k_{CR} = (1.12 \text{ ns})^{-1}$ exhibiting no evidence of triplet excited state of PDI and k_{SB-CS}/k_{CR} of trimer **8** was found to be 93.3.

1.5.5. SB-CS in angularly arranged PDI dimers. So far, we have discussed the SB-CS and CR processes of the bottom-up tailored PDI dimers (**1-7**) and trimer (**8**) architecture that are covalently linked through the imide region of PDI chromophores. A diverse and innovative design of connecting monomeric units by exploring the perylene core of PDI was reported by Xia, Wang, and co-workers.⁹³ N-annulated PDI dimers linked via a phenyl bridge at the para- and meta-positions (denoted as **9**, Figure 1.12) exhibit symmetry-breaking charge separation in polar solvents. The steady-state absorption and emission spectra of para- and meta-substituted PDI dimer (**9a** and **9b**, respectively) retained the spectral feature of ref-PDI in toluene with a slight decrease in the absorption A_{0-0}/A_{0-1} ratio, indicating the presence of electronic communication between the two adjacent PDI units through the phenyl bridge and excitation may have localized on one of the PDIs in dimers. The fluorescence quantum yields of dimers are sensitive to the surrounding dielectric medium and dramatically decreases as the solvent polarity increases, signifying the presence of another effective deactivation channel. fs-TA measurement unravels the fluorescence quenching mechanisms; **9a** and **9b** dimers exhibit SB-CS in polar solvents. The rate constant of charge-separation for meta-substituted dimer **9b** ($k_{SB-CS} = (\sim 323 \text{ ps})^{-1}$) is approximately ~ 29 times slower than the para-substituted PDI dimer **9a** analogs, $k_{SB-CS} = (\sim 12.4 \text{ ps})^{-1}$ in THF. In the same solvent, the difference in total reorganization energy (λ) and Gibbs free energy change of CS is negligible ($\Delta G_{SB-CS} = -0.196 \text{ eV}$ for **9a** and -0.246 eV for **9b**). The fast SB-CS in para-substituted derivatives is mainly due to the effective electronic communication or conjugation through the para-substituted phenyl bridge compared to the meta-substitution, further confirmed by quantum chemical calculation. The electronic coupling (V) between LE state and SB-CS state has been calculated using Generalization of Mulliken Hush (GMH) approximations⁹⁴ and offered the magnitude of 0.0428 eV ($V = 345.2 \text{ cm}^{-1}$) and 0.0089 eV ($V = 71.8 \text{ cm}^{-1}$) for **9a** and **9b**, respectively. The charge-separated state of dimer **9a** decay to the ground state with a rate constant of $k_{CR} = (1.94 \text{ ns})^{-1}$ and k_{SB-CS}/k_{CR} of **9a** amounts to 156.4. This work reiterates the importance of charge transfer integrals in tuning the rate constant of charge separation.

Wan, Tang, Xia, and co-workers registered intramolecular excited-state CS and CR dynamics of diphenyl-methane-bridged PDI dimer (denoted as **10** in Figure 1.12) in different solvents.⁹⁵ Geometry optimization of dimer **10** showed a highly twisted structure with a torsional angle of 73°

between PDI units and exhibiting a conformational change in the excited state due to the attachment of PDIs to a rotatable single bond. The UV-Vis absorption spectra of dimer **10** in toluene (TOL, $\epsilon = 2.38$), and dimethylformamide (DMF, $\epsilon = 36.7$) are almost identical and exhibit a slight bathochromic shift (8 nm) of the 0-0 absorption band and decrease in the A_{0-0}/A_{0-1} ratio as compared to ref-PDI, indicating the excitonic coupling among the PDI chromophores. The fluorescence emission quantum yield of dimer **10** drastically quenches as the solvent polarity increases and displays broader, less structured, and red-shifted emission spectra, indicating the dipolar character of the emissive state and the presence of different deactivation pathways. A comprehensive picture of the dynamics of dimer **10** in different solvents was provided by fs-TA measurement (Figure 1.16). The initial (delay time = 0.2 ps) fs-TA spectra of dimer **10** (Figure 1.16a) in toluene closely resemble the fs-TA spectra of ref-PDI, ascribed to the locally excited state of PDI dimer. As the time delay progress to 15 ps, the fs-TA spectra of dimer **10** shows (Figure 1.16b) a gradually red-shifted stimulated emission signal (SE ~ 600 nm), and the broadening of the ESA features around 700–780 nm, implying the formation of a new species having a dipolar character (the relaxed S_1 state). The theoretical calculation confirmed the dipolar nature of the relaxed S_1 (CT state) state. The optimized S_1 state shows a dihedral angle of 43° , which is lower than the ground state dihedral angle of 73° . For the relaxed S_1 state, the dipole moment of dimer **10** increases from the ground state magnitude, $\mu_{S_0} = 0.4$ D to $\mu_{S_1} = 9.4$ D. The difference in the dipole moment between the ground state and relaxed S_1 state is attributed to the excited-state conf-

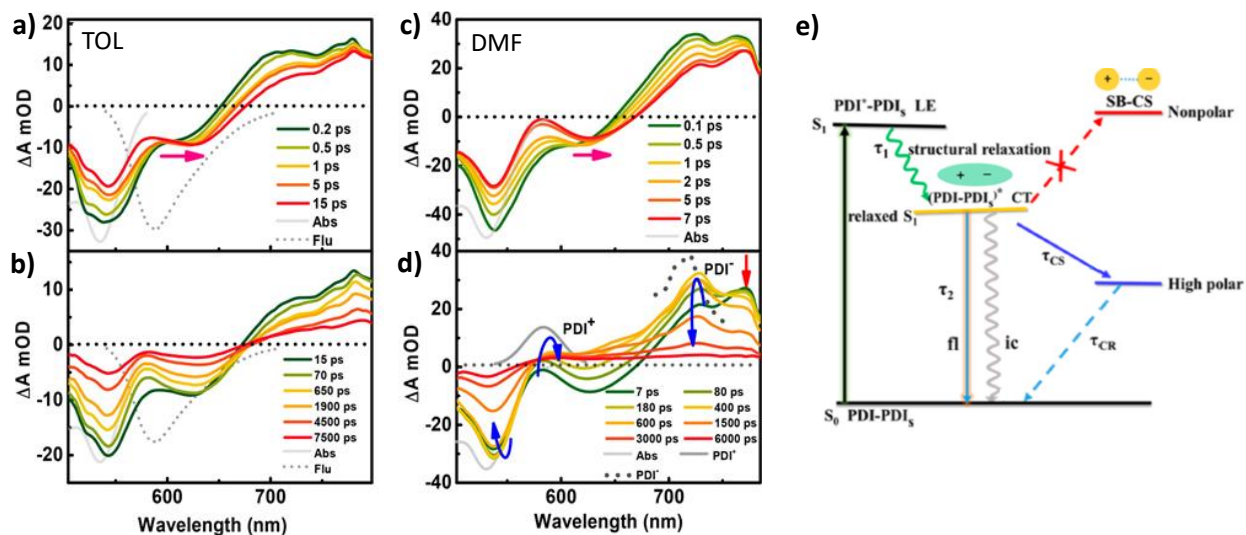


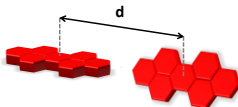

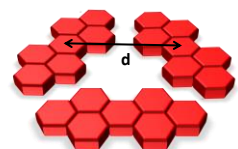
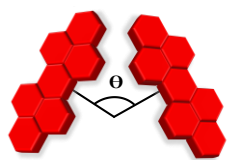
Figure 1.16: a-d) fs-TA spectra of **10** in toluene (TOL, a and b) and dimethylformamide (DMF, c and d) in short delay time (a and c) and long delay time (b and d). e) Simplified energy diagram showing relaxed-singlet state mediated symmetry-breaking charge separation in dimer **10**.

ormational change. In the more extended delay time, ESA and SE bands decay slowly without the evolution of SB-CS signature, which is consistent with positive $\Delta G_{SB-CS} = +0.47$ (The CS process of **10** is disfavored in toluene). The fs-TA spectra of dimer **10** in DMF show similar spectral features initially (Figure 1.16 c, d). However, the increase in the delay time triggered the evolution of a new ESA band at 590 nm (radical cation) and 720 nm (radical anion) with an apparent growth of the GSB signal simultaneously, corresponding to the SB-CS state formation. The new absorption bands unambiguously indicate SB-CS formation ($\tau_{SB-CS} = 241.7$ ps) from a relaxed singlet state (CT state). At the end of the delay time, the charge-separated state completely decay to the ground state with a rate constant of $k_{CR} = (1.90 \text{ ns})^{-1}$ and the ratio k_{SB-CS}/k_{CR} of **10** was found to be 7.9. Figure 1.16e showing energy level diagram of dimer **10** exhibiting solvent-dependent SB-CS processes proceeded via relaxed singlet state (CT state). When SB-CS of multichromophoric system competes with the energy dissipating processes such as relaxed singlet state formation (emissive CT state), fluorescence emission, and radiationless transitions, the effectiveness of the charge-separated state is limited. The use of flexible linkers in holding two chromophores at the desired position is not considered as an efficient strategy because it imparts a high degree of freedom around the linker, which opens up unwanted deactivation pathways and minimizes the desired end product, CS state. The essential rigidity could be the reason why nature preferred to keep necessary photonic components embedded in a protein scaffold with an extensive hydrogen-bonded network.^{35,75}

To gain a comprehensive understanding of the interplay of different parameters in achieving enhanced lifetime of SB-CS state in multichromophoric PDI materials, we tabulate key parameters that define the fate of SB-CS (Table 1). The recent experimental and theoretical exploration of multichromophoric organic electronic materials have significantly enhanced our fundamental understanding of SB-CS and hole-electron recombination processes. A substantial amount of understanding has evolved regarding how various parameters such as electronic coupling, Gibbs free energy change, solvent polarization, and different wasteful deactivation channels affect the energy landscape of charge separation (CS) and charge recombination (CR) processes. However, a comprehensive picture of how the relative spatial orientation of chromophoric dimers/trimer affects the rate constant of SB-CS and CR remain elusive.

The generation of the long-lived CS state is the essential requirement for producing renewable solar electricity using molecular photovoltaics and artificial photosynthesis. Out of all the parameters that affect the SB-CS and CR, the electronic coupling matrix (V) elements play a

Table 1.1: The effects of the different parameters on the SB-CS processes of multichromophoric PDI are discussed in chapter 1.

| SB-CS in linearly arranged PDI dimers | | | | | | | | | |
|---|-----------|--------------|-----------------------|-------------------------|---------------------------------|---------------------|------------------|----------------------------|--------------------------------------|
|  | No | d (Å) | V (cm ⁻¹) | ΔG_{SB-CS} (eV) | Solvent | τ_{SB-CS} (ps) | τ_{CR} (ns) | $\frac{k_{SB-CS}}{k_{CR}}$ | p* |
| | 1 | 12.7 | - | - | MTHF | 55.0 | 0.099 | 1.8 | Radiative emission from LE state |
| | 2a | 12.9 | 97 | - | DMF | 59.8 | 2.26 | 37.8 | |
| | 2b | 21.6 | 51 | - | DMF | 291.5 | 1.22 | 4.2 | |
| SB-CS in cofacially arranged PDI dimers | | | | | | | | | |
|  | No | d (Å) | V (cm ⁻¹) | ΔG_{SB-CS} (eV) | Solvent | τ_{SB-CS} (ps) | τ_{CR} (ns) | $\frac{k_{SB-CS}}{k_{CR}}$ | p* |
| | 4a | 3.7 | - | - | TOL | 0.52 | 0.22 | 426.9 | - |
| | 5a | 3.24 | - | -0.55 ^a | CHCl ₃ | 36.0 | 1.1 | 30.5 | Excimer formation |
| | 6a | ~7 | - | -0.32 | CH ₂ Cl ₂ | 161 | 8.9 | 55.3 | Triplet state formation |
| | 7 | 6.4 | - | -0.28 | CH ₂ Cl ₂ | 22 | 7.3 | 331.8 | |
| | 6b | 10.8 | - | -0.24 | CH ₂ Cl ₂ | - | 7.05 | - | |
| SB-CS in triangularly arranged PDI trimer | | | | | | | | | |
|  | No | d (Å) | V (cm ⁻¹) | ΔG_{SB-CS} (eV) | Solvent | τ_{SB-CS} (ps) | τ_{CR} (ns) | $\frac{k_{SB-CS}}{k_{CR}}$ | p* |
| | 8 | 8.8 | - | -0.19 | CH ₂ Cl ₂ | 12.0 | 1.12 | 93.3 | - |
| SB-CS in angularly arranged PDI dimers | | | | | | | | | |
|  | No | Θ (°) | V (cm ⁻¹) | ΔG_{SB-CS} (eV) | Solvent | τ_{SB-CS} (ps) | τ_{CR} (ns) | $\frac{k_{SB-CS}}{k_{CR}}$ | p* |
| | 9a | 180 | 345.2 | -0.20 | THF | 12.4 | 1.94 | 156.4 | Relaxed singlet (CT) state formation |
| | 9b | 69.7 | 71.8 | -0.25 | THF | 323.0 | - | - | |
| | 10 | 73 | 43.55 | -0.52 | DMF | 241.7 | 1.9 | 7.9 | |

vital role in achieving an ultrafast SB-CS. The tuning of the molecular architecture to a configuration where a significant amount of molecular orbital overlap persists and deactivation of all the unwanted decay pathways is requisite for efficient charge separation. In addition, systematic variation of the energetics of different excited states (LE state and CS state) by incorporating the

electron-donating group and varying interchromophoric interaction gives insight into the lifetime of CS state. The competitive decay pathways of CS and CR processes such as fluorescence emission, excimer formation, presence of relaxed singlet state, and triplet formation are not desired decay channels.

For efficient functioning of organic solar cells, energy dissipation through radiative and/or non-radiative decay channels has to be minimized. The origin of these undesired deactivation pathways has a dependency on the chromophoric arrangement, for example, excimer formation observed in cofacial stacked dimer with small interplanar distance (d). The excimer state disappears when the interplanar distance increases. However, such a system suffers from another bottleneck, such as the triplet state. In addition to these structural features, rigidification of the multichromophoric system enables us to avoid the formation of an unwanted emissive relaxed singlet state. Generally, the SB-CS state of multichromophoric systems is accessible only in a polar solvent, where the solvent's polarity stabilizes the CS state. Photoexcitation of inorganic semiconductors with a high dielectric constant, $\epsilon > 10$, generates unbound electron-hole pairs (free charges) collected at the electrodes. However, organic photovoltaics (OPVs) with low dielectric constant ($\epsilon = 3-4$) generate only Coulombically coupled bound hole-electron pair (exciton) upon photoexcitation. So, it is essential to develop the SB-CS material exhibiting charge separation in non-or weakly polar media such as molecular solids. A challenge that most SB-CS materials face is short-lived photoexcited charge-separated states. The desired function of collecting charges at the electrodes in photovoltaics requires a much long-lived excited CS state (microseconds). An innovative strategy to achieve a prolonged charge-separated state is to drive charge recombination into the inverted region, i.e., pushing the singlet state excitation energy (precursor of SB-CS) of the multichromophoric system to the higher energy region by structural engineering, where photovoltaics based devices can function efficiently.

Over the past few years, SB-CS has been recognized as one of the most promising routes to increase the open-circuit voltage of the organic solar cell. A practical route to improve the organic photovoltaics efficiency is to employ SB-CS material as an active layer and develop strategies that increase charge-separated state lifetime while reducing the loss of thermodynamic driving forces. The promising strategies that control the charge transfer dynamics are tuning the spatial orientation of multichromophoric systems and functionalizing chromophoric units.

1.6. Aim and Objectives of the Thesis

A comprehensive understanding of the evolution of diverse excited state dynamics as a function of the relative spatial orientation and electronic communication among the distinct chromophoric assembly is quintessential for developing advanced optoelectronic devices. In this thesis, we attempt to achieve diverse orthogonal or near-orthogonal chromophoric arrangements and probed concomitant photoexcited state spectral evolution in various dielectric environments. In Chapter 2, the first crystalline evidence for chromophoric Greek cross (+) stacking in **Br₂-PTE** crystal exhibiting null excitonic coupling and selective hole transfer characteristics is explored. Current work suggests that Greek cross aggregate is an ideal strategy for achieving monomer-like optical properties and selective hole transfer mobility in the crystalline state. The unequivocal evidence for the prolonged SB-CS state ($k_{CS}/k_{CR} = 2647$ in ACN) in a null exciton-coupled spiro-conjugated perylenediimide dimer (**Sp-PDI₂**) is explored in Chapter 3. This work integrates two fundamental concepts of photophysics, null exciton splitting and symmetry-breaking charge separation, as an innovative strategy to generate an efficient long-lived charge-separated state. Chapter 4 showcases the transformation of the initially populated SB-CS state to a detrimental excimer state due to the excited-state conformational changes. Rigidification of the near-orthogonal arranged dimers emerges as an ideal strategy for achieving a long-lived charge-separated state and diminishing the unwanted deactivation pathway.

1.7. References

- (1) Marais, A.; Sinayskiy, I.; Petruccione, F.; Van Grondelle, R. A Quantum Protective Mechanism in Photosynthesis. *Sci. Rep.* **2015**, *5*, 1–8.
- (2) Yang, M.; Damjanović, A.; Vaswani, H. M.; Fleming, G. R. Energy Transfer in Photosystem I of Cyanobacteria *Synechococcus Elongatus*: Model Study with Structure-Based Semi-Empirical Hamiltonian and Experimental Spectral Density. *Biophys. J.* **2003**, *85*, 140–158.
- (3) Mirkovic, T.; Ostroumov, E. E.; Anna, J. M.; Van Grondelle, R.; Govindjee; Scholes, G. D. Light Absorption and Energy Transfer in the Antenna Complexes of Photosynthetic Organisms. *Chem. Rev.* **2017**, *117*, 249–293.
- (4) Brixner, T.; Hildner, R.; Köhler, J.; Lambert, C.; Würthner, F. Exciton Transport in Molecular Aggregates – From Natural Antennas to Synthetic Chromophore Systems. *Adv. Energy Mater.* **2017**, *7*, 1700236.
- (5) Madigan, M. T.; Jung, D. O. An Overview of Purple Bacteria: Systematics, Physiology, and Habitats. **2009**, 1–15.
- (6) Sauer, K.; Cogdell, R. J.; Prince, S. M.; Freer, A.; Isaacs, N. W.; Scheer, H. Structure-Based Calculations of the Optical Spectra of the LH2 Bacteriochlorophyll-Protein Complex from *Rhodospseudomonas Acidophila*. *Photochem. Photobiol.* **1996**, *64*, 564–576.
- (7) Bacterial Photosynthesis <http://photobiology.info/Jones.html> (accessed Jun 15, 2022).
- (8) Yang, J.; Yoon, M. C.; Yoo, H.; Kim, P.; Kim, D. Excitation Energy Transfer in Multiporphyrin Arrays with Cyclic Architectures: Towards Artificial Light-Harvesting Antenna Complexes. *Chem. Soc. Rev.* **2012**, *41*, 4808–4826.
- (9) Scheibe, G. Über Die Veränderlichkeit Der Absorptionsspektren in Lösungen Und Die Nebenvalenzen Als Ihre Ursache. *Angew. Chem. Int. Ed.* **1937**, *50*, 212–219.
- (10) Heyne, B. Self-Assembly of Organic Dyes in Supramolecular Aggregates. *Photochem. Photobiol. Sci.* **2016**, *15*, 1103–1114.
- (11) Kasha, M. Energy Transfer Mechanisms and the Molecular Exciton Model for Molecular Aggregates. *Radiat. Res.* **1963**, *20*, 55–70.
- (12) Gierschner, J.; Shi, J.; Milián-Medina, B.; Roca-Sanjuán, D.; Varghese, S.; Park, S. Y.; Gierschner, J.; Shi, J.; Milián-Medina, B.; Beltrán Martínez, J.; 46980, V.; Varghese, S.; Park, S. Y. Luminescence in Crystalline Organic Materials: From Molecules to Molecular Solids. *Adv. Opt. Mater.* **2021**, *9*, 2002251.
- (13) Da Como, E.; von Hauff, E. The WSPC Reference on Organic Electronics: Organic Semiconductors. Materials and Energy Series. Volume 1: Basic Concepts, Volume 2: Fundamental Aspects of Materials and Applications. Edited by Jean-Luc Brédas and Seth R. Marder. *Angew. Chem. Int. Ed.* **2017**, *56*, 4915–4916.
- (14) Bardeen, C. J. The Structure and Dynamics of Molecular Excitons. *Annu. Rev. Phys. Chem.* **2014**, *65*, 127–148.
- (15) Davydov, A. S. The Theory of Molecular Excitons. *Sov. Phys. Uspekhi* **1964**, *7*, 145.
- (16) Kasha, M.; Rawls, H. R.; El-Bayoumi, M. A. The Exciton Model in Molecular Spectroscopy. *Pure Appl. Chem.* **1965**, *11*, 371–392.
- (17) Fassioli, F.; Dinshaw, R.; Arpin, P. C.; Scholes, G. D. Photosynthetic Light Harvesting:

- Excitons and Coherence. *J. R. Soc. Interface* **2014**, *11*.
- (18) Yamagata, H.; Pochas, C. M.; Spano, F. C. Designing J- and H-Aggregates through Wave Function Overlap Engineering: Applications to Poly(3-Hexylthiophene). *J. Phys. Chem. B* **2012**, *116*, 14494–14503.
- (19) Kreger, K.; Schmidt, H.-W.; Hildner, R.; Bricks, J. L.; Slominskii, Y. L.; Panas, I. D.; Demchenko, A. P. Fluorescent J-Aggregates of Cyanine Dyes: Basic Research and Applications Review. *Methods Appl. Fluoresc.* **2017**, *6*, 012001.
- (20) Zhou, J.; Zhang, W.; Jiang, X. F.; Wang, C.; Zhou, X.; Xu, B.; Liu, L.; Xie, Z.; Ma, Y. Magic-Angle Stacking and Strong Intermolecular π - π Interaction in a Perylene Bisimide Crystal: An Approach for Efficient Near-Infrared (NIR) Emission and High Electron Mobility. *J. Phys. Chem. Lett.* **2018**, *9*, 596–600.
- (21) Hestand, N. J.; Spano, F. C. Expanded Theory of H- and J-Molecular Aggregates: The Effects of Vibronic Coupling and Intermolecular Charge Transfer. *Chem. Rev.* **2018**, *118*, 7069–7163.
- (22) Hestand, N. J.; Spano, F. C. Molecular Aggregate Photophysics beyond the Kasha Model: Novel Design Principles for Organic Materials. *Acc. Chem. Res.* **2017**, *50*, 341–350.
- (23) Hestand, N. J.; Spano, F. C. Interference between Coulombic and CT-Mediated Couplings in Molecular Aggregates: H- to J-Aggregate Transformation in Perylene-Based π -Stacks. *J. Chem. Phys.* **2015**, *143*, 244707.
- (24) Scholes, G. D.; Ghiggino, K. P. Electronic Interactions and Interchromophore Excitation Transfer. *J. Phys. Chem.* **1994**, *98*, 4580–4590.
- (25) Krueger, B. P.; Scholes, G. D.; Fleming, G. R. Calculation of Couplings and Energy-Transfer Pathways between the Pigments of LH2 by the Ab Initio Transition Density Cube Method. *J. Phys. Chem. B* **1998**, *102*, 5378–5386.
- (26) Cornil, J. Influence of Interchain Interactions in the Absorption and Luminescence of Conjugated Oligomers and Polymers: A Quantum-Chemical Characterization. *J. Am. Chem. Soc.* **1998**, *120*, 1289–1299.
- (27) Kaufmann, C.; Bialas, D.; Stolte, M.; Würthner, F. Discrete π -Stacks of Perylene Bisimide Dyes within Folda-Dimers: Insight into Long- and Short-Range Exciton Coupling. *J. Am. Chem. Soc.* **2018**, *140*, 9986–9995.
- (28) Feng, X.; Pisula, W.; Müllen, K. From Helical to Staggered Stacking of Zigzag Nanographenes. *J. Am. Chem. Soc.* **2007**, *129*, 14116–14117.
- (29) Hansen, M. R.; Schnitzler, T.; Pisula, W.; Graf, R.; Müllen, K.; Spies, H. W. G. Cooperative Molecular Motion within a Self-Assembled Liquid-Crystalline Molecular Wire: The Case of a TEG-Substituted Perylenediimide Disc. *Angew. Chem. Int. Ed.* **2009**, *48*, 4621–4624.
- (30) Sanyal, N.; Lahti, P. Hydrogen-Bond-Assisted, Crossed Dipole π -Stacking in 1,4-Bis(Phenylethynyl)Benzene. *Cryst. Growth Des.* **2006**, *6*, 1253–1255.
- (31) Tamura, H. Diabatization for Time-Dependent Density Functional Theory: Exciton Transfers and Related Conical Intersections. *J. Phys. Chem. A* **2016**, *120*, 9341–9347.
- (32) Baker, L. A.; Habershon, S. Photosynthetic Pigment-Protein Complexes as Highly Connected Networks: Implications for Robust Energy Transport. *Proc. R. Soc. A* **2017**, *473*,
-

- 1–25.
- (33) Grondelle, R. van; Sundström, V. Excitation Energy Transfer In Photosynthesis. In *Photosynthetic Light-Harvesting Systems. Organization and Function*; De Gruyter, **2019**, 403–438.
- (34) Romero, E.; Augulis, R.; Novoderezhkin, V. I.; Ferretti, M.; Thieme, J.; Zigmantas, D.; Van Grondelle, R. Quantum Coherence in Photosynthesis for Efficient Solar-Energy Conversion. *Nat. Phys.* **2014**, *10*, 676–682.
- (35) Savikhin, S.; Jankowiak, R. Mechanism of Primary Charge Separation in Photosynthetic Reaction Centers. *Biophys. Photosynth.* **2014**, 193–240.
- (36) Barter, L. M. C.; Durrant, J. R.; Klug, D. R. A Quantitative Structure–Function Relationship for the Photosystem II Reaction Center: Supermolecular Behavior in Natural Photosynthesis. *Proc. Natl. Acad. Sci.* **2003**, *100*, 946–951.
- (37) Cardona, T.; Sedoud, A.; Cox, N.; Rutherford, A. W. Charge Separation in Photosystem II: A Comparative and Evolutionary Overview. *Biochim. Biophys. Acta - Bioenerg.* **2012**, *1817*, 26–43.
- (38) Cherepanov, D. A.; Shelaev, I. V.; Gostev, F. E.; Petrova, A.; Aybush, A. V.; Nadtochenko, V. A.; Xu, W.; Golbeck, J. H.; Semenov, A. Y. Primary Charge Separation within the Structurally Symmetric Tetrameric Chl2APAPBChl2B Chlorophyll Exciplex in Photosystem I. *J. Photochem. Photobiol. B Biol.* **2021**, *217*, 112154.
- (39) Laible, P. D.; Hanson, D. K.; Buhrmaster, J. C.; Tira, G. A.; Faries, K. M.; Holten, D.; Kirmaier, C. Switching Sides—Reengineered Primary Charge Separation in the Bacterial Photosynthetic Reaction Center. *Proc. Natl. Acad. Sci.* **2020**, *117*, 865–871.
- (40) Krishnapriya, K. C.; Musser, A. J.; Patil, S. Molecular Design Strategies for Efficient Intramolecular Singlet Exciton Fission. *ACS Energy Lett.* **2018**, *4*, 192–202.
- (41) Young, R. M.; Wasielewski, M. R. Mixed Electronic States in Molecular Dimers: Connecting Singlet Fission, Excimer Formation, and Symmetry-Breaking Charge Transfer. *Acc. Chem. Res.* **2020**, *53*, 1957–1968.
- (42) Vauthey, E. Photoinduced Symmetry-Breaking Charge Separation. *ChemPhysChem* **2012**, *13*, 2001–2011.
- (43) Ramakrishnan, R.; Niyas, M. A.; Lijina, M. P.; Hariharan, M. Distinct Crystalline Aromatic Structural Motifs: Identification, Classification, and Implications. *Acc. Chem. Res.* **2019**, *52*, 3075–3086.
- (44) Sandeep, K.; Manoj, B.; Thomas, K. G. Gold Nanoparticle on Semiconductor Quantum Dot: Do Surface Ligands Influence Fermi Level Equilibration. *J. Chem. Phys.* **2020**, *152*, 044710.
- (45) Wang, C.; Zhang, Z.; Pejić, S.; Li, R.; Fukuto, M.; Zhu, L.; Sauv e, G. High Dielectric Constant Semiconducting Poly(3-Alkylthiophene)s from Side Chain Modification with Polar Sulfinyl and Sulfonyl Groups. *Macromolecules* **2018**, *51*, 9368–9381.
- (46) Thomas, A.; Sandeep, K.; Somasundaran, S. M.; Thomas, K. G. How Trap States Affect Charge Carrier Dynamics of CdSe and InP Quantum Dots: Visualization through Complexation with Viologen. *ACS Energy Lett.* **2018**, *3*, 2368–2375.
- (47) Markovic, V.; Villamaina, D.; Barabanov, I.; Lawson Daku, L. M.; Vauthey, E.

- Photoinduced Symmetry-Breaking Charge Separation: The Direction of the Charge Transfer. *Angew. Chem. Int. Ed.* **2011**, *50*, 7596–7598.
- (48) Tamar van der Boom; Ryan T. Hayes; Yongyu Zhao; Patrick J. Bushard; Emily A. Weiss, and; Wasielewski, M. R. Charge Transport in Photofunctional Nanoparticles Self-Assembled from Zinc 5,10,15,20-Tetrakis(Perylenediimide)Porphyrin Building Blocks. *J. Am. Chem. Soc.* **2002**, *124*, 9582–9590.
- (49) Scholes, G. D.; Fournier, T.; Parker, A. W.; Phillips, D. Solvation and Intramolecular Reorganization in 9,9'-Bianthryl: Analysis of Resonance Raman Excitation Profiles and Ab Initio Molecular Orbital Calculations. *J. Chem. Phys.* **1999**, *111*, 5999.
- (50) Trinh, C.; Kirlikovali, K.; Das, S.; Ener, M. E.; Gray, H. B.; Djurovich, P.; Bradforth, S. E.; Thompson, M. E. Symmetry-Breaking Charge Transfer of Visible Light Absorbing Systems: Zinc Dipyrrins. *J. Phys. Chem. C* **2014**, *118*, 21834–21845.
- (51) Dereka, B.; Svechkarov, D.; Rosspeintner, A.; Aster, A.; Lunzer, M.; Liska, R.; Mohs, A. M.; Vauthey, E. Solvent Tuning of Photochemistry upon Excited-State Symmetry Breaking. *Nat. Commun.* **2020**, *11*, 1–11.
- (52) Roy, P.; Bressan, G.; Gretton, J.; Cammidge, A. N.; Meech, S. R. Ultrafast Excimer Formation and Solvent Controlled Symmetry Breaking Charge Separation in the Excitonically Coupled Subphthalocyanine Dimer. *Angew. Chem. Int. Ed.* **2021**, *60*, 10568–10572.
- (53) Khandelwal, H.; Mallia, A. R.; Cheriya, R. T.; Hariharan, M. Effect of Temperature on Symmetry Breaking Excited State Charge Separation: Restoration of Symmetry at Elevated Temperature. *Phys. Chem. Chem. Phys.* **2012**, *14*, 15282–15285.
- (54) Ramirez, C. E.; Chen, S.; Powers-Riggs, N. E.; Schlesinger, I.; Young, R. M.; Wasielewski, M. R. Symmetry-Breaking Charge Separation in the Solid State: Tetra(Phenoxy)Perylenediimide Polycrystalline Films. *J. Am. Chem. Soc.* **2020**, *142*, 18243–18250.
- (55) Zhang, M.; Zhu, L.; Zhou, G.; Hao, T.; Qiu, C.; Zhao, Z.; Hu, Q.; Larson, B. W.; Zhu, H.; Ma, Z.; Tang, Z.; Feng, W.; Zhang, Y.; Russell, T. P.; Liu, F. Single-Layered Organic Photovoltaics with Double Cascading Charge Transport Pathways: 18% Efficiencies. *Nat. Commun.* **2021**, *12*, 1–10.
- (56) Nilsson, Z.; Erdewyk, M. Van; Wang, L.; Sambur, J. B. Molecular Reaction Imaging of Single-Entity Photoelectrodes. *ACS Energy Lett.* **2020**, *5*, 1474–1486.
- (57) Brédas, J. L.; Sargent, E. H.; Scholes, G. D. Photovoltaic Concepts Inspired by Coherence Effects in Photosynthetic Systems. *Nat. Mater.* **2016**, *16*, 35–44.
- (58) Gillett, A. J.; Privitera, A.; Dilmurat, R.; Karki, A.; Qian, D.; Pershin, A.; Londi, G.; Myers, W. K.; Lee, J.; Yuan, J.; Ko, S.-J.; Riede, M. K.; Gao, F.; Bazan, G. C.; Rao, A.; Nguyen, T.-Q.; Beljonne, D.; Friend, R. H. The Role of Charge Recombination to Triplet Excitons in Organic Solar Cells. *Nature* **2021**, *597*, 666–671.
- (59) Coropceanu, V.; Chen, X. K.; Wang, T.; Zheng, Z.; Brédas, J. L. Charge-Transfer Electronic States in Organic Solar Cells. *Nat. Rev. Mater.* **2019**, *4*, 689–707.
- (60) Kellogg, M.; Akil, A.; Ravinson, D. S. M.; Estergreen, L.; Bradforth, S. E.; Thompson, M.
-

- E. Symmetry Breaking Charge Transfer as a Means to Study Electron Transfer with No Driving Force. *Faraday Discuss.* **2019**, *216*, 379–394.
- (61) Bartynski, A. N.; Gruber, M.; Das, S.; Rangan, S.; Mollinger, S.; Trinh, C.; Bradforth, S. E.; Vandewal, K.; Salleo, A.; Bartynski, R. A.; Bruetting, W.; Thompson, M. E. Symmetry-Breaking Charge Transfer in a Zinc Chlorodipyrrin Acceptor for High Open Circuit Voltage Organic Photovoltaics. *J. Am. Chem. Soc.* **2015**, *137*, 5397–5405.
- (62) Jovan M. Giaimo; Alexey V. Gusev, and; Wasielewski, M. R. Excited-State Symmetry Breaking in Cofacial and Linear Dimers of a Green Perylenediimide Chlorophyll Analogue Leading to Ultrafast Charge Separation. *J. Am. Chem. Soc.* **2002**, *124*, 8530–8531.
- (63) Sebastian, E.; Philip, A. M.; Benny, A.; Hariharan, M. Null Exciton Splitting in Chromophoric Greek Cross (+) Aggregate. *Angew. Chem. Int. Ed.* **2018**, *57*, 15696–15701.
- (64) Würthner, F.; Saha-Möller, C. R.; Fimmel, B.; Ogi, S.; Leowanawat, P.; Schmidt, D. Perylene Bisimide Dye Assemblies as Archetype Functional Supramolecular Materials. *Chem. Rev.* **2015**, *116*, 962–1052.
- (65) Michael W. Holman; Ruchuan Liu; Ling Zang, †; Ping Yan; Sara A. DiBenedetto; Robert D. Bowers, and; Adams, D. M. Studying and Switching Electron Transfer: From the Ensemble to the Single Molecule. *J. Am. Chem. Soc.* **2004**, *126*, 16126–16133.
- (66) Wu, Y.; Young, R. M.; Frasconi, M.; Schneebeli, S. T.; Spent, P.; Gardner, D. M.; Brown, K. E.; Würthner, F.; Stoddart, J. F.; Wasielewski, M. R. Ultrafast Photoinduced Symmetry-Breaking Charge Separation and Electron Sharing in Perylenediimide Molecular Triangles. *J. Am. Chem. Soc.* **2015**, *137*, 13236–13239.
- (67) Marcus, R. A. Electron Transfer Reactions in Chemistry. Theory and Experiment The Use of Chemically Modified 599 600 Rudolph A. Marcus: Electron Transfer Reactions in Chemistry Developments in Electron Transfer Reactions ET at Liquid-Liquid Interfaces ET at Polymer-Liq; 1993; Vol. 65.
- (68) Closs, G. L.; Calcaterra, L. T.; Green, N. J.; Penfield, K. W.; Miller, J. R. Distance, Stereoelectronic Effects, and the Marcus Inverted Region in Intramolecular Electron Transfer in Organic Radical Anions. *J. Phys. Chem.* **2002**, *90*, 3673–3683.
- (69) Miller, J. R.; Calcaterra, L. T.; Closs, G. L. Intramolecular Long-Distance Electron Transfer in Radical Anions. The Effects of Free Energy and Solvent on the Reaction Rates. *J. Am. Chem. Soc.* **2002**, *106*, 3047–3049.
- (70) Heller, E. R.; Richardson, J. O. Semiclassical Instanton Formulation of Marcus–Levich–Jortner Theory. *J. Chem. Phys.* **2020**, *152*, 244117.
- (71) Weller, A. Photoinduced Electron Transfer in Solution: Exciplex and Radical Ion Pair Formation Free Enthalpies and Their Solvent Dependence. *Zeitschrift für Phys. Chemie* **1982**, *133*, 93–98.
- (72) Rehm, D.; Weller, A. Kinetics of Fluorescence Quenching by Electron and H-Atom Transfer. *Isr. J. Chem.* **1970**, *8*, 259–271.
- (73) Higashino, T.; Yamada, T.; Yamamoto, M.; Furube, A.; Tkachenko, N. V.; Miura, T.; Kobori, Y.; Jono, R.; Yamashita, K.; Imahori, H. Remarkable Dependence of the Final Charge Separation Efficiency on the Donor–Acceptor Interaction in Photoinduced Electron
-

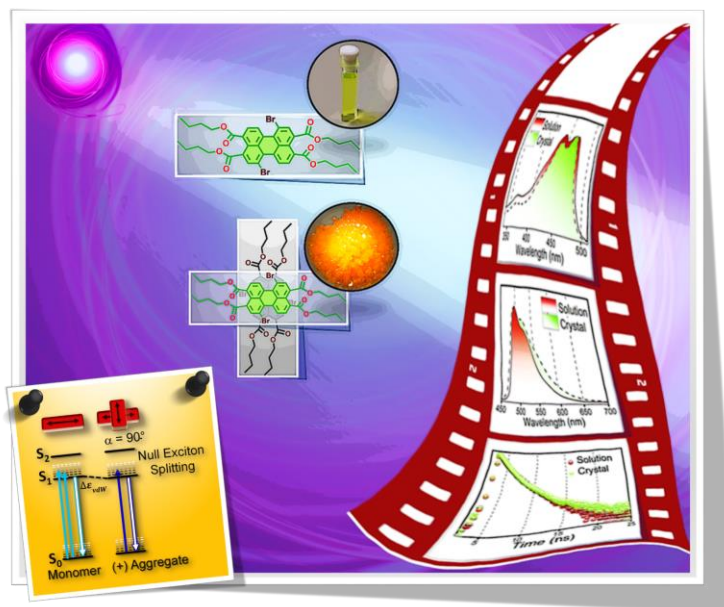
- Transfer. *Angew. Chem. Int. Ed.* **2016**, *128*, 639–643.
- (74) Purc, A.; Espinoza, E. M.; Nazir, R.; Romero, J. J.; Skonieczny, K.; Jeżewski, A.; Larsen, J. M.; Gryko, D. T.; Vullev, V. I. Gating That Suppresses Charge Recombination—The Role of Mono-N-Arylated Diketopyrrolopyrrole. *J. Am. Chem. Soc.* **2016**, *138*, 12826–12832.
- (75) Harvey, P. D. What Can We Learn from Artificial Special Pairs? *Can. J. Chem.* **2014**, *92*, 355–368.
- (76) Jacob J. Piet; Wouter Schuddeboom; Bastiaan R. Wegewijs; Ferdinand C. Grozema, and; Warman, J. M. Symmetry Breaking in the Relaxed S1 Excited State of Bianthryl Derivatives in Weakly Polar Solvents. *J. Am. Chem. Soc.* **2001**, *123*, 5337–5347.
- (77) Michael W. Holman; Ping Yan; David M. Adams; Sebastian Westenhoff, and; Carlos Silva. Ultrafast Spectroscopy of the Solvent Dependence of Electron Transfer in a Perylenebisimide Dimer. *J. Phys. Chem. A* **2005**, *109*, 8548–8552.
- (78) Lefler, K. M.; Brown, K. E.; Salamant, W. A.; Dyar, S. M.; Knowles, K. E.; Wasielewski, M. R. Triplet State Formation in Photoexcited Slip-Stacked Perylene-3,4:9,10-Bis(Dicarboximide) Dimers on a Xanthene Scaffold. *J. Phys. Chem. A* **2013**, *117*, 10333–10345.
- (79) Jovan M. Giaimo; Jenny V. Lockard; Louise E. Sinks; Amy M. Scott; Thea M. Wilson, and; Wasielewski*, M. R. Excited Singlet States of Covalently Bound, Cofacial Dimers and Trimers of Perylene-3,4:9,10-Bis(Dicarboximide). *J. Phys. Chem. A* **2008**, *112*, 2322–2330.
- (80) Veldman, D.; Chopin, S. M. A.; Meskers, S. C. J.; Groeneveld, M. M.; Williams, R. M.; Janssen, R. A. J. Triplet Formation Involving a Polar Transition State in a Well-Defined Intramolecular Perylenediimide Dimeric Aggregate. *J. Phys. Chem. A* **2008**, *112*, 5846–5857.
- (81) Brown, K. E.; Salamant, W. A.; Shoer, L. E.; Young, R. M.; Wasielewski, M. R. Direct Observation of Ultrafast Excimer Formation in Covalent Perylenediimide Dimers Using Near-Infrared Transient Absorption Spectroscopy. *J. Phys. Chem. Lett.* **2014**, *5*, 2588–2593.
- (82) Sung, J.; Nowak-Król, A.; Schlosser, F.; Fimmel, B.; Kim, W.; Kim, D.; Würthner, F. Direct Observation of Excimer-Mediated Intramolecular Electron Transfer in a Cofacially-Stacked Perylene Bisimide Pair. *J. Am. Chem. Soc.* **2016**, *138*, 9029–9032.
- (83) Nowak-Król, A.; Fimmel, B.; Son, M.; Kim, D.; Würthner, F. Photoinduced Electron Transfer (PET) versus Excimer Formation in Supramolecular p/n-Heterojunctions of Perylene Bisimide Dyes and Implications for Organic Photovoltaics. *Faraday Discuss.* **2015**, *185*, 507–527.
- (84) Schubert, A.; Settels, V.; Liu, W.; Würthner, F.; Meier, C.; Fink, R. F.; Schindlbeck, S.; Lochbrunner, S.; Engels, B.; Engel, V. Ultrafast Exciton Self-Trapping upon Geometry Deformation in Perylene-Based Molecular Aggregates. *J. Phys. Chem. Lett.* **2013**, *4*, 792–796.
- (85) Birks, J. B. Excimers. *Reports Prog. Phys.* **1975**, *38*, 903.
- (86) Singh, R.; Kim, M.; Lee, J.-J.; Ye, T.; Keivanidis, P. E.; Cho, K. Excimer Formation Effects and Trap-Assisted Charge Recombination Loss Channels in Organic Solar Cells of Perylene Diimide Dimer Acceptors. *J. Mater. Chem. C* **2020**, *8*, 1686–1696.
-

- (87) Kim, W.; Nowak-Król, A.; Hong, Y.; Schlosser, F.; Würthner, F.; Kim, D. Solvent-Modulated Charge-Transfer Resonance Enhancement in the Excimer State of a Bay-Substituted Perylene Bisimide Cyclophane. *J. Phys. Chem. Lett.* **2019**, *10*, 1919–1927.
- (88) Spenst, P.; Young, R. M.; Wasielewski, M. R.; Würthner, F. Guest and Solvent Modulated Photo-Driven Charge Separation and Triplet Generation in a Perylene Bisimide Cyclophane. *Chem. Sci.* **2016**, *7*, 5428–5434.
- (89) Sasikumar, D.; John, A. T.; Sunny, J.; Hariharan, M. Access to the Triplet Excited States of Organic Chromophores. *Chem. Soc. Rev.* **2020**, *49*, 6122–6140.
- (90) Coleman, A. F.; Chen, M.; Zhou, J.; Shin, J. Y.; Wu, Y.; Young, R. M.; Wasielewski, M. R. Reversible Symmetry-Breaking Charge Separation in a Series of Perylenediimide Cyclophanes. *J. Phys. Chem. C* **2020**, *124*, 10408–10419.
- (91) Veldman, D.; Chopin, S. M. A.; Meskers, S. C. J.; Groeneveld, M. M.; Williams, R. M.; Janssen, R. A. J. Triplet Formation Involving a Polar Transition State in a Well-Defined Intramolecular Perylenediimide Dimeric Aggregate. *J. Phys. Chem. A* **2008**, *112*, 5846–5857.
- (92) Kotova, M. S.; Londi, G.; Junker, J.; Dietz, S.; Privitera, A.; Tvingstedt, K.; Beljonne, D.; Sperlich, A.; Dyakonov, V. On the Absence of Triplet Exciton Loss Pathways in Non-Fullerene Acceptor Based Organic Solar Cells. *Mater. Horizons* **2020**, *7*, 1641–1649.
- (93) Guo, Y.; Ma, Z.; Niu, X.; Zhang, W.; Tao, M.; Guo, Q.; Wang, Z.; Xia, A. Bridge-Mediated Charge Separation in Isomeric N-Annulated Perylene Diimide Dimers. *J. Am. Chem. Soc.* **2019**, *141*, 12789–12796.
- (94) Cave, R. J.; Newton, M. D. Calculation of Electronic Coupling Matrix Elements for Ground and Excited State Electron Transfer Reactions: Comparison of the Generalized Mulliken–Hush and Block Diagonalization Methods. *J. Chem. Phys.* **1998**, *106*, 9213.
- (95) Kong, J.; Zhang, W.; Li, G.; Huo, D.; Guo, Y.; Niu, X.; Wan, Y.; Tang, B.; Xia, A. Excited-State Symmetry-Breaking Charge Separation Dynamics in Multibranched Perylene Diimide Molecules. *J. Phys. Chem. Lett.* **2020**, *11*, 10329–10339.

Chapter 2

Null Exciton Splitting in Chromophoric Greek Cross (+)-Aggregate

Abstract: Exciton interactions in molecular aggregates play a crucial role in tailoring the optical behavior of π -conjugated materials. Though vital for optoelectronic applications, ideal Greek cross-dipole ($\alpha=90^\circ$) stacking of chromophores remains elusive. We report a novel Greek cross (+) assembly of 1,7-dibromoperylene-3,4,9,10-tetracarboxylic tetrabutylester (**PTE-Br₂**) which exhibits null exciton coupling mediated monomer-like optical characteristics in crystalline state. Contrastingly, nonzero exciton coupling in X-type ($\alpha=70.2^\circ$, **PTE-Br₀**) and J-type ($\alpha=0^\circ$, $\theta=48.4^\circ$, **PTE-Br₄**) assemblies render perturbed optical properties. Additionally, the semi-classical Marcus theory of charge-transfer rates predicts a selective hole transport phenomenon in the orthogonally stacked **PTE-Br₂**. Precise rotation



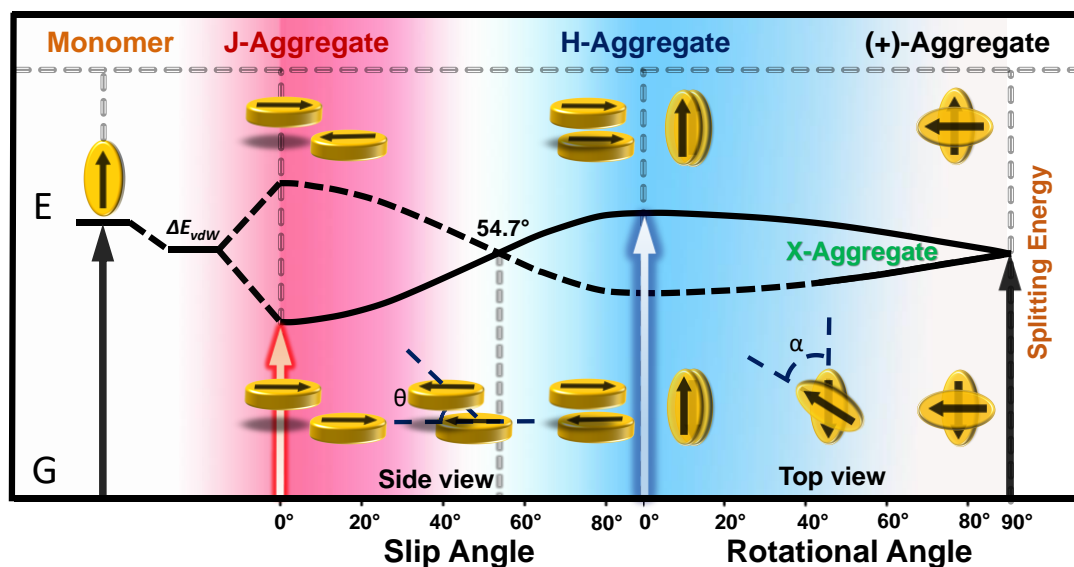
angle-dependent optoelectronic properties in crystalline **PTE-Br₂** can have consequences in the rational design of novel π -conjugated materials for photonic and molecular electronic applications.

2.1. Introduction

The molecular coalition of organic chromophores into hierarchical architectures has proved pivotal in realizing efficient photonic and optoelectronic devices.¹⁻³ Three-dimensional (3D) ordering of π -conjugated materials play a crucial role in dictating the ‘light-matter interactions’,⁴

an inevitable phenomenon for photofunctional applications.⁵⁻⁷ Geometrical rulers i.e. relative spatial orientation,^{8,9} π -overlap¹⁰ and intermolecular distances (d) midst the chromophores govern the electronic communication and synchronously the optical response of the crystalline scaffold.^{7,11-15} Inevitably, the assemblage of π -chromophores typically encounter bottlenecks such as concentration fluorescence quenching mediated by trap states and/or exciton coupling.¹⁶ Molecular exciton theory^{17,18} accounts coherent coupling among co-facial, parallel transition dipoles (H-aggregate) for the quenched fluorescence (Scheme 2.1).^{7,19-21} Though, H-aggregates are detrimental to fluorescence, they exhibit high charge transport efficiencies.²²⁻²⁵ Conversely, exciton coupling among the staggered transition dipoles (J-aggregate) exhibit strong fluorescence character, albeit with weak charge transport character.

Molecular aggregates exhibiting minimal exciton interactions can have important implications in photonic devices.²⁶ Chromophoric “M-aggregates”²⁷ possessing magic angle stacking ($\theta=54.7^\circ$) and “Null aggregates”^{14,28} have been reported to possess minimal net exciton interaction in the condensed state. Cross-stacked chromophoric assemblies with near-orthogonal transition dipoles ($\alpha=90^\circ$) can also ensue minimal exciton interactions.²⁶ Though, having a co-facial orientation, these aggregates exhibit strong luminescence and can create proficient transport π -ways for the charge carriers.²⁹⁻³¹ Kasha and co-workers in their pioneering work and later Bredas and co-workers provided the theoretical conception of such system with negligible exciton interaction.^{18,32} Ma and co-workers provided an experimental demonstration of cross-dipole ($\alpha=70^\circ$, X-aggregate)^{26,33} stacks in distyrylbenzene derivatives and subsequently several cross-



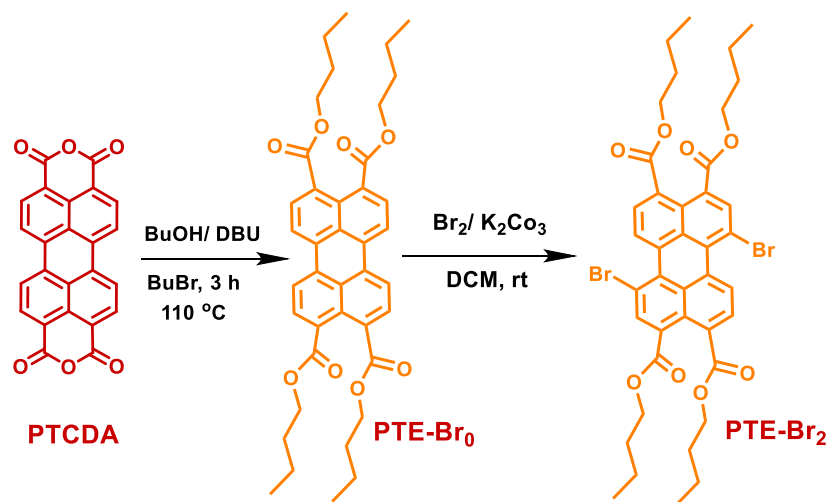
Scheme 2.1: Exciton splitting diagram for a molecular dimer with staggered (J-aggregate), co-facial (H-aggregate), and Greek cross (+-aggregate) configurations.

dipole ($0^\circ < \alpha < 90^\circ$) assemblies evolved (Table A2.1).^{21,30,34–39}

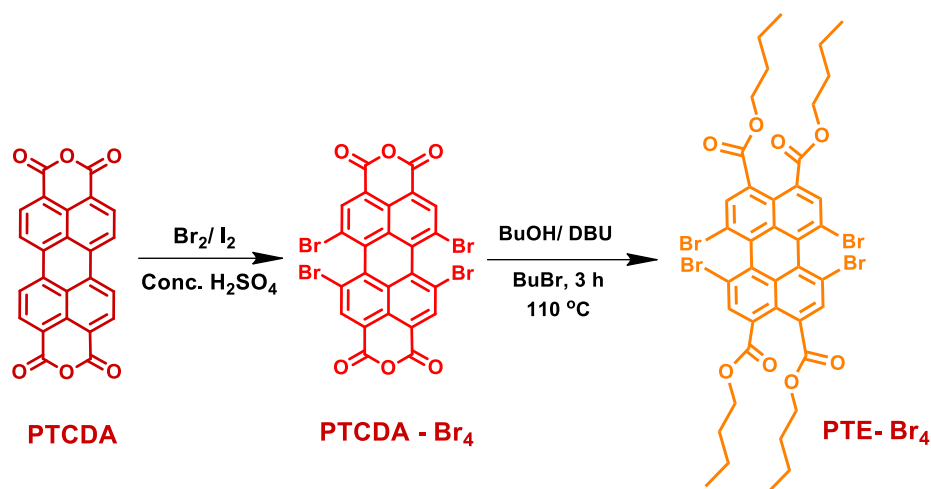
To date, chromophoric aggregates possessing orthogonal geometry ($\alpha = 90^\circ$) has only been proposed by employing solid-state NMR spectroscopy, two-dimensional wide-angle x-ray scattering (2D-WAXS), and molecular modeling methods.^{40–42} Though thermodynamically⁴³ accessible in columnar liquid crystals,^{40–42} realization of a single crystalline architectures cross stacked precisely at right angle ($\alpha = 90^\circ$) remains elusive, predictably due to the sterics (among the peripheral substituents) mediated inefficient packing of the aromatic chromophores.³⁸ To the best of our knowledge, we report the first crystal evidence for null exciton interaction in Greek cross (+) chromophoric assembly possessing an impeccable orthogonal ($\alpha = 90^\circ$) geometry between the chromophores in 1,7-dibromoperylene-3,4,9,10-tetracarboxylic tetrabutylester (**PTE-Br₂**). As surmised theoretically, null Coulomb coupling in the Greek cross (+) chromophoric aggregate renders a monomer-like optical character and an unprecedented anisotropic charge-filtering (selective hole mobility) phenomenon in **PTE-Br₂**.

2.2. Result and Discussion

2.2.1. Synthesis and single-crystal structure. our continuous efforts toward moderating the photogenerated exciton and charge-transfer dynamics in crystalline^{44–46} and nonplanar donor-acceptor (D-A)^{46–48} assemblies prompted us to explore the structure-optical property relation in an array of **PTE** (**PTE-Br_{0,2,4}**) derivatives. The **PTE** derivatives were synthesized and characterized as per the previous literature reports (Schemes 2.2 and 2.3).^{49,50} Slow evaporation of solvent from a homogenous solution of **PTE-Br_{0,2}** (in 1:1, dichloromethane/acetonitrile) and **PTE-Br₄** (in 1:1, dichloromethane/methanol) led to good quality yellow-orange crystals for single-crystal X-ray



Scheme 2.2: The synthesis scheme of **PTE-Br₀** and **PTE-Br₂**.



Scheme 2.3: The synthesis scheme of **PTE-Br₄**.

diffraction. The PTE derivatives crystallized in monoclinic ($C 2/c$, **PTE-Br₀**), tetragonal ($I 4_1/a$, **PTE-Br₂**) and triclinic ($P\bar{1}$, **PTE-Br₄**) crystal systems with 4, 8 and 2 molecules per unit cell, respectively (Figure A2.1 and Table 2.1). The molecular structure of **PTE-Br₀** reveals a planar perylene core with a pliant butyl ester group (Figures 2.1). The molecular structure of **PTE-Br_{2,4}** reveals a highly twisted π -core, (dihedral angle = 24.8° (**PTE-Br₂**) and 38° (**PTE-Br₄**) arising from the steric obstruct of the substituted bromine atoms at the bay region of PTE core (Figure 2.1).⁵¹

2.2.2. Crystal close packing analysis. Subsequently, close-packing analyses of the **PTE-Br_{0,2,4}** derivatives were carried out to probe the role of the synergistic weak intermolecular interactions and get an in-depth understanding of the structure-packing-property correlation (Figure 2.2). The molecular assembly of **PTE-Br₀** reveals a co-facially stacked nearest-neighbor oriented at a rotation angle (α) of 70.2° with respect to the long axis of the perylene core (Figure

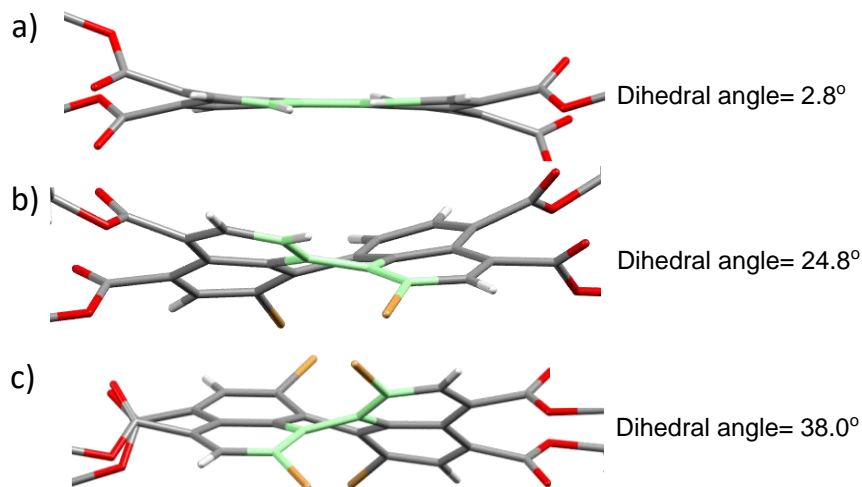


Figure 2.1: Dihedral angle (torsion angle) along the bay region (highlighted in light green) of **PTE-Br₀** (a), **PTE-Br₂** (b) and **PTE-Br₄** (c), respectively.

Table 2.1: Crystallographic data and refinement parameters for **PTE-Br_{0,2,4}** crystal derivatives.

| Parameters | PTE-Br₀ | PTE-Br₂ | PTE-Br₄ |
|--|--|--|--|
| <i>Formula</i> | C ₄₀ H ₄₄ O ₈ | C ₄₀ H ₄₂ Br ₂ O ₈ | C ₄₀ H ₃₈ Br ₄ O ₈ |
| <i>Formula wt.</i> | 652.75 | 810.55 | 966.34 |
| <i>colour, shape</i> | Yellow, needle | Yellow, needle | Yellow, thin-long-plate |
| <i>dimens, mm³</i> | 0.30 x 0.05 x 0.05 | 0.24 x 0.10 x 0.08 | 0.25 x 0.12 x 0.03 |
| <i>crystal system</i> | Monoclinic | Tetragonal | Triclinic |
| <i>space group, Z</i> | <i>C</i> 2/ <i>c</i> , 4 | <i>I</i> 41/ <i>a</i> , 8 | <i>P</i> $\bar{1}$, 2 |
| <i>a, Å</i> | 23.339(3) | 30.4429(16) | 9.6576(11) |
| <i>b, Å</i> | 20.177(3) | 30.4429(16) | 10.7767(13) |
| <i>c, Å</i> | 7.6692(11) | 8.1646(6) | 20.073(3) |
| <i>α, deg</i> | 90° | 90° | 75.506(5)° |
| <i>β, deg</i> | 106.817(8)° | 90° | 79.991(5)° |
| <i>γ, deg</i> | 90° | 90° | 87.797(5)° |
| <i>V, Å³</i> | 3457.0(9) | 7566.7(10) | 1991.9(4) |
| <i>temp, K</i> | 296(2) | 150(2) | 296(2) |
| <i>d_{calcd}, mg/m³</i> | 1.254 | 1.423 | 1.611 |
| <i>no. of reflections collected</i> | 14393 | 17615 | 29833 |
| <i>no. of unique reflections</i> | 3394 | 4671 | 7006 |
| <i>2θ_{max}, deg</i> | 52° | 56.54° | 50° |
| <i>no. of parameters</i> | 217 | 220 | 454 |
| <i>R1, wR2 (I > 2s(I))</i> | 0.0791, 0.2176 | 0.0521, 0.1478 | 0.0608, 0.1735 |
| <i>R1, wR2 (all data)</i> | 0.1998, 0.3033 | 0.0765, 0.1610 | 0.1049, 0.2042 |
| <i>goodness of fit</i> | 1.007 | 1.076 | 1.056 |
| <i>CCDC Deposition number</i> | 1865424 | 1865425 | 1865426 |

2.2a and Figure A2.2). The close-packing analysis of the **PTE-Br₀** assembly reveals that the C-H...O ($d = 2.68$ Å, ab-plane), C...O ($d = 3.2$ Å, c-axis) and π - π ($d = 3.46$ - 3.6 Å, c-axis) interactions guide the progression of the axially rotated ($\alpha = 70.2^\circ$) columnar stacks (Figures A2.3 and A2.4). On the other hand, **PTE-Br₄** molecular assembly reveals a slip-stacked ($\theta = 48.4^\circ$) organization (with longitudinal and transverse translations), typically observed in core twisted **PDI** derivatives with bulky substituents at the bay region (Figures 2.2c, A2.2, and A2.5-A2.6).⁵¹ Close-packing analyses of **PTE-Br₄** reveals that C-H... π ($d = 2.75$ and 2.9 Å, *a*-axis), π - π ($d = 3.64$ Å, *a*-axis),

$\text{Br}\cdots\text{Br}$ ($d = 3.68 \text{ \AA}$, b -axis) and $\text{C-H}\cdots\pi$ ($d = 2.87 \text{ \AA}$, b -axis) interactions propagate the growth of the two-dimensional (2D) crystalline assembly (Figure A2.6).

Interestingly, the molecular assembly in **PTE-Br₂** reveals a unique columnar organization wherein the nearest co-facial neighbors are oriented in a seamless orthogonal geometry ($\alpha=90^\circ$) with respect to the long axis of the perylene core (Figures 2.2b, A2.2 and A2.7). The close-packing in **PTE-Br₂** reveals that the inter-stack $\text{C-H}\cdots\pi$ ($d = 2.78 \text{ \AA}$), $\text{CH}\cdots\text{O}$ ($d = 2.64 \text{ \AA}$) and dihydrogen ($\text{C-H}\cdots\text{H-C}$, $d = 2.38 \text{ \AA}$) interactions guide the propagation of the assembly along the a -axis (Figure A2.8). The nearest co-facial neighbors in the columnar assembly reveal two different stacked dimers, i.e. convex and concave shaped dimers, in **PTE-Br₂** (Figure 2.3). The strong π - π

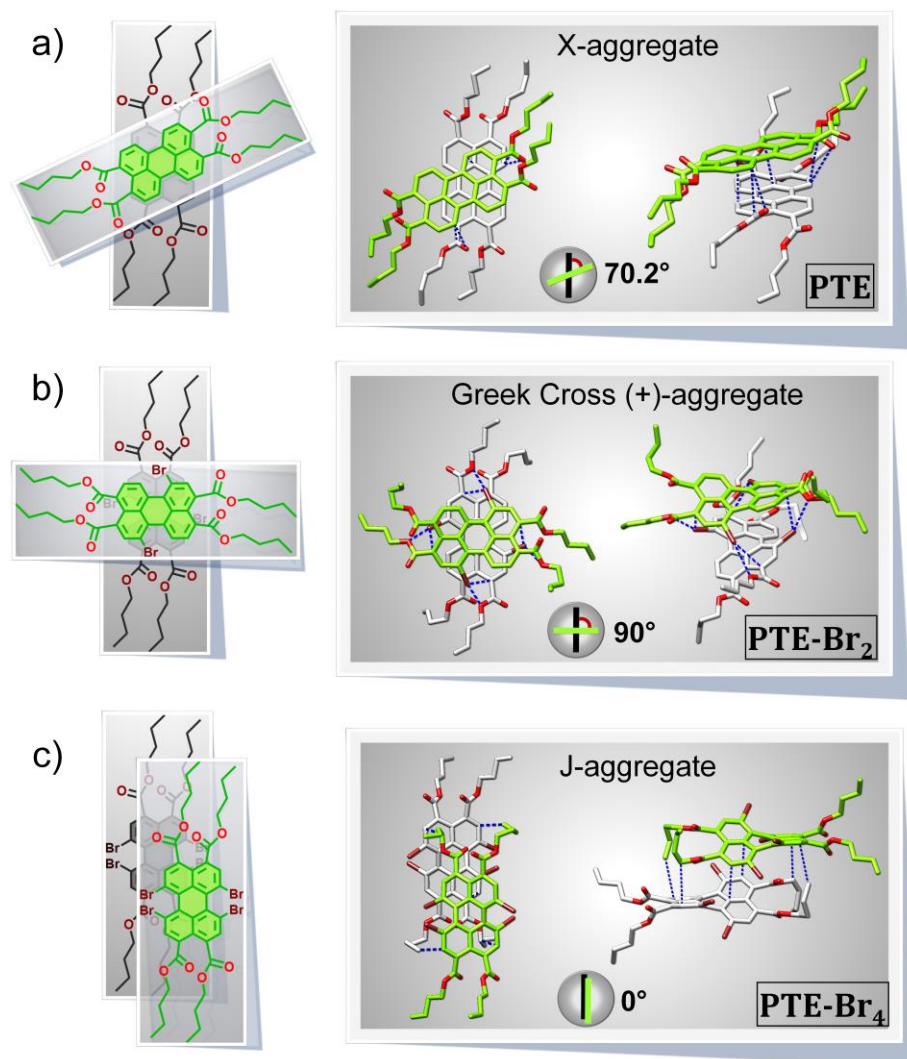


Figure 2.2: Schematic representation of molecular structure (left) and the close-packing depicting weak intermolecular interactions (right) in a) **PTE-Br₀** ($\text{C}\cdots\text{O}$, π - π), b) **PTE-Br₂** ($\text{Br}\cdots\text{O}$, $\text{C}\cdots\text{Br}$), and c) **PTE-Br₄** (π - π , $\text{C}\cdots\text{C}$) stacked dimers. Rotation angle (α) among the dimers with respect to their long molecular axis are 70.2° (**PTE-Br₀**); 90° (**PTE-Br₂**) and 0° (**PTE-Br₄**).

($d=3.39$ Å) interactions play a major role in guiding the convex-shaped dimer, whereas the C \cdots Br ($d=3.54$ Å) and Br \cdots O ($d=3.01$ Å) interactions leads a concave-shaped dimer progression along the c-axis (Figure A2.7). The intra-stack C \cdots Br ($d=3.54$ Å) and inter-stack C-H \cdots O ($d=2.65$ Å) interactions play a crucial role in guiding the 3D progression of the Greek cross columnar assembly in **PTE-Br₂** (Figures 2.3 and A2.7). Thus, the consensus among the weak intermolecular interactions renders X-type (**PTE-Br₀**, $\alpha=70.2^\circ$), ideal Greek cross (**PTE-Br₂**, $\alpha=90^\circ$) columnar and slip-stacked (**PTE-Br₄**, $\theta=48.4^\circ$) nearest co-facial neighbors in the crystalline assembly (Figure 2.2).

2.2.3. QTAIM, Hirshfeld Surface, and SAPT(0) analysis. To get additional insights into the weak intermolecular forces driving the molecular assembly, quantum theory of atoms in molecules (QTAIM),⁵² Hirshfeld surface (HS),⁵³ and truncated symmetry adapted perturbation Theory (SAPT(0))^{54,55} investigations of crystalline **PTE-Br_{0,2,4}** derivatives were performed.⁴⁴ QTAIM exemplified weak intermolecular interactions in crystalline assembly via electron density at the (3, -1) bond critical point (BCP; $\rho_b(r)$), it's Laplacian ($\Delta^2\rho_b(r)$), interaction distances (d) and their relative strengths in crystal-line **PTE-Br₀** (C \cdots O and C \cdots C); **PTE-Br₂** (C \cdots Br, Br \cdots O and C \cdots C), and **PTE-Br₄** (C-H \cdots C, Figure 2.4 and Table A2.2).

HS analyses allowed the quantification of weak intermolecular interactions in **PTE-Br_{0,2,4}** crystalline assembly (Figure 2.5, Tables 2.2 and 2.3). Ratio (ρ) of %C \cdots H and %C \cdots C interactions defined a π -motif arrangement in **PTE-Br_{0,2}** (54% [**PTE-Br₀**] and 49.2% [**PTE-Br₂**] π -overlap) and a sandwich herringbone assembly in **PTE-Br₄** (12% [**PTE-Br₄**] π -overlap, Figure A2.9).^{44,56} In addition to the earlier reports of co-facial dimers, Møller-Plesset (MP2.X)⁴³ and SAPT(0)

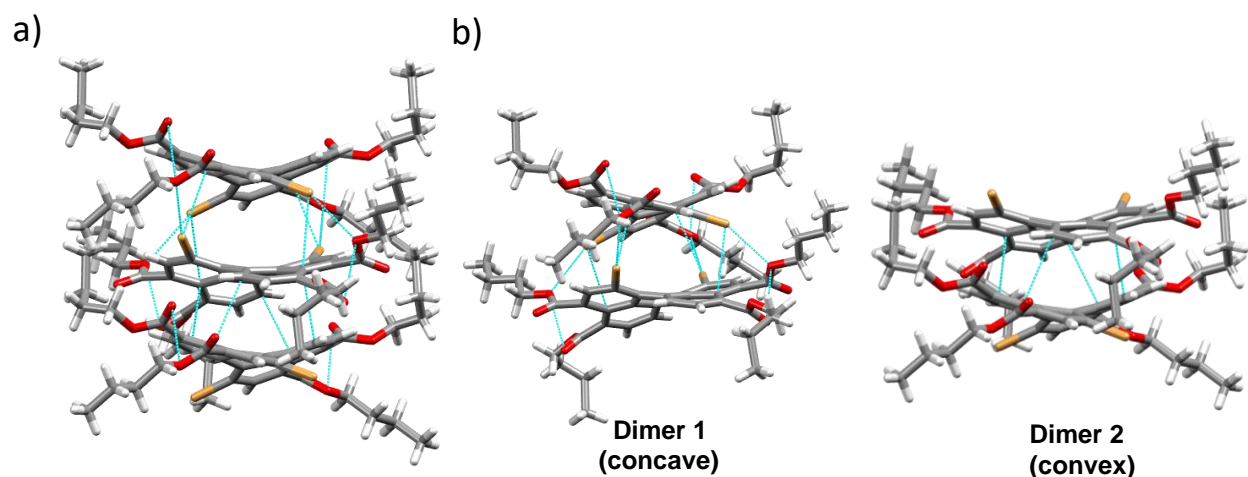


Figure 2.3: a) Columnar assembly of **PTE-Br₂** along c-axis and b) two different dimers (concave (Dimer 1) and convex (Dimer 2) shaped) in the columnar stacking.

suggests that the cross-stacked geometry are equally stable and dispersion⁵⁷ interactions play a crucial role in guiding the π -stacks in perylene dimers, respectively (Table 2.3).

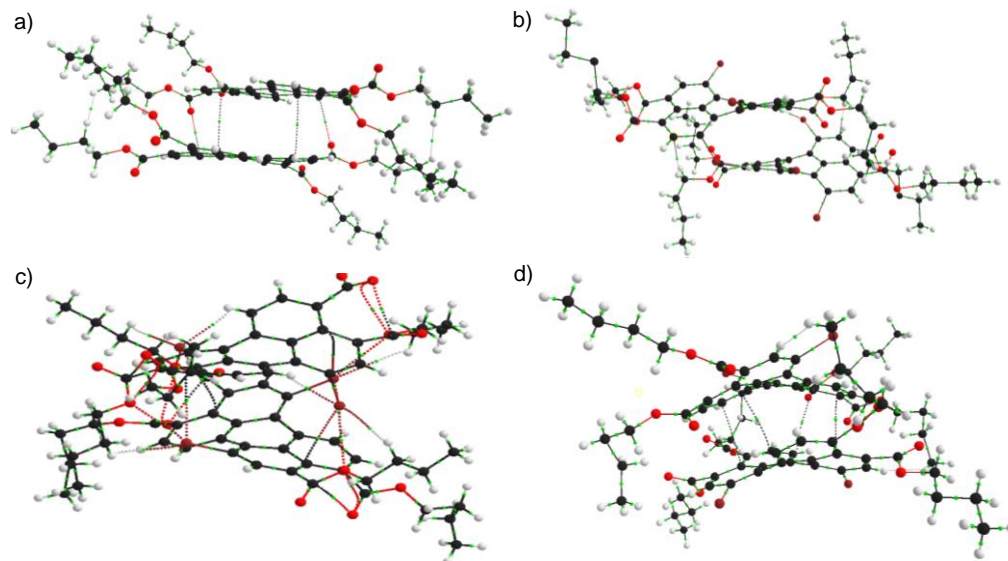


Figure 2.4: QTAIM electron density map depicting intermolecular interaction in crystalline **PTE-Br₀** (a), **PTE-Br₄** (b) and **PTE-Br₂** (c [dimer 1] and d [dimer 2]).

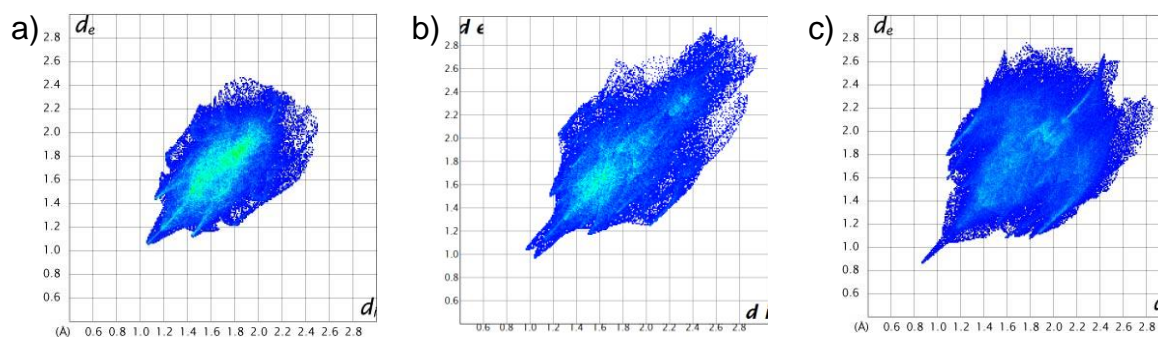


Figure 2.5: Hirshfeld 2D fingerprint plot for crystalline **PTE-Br₀** (a), **PTE-Br₂** (b) and **PTE-Br₄** (c).

Table 2.2: Relative % percentage of intermolecular interactions between monomers of crystalline **PTE-Br_{0,2,4}** obtained from Hirshfeld analysis.

| Interaction | % C...C | % C...H | % C...O | % C...Br | % H...H | % H...O | % H...Br | % O...O | % O...Br | % Br...Br | ρ |
|---------------------------|------------|------------|------------|-------------|------------|------------|-------------|------------|-------------|--------------|--------|
| PTE | 9.8 | 7.8 | 0.5 | - | 61.3 | 20.6 | - | 0.0 | - | - | 0.80 |
| PTE-Br₂ | 7.2 | 5.5 | 0.0 | 4.4 | 58.9 | 15.4 | 5.4 | 0.0 | 3.2 | 0.0 | 0.76 |
| PTE-Br₄ | 3.1 | 12.6 | 3.9 | 3.2 | 41.8 | 11.3 | 19.5 | 0.1 | 2.2 | 2.3 | 4.06 |

^atotal percentage of intermolecular contacts is 100% in PTE, PTE-Br₂ and PTE-Br₄. $\rho = [(\%C...H)/(\%C...C)]$.
Herringbone ($\rho > 4.5$), sandwich herringbone ($3.2 < \rho < 4.0$), γ ($1.2 < \rho < 2.7$) and β ($0.46 < \rho < 1.0$)

Table 2.3: The interaction energies in selected dimers determined by SAPT(0)/jun-cc-pvdz calculations and SAPT(0) energy components for crystalline **PTE-Br_{0,2,4}**.

| Dimer | Electrostatics (kJ/mol) | Exchange (kJ/mol) | Induction (kJ/mol) | Dispersion (kJ/mol) | SAPT0 (kJ/mol) |
|---------------------------|-------------------------|-------------------|--------------------|---------------------|----------------|
| PTE | -55.912 | 95.84 | -12.48 | -189.54 | -162.12 |
| PTE-Br₂ | -76.86 | 137.75 | -20.81 | -245.57 | -205.46 |
| PTE-Br₄ | -44.17 | 129.70 | -12.99 | -238.04 | -165.52 |

2.2.4. Optical Properties. Spectroscopic investigations were further performed to evaluate the influence of the assembly on photoexcited state processes of **PTE-Br_{0,2,4}** derivatives in dilute solution (chloroform) and crystalline state (Figure 2.6). The UV-vis absorption and fluorescence excitation spectra of **PTE-Br_{0,2,4}** in chloroform reveal a typical π - π^* (HOMO \rightarrow LUMO) transition of perylene chromophore with characteristic vibronic features in the 300-510 nm region (Figures 2.6 and Tables A2.3-A2.4). As the number of bromines increase at the bay region, the UV-vis absorption of **PTE-Br_{0,2,4}** reveal a minor hypsochromic shift (~ 10 nm) with a concomitant broad-

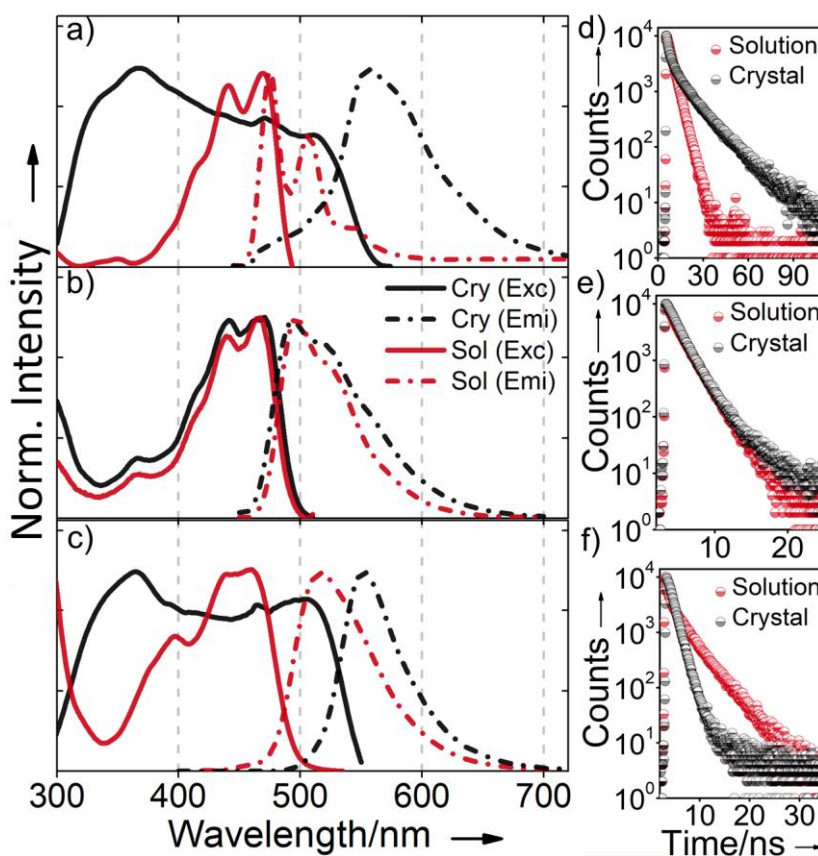


Figure 2.6: Fluorescence excitation (solid), emission (broken) and time-resolved fluorescence decay profiles of **PTE-Br₀** (a, d), **PTE-Br₂** (b, e) and **PTE-Br₄** (c, f) in dilute chloroform solution (brown) and crystalline state (black).

Table 2.4: Photophysical properties of **PTE-Br_{0,2,4}** in monomeric (CHCl_3).

| | Solution State | | | | | |
|---------------------------|-------------------------|-------------------------|----------|--------------------------------------|------------------------------------|---------------------------------------|
| | λ_{abs} (nm) | λ_{emi} (nm) | ϕ_f | ^a τ (ns) [% Amp.] | k_f (10^8 s^{-1}) | k_{nr} (10^8 s^{-1}) |
| PTE-Br₀ | 472 | 475 | 0.88 | 3.71 (100) | 2.38 | 0.32 |
| PTE-Br₂ | 468 | 497 | 0.23 | 2.00 (70) 0.79 (30) | 1.19 | 3.81 |
| PTE-Br₄ | 462 | 519 | 0.06 | 2.75 (75) 0.58 (25) | 0.82 | 2.83 |

abs – absorption; emi – fluorescence emission; ^aCollected at the respective emission maxima in solution state. The biexponential decay observed in PTE-Br_{2,4} (moderate-to-low ϕ_f) is attributed to scattering from the solvent and sample.

ening and augmented population of the higher excited states (Tables 2.4 and A2.3).^{50,51} The emission spectrum of **PTE-Br_{0,2,4}** in chloroform reveal a vibronically resolved fluorescence (450-620 nm) with a mirror image symmetry to the UV-vis absorption. Successive addition of the bromine atoms in the PTE core results in 1) decreased vibronic character 2) increased Stokes shift and 3) dramatic quenching of the fluorescence emission (Figures 2.6 and A2.10, Table 2.4). Gradual broadening and the loss of the fine vibronic structure of fluorescence emission and excitation in **PTE-Br_{0,2,4}** can be attributed to the cumulative increment of bromines at the bay region and subsequent out-of-plane core distortion.⁵¹ The fluorescence lifetime analyses of **PTE-Br_{0,2,4}** derivatives in dilute chloroform reveal a slow monoexponential (**PTE-Br₀**) and a fast biexponential (**PTE-Br_{2,4}**) decay of the fluorescence emission (Table 2.4). Dramatic quenching of the fluorescence emission with the increasing bromine atoms suggest access to an alternate decay channel, i.e., triplet excited state in **PTE-Br_{0,2,4}**.^{51,44}

Interestingly, the photoexcited state properties of crystalline **PTE-Br_{0,2,4}** reveal distinct spectroscopic signatures instigating from the discrete packing of the nearest co-facial neighbors in the molecular assembly (Figure 2.6, Table 2.5). The Kubelka-Munk (K-M) diffuse reflectance and fluorescence excitation spectra of crystalline **PTE-Br₀** ($\alpha = 70.2^\circ$, X-aggregate) and **PTE-Br₄** ($\theta = 48.4^\circ$, J-type aggregate) reveal a broad bathochromic-shift (300-570 nm) as compared to the monomeric solution (Figures 2.6a, c, and A2.10, Table A2.4). The fluorescence spectra of PTE-Br₀ ($\phi_f \approx 0.47$, X-aggregate) assembly reveal an analogous broad, red-shifted emission compared to the chloroform solution with a residual monomer component (Figure 2.6a). The picosecond time-resolved lifetime analysis of crystalline **PTE-Br₀** (X-aggregate) reveal a biexponential decay ($\tau_f = 2.18$ and 10.9 ns) of the singlet excited state with a higher average lifetime as compared to that observed in chloroform solution (Figure 2.6 d). A broad red-shifted emission, reduced k_r and

the high lifetime of the excited state in crystalline **PTE-Br₀** assembly suggests the dual influence of dipole coupling ($\alpha = 70^\circ$) in the X-aggregate and the geometric overlap (54%) mediated population of an excimer-like delocalized exciton state (Figures 2.7 and 2.8).⁵⁸

In contrast, the fluorescence emission in slip-stacked **PTE-Br₄** ($fwhm = 61$ nm, $\phi_f=0.15$) assembly reveal an archetypal J-aggregate character i.e. red-shifted, moderately narrow emission and increased quantum yields as compared to the monomeric solution ($fwhm = 73$ nm, $\phi_f = 0.06$).²⁴ The fluorescence lifetime analysis of crystalline **PTE-Br₄** reveal a reduced lifetime ($\tau_f = 0.79$ and 1.34 ns) and exhibits a nearly ten-fold increase in the radiative decay rate compared to the chloroform solution (Table 2.5). Narrow fluorescence emission (low $fwhm$), reduced lifetime (high k_r) and the high fluorescence quantum yield in the slip-stacked assembly reinforce a J-type aggregate behavior in slip-stacked crystalline **PTE-Br₄**.

Table 2.5: Photophysical properties of **PTE-Br_{0,2,4}** in the crystalline state.

| | Crystal State | | | | | |
|---------------------------|-------------------------|-------------------------|----------|--------------------------------------|-------------------------------------|--|
| | λ_{abs} (nm) | λ_{emi} (nm) | ϕ_f | ^a τ (ns) [% Amp.] | k_f (10^8 s ⁻¹) | k_{nr} (10^8 s ⁻¹) |
| PTE-Br₀ | 420 | 562 | 0.47 | 10.9 (56) 2.18(44) | 0.48 | 0.54 |
| PTE-Br₂ | 415 | 495 | 0.20 | 1.98(64) 0.6(36) | 1.01 | 3.99 |
| PTE-Br₄ | 400 | 537 | 0.15 | 1.34(70) 0.79(30) | 1.10 | 6.36 |

abs – absorption; emi – fluorescence emission; ^aCollected at the respective emission maxima in the crystalline state. The biexponential decay observed in PTE-Br_{2,4} (moderate-to-low ϕ_f) is attributed to scattering from glass coverslip used to pack the samples in the crystalline state

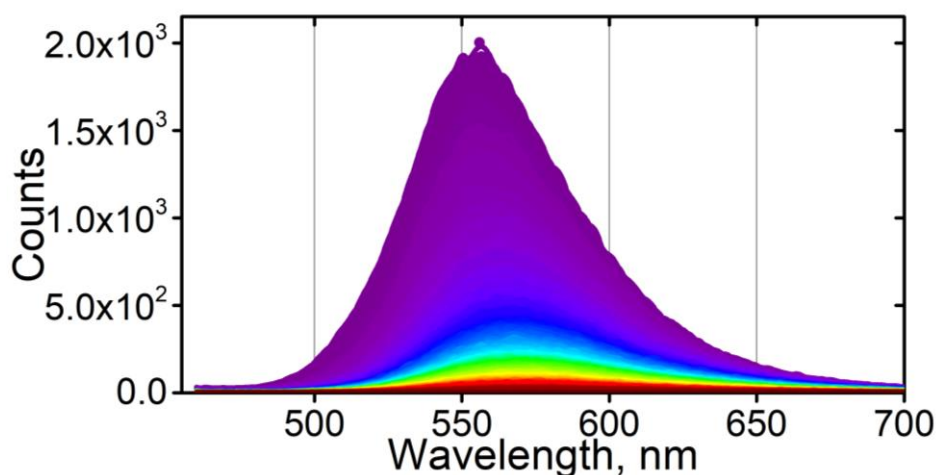


Figure 2.7: Time-resolved emission spectrum (TRES, $\lambda_{ex}=440$ nm) of crystalline **PTE-Br₀** assembly (X-aggregate).

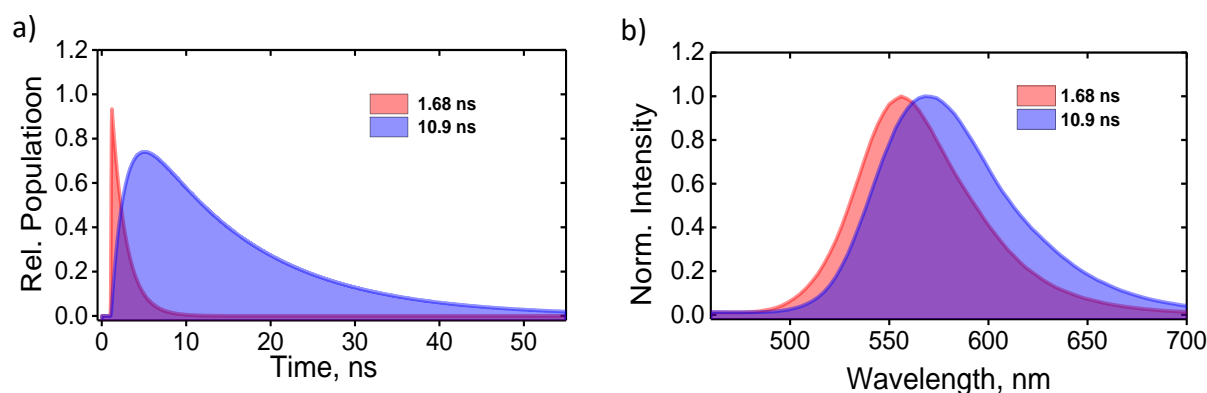


Figure 2.8: Evolution-associated spectra (EAS; a) and the relative population profiles (b) of the crystalline **PTE-Br₀** assembly (X-aggregate).

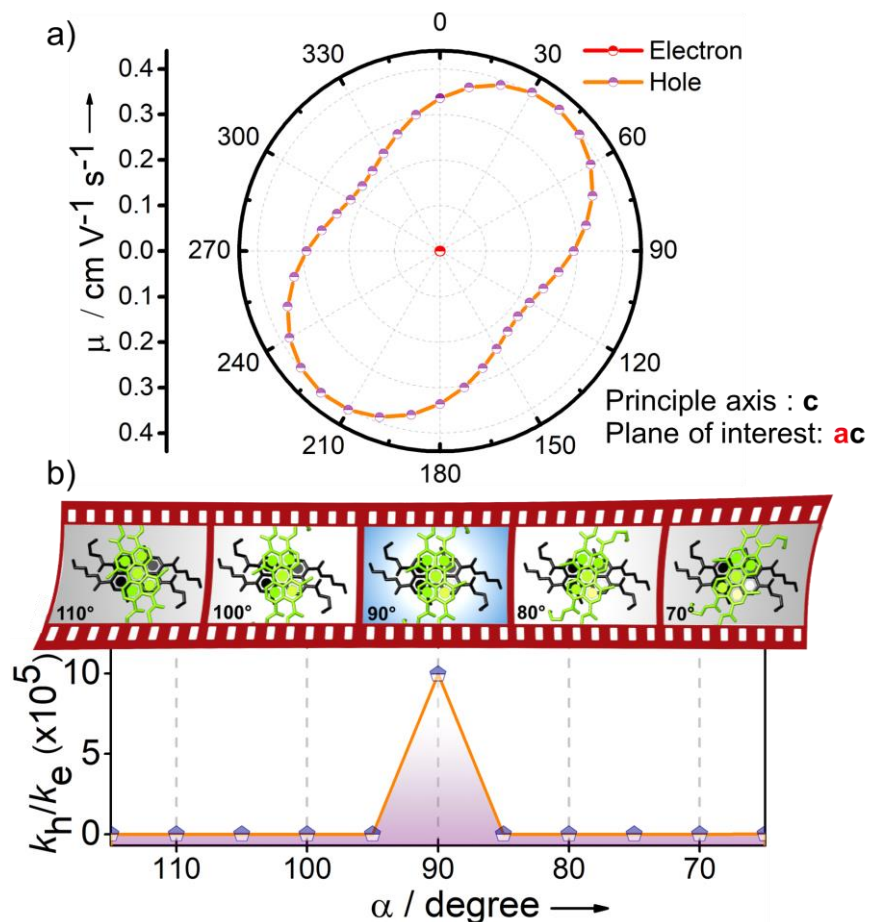
Fascinatingly, in concurrence with the theoretical predictions,²⁴ crystalline **PTE-Br₂** wherein the transition dipoles of the nearest neighbors are orthogonally ($\alpha = 90^\circ$) oriented in a Greek cross (+) fashion, reveal a virtually unperturbed fluorescence excitation and emission ($\phi_f \approx 0.20$) spectra as compared to the monomeric solution ($\phi_f \approx 0.23$, Figure 2.6 b). Marginal variation among the steady-state absorption/emission in **PTE-Br₂** solution (chloroform) and crystalline state can be a consequence of the van der Waals stabilisation ($\Delta\varepsilon_{vdW}$) achieved in the crystalline state. Picosecond time-resolved lifetime analysis of the Greek cross (+) aggregate in crystalline **PTE-Br₂** reveal an identical fluorescence lifetime ($\tau_f = 0.60$ and 1.98 ns) as that of the monomeric solution. Unperturbed photoexcited-state properties (fluorescence excitation, emission, lifetime and quantum yield) in crystalline **PTE-Br₂** Greek cross (+) aggregate as compared to the monomeric solution, suggests negligible Coulomb coupling among the transition dipoles in an orthogonal array.^{26,33} Excellent agreement between the rates of the radiative (k_r) and non-radiative decay (k_{nr}) in the solution and crystalline state reinforce that the cross stacking among the nearest-neighbors can nullify the dipole interactions in crystalline **PTE-Br₂** assembly. Observed minor discrepancy among the fluorescence quantum yields in crystalline and solution state could be a consequence of the self-absorption mediated fluorescence quenching of the excited-state in **PTE-Br₂** molecular assembly (Figure A2.11).^{59,60}

2.2.5. Charge transport analysis. Having evaluated the photoexcited-state properties, the influence of the assembly on the charge transport properties of **PTE-Br_{0,2,4}** were further calculated employing the method established by Goddard and Deng (see mobility calculation details in the experimental section).^{48,54,61} Charge transport properties computed employing the semi-classical Marcus theory of charge transfer estimates a high hole (μ_h) and a low electron (μ_e) mobility in

Table 2.6: Charge transport properties (hole/electron reorganization energies and mobility) in *PTE-Br_{0,2,4}* assemblies.

| Derivative | Hole reorganization energy (λ_h)/eV | Electron reorganization energy (λ_e)/eV | Hole mobility (μ_h)/cm ² V ⁻¹ s ⁻¹ | Electron mobility (μ_e)/cm ² V ⁻¹ s ⁻¹ | μ_h/μ_e |
|---------------------------|---|---|---|---|---------------|
| PTE-Br₀ | 0.251163 | 0.386768 | 0.1036 | 0.0267 | 3.86 |
| PTE-Br₂ | 0.26334 | 0.38623 | 0.2566 | 0.0003 | 575.80 |
| PTE-Br₄ | 0.28233 | 0.394976 | 0.8233 | 0.1293 | 6.36 |

crystalline **PTE-Br_{0,2,4}** assembly (Figure 2.9 and A2.11, Table 2.6, Appendix 2.7.6). Interestingly, the ratio of hole and electron mobility exhibit a remarkably unique trend in **PTE-Br₂** ($\mu_h/\mu_e = 575.8$) as compared to **PTE-Br_{0,4}** ($\mu_h/\mu_e = 3.86$ [**PTE-Br₀**] and 6.36 [**PTE-Br₄**], Figure 2.9a, Table 2.6). Observation of higher hole mobility in **PTE-Br₂** implies a charge-filtering capability of the Greek cross (+) stacks, probably due to the low geometric restriction of the hole delocalization in

**Figure 2.9.** a) Computed anisotropic mobility along the *ac* plane and b) schematic depiction of the charge-filtering (selective hole transfer (k_h)) phenomenon in **PTE-Br₂** Greek cross (+)-aggregate.

sterically hindered stacked assemblies (Figure 2.10).⁶² Intrigued by the unique trend in **PTE-Br₂**, rotation angle (α) dependent computation of the hole/electron transfer rates (k) and electronic coupling (V) in **PTE-Br_{0,2,4}** were carried out (Figures 2.9b, 2.11 and 2.12, Tables A2.5 and A2.6). The rotation angle-dependent charge transfer rates (k_h (hole) or k_e electronic coupling (V_h (hole) or V_e (electron)) in **PTE-Br_{0,2,4}** and the model derivative perylene reinforce that the selective hole transport trend occurs at a near-orthogonal geometry ($\alpha \approx 90^\circ$, Figure A2.13). Variation in the rotational-angle-dependent transport property in crystalline **PTE-Br₄** is due to the large longitudinal and transverse slips in the slip-stacked molecular assembly. For comparison with **PTE-Br₂**, molecular centroids of the two molecules of **PTE-Br₄** were collimated via nullifying the longitudinal and the transverse slips (Table A2.6, Figure 12). A close look into the relative charge transfer (t_e and t_h) integrals can provide deeper insights to the observed unique charge transport property.^{28,63} As reported by Spano and co-workers, a zero electron (t_e) and a nonzero hole transfer integral (t_h) and the concomitant electronic coupling (V_h/V_e) term could potentially provide access to the selective hole transport in the cross-stacked perylene aggregates (Appendix 2.7.6).^{28,63} The minor discrepancy in the observed charge-filtering orientation in **PTE-Br₀** ($\alpha = 100^\circ$) can be a consequence of small longitudinal (0.97 Å) and transverse slips (0.7 Å) in the molecular assembly.

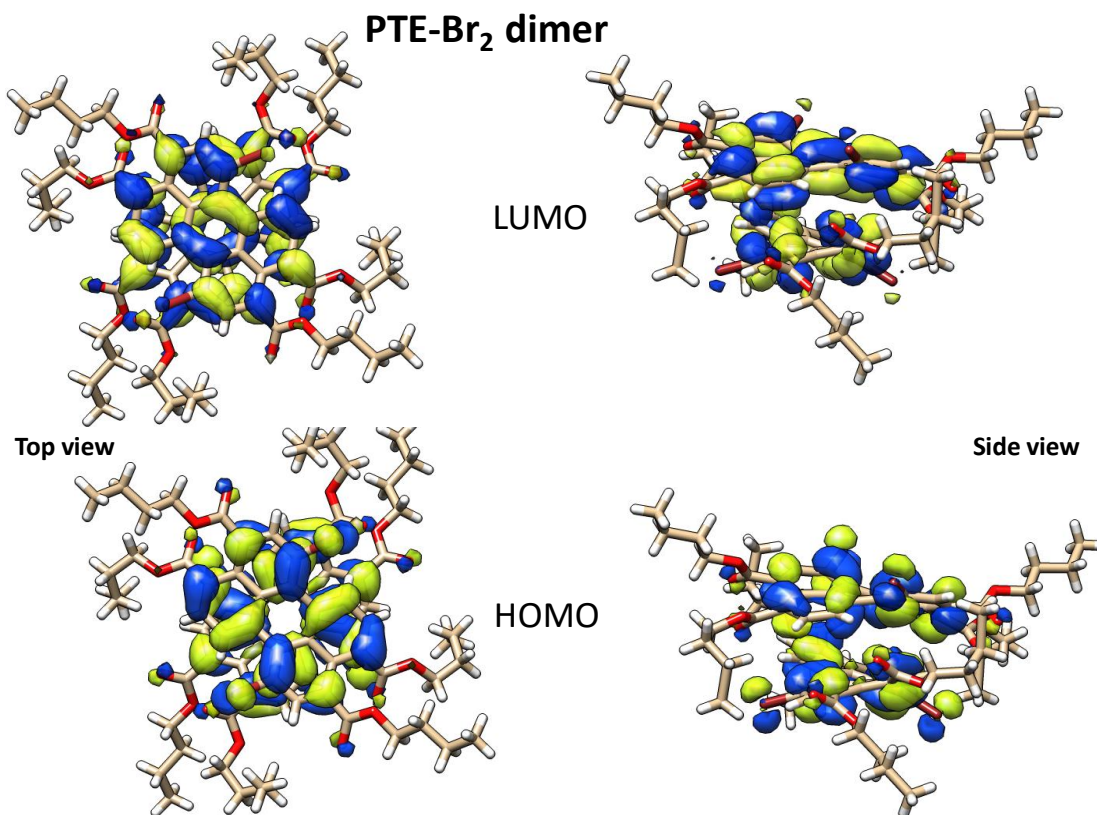


Figure 2.10. HOMO and LUMO orbital geometries of **PTE-Br₂** dimer

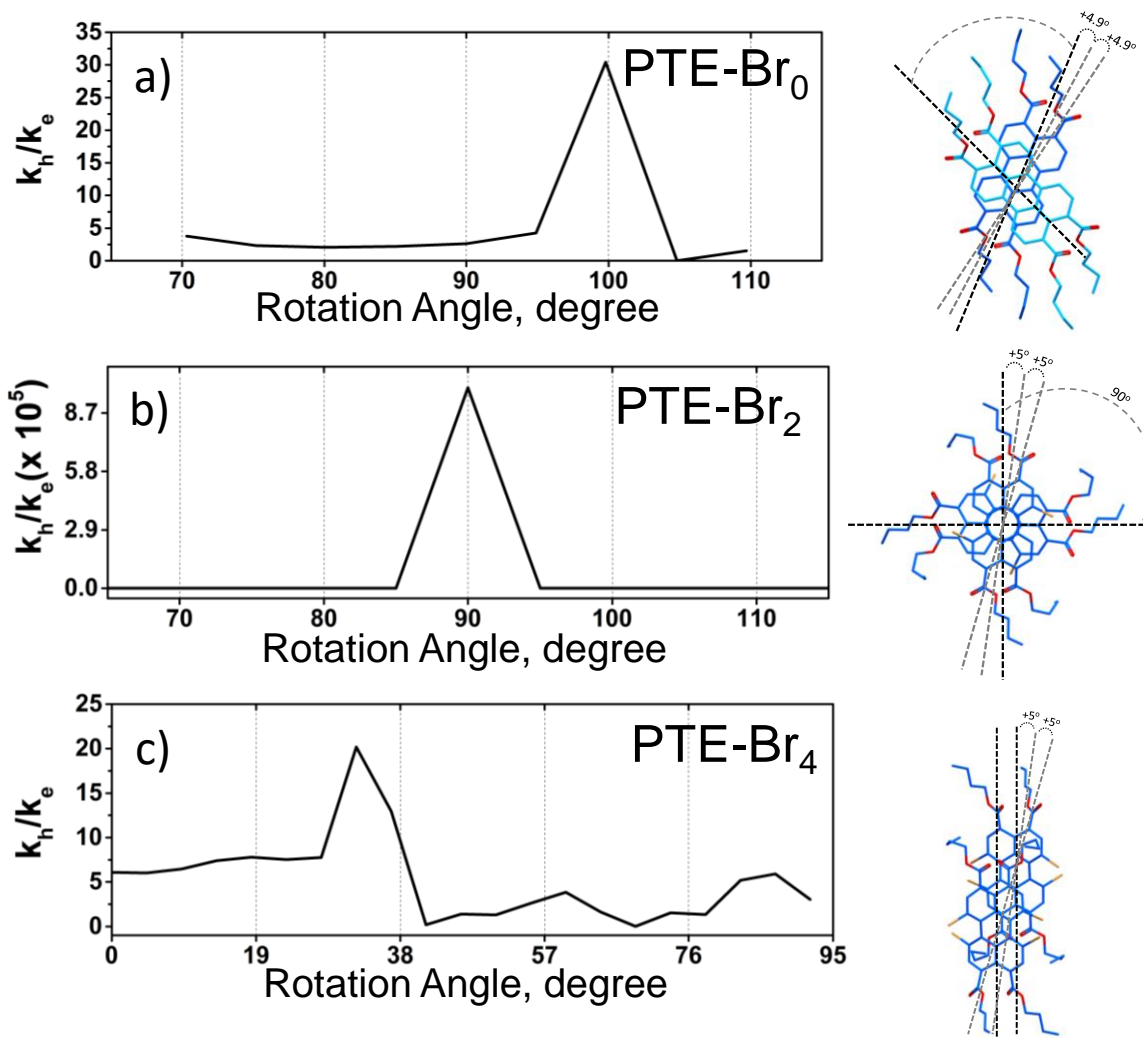


Figure 2.11: Rotation angle (α) dependent ratio of charge transfer rates ($\frac{k_n}{k_e}$) in **PTE-Br_{0,2,4}** (left) and the depiction of corresponding original molecular dimers (taken from the crystal structure) rotated about the long molecular axis of perylene (right). Minor (**PTE-Br₀**, X-aggregate) and major (**PTE-Br₄**, Slip-stacked dimer) discrepancy in the charge-filtering effect is a consequence of the minor (**PTE-Br₀**, X-aggregate) and major (**PTE-Br₄**, Slip-stacked dimer) longitudinal and transverse molecular slips.

Though the charge-filtering effect has been observed at a near-orthogonal geometry in **PTE-Br_{0,2,4}** the phenomenon could not be generalized to other chromophoric systems as the relative geometries of the HOMO and LUMO orbitals could potentially perturb the electronic coupling and charge-transport characteristics. Thus, the remarkable Greek cross (+) chromophoric assembly in **PTE-Br₂** can have vital importance in arenas wherein a monomer-like excited-state characteristics is desired while relishing the crystalline assembly for anisotropic hole transport applications.

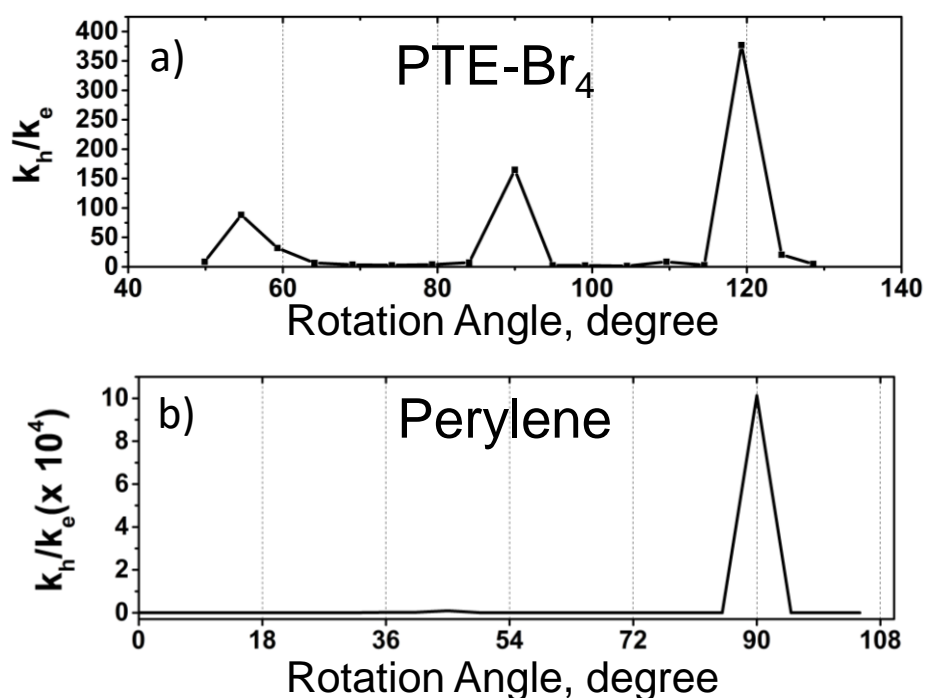


Figure 2.12: Rotation angle (α) dependent ratio of charge transfer rates ($\frac{k_h}{k_e}$) of centroid matched **PTE-Br₄** (a) and model derivative perylene (b). To remove the discrepancy arising from the large longitudinal and transverse molecular slips in **PTE-Br₄** and perylene, the molecular dimers were manually adjusted via overlapping the centroids of the co-facial dimers and subsequently the rotation angle-dependent charge transfer rates were computed.

2.3. Conclusion

To conclude, we report the first unequivocal evidence (Table A2.1) of a Greek cross (+) chromophore array ($\alpha = 90^\circ$) mediated null exciton splitting in crystalline **PTE-Br₂**. Null Coulomb coupling facilitated monomer-like spectroscopic signatures in the Greek cross (+) crystalline assembly emphasizes the critical role of the cross-dipole orientation on the optical characteristics of crystalline solids. Contrarily, X- ($\alpha = 70.2^\circ$, **PTE-Br₀**) and J-type ($\alpha = 0^\circ$, $\theta = 48.4^\circ$, **PTE-Br₄**) crystalline assemblies afford exciton coupling mediated perturbed spectroscopic behavior as compared to the monomeric solutions. Furthermore, investigations based on the semi-classical Marcus theory of charge transfer envisages a unique charge-filtering (selective hole transport) phenomenon in PTE chromophoric units arranged in an orthogonal array. Experimental efforts in the crystalline and thin films state are underway to conform the theoretically observed selective hole transfer coupling. We believe that the null exciton splitting mediated persistent monomer-like

spectroscopic behavior and the selective hole transport phenomenon observed in Greek cross (+) assembly can advance the design of novel crystalline solids for photonic and semiconducting applications. Further efforts are progressing in our group to achieve novel orthogonal cross-stacked assembly without the incorporation of the bromine atoms.

2.4. Experimental Section

2.4.1. Synthesis of perylene-3,4,9,10-tetracarboxy tetrabutylester (PTE-Br₀).⁶⁴

In a 250 mL round-bottom flask, a solution of PTCDA (800 mg, 1.13 mmol), *n*-butanol (680 mg, 9.18 mmol) and DBU (692 mg, 4.55 mmol) were refluxed under a nitrogen atmosphere for 45 min. 1-Bromobutane (122.5 mg, 8.94 mmol) was added dropwise and the reaction mixture was allowed to stir under reflux for 120 min. After the reaction was complete (TLC monitoring), the reaction mixture was poured into water. The solution was extracted with chloroform, washed with water, brine and dried over MgSO₄. The crude product was purified by column chromatography (silica, CH₂Cl₂ and *n*-hexane), the final yield was 1.07 g (80%).

Mp: 165 °C;

¹H NMR (500 MHz, CDCl₃, ppm) δ = 7.97 (d, *J* = 7.8 Hz, 4H), 7.83 (d, *J* = 7.8 Hz, 4H), 4.27 (t, 8H, *J* = 6.8 Hz), 1.73 (m, 8H), 1.42 (m, 8H), 0.94 (m, 12H);

¹³C NMR (125 MHz, CDCl₃, ppm) δ = 168.8, 132.9, 130.5, 129, 128.8, 121.5, 65.5, 30.9, 19.5, 14;

HRMS (ESI) *m/z* calculated for C₄₀H₄₄NaO₈ [(M+Na)⁺]: 675.2897, found 675.2920.

2.4.2. Synthesis of 1,7-dibromoperylene-3,4,9,10-tetracarboxy tetrabutylester (PTE – Br₂).⁶⁵

In a 250 mL round-bottom flask, PTE-Br₀ (5 g, 7.4 mmol) and K₂CO₃ (2.5 g, 18.1 mmol) were taken, and CH₂Cl₂ (125 mL) was added. To this mixture, subsequently, bromine (2.5 mL, 48.78 mmol) was added dropwise. The reaction mixture was stirred for 12 h at room temperature. Thereafter, a saturated aqueous solution of NaHSO₃ was added dropwise to the reaction mixture with stirring. The organic layer was washed with several portions of water and dried over Na₂SO₄. The solvent was removed by rotary evaporation to afford the crude product (6.14 g, ca. 99%) consisting of a mixture of 1, 7- and 1, 6-dibromoperylene-3,4,9,10-tetracarboxy tetrabutylester isomers. Isolation of regioisomerically pure 1,7-dibromoperylene-tetracarboxy tetrabutylester isomer was achieved by a multiple crystallization from dichloromethane/acetonitrile, the final yield was 2.50 g (62%).

Mp: 126 °C;

¹H NMR (500 MHz, CDCl₃, ppm): δ = 8.95 (d, *J* = 8.0 Hz, 2H), 8.29 (s, 2H), 8.09 (d, *J* = 8.0 Hz, 2H), 4.34 (t, *J* = 6.8 Hz, 8H), 1.80–1.77 (m, 8H), 1.54–1.46 (m, 8H), 1.01–0.98 (m, 12H);

¹³C NMR (125 MHz, CDCl₃, ppm): δ = 13.8, 19.2, 19.2, 30.1, 65.6, 65.8, 118.6, 126.4, 127.5, 128.9, 130.3, 130.4, 131.0, 132.0, 136.6, 167.1, 167.9;

HRMS (ESI): m/z calculated for C₄₀H₄₂Br₂NaO₈ [(M+Na)⁺]: 833.1139; found: 833.1110.

2.4.3. Synthesis of 1,6,7,12-tetrabromoperylene-3,4,9,10-tetracarboxylic dianhydride (PTCDA-Br₄).^{64,66}

300 mg of perylene-3, 4, 9, 10-tetracarboxylic dianhydride (PTCDA) was stirred with 50 mL of concentrated sulphuric acid for 5 hours. Catalytic amount of elemental iodine was added and the reaction mixture was heated to 110°C. 4.4 equivalents of elemental bromine was added drop wise to synthesize the tetrabromo PTCDA. The reaction mixture was refluxed for 24 hours. After 24 hours, the product was precipitated by pouring the reaction mixture into 100 mL of ice water. The product (PTCDA-Br₄) was filtered and dried in hot air oven. Owing to the insolubility of the compounds, they were taken for next step of synthesis without any characterization.

2.4.4. Synthesis of 1,6,7,12-Tetrabromoperylene-3,4,9,10-tetracarboxy tetrabutylester (PTE-Br₄).⁶⁴

In a 250 mL round-bottom flask, a solution of PTCDA – Br_{0,2,4} (800 mg, 1.13 mmol), *n*-butanol (680 mg, 9.18 mmol) and DBU (692 mg, 4.55 mmol) were refluxed under nitrogen atmosphere for 45 min. 1-Bromobutane (122.5 mg, 8.94 mmol) was added dropwise and the reaction mixture was allowed to stir under reflux for 90 min. After the reaction was complete (TLC monitoring), the reaction mixture was poured into water. The solution was extracted with chloroform, washed with water, brine and dried over MgSO₄. The crude product was purified by column chromatography (silica, CH₂Cl₂ and *n*-hexane), the final yield was 380 mg (35 %).

Mp: 190 °C;

¹H NMR (500 MHz, CDCl₃, ppm): δ = 8.23 (s, 4H), 4.36 (m, 8H), 1.81 (m, 8H), 1.51 (m, 8H), 1.01 (t, *J* = 7.4 Hz, 12H);

¹³C NMR (125 MHz, CDCl₃, ppm) δ = 167.0, 135.1, 134.0, 130.6, 130.4, 123.8, 122.7, 60.2, 30.7, 19.4, 13.9;

HRMS (ESI): m/z calculated for C₄₀H₄₀Br₄NaO₈ [M + Na]⁺: 986.9349, found 986.9362.

2.5. Additional Tables

Table A2.1: A comparative account of rotation angle (α) dependent molecular stacking in literature reports.

| | Contributed by | Molecule* (Reference) | Rotation angle (α) | Slip angle (θ) |
|---|--|--|-----------------------------|-------------------------|
| 1 | Paul M. Lahti and co-workers | 2,5-Bis(2-hydroxyethoxy)-1,4-bis(phenylethynyl)benzene (BHE-PE2.5) <i>Cryst. Growth & Design</i> , 2006 , 6, 6 | 99.2° | na |
| 2 | Mahesh Hariharan and co-workers [#] | 1, 7-Dibromoperylene-3, 4, 9, 10-tetracarboxy tetrabutylester (PTE-Br ₂) [#] Current work | 90° | 0° |
| 3 | Wallace W. H. Wong and co-workers | <i>N,N</i> -bis(5'-butyl-[1,1':3',1''-terphenyl]-2'-yl)perylene-3,4:9,10-tetracarboxylic diimide (bPDI2) <i>Chem. Mater.</i> , 2017 , 29, 8395 | †85.6° | † |
| 4 | Yuguang Ma and co-workers | 2,5-Diphenyl-1,4-distyrylbenzene (trans-DPDSB) <i>J. Am. Chem. Soc.</i> , 2005 , 127, 14152 | 70° | na |
| 4 | Yuguang Ma and co-workers | 2,5,2',5',2'',5''-hexastyryl-[1,1';4',1'']terphenyl (HSTP) <i>Adv. Mater.</i> , 2005 , 17, 2710 | 70° | na |
| 5 | Wenping Hu and co-workers | 2,6-diphenylanthracene-9,10-diyl)bis(ethyne-2,1-diyl)bis(triethylsilane) (TES-DPA) <i>J. Mater. Chem. C</i> , 2015 , 3, 3068 | 60° | na |
| 6 | Bin Xu, Wenjing Tian and co-workers | 1,4-Bis(2,2-diphenylvinyl)benzene (BDPVB) <i>Adv. Optical Mater.</i> , 2015 , 3, 763 | 62° | na |
| 7 | Ling Zhang and co-workers | <i>N,N</i> -bis(cyclohexyl)perylene-3,4:9,10-tetracarboxylic diimide (CH-PTCDI) <i>Chem. Mater.</i> , 2009 , 21, 2930 | 40° | na |
| 8 | Frank Würthner and co-workers | Merocyanine dye <i>Angew. Chem. Int. Ed.</i> , 2006 , 45, 7026 | 10° | 59.9° |

na - not available; †Possess longitudinal and transverse molecular slips (centroids does not overlap); [#]Our data corresponding to the Greek cross (+) stacking (centroids overlap). *Chromophoric aggregates possessing orthogonal geometry ($\alpha = 90^\circ$) has been proposed employing solid-state NMR (*Angew. Chem. Int. Ed.*, **2009**,

48, 4621), two-dimensional wide-angle x-ray scattering (2D WAXS, *J. Am. Chem. Soc.*, **2007**, *129*, 14116), and molecular modelling (*Adv. Funct. Mater.*, **2004**, *14*, 649) methods in columnar liquid crystals.

Table A2.2: Calculated topological properties of the electron density for the intermolecular interaction in crystalline PTE-Br_{0,2,4}.

| Description | Interaction | ^a <i>d</i> , (Å) | ^b $\rho_b(r)$, eÅ ⁻³ | ^c $\nabla^2\rho_b(r)$, eÅ ⁻⁵ | ^d DE, kJ/mol |
|---|-------------|--------------------------------|--|--|----------------------------|
| PTE-Br₀ | H80-H130 | 2.500 | 0.029 | 0.310 | 2.875 |
| | C58-O137 | 3.205 | 0.042 | 0.528 | 4.696 |
| | C47-C104 | 3.464 | 0.036 | 0.358 | 3.119 |
| | C12-C139 | 3.464 | 0.036 | 0.358 | 3.119 |
| | O45-C150 | 3.205 | 0.042 | 0.528 | 4.696 |
| | H38-H172 | 2.500 | 0.029 | 0.310 | 2.875 |
| PTE-Br₂ (Dimer 1) | Br88-O178 | 3.056 | 0.079 | 0.997 | 10.446 |
| | Br88-H159 | 3.270 | 0.025 | 0.030 | 2.222 |
| | Br88-H53 | 2.612 | 0.103 | 1.324 | 12.237 |
| | Br88-C149 | 3.588 | 0.043 | 0.482 | 3.689 |
| | O178-O176 | 2.837 | 0.098 | 1.380 | 14.016 |
| | O178-C152 | 2.665 | 0.101 | 1.395 | 14.549 |
| | Br180-C11 | 3.588 | 0.043 | 0.482 | 3.388 |
| | Br180-H21 | 3.270 | 0.024 | 0.304 | 2.222 |
| | Br180-O40 | 3.057 | 0.079 | 0.997 | 10.406 |
| | Br180-H145 | 2.613 | 0.103 | 1.323 | 12.236 |
| | O38-O40 | 2.837 | 0.098 | 1.380 | 14.016 |
| | C14-O38 | 2.665 | 0.101 | 1.395 | 14.549 |
| | Br134-H99 | 2.613 | 0.103 | 1.323 | 12.235 |
| | Br134-C57 | 3.588 | 0.043 | 0.482 | 3.743 |
| | Br134-H67 | 3.270 | 0.024 | 0.304 | 2.222 |
| | Br134-O86 | 3.057 | 0.079 | 0.997 | 10.406 |
| | O84-O86 | 2.837 | 0.098 | 1.380 | 14.049 |
| | O84-C60 | 2.665 | 0.101 | 1.395 | 14.548 |
| | Br42-H7 | 2.613 | 0.103 | 1.323 | 12.237 |
| | Br42-C103 | 3.588 | 0.043 | 0.482 | 3.743 |
| Br42-O132 | 3.057 | 0.079 | 0.997 | 10.406 | |
| Br42-H113 | 3.270 | 0.024 | 0.304 | 2.222 | |
| O130-O132 | 2.837 | 0.098 | 1.380 | 14.015 | |
| O130-C106 | 2.665 | 0.101 | 1.395 | 14.547 | |
| PTE-Br₂ (Dimer 2) | C6-C103 | 3.420 | 0.034 | 0.365 | 2.969 |
| | C57-C98 | 3.420 | 0.034 | 0.365 | 2.969 |
| | H2-H136 | 2.467 | 0.023 | 0.256 | 2.370 |
| | H90-H94 | 2.470 | 0.023 | 0.391 | 2.371 |

| | | | | | |
|---------------------------|-----------|-------|-------|-------|-------|
| | C52-C149 | 3.635 | 0.034 | 0.365 | 2.969 |
| | C11-C144 | 3.420 | 0.034 | 0.365 | 2.968 |
| | H48-H182 | 2.460 | 0.023 | 0.256 | 2.371 |
| PTE-Br₄ | H14-Br177 | 3.163 | 0.030 | 0.307 | 2.527 |
| | H68-C93 | 2.769 | 0.042 | 0.422 | 3.765 |
| | Br87-H104 | 3.162 | 0.030 | 0.307 | 2.526 |
| | C3-H158 | 2.769 | 0.042 | 0.422 | 3.765 |

^a*d* = distance, ^b $\rho_{bb}(r)$ =electron density at the BCP and ^c $\nabla^2 \rho_b(r)$ = Laplacian of the electron density at the BCP, ^dDE = dissociation energy.

Table A2.3: Oscillator strength for different transitions of **PTE-Br_{0,2,4}** (monomer) calculated at TD-B3LYP/6-311G+(*d, p*) level of theory.

| Derivative | Excitation | | Energy (eV) | Wavelength (nm) | Main Transition Orbital |
|---------------------------|----------------|---------------------|-------------|-----------------|-------------------------|
| | State | Oscillator Strength | | | |
| PTE-Br₀ | S ₁ | 0.771 | 2.450 | 505.96 | HOMO → LUMO |
| | S ₂ | 0.000 | 3.413 | 363.28 | HOMO-1 → LUMO |
| | | | | | HOMO → LUMO+1 |
| | S ₃ | 0.000 | 3.534 | 350.83 | HOMO-4 → LUMO |
| | | | | | HOMO-2 → LUMO |
| | | | | | HOMO-1 → LUMO |
| S ₄ | 0.000 | 3.557 | 348.60 | HOMO → LUMO+2 | |
| | | | | HOMO → LUMO+3 | |
| | | | | HOMO-2 → LUMO | |
| S ₅ | 0.051 | 3.661 | 338.68 | HOMO → LUMO+1 | |
| | | | | HOMO-3 → LUMO | |
| | | | | HOMO → LUMO+4 | |
| S ₆ | 0.000 | 3.757 | 329.96 | HOMO-4 → LUMO | |
| | | | | HOMO → LUMO+2 | |
| | | | | | |
| PTE-Br₂ | S ₁ | 0.566 | 2.463 | 503.49 | HOMO → LUMO |
| | S ₂ | 0.003 | 2.342 | 371.00 | HOMO-1 → LUMO |
| | S ₃ | 0.118 | 3.480 | 356.32 | HOMO-2 → LUMO |
| | S ₄ | 0.015 | 3.540 | 350.31 | HOMO-1 → LUMO |
| | | | | | HOMO → LUMO+1 |
| S ₅ | 0.010 | 3.626 | 342.01 | HOMO → LUMO+2 | |
| | | | | | HOMO-3 → LUMO |

| | | | | | |
|---------------------------|----------------|--------|-------|--------|--|
| PTE-Br₄ | | | | | HOMO-1 → LUMO HOMO → LUMO+1 HOMO → LUMO+2 |
| | S ₆ | 0.030 | 3.636 | 341.06 | HOMO-4 → LUMO HOMO-3 → LUMO HOMO-1 → LUMO HOMO → LUMO+1 |
| | S ₁ | 0.0038 | 2.230 | 556.06 | HOMO-1 → LUMO+1 |
| | S ₂ | 0.4453 | 2.475 | 501.14 | HOMO → LUMO |
| | S ₃ | 0.0006 | 2.559 | 484.61 | HOMO-1 → LUMO |
| | S ₄ | 0.1652 | 2.965 | 418.27 | HOMO-2 → LUMO HOMO → LUMO+4 |
| | S ₅ | 0.0242 | 3.121 | 397.29 | HOMO-3 → LUMO HOMO → LUMO+3 HOMO → LUMO+5 |
| | S ₆ | 0.0004 | 3.270 | 379.17 | HOMO → LUMO+1 |

Table A2.4: Oscillator strength, energy and wavelength of different transitions of PTE-Br_{0,2,4} (dimer) calculated at TD-B3LYP/6-311G+(d, p) level of theory.

| Derivative | Excitation | | Energy (eV) | Wavelength (nm) | Main Transition Orbital |
|---------------------------|----------------|---------------------|-------------|-----------------|--|
| | Transition | Oscillator Strength | | | |
| PTE-Br₀ | S ₁ | 0.010 | 2.223 | 560.15 | HOMO-1 → LUMO+1 HOMO → LUMO |
| | S ₂ | 0.005 | 2.234 | 554.93 | HOMO-1 → LUMO HOMO → LUMO+1 |
| | S ₃ | 0.199 | 2.479 | 500.17 | HOMO-1 → LUMO+1 |
| | S ₄ | 0.686 | 2.550 | 486.19 | HOMO → LUMO+1 |
| | S ₅ | 0.000 | 2.937 | 422.17 | HOMO-4 → LUMO HOMO-2 → LUMO HOMO-1 → LUMO+2 HOMO → LUMO+3 |
| | S ₆ | 0.000 | 3.1304 | 396.06 | HOMO-7 → LUMO HOMO-1 → LUMO+3 HOMO → LUMO+2 |
| PTE-Br₂ | S ₁ | 0.000 | 2.392 | 518.24 | HOMO → LUMO |
| (Dimer 1) | S ₂ | 0.000 | 2.393 | 518.20 | HOMO-1 → LUMO+1 |

| | | | | | |
|---|----------------|--------|-------|--------|--|
| | | | | | HOMO → LUMO+1 |
| | S ₃ | 0.290 | 2.530 | 490.05 | HOMO-1 → LUMO HOMO → LUMO |
| | S ₄ | 0.290 | 2.530 | 490.00 | HOMO-1 → LUMO+1 |
| | S ₅ | 0.000 | 3.134 | 395.60 | HOMO-3 → LUMO HOMO-2 → LUMO+1 HOMO-1 → LUMO+3 HOMO → LUMO+6 |
| | S ₆ | 0.003 | 3.136 | 395.39 | HOMO-2 → LUMO+1 HOMO-1 → LUMO+2 |
| PTE-Br₂ (Dimer 2) | S ₁ | 0.0249 | 2.326 | 533.13 | HOMO → LUMO |
| | S ₂ | 0.0249 | 2.326 | 533.09 | HOMO-1 → LUMO+1 HOMO → LUMO+1 |
| | S ₃ | 0.2589 | 2.554 | 485.00 | HOMO-1 → LUMO HOMO → LUMO |
| | S ₄ | 0.2589 | 2.559 | 485.00 | HOMO-1 → LUMO+1 HOMO-3 → LUMO+1 HOMO-2 → LUMO |
| | S ₅ | 0.0002 | 2.896 | 428.18 | HOMO-2 → LUMO+1 HOMO-1 → LUMO+3 HOMO → LUMO+2 |
| | S ₆ | 0.000 | 3.119 | 397.52 | HOMO-3 → LUMO HOMO-3 → LUMO+1 HOMO-2 → LUMO+1 |
| PTE-Br₄ | S ₁ | 0.0019 | 1.768 | 701.17 | HOMO - 2 → LUMO HOMO - 2 → LUMO+2 |
| | S ₂ | 0.0019 | 1.769 | 701.08 | HOMO - 3 → LUMO HOMO - 3 → LUMO+1 HOMO - 3 → LUMO+2 |
| | S ₃ | 0.2532 | 2.402 | 516.20 | HOMO → LUMO |
| | S ₄ | 0.000 | 2.445 | 507.13 | HOMO-1 → LUMO+2 HOMO → LUMO+1 HOMO → LUMO+3 |
| | S ₅ | 0.000 | 2.461 | 503.87 | HOMO-1 → LUMO+1 HOMO → LUMO HOMO → LUMO+1 |

| | | | | | |
|--|----------------|-------|-------|--------|-----------------|
| | | | | | HOMO → LUMO+2 |
| | | | | | HOMO-1 → LUMO |
| | S ₆ | 0.000 | 2.461 | 503.80 | HOMO-1 → LUMO+2 |
| | | | | | HOMO → LUMO+1 |

Table A2.5: Rotation angle (α) dependent hole and electron hopping rates in dimers (Centroid co-ordinates unchanged) of **PTE-Br_{0,2,4}**.

| Derivative | Angle /degree | Electronic Coupling (V_h)/eV | Electronic Coupling (V_e)/eV | Hole hopping rate (k_h)/s ⁻¹ | Electron hopping rate (k_e)/s ⁻¹ | k_h/k_e |
|---------------------------|---------------|----------------------------------|----------------------------------|---|---|-----------|
| PTE-Br₀ | 75.2 | 0.0591 | 0.0830 | 1.02 x 10 ¹³ | 4.34 x 10 ¹² | 2.339607 |
| | 80.1 | 0.0585 | 0.0885 | 1 x 10 ¹³ | 4.93 x 10 ¹² | 2.032892 |
| | 85.1 | 0.0564 | 0.0816 | 9.24 x 10 ¹² | 4.19 x 10 ¹² | 2.20342 |
| | 90 | 0.0495 | 0.0662 | 7.17 x 10 ¹² | 2.76 x 10 ¹² | 2.602062 |
| | 94.9 | 0.0388 | 0.0403 | 4.38 x 10 ¹² | 1.02 x 10 ¹² | 4.282026 |
| | 99.8 | 0.0236 | 0.0088 | 1.63 x 10 ¹² | 5.36 x 10 ¹⁰ | 30.41814 |
| | 104.8 | 0.0006 | 0.0226 | 1.54 x 10 ⁹ | 3.22 x 10 ¹¹ | 0.00478 |
| | 109.7 | 0.0285 | 0.0497 | 2.37 x 10 ¹² | 1.56 x 10 ¹² | 1.517089 |
| PTE-Br₂ | 65 | 0.1345 | 0.0114 | 4.52 x 10 ¹³ | 8.4 x 10 ¹⁰ | 537.8824 |
| | 70 | 0.0564 | 0.0651 | 7.96 x 10 ¹² | 2.63 x 10 ¹² | 3.024712 |
| | 75 | 0.0138 | 0.0864 | 4.87 x 10 ¹¹ | 4.64 x 10 ¹² | 0.104834 |
| | 80 | 0.0675 | 0.0714 | 1.15 x 10 ¹³ | 3.18 x 10 ¹² | 3.619948 |
| | 85 | 0.1202 | 0.0509 | 3.65 x 10 ¹³ | 1.64 x 10 ¹² | 22.26228 |
| | 90 | 0.1325 | 0.0001 | 4.41 x 10 ¹³ | 4.42 x 10 ⁷ | 995634.7 |
| | 95 | 0.1195 | 0.0504 | 3.62 x 10 ¹³ | 1.61 x 10 ¹² | 22.50217 |
| | 100 | 0.0668 | 0.0706 | 1.14 x 10 ¹³ | 3.19 x 10 ¹² | 3.569228 |
| | 105 | 0.0150 | 0.0856 | 5.68 x 10 ¹¹ | 4.69 x 10 ¹² | 0.12106 |
| | 110 | 0.0562 | 0.0639 | 8.11 x 10 ¹² | 2.64 x 10 ¹² | 3.075331 |
| | 115 | 0.1315 | 0.0141 | 4.39 x 10 ¹³ | 1.25 x 10 ¹¹ | 352.5979 |
| PTE-Br₄ | 0 | 0.1159 | 0.0885 | 2.73 x 10 ¹³ | 4.49 x 10 ¹² | 6.08169 |
| | 4.6 | 0.1202 | 0.0921 | 2.93 x 10 ¹³ | 4.86 x 10 ¹² | 6.016579 |
| | 9.2 | 0.1207 | 0.0892 | 2.95 x 10 ¹³ | 4.56 x 10 ¹² | 6.467087 |
| | 13.8 | 0.1094 | 0.0758 | 2.43 x 10 ¹³ | 3.29 x 10 ¹² | 7.398459 |
| | 18.4 | 0.0963 | 0.0652 | 1.89 x 10 ¹³ | 2.43 x 10 ¹² | 7.782686 |

| | | | | | |
|------|--------|--------|-----------------------|-----------------------|----------|
| 23 | 0.0866 | 0.0594 | 1.51×10^{13} | 2.02×10^{12} | 7.507841 |
| 27.6 | 0.0648 | 0.0442 | 8.66×10^{12} | 1.11×10^{12} | 7.767415 |
| 32.2 | 0.0448 | 0.0185 | 4.03×10^{12} | 1.99×10^{11} | 20.17939 |
| 36.8 | 0.0189 | 0.0102 | 7.2×10^{11} | 5.56×10^{10} | 12.94615 |
| 41.4 | 0.0055 | 0.0241 | 6.22×10^{10} | 3.22×10^{11} | 0.193333 |
| 46 | 0.0241 | 0.0396 | 1.15×10^{12} | 8.35×10^{11} | 1.377665 |
| 50.6 | 0.0279 | 0.0476 | 1.61×10^{12} | 1.24×10^{12} | 1.295172 |
| 55.2 | 0.0337 | 0.0395 | 2.3×10^{12} | 8.8×10^{11} | 2.610517 |
| 59.8 | 0.0315 | 0.0303 | 2.01×10^{12} | 5.24×10^{11} | 3.8353 |
| 64.4 | 0.0166 | 0.0241 | 5.56×10^{11} | 3.38×10^{11} | 1.6418 |
| 69 | 0.0026 | 0.0269 | 1.15×10^{10} | 4.12×10^{11} | 0.0278 |
| 73.6 | 0.0169 | 0.0261 | 5.84×10^{11} | 3.82×10^{11} | 1.5306 |
| 78.2 | 0.0176 | 0.0289 | 6.26×10^{11} | 4.69×10^{11} | 1.3329 |
| 82.8 | 0.0177 | 0.0145 | 6.25×10^{11} | 1.2×10^{11} | 5.1845 |
| 87.4 | 0.0094 | 0.0076 | 1.92×10^{11} | 3.25×10^{10} | 5.8927 |
| 92 | 0.0059 | 0.0057 | 6.22×10^{10} | 2.05×10^{10} | 3.0321 |

Table A2.6: Rotation angle (α) dependent hole and electron hopping rates in dimers (Centroid co-ordinates modified) of **PTE-Br₄** and the model derivative perylene.

| Derivative | Angle /degree | Electronic Coupling (V_h)/eV | Electronic Coupling (V_e)/eV | Hole hopping rate (k_h)/s ⁻¹ | Electron hopping rate (k_e)/s ⁻¹ | k_h/k_e |
|---------------------------|---------------|----------------------------------|----------------------------------|---|---|-----------|
| PTE-Br₄ | 49.9 | 0.1672 | 0.1095 | 5.71×10^{13} | 6.71×10^{12} | 8.5036 |
| | 54.6 | 0.1775 | 0.0359 | 6.44×10^{13} | 7.3×10^{11} | 88.2639 |
| | 59.3 | 0.1743 | 0.0573 | 6.19×10^{13} | 1.95×10^{12} | 31.8399 |
| | 64.1 | 0.1521 | 0.1135 | 4.71×10^{13} | 7.33×10^{12} | 6.4244 |
| | 69 | 0.1391 | 0.1345 | 3.95×10^{13} | 1.03×10^{13} | 3.8405 |
| | 74.1 | 0.1176 | 0.1361 | 2.82×10^{13} | 1.05×10^{13} | 2.6801 |
| | 79.3 | 0.0891 | 0.0859 | 1.62×10^{13} | 4.18×10^{12} | 3.8769 |
| | 84.1 | 0.0627 | 0.0446 | 8.05×10^{12} | 1.13×10^{12} | 7.1012 |
| | 90 | 0.0448 | 0.0065 | 4.1×10^{12} | 2.49×10^{10} | 164.8717 |
| | 94.9 | 0.0517 | 0.0611 | 5.49×10^{12} | 2.1×10^{12} | 2.6074 |
| | 99.1 | 0.0735 | 0.0933 | 1.1×10^{13} | 4.96×10^{12} | 2.2182 |
| | 104.5 | 0.0795 | 0.1199 | 1.28×10^{13} | 8.23×10^{12} | 1.5614 |

| | | | | | | |
|----------|--------|--------|-----------------------|-----------------------|-----------------------|----------|
| | 109.6 | 0.1174 | 0.0759 | 2.8×10^{13} | 3.3×10^{12} | 8.4791 |
| | 114.5 | 0.0966 | 0.1080 | 1.9×10^{13} | 6.61×10^{12} | 2.8764 |
| | 119.3 | 0.1334 | 0.0129 | 3.61×10^{13} | 9.59×10^{10} | 376.7364 |
| | 124.5 | 0.1429 | 0.0596 | 4.16×10^{13} | 2.01×10^{12} | 20.6391 |
| | 128.6 | 0.1412 | 0.1210 | 4.04×10^{13} | 8.38×10^{12} | 4.8243 |
| Perylene | 0 | 0.5521 | 0.6247 | 3.55×10^{15} | 3.32×10^{15} | 1.0690 |
| | 5 | 0.5311 | 0.5962 | 3.28×10^{15} | 3.03×10^{15} | 1.0832 |
| | 10 | 0.4642 | 0.5126 | 2.51×10^{15} | 2.24×10^{15} | 1.1200 |
| | 15 | 0.3611 | 0.3914 | 1.52×10^{15} | 1.31×10^{15} | 1.1609 |
| | 20 | 0.2345 | 0.2585 | 6.4×10^{14} | 5.7×10^{14} | 1.1228 |
| | 25 | 0.0988 | 0.1326 | 1.14×10^{14} | 1.5×10^{14} | 0.7592 |
| | 30 | 0.0317 | 0.0356 | 1.18×10^{13} | 1.08×10^{13} | 1.0893 |
| | 35 | 0.1456 | 0.0188 | 2.46×10^{14} | 3.04×10^{12} | 81.0044 |
| | 40 | 0.2328 | 0.0255 | 6.28×10^{14} | 5.57×10^{12} | 112.7878 |
| | 45 | 0.2879 | 0.0109 | 9.62×10^{14} | 1.03×10^{12} | 933.6816 |
| | 50 | 0.3106 | 0.0780 | 1.12×10^{15} | 5.2×10^{13} | 21.4886 |
| | 55 | 0.2988 | 0.1592 | 1.04×10^{15} | 2.17×10^{14} | 4.7785 |
| | 60 | 0.2589 | 0.2331 | 7.79×10^{14} | 4.62×10^{14} | 1.6860 |
| | 65 | 0.2021 | 0.2845 | 4.74×10^{14} | 6.91×10^{14} | 0.6862 |
| | 70 | 0.1378 | 0.2976 | 2.2×10^{14} | 7.56×10^{14} | 0.2915 |
| | 75 | 0.0757 | 0.2699 | 6.65×10^{13} | 6.22×10^{14} | 0.1068 |
| | 80 | 0.0219 | 0.2061 | 5.55×10^{12} | 3.63×10^{14} | 0.0153 |
| | 85 | 0.0148 | 0.1130 | 2.58×10^{12} | 1.09×10^{14} | 0.0236 |
| | 90 | 0.0265 | 0.0001 | 8.14×10^{12} | 80367610 | 101277 |
| | 95 | 0.0148 | 0.1133 | 2.56×10^{12} | 1.1×10^{14} | 0.0232 |
| 100 | 0.0213 | 0.2062 | 5.34×10^{12} | 3.64×10^{14} | 0.01469 | |
| 105 | 0.0754 | 0.27 | 6.64×10^{13} | 6.23×10^{14} | 0.1065 | |

2.6. Additional Figures

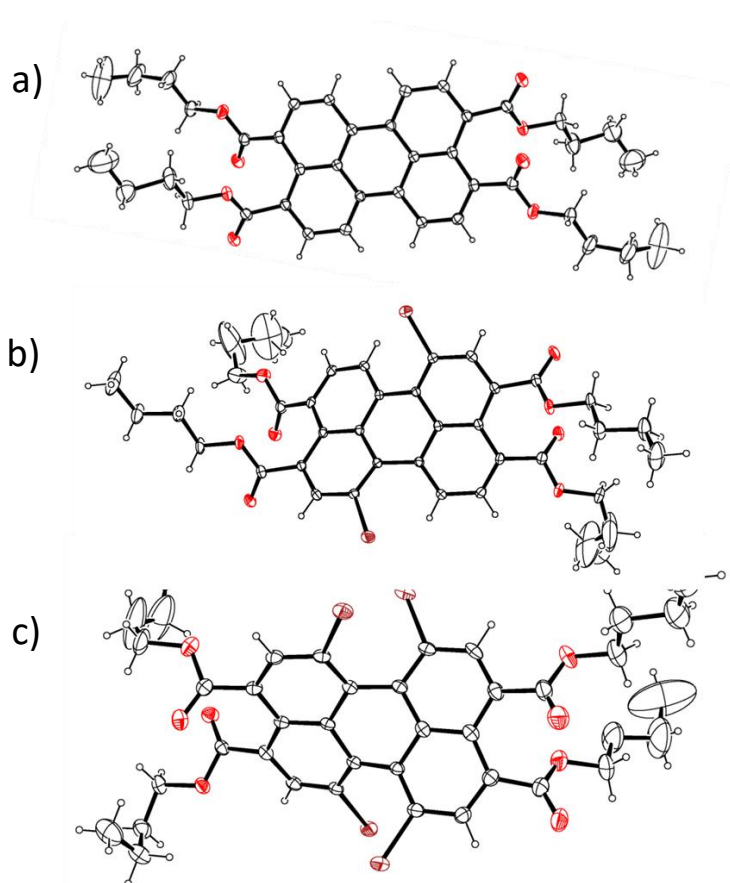


Figure A2.1: The ORTEP diagrams representing the molecular structure of of PTE-Br₀ (A), PTE-Br₂ (B) and PTE-Br₄ (C) with thermal ellipsoids drawn at the 50% probability level.

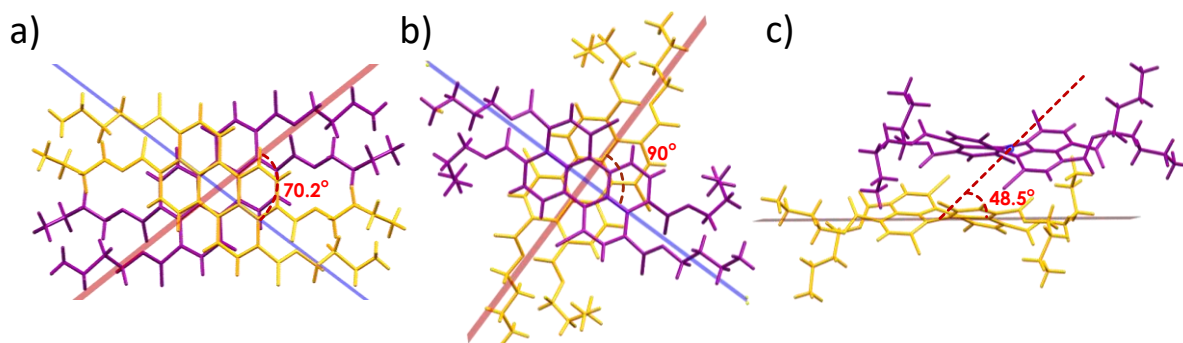


Figure A2.2: Stacked dimer with the intermolecular rotational angle (α) of 70.20° for PTE-Br₀ (a), 90.0° for PTE-Br₂ (b). stacked dimer with the intermolecular slip angle (θ) 48.40° for PTE-Br₄(c).

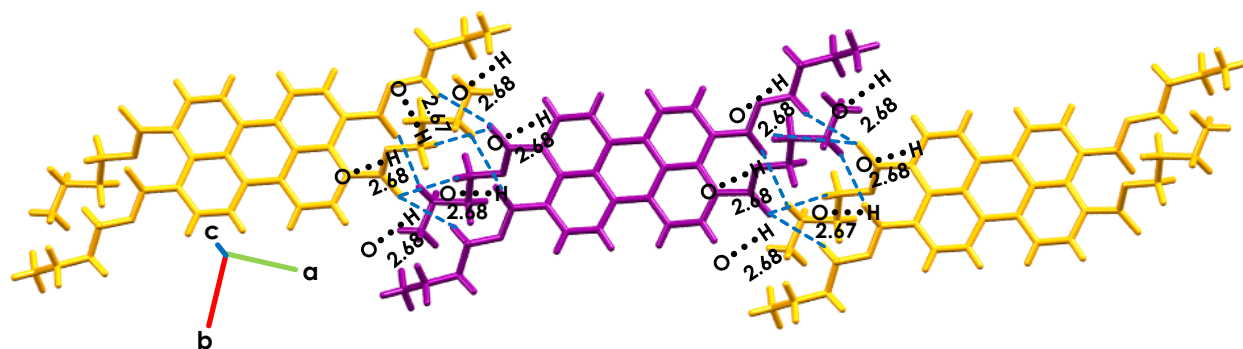


Figure A2.3: Two-dimensional propagation of the stacks via C-H...O as viewed along *ab*-plane in the crystalline *PTE-Br*₀. The intermolecular distances in Figure A2.3 are reported in unit angstroms (Å).

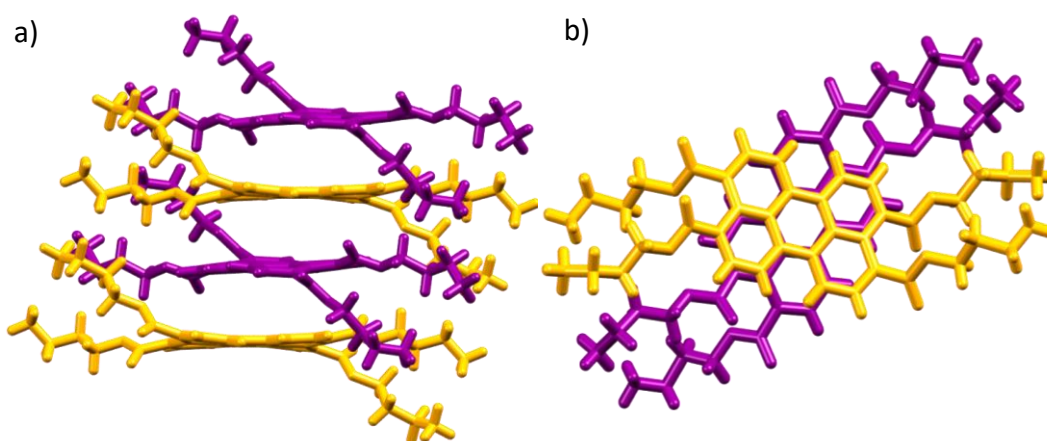


Figure A2.4: Depicting side view (a) and top view (b) of *PTE-Br*₀ molecule stacks along the *c*-axis, respectively.

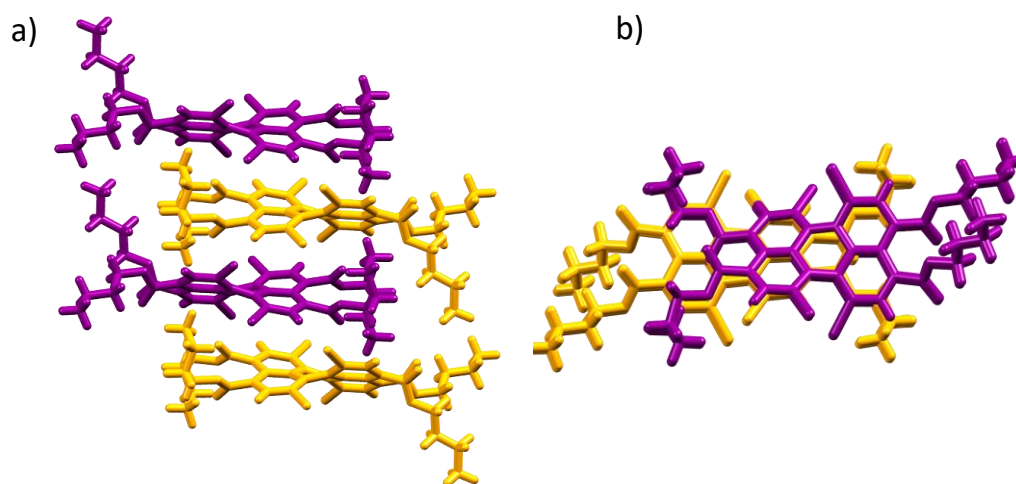


Figure A2.5: Depicting side view (A) and top view (B) of *PTE-Br*₄ molecule stacks along the *a*-axis, respectively

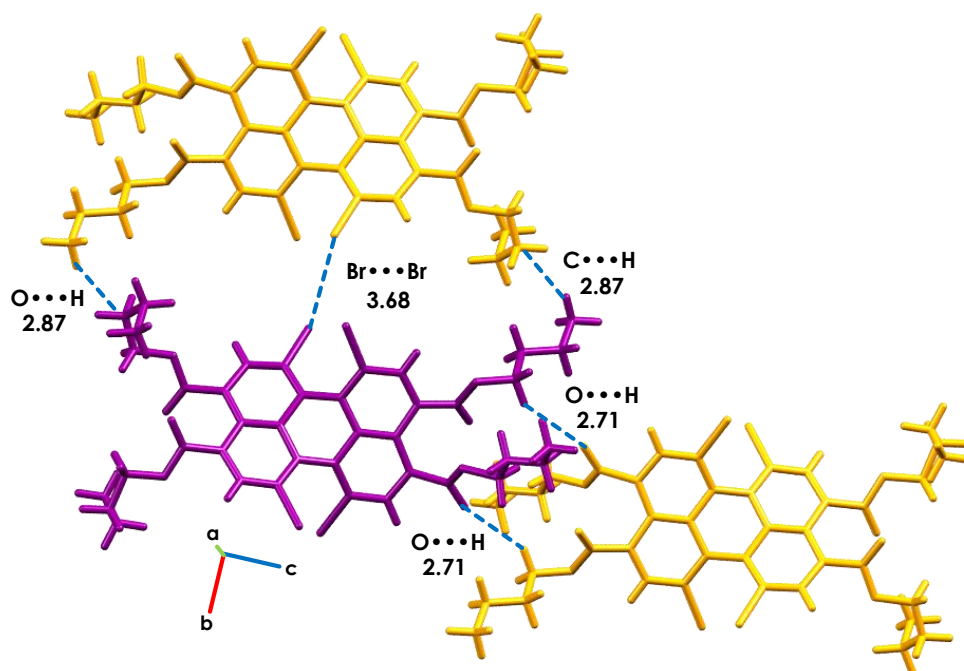


Figure A2.6: Two-dimensional propagation of the stacks via $C-H\cdots O-C$, $C-H\cdots C$ and $C-Br\cdots Br-C$ as viewed along bc -plane in the crystalline $PTE-Br_4$. The intermolecular distances in Figure A2.6 are reported in unit angstroms (\AA).

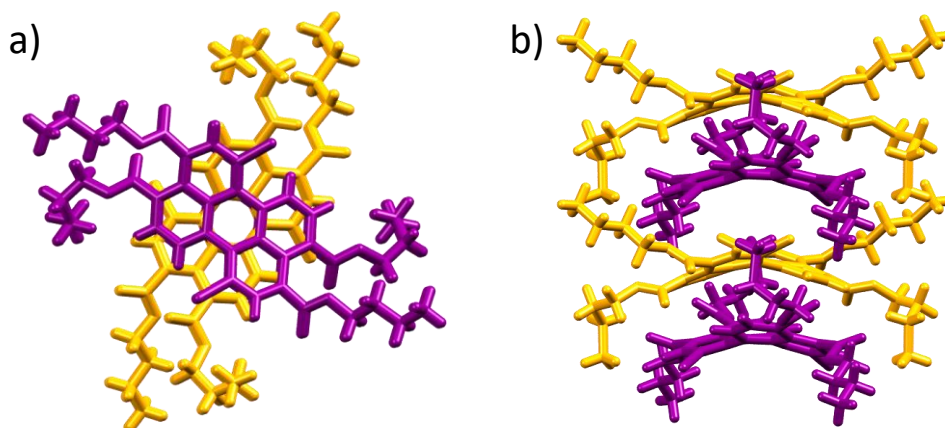


Figure A2.7: Depicting top view (a) and side view (b) of $PTE-Br_2$ stacks along the c -axis.

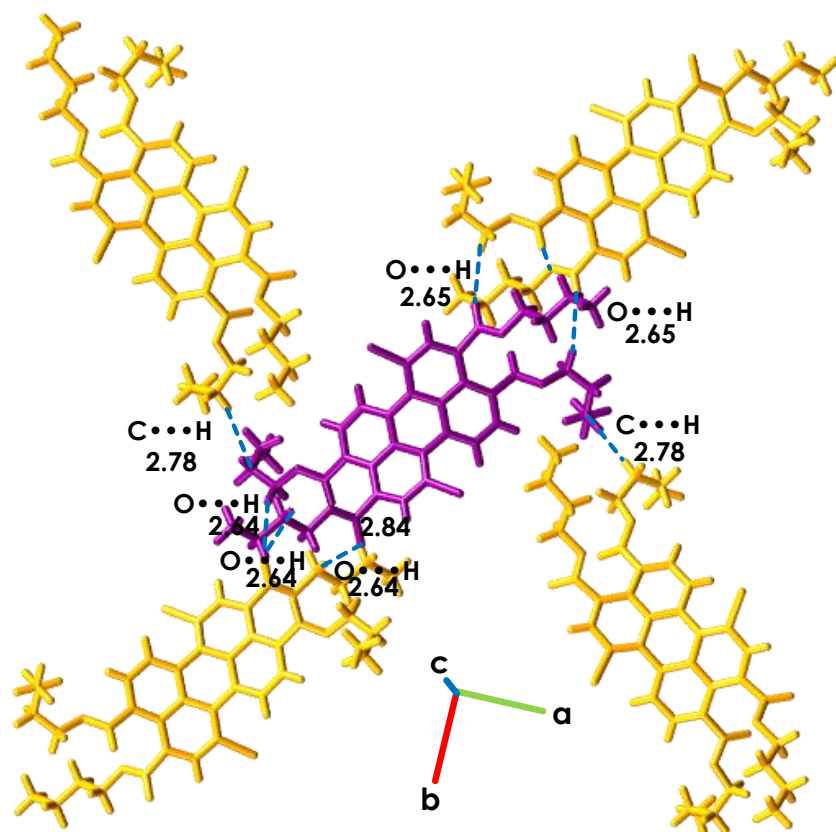


Figure A2.8: Two-dimensional propagation of the stacks via $C-H\cdots O$ and $C-H\cdots C$ as viewed along the ab -plane in the crystalline $PTE-Br_2$. The intermolecular distances in Figure A2.8 are reported in unit angstroms (\AA).

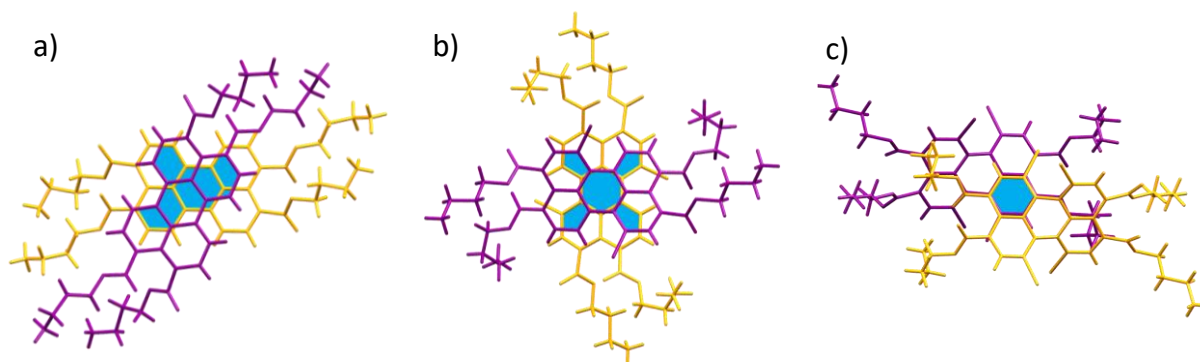


Figure A2.9: The stacking pattern depicting a) 54 %, b) 49.23 % and c) 12.0 % overlap in $PTE-Br_0$, $PTE-Br_2$ and $PTE-Br_4$, respectively.

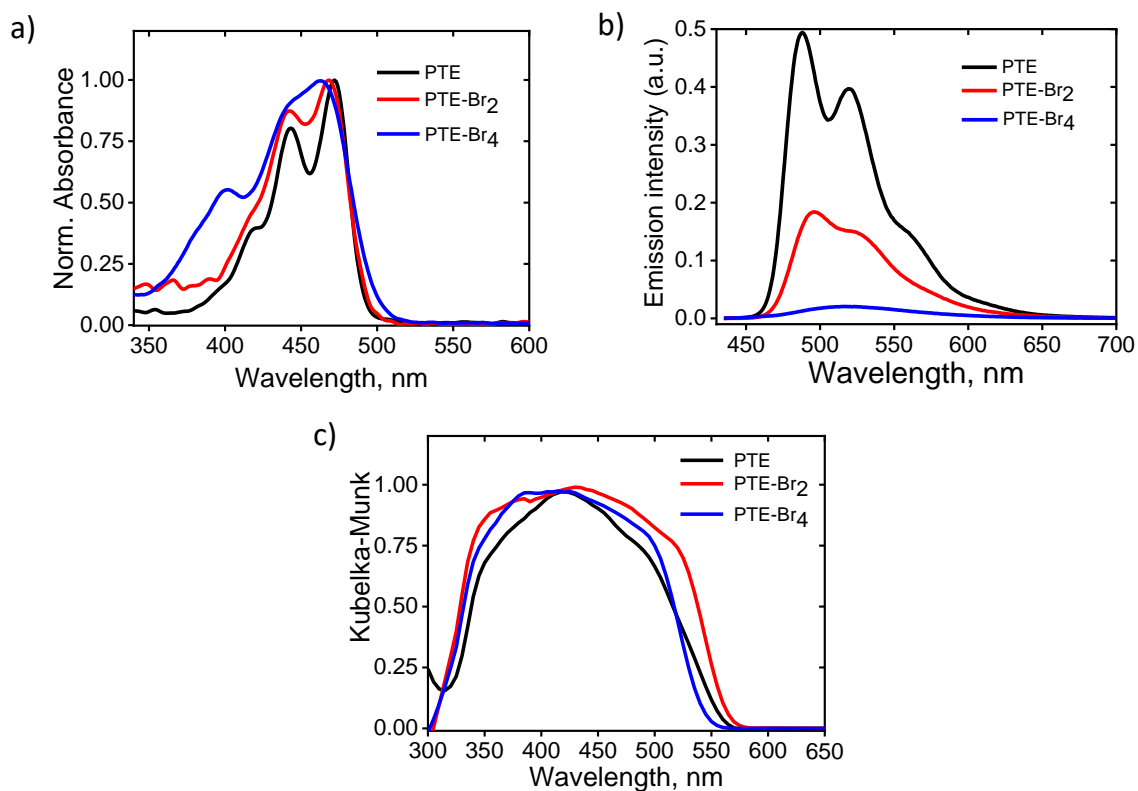


Figure A2.10: Normalized absorption (a) and non-normalized emission spectra (b) of *PTE-Br*_{0,2,4} in chloroform solution. Kubelka-Munk transformed diffuse reflectance spectra of *PTE-Br*_{0,2,4} in the crystalline state (c).

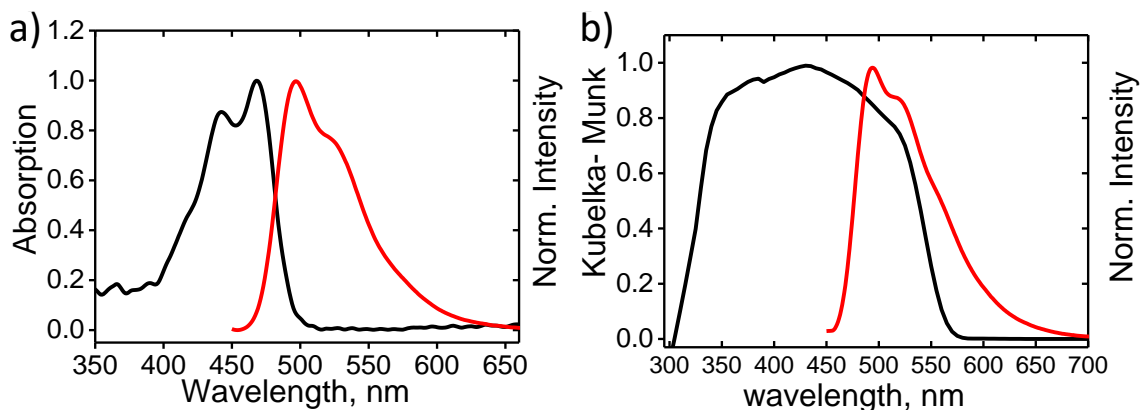


Figure A2.11: Steady-state absorption (black) and fluorescence emission (red) spectra of *PTE-Br*₂ in chloroform solution (a). Kubelka-Munk transformed diffuse reflectance spectra and emission spectra of crystalline *PTE-Br*₂ (b).

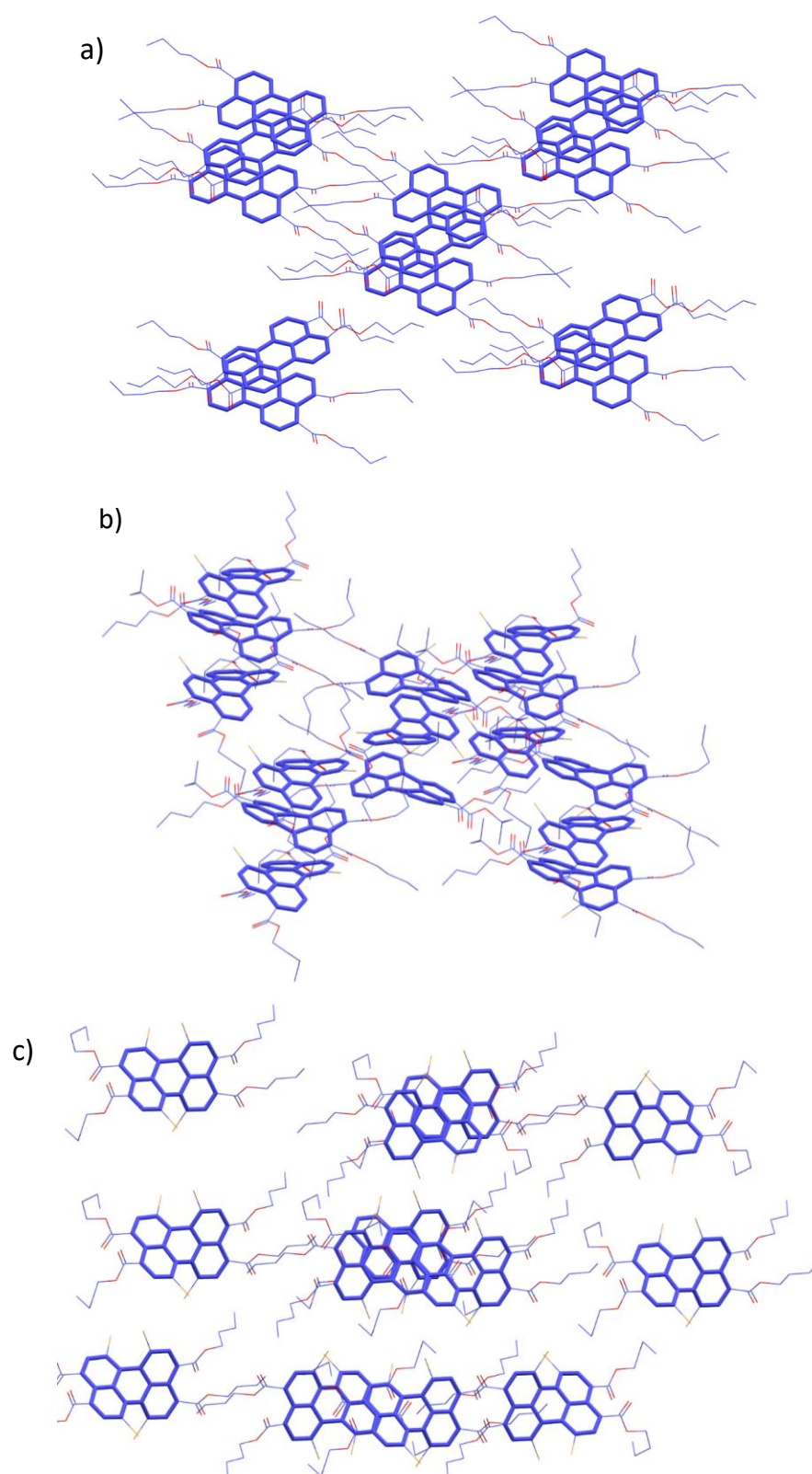


Figure A2.12: The ensemble of molecules (*PTE-Br₀* (A), *PTE-Br₂* (B) and *PTE-Br₄*) selected from the crystal packing for the mobility (electronic coupling) calculations in Schrödinger Materials

Science Suite using Jaguar DFT engine. The molecules within the 4.2 Å distance from the central molecule () were selected for the mobility calculation.

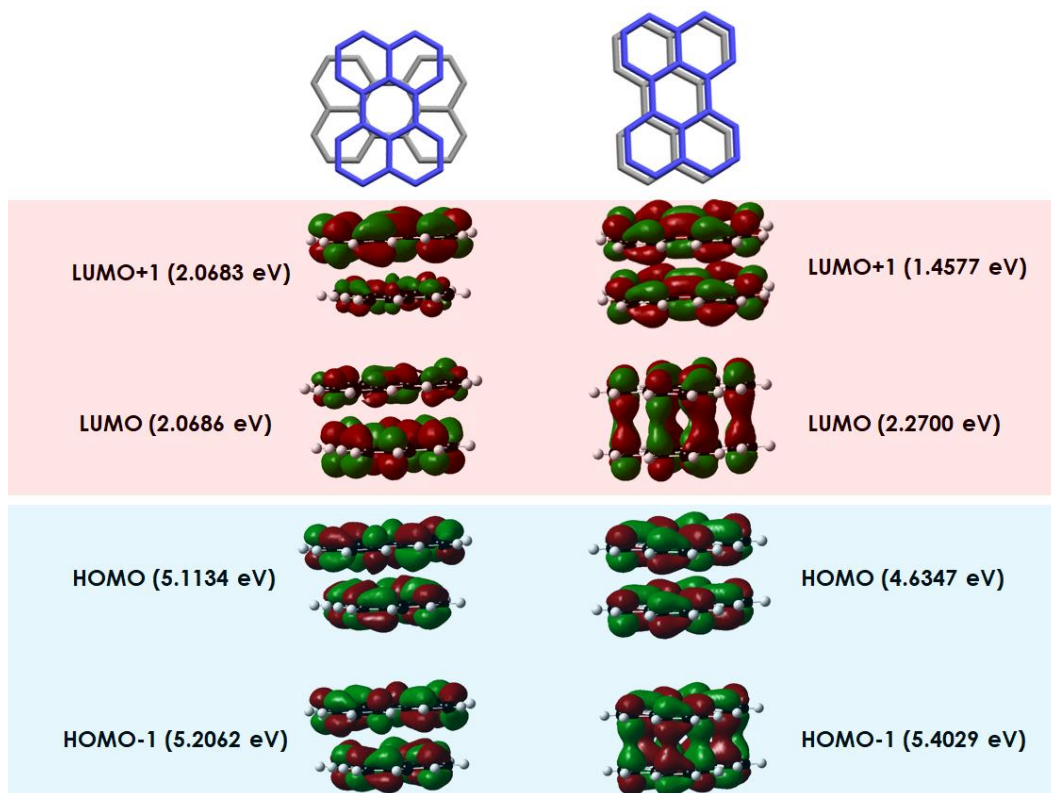


Figure A2.13. Frontier molecular orbital analyses for the cofacial parallel and cofacial orthogonal dimer in model derivative perylene.

2.7 Appendix

2.7.1. Materials and Methods.

All chemicals were obtained from commercial suppliers and used as received without further purification. All reactions were carried out in oven-dried glassware prior to use and wherever necessary, were performed under dry nitrogen in dried, anhydrous solvents using standard gastight syringes, cannula, and septa. Solvents were dried and distilled by standard laboratory purification techniques. TLC analyses were performed on recoated aluminium plates of silica gel 60 F254 plates (0.25 mm, Merck) and developed TLC plates were visualized under short and long wavelength UV lamps. Flash column chromatography was performed using silica gel of 200-400 mesh employing a solvent polarity correlated with the TLC mobility observed for the substance of interest. Yields refer to chromatographically and spectroscopically homogenous substances. Melting points were obtained using a capillary melting point apparatus. ^1H and ^{13}C NMR spectra were measured on a 500 MHz Bruker avance DPX spectrometer. Internal standard used for ^1H and ^{13}C NMR is tetramethyl silane (TMS). High resolution mass spectra (HRMS) were recorded on Thermo scientific Q exactive mass spectrometer using electrospray ionization (ESI, positive mode) technique. Photophysical measurements of the derivatives were carried out in a cuvette of 3 mm path length. Absorption and emission spectra were recorded on Shimadzu UV-3600 UV-VIS-NIR and Horiba Jobin Yvon Fluorolog spectrometers respectively. The UV-vis absorption spectra in the solution state were measured using the transmission mode and the Kubelka-Munk transformed reflectance spectra in the crystalline state were measured in the diffuse reflectance mode.⁶⁷ The Kubelka-Munk model is quite accurate when the particle size is smaller or similar to the wavelength of the excitation. The diffuse reflectance spectra allows no separation of the reflection, refraction and diffraction occurring from the crystalline samples.⁶⁸ As a result the diffuse reflectance spectra is not as sensitive compared to the UV-vis absorption spectra and can possibly be broader as compared to the typical absorbance and fluorescence excitation spectra.^{67,68}

Lifetime measurements were carried out in an IBH picosecond time correlated single photon counting (TCSPC) system.⁶⁹ Pulse width of the excitation ($\lambda_{ex}=439$ nm) source is determined to be <100 ps and 455 nm long-pass filter (Newport) were used to minimize the scatter arising from the laser source. Though, long-pass filters were used, a minor scattering component is observed in diluted solution (chloroform) and crystalline state of **PTE-Br₂** and **PTE-Br₄** which could not be completely eliminated due to the moderate-to-low fluorescence quantum yields. The

scattering component becomes evident as a marginal fluorescence lifetime component in **PTE-Br_{2,4}** (in chloroform, and crystalline state). The short-lived component consistently arising in **PTE-Br_{2,4}** (possessing moderate to low quantum yield) were considered as a scattering generated from the solvent (chloroform) and the glass coverslips used to pack the sample during the lifetime measurements in solution and crystalline state, respectively.

The scatter component becomes more prominent when the quantum yield of the samples is moderate-to-low, i.e., **PTE-Br₂** and **PTE-Br₄** in this case. Herein, the number of photons reaching the detector is low and concomitantly the acquisition time is more, which leads to the increase in the scattering component contribution compared to the decay profile of the samples. When the quantum yield of the sample is high, akin **PTE-Br₀**, the number of photons reaching the detector is more as compared to the scatter component and acquisition time is fast. Thus, the scattering component now becomes insignificant compared to the decay profile of the sample and hence **PTE-Br₀** exhibits a monoexponential decay in the solution state.

The fluorescence decay profiles were de-convoluted using DAS6.3, and fitted with exponential decay, minimizing the χ^2 values. While recording the fluorescence emission, excitation and lifetime, the **PTE** crystals (optimized size) were cautiously placed at a particular angle, wherein the self-absorption could be minimalized. Radiative (k_r) and non-radiative (k_{nr}) decay rate constants can be calculated by using the equation.⁷⁰

$$\Phi_f = \frac{k_r}{k_r + k_{nr}} \quad (\text{Eq 1})$$

$$\tau_f = \frac{1}{k_r + k_{nr}} \quad (\text{Eq 2})$$

$$k_r = \frac{\Phi_f}{\tau_f} \quad (\text{Eq 3})$$

$$k_{nr} = \frac{1}{\tau_f} - k_r \quad (\text{Eq 4})$$

In solution and crystalline state radiative (k_r) and non-radiative (k_{nr}) rate constants were calculated by employing the long lifetime component.

In the case of biexponential decay of crystalline **PTE**, the weighted average of the fluorescence lifetime values was used for estimation of rates of radiative and non-radiative processes which could be calculated using Eq 5.⁷⁰

$$\tau_f = \frac{a_1\tau_1^2 + a_2\tau_2^2 + a_3\tau_3^2 + \dots}{a_1\tau_1 + a_2\tau_2 + a_3\tau_3 + \dots} \quad (\text{Eq 5})$$

Where α = amplitude corresponding to the fluorescence lifetime (τ_f) decay

Absolute quantum yield measurements of **PTE-Br₀**, **PTE-Br₂**, and **PTE-Br₄** in solution and crystalline state were performed using Horiba quanta- ϕ integration sphere at excitation of respective emission maximum. The accuracy of the integrating sphere was verified using rhodamine 6G (observed Φ_f : 0.89 ± 0.03 ; reported $\Phi_f = 0.95$)⁷¹ and tris-(8-hydroxyquinoline) aluminium (Alq₃) (observed Φ_f : 0.37 ± 0.04 ; reported $\Phi_f = 0.40$)⁷² as a standard for solution state and solid-state, respectively.

2.7.2. X-ray crystallography.

High-quality specimen of approximate $0.20 \times 0.15 \times 0.10$ mm³ dimension of PTE, PTE-Br₂, and PTE-Br₄ were selected for the X-ray diffraction experiments. The single crystal was mounted using oil (Infineum V8512) on a glass fibre. All measurements were made on a CCD area detector with graphite monochromated Mo K α radiation. The data was collected using Bruker APEXII detector and processed using APEX2 from Bruker. The structure was solved by direct method and expanded using Fourier technique. The non-hydrogen atoms were refined anisotropically. Hydrogen atoms were included in idealized positions, but not refined. Their positions were constrained relative to their parent atom using the appropriate HFIX command in SHELX-97.⁷³ All programs used during the crystal structure analysis are incorporated in the WINGX software.^{74,75} The full validation of CIF and structure factor of **PTE-Br₀**, **PTE-Br₂**, and **PTE-Br₄** was performed using the checkCIF utility and found to be free of major alert levels. 3D structure visualization and the exploration of the crystal packing of **PTE-Br₀**, **PTE-Br₂**, and **PTE-Br₄** were carried out using Mercury 3.5.1.⁷⁶ The face-to-face overlap between the molecular stacks was visualized and imaged from the crystal structure. The ratio of the overlapped area and the total area of the molecular rings gave the percentage (%) overlap between the face-to-face stacked.⁷⁷

2.7.3. Computational Analyses.

Ground-state optimized structure, harmonic oscillator frequencies and energy of **PTE-Br₀**, **PTE-Br₂**, and **PTE-Br₄** monomer and dimer were computed using density functional theory (DFT) at the Becke's three parameter functional in combination with the Lee-Yang-Parr correlation functional (B3LYP) and 6-311G+ (d, p) basis set. The vertical excitation energies and oscillator strengths were calculated employing time dependent DFT (TD-DFT) calculations at B3LYP /6-

311G+ (d, p) level of theory. All the computations were performed employing Gaussian 09 Rev.A.02 and were visualized employing GaussView 5.0.⁷⁸

2.7.4. Quantum Theory of Atoms and Molecules.⁷⁹

The wave function for the derivatives of **PTE-Br₀**, **PTE-Br₂**, and **PTE-Br₄** were obtained employing the geometries taken from the crystal structure using Gaussian set of codes at B3LYP/6-311G(d, p)+ level. Quantum theory of atoms in molecules (QTAIM) analyses help to understand the description of interatomic interaction in the single-crystal X-ray structure. A bond is defined along the bond line between two nuclei, called a bond path, along which electron density is concentrated. In a three-dimensional space there are four types of critical points, corresponding to non-degenerate points: termed (3, -3), (3, -1), (3, +1) and (3, +3). The (3, -3) and (3, +3) types represent a maximum (which corresponds to a nuclear position) and a minimum, respectively. While (3, -1) and (3, +1) types represent saddle points called bond critical points and the ring critical points, respectively. There is also a second set of special gradient paths conjugated to the bond paths which starts at infinity but terminates at the bond critical point instead of being attracted to a nucleus. Therefore, this bundle of paths does not belong to any atom and form a surface called the interatomic surface. The bond critical point (BCP) is a point along the bond path at the interatomic surface, where the shared electron density reaches a minimum. The physical characteristics of the BCPs [the electron density at BCP $\rho(rBCP)$, and its Laplacian, $\nabla^2\rho(rBCP)$] reveal the approximate measure of the amount of electron density built up in the bonding region and as such could be taken as characteristic of the bond. When $\nabla^2\rho(rBCP) < 0$ and is large in magnitude, $\rho(rBCP)$, is also large which means that there is a concentration of electronic charge in the internuclear region. This is also an indication of a sharing of electronic charge between both nuclei that defines the covalent (polar) bond. When $\nabla^2\rho(rBCP) > 0$ there is a depletion of electronic charge in the internuclear region. Using the AIM 2000 software package, the electron density was integrated over atomic basins according to the quantum theory of atoms in molecules using PROAIM, and thus the BCP data and the molecular graphs were obtained.

2.7.5. Hirshfeld Analyses.^{80,81}

Important intermolecular interactions within the crystal structure of **PTE-Br₀**, **PTE-Br₂**, and **PTE-Br₄** were identified through Hirshfeld surface analyses using Crystal Explorer 3.1.⁸² The Hirshfeld surface is defined as a set of points in 3D space where the ratio of pro molecule and pro crystal electron densities is equal to 0.5. The exploration of intermolecular contacts is provided by mapping normalized contact distances (d_{norm}), which is a function of a closest distance from the

point to the nuclei interior (d_i) and exterior (d_e) to the surface as well as on the van der Waals radii (r^{vdw}). 2D fingerprint which were generated by deriving from the Hirshfeld surface by plotting the fraction of points on the surface as the function of d_i and d_e which provide a visual summary of intermolecular contacts within the crystal.

2.7.6. Charge Transport and Mobility Calculations.

The Jaguar DFT module from Schrodinger Materials Science Suite 2016-4 was used for charge carrier mobility calculations.^{83,84} All the calculations were carried out at the B3LYP-D3/6-311G** level of theory. The charge transfer rate k_i was obtained from Marcus-Hush equation,⁸⁵

$$k_i = \frac{V^2}{\hbar} \left(\frac{\pi}{\lambda k_B T} \right)^{\frac{1}{2}} e^{-\frac{\lambda}{4k_B T}} \quad (\text{Eq 5})$$

where V is the electronic coupling between the monomers in each dimer, λ is the reorganization energy, T is the temperature (300 K), and k_B is the Boltzmann constant. Adiabatic potential energy surfaces method was used for hole reorganization energy (λ_h) and electron reorganization energy (λ_e) calculation.

$$\lambda_h = (E_0 - E_0^*) - (E_+ - E_0^*) \quad (\text{Eq 6})$$

$$\lambda_e = (E_0 - E_0^*) - (E_- - E_-^*) \quad (\text{Eq 7})$$

where E_0 , E_- and E_+ are the energies at lowest geometries of the neutral, anionic and cationic species respectively. E_0^* is the energy of the neutral molecule at cation geometry for hole reorganization energy calculation and anion geometry for electron reorganization energy calculation, E_+^* is the energy of the cationic state at neutral geometry and E_-^* is the energy of the anionic state at neutral geometry.

The diffusion coefficient (D) was evaluated from hopping rates as,

$$D = \frac{1}{6} \sum_i r^2 k_i P_i \quad (\text{Eq 8})$$

where r is the dimer separation distance and P_i is probability of hopping rate given as follows:

$$P_i = \frac{k_i}{\sum_i k_i} \quad (\text{Eq 9})$$

The Einstein's relation was used to compute the drift mobility, μ , of hopping,

$$\mu = \frac{e}{k_B T} D \quad (\text{Eq 10})$$

In the study of angle dependence of dimer orientation on charge transfer rate, the most contributing dimer in the crystal structure of each derivative was selected, and the co-ordinates of one monomer with respect to other were changed without altering the centroid distance between the monomers in Schrodinger Maestro suite, and the extend of rotation were restricted considering the steric block among the molecules.

The electronic coupling values (V) and the hopping rates (k) for each of the rotationally oriented dimers have been calculated for the **PTE-Br_{0,2,4}** derivatives and the model derivative perylene. The rotation angle-dependent hopping rates (k_h and k_e) depicts that selective hole hopping is preferred in the orthogonal stacks. The hole/electron hopping rates (k_h and k_e) depends essentially on the electronic coupling (V_h [hole] and V_e [electron]) and the reorganization energies (λ_h and λ_e). The electronic coupling term (V_h or V_e) in turn depends on the charge transfer and the overlap integrals of the selected rotationally oriented dimers.^{86,87} As reported by Spano and co-worker, the zero electron transfer integral (t_e) and the nonzero hole transfer integral can potentially provide a selective hole transport phenomena in stacked perylene derivatives.⁸⁸ The frontier molecular orbitals (FMO) analysis also were carried out to perceive the relative HOMO and LUMO orbital orientations in the parallel co-facial and orthogonal perylene dimers as a model derivative (Figure A2.13).⁸⁹ The FMO analysis shows that in the parallel co-facial dimer, the HOMOs and LUMOs are cofacial and in the proximity of each other, lending sufficient charge transfer and overlap integrals. In the orthogonal dimers, the HOMOs still retain a sufficient overlap. However, the overlap among the LUMOs are drastically reduced as compared to the parallel cofacial dimers in concurrence with the null aggregate reports by Spano and co-workers. Drastic reduction of the LUMO overlap and the concomitant reduction in the electron transfer integral (t_e) might be the possible reason for the observed selective hole transport in the Greek-cross aggregate. The trend observed in the planar derivative perylene can be effectively extended to the **PTE-Br_{0,2,4}** derivatives as the arene core is identical.

2.7.7. SAPT.

Total interaction energies and the magnitudes of noncovalent interactions were determined by using SAPT(0); the SAPT module of the Psi4 code⁹⁰ was employed, with the jun-cc-pvdz basis set.

2.7.8. Time-Resolved Emission Spectral (TRES) Analysis.

Time-resolved emission spectral (TRES) measurements followed by global analysis (GA) of the kinetic traces (at all wavelengths) were performed in an IBH picosecond time correlated single photon counting (TCSPC) system and glotaran software respectively. The singular value decomposition (SVD) followed by the GA of the time vs. wavelength plots furnished an evolution associated spectra (EAS) based de-convolution of the temporal components in the fluorescence emission. Time-resolved emission spectral (TRES) investigation of crystalline PTE-Br₀ derivatives was carried out by exciting at 439 nm (NanoLED-439L; pulse width = 100 ps) and the fluorescence decay profiles were collected in the spectral range of 455-750 nm (3 nm interval) with a 455 nm long-pass filter (Newport) to minimize the scatter arising from the laser source. Decay at each wavelength was collected with an identical acquisition time and the emission observed immediately after the laser excitation pulse was assigned as zero time.

2.8. Reference

- (1) Anthony, J. E. The Larger Acenes: Versatile Organic Semiconductors. *Angew. Chem., Int. Ed.* **2008**, *47*, 452–483.
- (2) Park, S. K.; Kim, J. H.; Park, S. Y. Organic 2D Optoelectronic Crystals: Charge Transport, Emerging Functions, and Their Design Perspective. *Adv. Mater.* **2018**, *30*, 1704759.
- (3) Gierschner, J.; Varghese, S.; Park, S. Y. Lasing: Organic Single Crystal Lasers: A Materials View (Advanced Optical Materials 3/2016). *Adv. Opt. Mater.* **2016**, *4*, 347–347.
- (4) Ebbesen, T. W. Hybrid Light-Matter States in a Molecular and Material Science Perspective. *Acc. Chem. Res.* **2016**, *49*, 2403–2412.
- (5) Sethy, R.; Kumar, J.; Métivier, R.; Louis, M.; Nakatani, K.; Mecheri, N. M. T.; Subhakumari, A.; Thomas, K. G.; Kawai, T.; Nakashima, T. Enantioselective Light Harvesting with Perylenediimide Guests on Self-Assembled Chiral Naphthalenediimide Nanofibers. *Angew. Chem., Int. Ed.* **2017**, *56*, 15053–15057.
- (6) Sugiyasu, K.; Fujita, N.; Shinkai, S. Visible-Light-Harvesting Organogel Composed of Cholesterol-Based Perylene Derivatives. *Angew. Chem., Int. Ed.* **2004**, *43*, 1229–1233.
- (7) Varghese, S.; Das, S. Role of Molecular Packing in Determining Solid-State Optical Properties of π -Conjugated Materials. *J. Phys. Chem. Lett.* **2011**, *2*, 863–873.
- (8) Ajayaghosh, A.; Vijayakumar, C.; Varghese, R.; George, S. J. Cholesterol-Aided Supramolecular Control over Chromophore Packing: Twisted and Coiled Helices with Distinct Optical, Chiroptical, and Morphological Features. *Angew. Chem., Int. Ed.* **2006**, *45*, 456–460.
- (9) Hongyu Zhang, B.; Zhang, Z.; Ye, K.; Zhang, J.; Wang, Y.; Wang, Y.; Zhang, H. Y.; Zhang, Z. L.; Ye, K. Q.; Zhang, J. Y. Organic Crystals with Tunable Emission Colors Based on a Single Organic Molecule and Different Molecular Packing Structures. *Adv. Mater.* **2006**, *18*, 2369–2372.
- (10) Hinoue, T.; Shigenoi, Y.; Sugino, M.; Mizobe, Y.; Hisaki, I.; Miyata, M.; Tohnai, N. Regulation of π -Stacked Anthracene Arrangement for Fluorescence Modulation of Organic Solid from Monomer to Excited Oligomer Emission. *Chem. – A Eur. J.* **2012**, *18*, 4634–4643.
- (11) Lewis, F. D.; Yang, J. S. Solid-State Fluorescence of Aromatic Dicarboxamides. Dependence upon Crystal Packing. *J. Phys. Chem. B* **1997**, *101*, 1775–1781.
- (12) Allen, F. H.; Hoy, V. J.; Howard, J. A. K.; Thalladi, V. R.; Desiraju, G. R.; Wilson, C. C.; McIntyre, G. J. Crystal Engineering and Correspondence between Molecular and Crystal Structures. Are 2- and 3-Aminophenols Anomalous? *J. Am. Chem. Soc.* **1997**, *119*, 3477–3480.
- (13) Crawford, A. G.; Liu, Z.; Mkhaliid, I. A. I.; Thibault, M. H.; Schwarz, N.; Alcaraz, G.; Steffen, A.; Collings, J. C.; Batsanov, A. S.; Howard, J. A. K.; Marder, T. B. Synthesis of 2- and 2,7-Functionalized Pyrene Derivatives: An Application of Selective CH Borylation. *Chem. – A Eur. J.* **2012**, *18*, 5022–5035.
- (14) Kaufmann, C.; Bialas, D.; Stolte, M.; Würthner, F. Discrete π -Stacks of Perylene Bisimide

- Dyes within Folda-Dimers: Insight into Long- and Short-Range Exciton Coupling. *J. Am. Chem. Soc.* **2018**, *140*, 9986–9995.
- (15) Yoon, S. J.; Chung, J. W.; Gierschner, J.; Kim, K. S.; Choi, M. G.; Kim, D.; Park, S. Y. Multistimuli Two-Color Luminescence Switching via Different Slip-Stacking of Highly Fluorescent Molecular Sheets. *J. Am. Chem. Soc.* **2010**, *132*, 13675–13683.
- (16) Park, S.; Kwon, J. E.; Park, S.-Y.; Kwon, O.-H.; Kim, J. K.; Yoon, S.-J.; Chung, J. W.; Whang, D. R.; Park, S. K.; Lee, D. K.; Jang, D.-J.; Gierschner, J. Crystallization-Induced Emission Enhancement and Amplified Spontaneous Emission from a CF₃-Containing Excited-State Intramolecular-Proton-Transfer Molecule. *Adv. Opt. Mater.* **2017**, *5*, 1700353.
- (17) Davydov, A. S. The Theory of Molecular Excitons. *Uspekhi Fiz. Nauk* **1964**, *82*, 393–448.
- (18) Kasha, M.; Rawls, H. R.; El-Bayoumi, M. A. The Exciton Model In Molecular Spectroscopy. *Pure Appl. Chem.* **1965**, *11*, 371–392.
- (19) Allampally, N. K.; Florian, A.; Mayoral, M. J.; Rest, C.; Stepanenko, V.; Fernández, G. H-Aggregates of Oligophenyleneethynylene (OPE)-BODIPY Systems in Water: Guest Size-Dependent Encapsulation Mechanism and Co-Aggregate Morphology. *Chem. – A Eur. J.* **2014**, *20*, 10669–10678.
- (20) Rösch, U.; Yao, S.; Wortmann, R.; Würthner, F. Fluorescent H-Aggregates of Merocyanine Dyes. *Angew. Chemie Int. Ed.* **2006**, *45*, 7026–7030.
- (21) Hestand, N. J.; Spano, F. C. Expanded Theory of H- and J-Molecular Aggregates: The Effects of Vibronic Coupling and Intermolecular Charge Transfer. *Chem. Rev.* **2018**, *118*, 7069–7163.
- (22) Kim, S. O.; An, T. K.; Chen, J.; Kang, I.; Kang, S. H.; Chung, D. S.; Park, C. E.; Kim, Y. H.; Kwon, S. K. H-Aggregation Strategy in the Design of Molecular Semiconductors for Highly Reliable Organic Thin Film Transistors. *Adv. Funct. Mater.* **2011**, *21*, 1616–1623.
- (23) Jelley, E. E. Spectral Absorption and Fluorescence of Dyes in the Molecular State. *Nat.* **1936**, *138*, 1009–1010.
- (24) Würthner, F.; Kaiser, T. E.; Saha-Möller, C. R. J-Aggregates: From Serendipitous Discovery to Supramolecular Engineering of Functional Dye Materials. *Angew. Chemie Int. Ed.* **2011**, *50*, 3376–3410.
- (25) Scheibe, G. Über Die Veränderlichkeit Der Absorptionsspektren in Lösungen Und Die Nebenvalenzen Als Ihre Ursache. *Angew. Chemie* **1937**, *50*, 212–219.
- (26) Xie, Z.; Yang, B.; Li, F.; Cheng, G.; Liu, L.; Yang, G.; Xu, H.; Ye, L.; Hanif, M.; Liu, S.; Ma, D.; Ma, Y. Cross Dipole Stacking in the Crystal of Distyrylbenzene Derivative: The Approach toward High Solid-State Luminescence Efficiency. *J. Am. Chem. Soc.* **2005**, *127*, 14152–14153.
- (27) Zhou, J.; Zhang, W.; Jiang, X. F.; Wang, C.; Zhou, X.; Xu, B.; Liu, L.; Xie, Z.; Ma, Y. Magic-Angle Stacking and Strong Intermolecular π - π Interaction in a Perylene Bisimide Crystal: An Approach for Efficient Near-Infrared (NIR) Emission and High Electron Mobility. *J. Phys. Chem. Lett.* **2018**, *9*, 596–600.
- (28) Hestand, N. J.; Spano, F. C. Interference between Coulombic and CT-Mediated Couplings in Molecular Aggregates: H- to J-Aggregate Transformation in Perylene-Based π -Stacks. *J.*
-

- Chem. Phys.* **2015**, *143*, 244707.
- (29) Feng, X.; Marcon, V.; Pisula, W.; Hansen, M. R.; Kirkpatrick, J.; Grozema, F.; Andrienko, D.; Kremer, K.; Müllen, K. Towards High Charge-Carrier Mobilities by Rational Design of the Shape and Periphery of Discotics. *Nat. Mater.* **2009**, *8*, 421–426.
- (30) Ma, S.; Zhang, J.; Qian, J.; Chen, J.; Xu, B.; Tian, W. Efficient Spontaneous and Stimulated Emission from 1,4-Bis(2,2-Diphenylvinyl)Benzene Single Crystals with Cross-Dipole Stacking. *Adv. Opt. Mater.* **2015**, *3*, 763–768.
- (31) Sanyal, S.; Manna, A. K.; Pati, S. K. Effect of Imide Functionalization on the Electronic, Optical, and Charge Transport Properties of Coronene: A Theoretical Study. *J. Phys. Chem. C* **2013**, *117*, 825–836.
- (32) Cornil, J. Influence of Interchain Interactions in the Absorption and Luminescence of Conjugated Oligomers and Polymers: A Quantum-Chemical Characterization. *J. Am. Chem. Soc.* **1998**, *120*, 1289–1299.
- (33) Zhou, J. D.; Zhang, W. Q.; Liu, L. L.; Xie, Z. Q.; Ma, Y. G. Aggregation Structures of Organic Conjugated Molecules on Their Optoelectronic Properties. *Chinese Chem. Lett.* **2016**, *27*, 1350–1356.
- (34) McKenzie, D. R.; Muller, D.; Pailthorpe, B. A.; K-F Shen, C.; Yu, H.; Juo, C.; Chien, K.; Ma, Y.; Wassdahl, N.; Skytt, P.; Guo, J.; Nordgren, J.; Johnson, P. D.; Rubensson, J. E.; Boske, T.; Eberhardt, W.; Kevan, S. D.; Feng He, B.; Xu, H.; Yang, B.; Duan, Y.; Tian, L.; Huang, K.; Ma, Y.; Liu, S.; Feng, S.; Shen, J. Oligomeric Phenylenevinylene with Cross Dipole Arrangement and Amorphous Morphology: Enhanced Solid-State Luminescence Efficiency and Electroluminescence Performance. *Adv. Mater.* **2005**, *17*, 2710–2714.
- (35) Sanyal, N.; Lahti, P. M. Hydrogen-Bond-Assisted, Crossed Dipole π -Stacking in 1,4-Bis(Phenylethynyl)Benzene. *Cryst. Growth Des.* **2006**, *6*, 1253–1255.
- (36) Liu, J.; Meng, L.; Zhu, W.; Zhang, C.; Zhang, H.; Yao, Y.; Wang, Z.; He, P.; Zhang, X.; Wang, Y.; Zhen, Y.; Dong, H.; Yi, Y.; Hu, W. A Cross-Dipole Stacking Molecule of an Anthracene Derivative: Integrating Optical and Electrical Properties. *J. Mater. Chem. C* **2015**, *3*, 3068–3071.
- (37) Xie, Z.; Xie, W.; Li, F.; Liu, L.; Wang, H.; Ma, Y. Controlling Supramolecular Microstructure to Realize Highly Efficient Nondoped Deep Blue Organic Light-Emitting Devices: The Role of Diphenyl Substituents in Distyrylbenzene Derivatives. *J. Phys. Chem. C* **2008**, *112*, 9066–9071.
- (38) Che, Y.; Yang, X.; Balakrishnan, K.; Zuo, J.; Zang, L. Highly Polarized and Self-Waveguided Emission from Single-Crystalline Organic Nanobelts. *Chem. Mater.* **2009**, *21*, 2930–2934.
- (39) Zhang, B.; Soleimaninejad, H.; Jones, D. J.; White, J. M.; Ghiggino, K. P.; Smith, T. A.; Wong, W. W. H. Highly Fluorescent Molecularly Insulated Perylene Diimides: Effect of Concentration on Photophysical Properties. *Chem. Mater.* **2017**, *29*, 8395–8403.
- (40) Hansen, M. R.; Schnitzler, T.; Pisula, W.; Graf, R.; Müllen, K.; Spies, H. W. G. Cooperative Molecular Motion within a Self-Assembled Liquid-Crystalline Molecular Wire: The Case of a TEG-Substituted Perylenediimide Disc. *Angew. Chem., Int. Ed.* **2009**, *48*, 4621–4624.
- (41) Feng, X.; Pisula, W.; Müllen, K. From Helical to Staggered Stacking of Zigzag
-

- Nanographenes. *J. Am. Chem. Soc.* **2007**, *129*, 14116–14117.
- (42) De Halleux, V.; Calbert, J. P.; Brocorens, P.; Cornil, J.; Declercq, J. P.; Brédas, J. L.; Geerts, Y. 1,3,6,8-Tetraphenylpyrene Derivatives: Towards Fluorescent Liquid-Crystalline Columns? *Adv. Funct. Mater.* **2004**, *14*, 649–659.
- (43) Cabaleiro-Lago, E. M.; Rodríguez-Otero, J. On the Nature of σ - σ , σ - π , and π - π Stacking in Extended Systems. *ACS Omega* **2018**, *3*, 9348–9359.
- (44) Rajagopal, S. K.; Philip, A. M.; Nagarajan, K.; Hariharan, M. Progressive Acylation of Pyrene Engineers Solid State Packing and Colour via C–H \cdots H–C, C–H \cdots O and π - π Interactions. *Chem. Commun.* **2014**, *50*, 8644–8647.
- (45) Nagarajan, K.; Gopan, G.; Cheriya, R. T.; Hariharan, M. Long Alkyl Side-Chains Impede Exciton Interaction in Organic Light Harvesting Crystals. *Chem. Commun.* **2017**, *53*, 7409–7411.
- (46) Cheriya, R. T.; Mallia, A. R.; Hariharan, M. Light Harvesting Vesicular Donor–Acceptor Scaffold Limits the Rate of Charge Recombination in the Presence of an Electron Donor. *Energy Environ. Sci.* **2014**, *7*, 1661–1669.
- (47) Mallia, A. R.; Salini, P. S.; Hariharan, M. Nonparallel Stacks of Donor and Acceptor Chromophores Evade Geminate Charge Recombination. *J. Am. Chem. Soc.* **2015**, *137*, 15604–15607.
- (48) Philip, A. M.; Mallia, A. R.; Hariharan, M. Prolonged Charge Separated States in Twisted Stacks of All-Carbon Donor and Acceptor Chromophores. *J. Phys. Chem. Lett.* **2016**, *7*, 4751–4756.
- (49) Sengupta, S.; Dubey, R. K.; Hoek, R. W. M.; Van Eeden, S. P. P.; Gunbaş, D. D.; Grozema, F. C.; Sudhölter, E. J. R.; Jager, W. F. Synthesis of Regioisomerically Pure 1,7-Dibromoperylene-3,4,9,10- Tetracarboxylic Acid Derivatives. *J. Org. Chem.* **2014**, *79*, 6655–6662.
- (50) Sengupta, S.; Dubey, R. K.; Hoek, R. W. M.; Van Eeden, S. P. P.; Deniz Gunbaş, D.; Grozema, F. C.; Sudhö, E. J. R.; Jager, W. F. Tetramethoxy-Bay-Substituted Perylene Bisimides by Copper-Mediated Cross-Coupling. *Org. Chem. Front.* **2016**, *3*, 537–544.
- (51) Nagarajan, K.; Mallia, A. R.; Reddy, V. S.; Hariharan, M. Access to Triplet Excited State in Core-Twisted Perylenediimide. *J. Phys. Chem. C* **2016**, *120*, 8443–8450.
- (52) Osamura, J. D.; Schaefer, Y.; Iii, F.; Am, J.; Bader, R. F. W.; Nguyen-Dang, T. T.; Nguyen Dang, T. T.; Tal, Y.; Essen, H.; Olah, G. A.; Surya Prakash, G. K.; Saunders, M. Atoms in Molecules. *Acc. Chem. Res.* **1985**, *18*, 9–15.
- (53) Spackman, M. A.; Jayatilaka, D. Hirshfeld Surface Analysis. *CrystEngComm* **2009**, *11*, 19–32.
- (54) Bhat, V.; Gopan, G.; Nair, N. G.; Hariharan, M. γ -Herringbone Polymorph of 6,13-Bis(Trimethylsilylethynyl)Pentacene: A Potential Material for Enhanced Hole Mobility. *Chem. A Eur. J.* **2018**, *24*, 8679–8685.
- (55) Jeziorski, B.; Moszynski, R.; Szalewicz, K. Perturbation Theory Approach to Intermolecular Potential Energy Surfaces of van Der Waals Complexes. *Chem. Rev.* **1994**, *94*, 1887–1930.
- (56) Loots, L.; Barbour, L. J. A Simple and Robust Method for the Identification of π - π Packing Motifs of Aromatic Compounds. *CrystEngComm* **2011**, *14*, 300–304.
-

- (57) Yang, L.; Brazier, J. B.; Hubbard, T. A.; Rogers, D. M.; Cockroft, S. L. Can Dispersion Forces Govern Aromatic Stacking in an Organic Solvent? *Angew. Chem., Int. Ed.* **2016**, *55*, 912–916.
- (58) Son, M.; Park, K. H.; Shao, C.; Würthner, F.; Kim, D. Spectroscopic Demonstration of Exciton Dynamics and Excimer Formation in a Sterically Controlled Perylene Bisimide Dimer Aggregate. *J. Phys. Chem. Lett.* **2014**, *5*, 3601–3607.
- (59) Morris, J. V.; Mahaney, M. A.; Huber, J. R. Fluorescence Quantum Yield Determinations. 9,10-Diphenylanthracene as a Reference Standard in Different Solvents. *J. Phys. Chem.* **1976**, *80*, 969–974.
- (60) Ahn, T. S.; Al-Kaysi, R. O.; Müller, A. M.; Wentz, K. M.; Bardeen, C. J. Self-Absorption Correction for Solid-State Photoluminescence Quantum Yields Obtained from Integrating Sphere Measurements. *Rev. Sci. Instrum.* **2007**, *78*, 086105.
- (61) Deng, W. Q.; Goddard, W. A. Predictions of Hole Mobilities in Oligoacene Organic Semiconductors from Quantum Mechanical Calculations. *J. Phys. Chem. B* **2004**, *108*, 8614–8621.
- (62) Wang, D.; Ivanov, M. V.; Kokkin, D.; Loman, J.; Cai, J. Z.; Reid, S. A.; Rathore, R. The Role of Torsional Dynamics on Hole and Exciton Stabilization in π -Stacked Assemblies: Design of Rigid Torsionomers of a Cofacial Bifluorene. *Angew. Chem., Int. Ed.* **2018**, *57*, 8189–8193.
- (63) Yamagata, H.; Maxwell, D. S.; Fan, J.; Kittilstved, K. R.; Briseno, A. L.; Barnes, M. D.; Spano, F. C. HJ-Aggregate Behavior of Crystalline 7,8,15,16-Tetraazaterrylene: Introducing a New Design Paradigm for Organic Materials. *J. Phys. Chem. C* **2014**, *118*, 28842–28854.
- (64) Leowanawat, P.; Nowak-Król, A.; Würthner, F. Tetramethoxy-Bay-Substituted Perylene Bisimides by Copper-Mediated Cross-Coupling. *Org. Chem. Front.* **2016**, *3*, 537–544.
- (65) Sengupta, S.; Dubey, R. K.; Hoek, R. W. M.; Van Eeden, S. P. P.; Gunbasç, D. D.; Grozema, F. C.; Sudhölter, E. J. R.; Jager, W. F. jager. Synthesis of Regioisomerically Pure 1,7-Dibromoperylene-3,4,9,10- Tetracarboxylic Acid Derivatives. *J. Org. Chem.* **2014**, *79*, 6655–6662.
- (66) Nagarajan, K.; Mallia, A. R.; Reddy, V. S.; Hariharan, M. Access to Triplet Excited State in Core-Twisted Perylenediimide. *J. Phys. Chem. C* **2016**, *120*, 8443–8450.
- (67) Zhang, Y.; Sun, J.; Zhuang, G.; Ouyang, M.; Yu, Z.; Cao, F.; Pan, G.; Tang, P.; Zhang, C.; Ma, Y. Heating and Mechanical Force-Induced Luminescence on-off Switching of Arylamine Derivatives with Highly Distorted Structures. *J. Mater. Chem. C* **2013**, *2*, 195–200.
- (68) Use of diffuse reflectance spectroscopy for optical characterization of un-supported nanostructures - NASA/ADS <https://ui.adsabs.harvard.edu/abs/2007RMxFS..53e..18E/abstract> (accessed Jun 1, 2022).
- (69) Cheriya, R. T.; Mallia, A. R.; Hariharan, M. Light Harvesting Vesicular Donor–Acceptor Scaffold Limits the Rate of Charge Recombination in the Presence of an Electron Donor. *Energy Environ. Sci.* **2014**, *7*, 1661–1669.
- (70) Lakowicz, J. R. Principles of Fluorescence Spectroscopy. *Princ. Fluoresc. Spectrosc.* **2006**, 1–954.
-

- (71) Cölle, M.; Gmeiner, J.; Milius, W.; Hillebrecht, H.; Brütting, W. Preparation and Characterization of Blue-Luminescent Tris(8-Hydroxyquinoline)-Aluminum (Alq₃). *Adv. Funct. Mater.* **2003**, *13*, 108–112.
- (72) Brouwer, A. M. Standards for Photoluminescence Quantum Yield Measurements in Solution (IUPAC Technical Report). *Pure Appl. Chem.* **2011**, *83*, 2213–2228.
- (73) Sheldrick, G. M.; IUCr. A Short History of SHELX. **2007**, *64*, 112–122.
- (74) Spek, A. L.; IUCr. Single-Crystal Structure Validation with the Program PLATON. **2003**, *36*, 7–13.
- (75) Farrugia, L. J.; IUCr. WinGX Suite for Small-Molecule Single-Crystal Crystallography. **1999**, *32*, 837–838.
- (76) Bruno, I. J.; Cole, J. C.; Edgington, P. R.; Kessler, M.; Macrae, C. F.; McCabe, P.; Pearson, J.; Taylor, R. New Software for Searching the Cambridge Structural Database and Visualizing Crystal Structures. **2002**, *58*, 389–397.
- (77) Philip, A. M.; Mallia, A. R.; Hariharan, M. Prolonged Charge Separated States in Twisted Stacks of All-Carbon Donor and Acceptor Chromophores. *J. Phys. Chem. Lett.* **2016**, *7*, 4751–4756.
- (78) G09 | Gaussian.com <https://gaussian.com/glossary/g09/> (accessed Jun 2, 2022).
- (79) R. F. W. Bader. *Atoms in Molecules: A Quantum Theory*, Oxford University Press. **1990**, 438.
- (80) Spackman, M. A.; Jayatilaka, D. Hirshfeld Surface Analysis. *CrystEngComm* **2009**, *11*, 19–32.
- (81) Rajagopal, S. K.; Philip, A. M.; Nagarajan, K.; Hariharan, M. Progressive Acylation of Pyrene Engineers Solid State Packing and Colour via C–H···H–C, C–H···O and π – π Interactions. *Chem. Commun.* **2014**, *50*, 8644–8647.
- (82) Spackman, P. R.; Turner, M. J.; McKinnon, J. J.; Wolff, S. K.; Grimwood, D. J.; Jayatilaka, D.; Spackman, M. A. CrystalExplorer: A Program for Hirshfeld Surface Analysis, Visualization and Quantitative Analysis of Molecular Crystals. *J. Appl. Crystallogr.* **2021**, *54*, 1006–1011.
- (83) Maestro | Schrödinger <https://www.schrodinger.com/products/maestro> (accessed Jun 2, 2022).
- (84) Bochevarov, A. D.; Harder, E.; Hughes, T. F.; Greenwood, J. R.; Braden, D. A.; Philipp, D. M.; Rinaldo, D.; Halls, M. D.; Zhang, J.; Friesner, R. A. Jaguar: A High-Performance Quantum Chemistry Software Program with Strengths in Life and Materials Sciences. *Int. J. Quantum Chem.* **2013**, *113*, 2110–2142.
- (85) Deng, W. Q.; Goddard, W. A. Predictions of Hole Mobilities in Oligoacene Organic Semiconductors from Quantum Mechanical Calculations. *J. Phys. Chem. B* **2004**, *108*, 8614–8621.
- (86) Huang, J. D.; Wen, S. H.; Deng, W. Q.; Han, K. L. Simulation of Hole Mobility in α -Oligofuran Crystals. *J. Phys. Chem. B* **2011**, *115*, 2140–2147.
- (87) Wen, S. H.; Li, A.; Song, J.; Deng, W. Q.; Han, K. L.; Goddard, W. A. First-Principles Investigation of Anisotropic Hole Mobilities in Organic Semiconductors. *J. Phys. Chem. B* **2009**, *113*, 8813–8819.
-

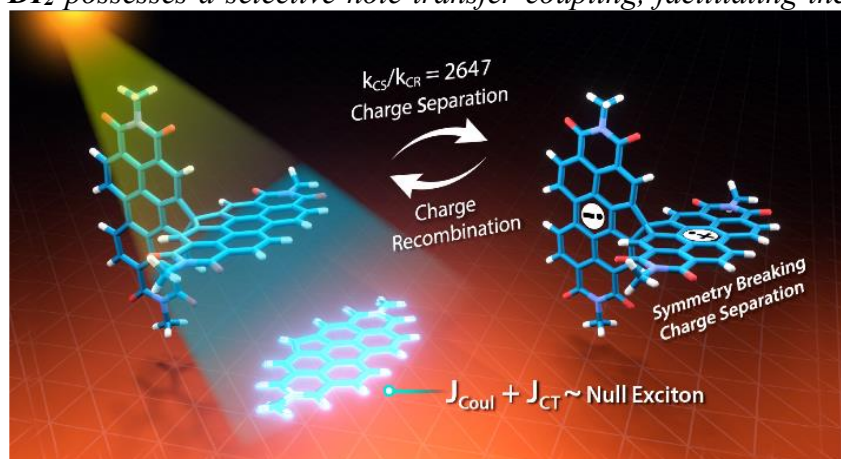
- (88) Hestand, N. J.; Spano, F. C. Interference between Coulombic and CT-Mediated Couplings in Molecular Aggregates: H- to J-Aggregate Transformation in Perylene-Based π -Stacks. *J. Chem. Phys.* **2015**, *143*, 244707.
- (89) Yamagata, H.; Maxwell, D. S.; Fan, J.; Kittilstved, K. R.; Briseno, A. L.; Barnes, M. D.; Spano, F. C. HJ-Aggregate Behavior of Crystalline 7,8,15,16-Tetraazaterrylene: Introducing a New Design Paradigm for Organic Materials. *J. Phys. Chem. C* **2014**, *118*, 28842–28854.
- (90) Smith, D. G. A.; Burns, L. A.; Simmonett, A. C.; Parrish, R. M.; Schieber, M. C.; Galvelis, R.; Kraus, P.; Kruse, H.; Di Remigio, R.; Alenaizan, A.; James, A. M.; Lehtola, S.; Misiewicz, J. P.; Scheurer, M.; Shaw, R. A.; Schriber, J. B.; Xie, Y.; Glick, Z. L.; Sirianni, D. A.; O'Brien, J. S.; Waldrop, J. M.; Kumar, A.; Hohenstein, E. G.; Pritchard, B. P.; Brooks, B. R.; Schaefer, H. F.; Sokolov, A. Y.; Patkowski, K.; Deprince, A. E.; Bozkaya, U.; King, R. A.; Evangelista, F. A.; Turney, J. M.; Crawford, T. D.; Sherrill, C. D. PSI4 1.4: Open-Source Software for High-Throughput Quantum Chemistry. *J. Chem. Phys.* **2020**, *152*, 184108.

Chapter 3

Null Exciton Coupled Chromophoric Dimer Exhibits Symmetry-Breaking Charge Separation

Abstract: *Comprehensive understanding of the structure-property relationships in multi-chromophoric architectures has pushed the limits for developing robust photosynthetic mimics and molecular photovoltaics. The elusive phenomenon of null exciton splitting has gathered immense attention in recent years owing to the occurrence in unique chromophoric architectures and consequent emergent properties. Herein, we unveil the hitherto unobserved null exciton coupling assisted highly efficient photoinduced symmetry-breaking charge separation (SB-CS) in a Greek cross (+)-oriented spiro-conjugated perylene diimide dimer (**Sp-PDI**₂). Quantum chemical calculations have rationalized the infrequent manifestation of null exciton coupling behavior in **Sp-PDI**₂. Negligible contribution of long-range Coulombic and short-range charge-transfer mediated coupling render monomer-like spectroscopic signature for **Sp-PDI**₂ in toluene. The Greek cross (+)-arranged **Sp-PDI**₂ possesses a selective hole-transfer coupling, facilitating the ultrafast dissociation of null exciton and evolution of the charge-separated state in polar solvents. Radical cationic and anionic spectroscopic signatures were characterized by employing femtosecond transient*

*absorption spectroscopy. The substantial hole transfer electronic coupling and lower activation energy barrier of **Sp-PDI**₂ accelerated the charge separation rate. The rate of charge recombination (CR) markedly decelerated due to falling into the inverted region of the Marcus parabola, where the driving force of CR is larger than the total reorganization energy for CR.*



*The substantial hole transfer electronic coupling and lower activation energy barrier of **Sp-PDI**₂ accelerated the charge separation rate. The rate of charge recombination (CR) markedly decelerated due to falling into the inverted region of the Marcus parabola, where the driving force of CR is larger than the total reorganization energy for CR.*

Hence, the ratio of the rates for SB-CS over CR of Sp-PDI₂ exhibited an unprecedentedly high value of 2647 in acetonitrile. The current study provides impeccable evidence for the role of selective charge filtering in governing efficient SB-CS and thereby novel insights towards the design of bio-mimics and advanced functional materials.

3.1. Introduction

The three-dimensional (3D) coalition of π -conjugated organic materials in photosynthesis, solar energy conversion, and optoelectronic devices play an imperative role in ensuring a high degree of solar energy harvesting, transport, and conversion.¹⁻⁶ Specifically, in the photosynthetic complexes, impinging solar photons are transferred into the reaction center through coherent exciton transport. The conversion of excitation energy to chemical energy at the reaction center is initiated by the symmetry-breaking charge separation process (SB-CS), which trigger the sequential electron transfer.^{7,8} The comprehensive understanding of the photophysical processes (exciton formation, energy transfer, and charge separation) in molecular dimers and its precise dependence on the spatial arrangement, π -overlap, and inter-molecular distances are essential for the design of efficient and robust artificial solar energy conversion systems.⁹⁻¹¹

Davydov¹² and Kasha¹³⁻¹⁵ independently worked out the molecular exciton theory in the 1960s based on inter-molecular Coulombic interactions (point-dipole approximation), eventually leading to the primary classification of J-aggregates ("head-to-tail" configuration) and H-aggregates ("sandwich" configuration). H-aggregates exhibit blue-shifted absorption bands, high charge transport character, and quenched fluorescence emission. Conversely, exciton coupling among the staggered transition dipoles (J-aggregate) exhibits a red-shifted absorption peak, weak charge transport behavior, and superradiant fluorescence character.^{16,17} However, in close-packed molecular aggregates, wave functions overlap among the neighboring molecules prompting an additional short-range charge transfer mediated exciton coupling (J_{CT}).¹⁸ The magnitude and the sign of CT coupling are governed by the electron and hole transfer integral derived from the extent of orbital overlap between the highest occupied molecular orbitals (HOMO) and lowest unoccupied molecular orbitals (LUMO).¹⁹⁻²¹ Consequently, the interference between long-range Coulombic coupling and short-range CT coupling defines the effective excitonic coupling in interacting chromophores. A substantial theoretical and experimental effort has been invested in understanding CT coupling and Coulombic coupling (J_{Coul}) interferences.²²⁻²⁵

Photoinduced SB-CS is a process where a symmetrical pair of identical chromophores forms a charge-separated excited state with the hole and electron on different chromophores, i.e., $M-M + h\nu \rightarrow M^+-M^-$ upon photoexcitation.²⁶ SB-CS has found wide applications in artificial photosynthesis and optoelectronic devices owing to the minimal energy loss during the charge-separated state formation (energy loss between the exciton and charge-separated state is <100 mV for SB-CS, in contrast to the value of ~500 mV or more for charge separation in the donor-acceptor systems).²⁷⁻²⁹ The rate of SB-CS mainly depends on the strength of electronic coupling and solvent environment.^{26,30} In a weak exciton coupling regime, the electronic absorption spectra of the interacting chromophores show minor variation when compared to the non-interacting systems. Theoretically, the excited states of the molecular dimer can be represented as locally excited singlet (LE) states and charge-separated (CS) states.^{31,32} SB-CS processes in weakly coupled dyad and the triad of perylenediimide,^{30,33-35} perylene,^{26,36,37} BODIPY,^{28,38} metallopyrrins,³⁸⁻⁴⁰ bianthryl,⁴¹ subphthalocyanine⁴² and terylenediimide^{43,44} are well explored and documented in the literature. Moreover, probing SB-CS processes in film samples and polymers is an emerging research topic.⁴⁵ Strong exciton coupled aggregates show shifted or split absorption bands and excimer formation.^{24,26,46} The excimer states can act as an exciton trap and compete with the desired products. In a strongly coupled system, the excitation energy is delocalized over the dimer molecule, and the excited state may lack the charge separation character.³⁶

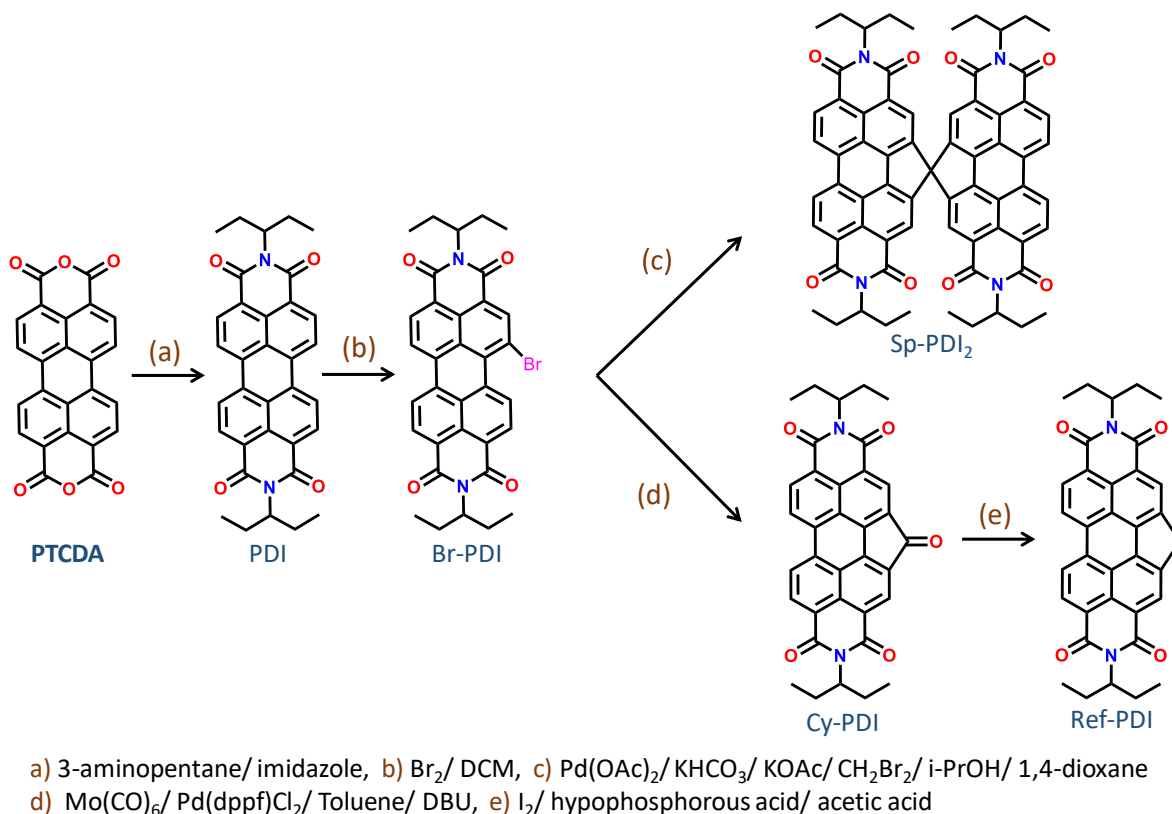
An exciting class of aggregates called "null aggregates," exhibiting monomeric optical properties in the condensed state, was initially proposed by Kasha and co-workers and later by Spano and co-workers.^{15,47} Besides the theoretical predictions, innovative designs exhibiting minimal exciton coupling have been reported in recent years.⁴⁹ Xie and co-workers reported minimal excitonic coupling in a perylenediimide crystal possessing magic angle (slip angle=54.7°) stacking.⁵⁰ Würthner and co-workers demonstrated very weak coupling in a molecular foldamer of perylenediimide (**PDI**) owing to the destructive interference between Coulombic and CT coupling.²⁵ Our group has devised an alternative strategy for constructing molecular aggregates with minimal excitonic interactions in a crystalline state through the orthogonal (face-to-face) stacking of chromophores at a 90° rotational angle. The first crystalline evidence for the Greek cross (+)-architecture with null exciton coupling mediated monomeric optical properties was reported in 1,7-dibromoperylene-3,4,9,10-tetracarboxylic tetrabutylester.⁵¹ Yet another example of null exciton splitting was realized in a series of pentacene derivatives in orthogonal molecular

stacks.⁵² The orthogonally cross-stacked linear and nonlinear acene dimers were found to exhibit mutually exclusive hole and electron transfer coupling.⁵³

Though vital for optoelectronic application, a comprehensive understanding of the excited-state dynamics of very weak/null excitonic coupled chromophores remains rare. Recently, Kim, Würthner and co-workers reported efficient multiexciton state generation in null exciton coupled perylenediimide foldamer by the large charge transfer coupling between the chromophores.⁵⁴ Our long-standing efforts to achieve chromophoric aggregates in Greek cross (+)-arrangement (face-to-face stack) and understand the diverse photo-excited state processes in self-assembled donor-acceptor systems,^{55,56} and bi-chromophoric systems,⁵⁷⁻⁵⁹ motivated us to dwell into the realm of null exciton and its concomitant effect on ultrafast excited-state dynamics. Herein, we report the null exciton coupling in spiro-conjugated perylenediimide (**Sp-PDI₂**), wherein two planar π -conjugated **PDI** chromophores are connected perpendicularly via a quaternary sp^3 carbon center (edge-to-edge arrangement) exhibiting ultrafast SB-CS. Unperturbed spectroscopic features of Greek cross (+)-arranged **Sp-PDI₂** in toluene evidence minimal excitonic coupling. Monomer-like spectral signatures displayed by **Sp-PDI₂** can be rationalized by the interference of negligible contribution from both long-range Coulombic and short-range charge-transfer mediated couplings. The orthogonally oriented **Sp-PDI₂** are found to possess a selective charge-filtering phenomenon (selectively hole-transfer coupling). Significant wave function overlap (hole transfer coupling) among monomeric chromophores of **Sp-PDI₂** facilitates efficient ultrafast SB-CS in polar solvents (THF and ACN). The rate of charge recombination (CR) processes of **Sp-PDI₂** is significantly decelerated due to the low molecular reorganization energy when compared to free energy change of CR ($\Delta G_{CR} > \lambda$). The ratio of rates of SB-CS over CR of **Sp-PDI₂** is estimated as 2647, which is the most long-lived charge separated state obtained so far among the multi-chromophoric **PDI** derivatives (Table A3.1).

3.2. Results and Discussion

3.2.1. Synthesis, single-crystal structure and geometry optimizations. PDI, Ref-PDI, and Sp-PDI₂. were synthesized and characterized according to the previous reports (Figure 3.1 & Scheme 3.1).^{60,61} **Ref-PDI** is the monomer unit of **Sp-PDI₂**. Slow evaporation of a homogenous solution of **Sp-PDI₂** (in a 1:1 chloroform/methanol solvent) at room temperature led to good quality crystals for single-crystal X-ray diffraction. The X-ray crystallography technique unambiguously



Scheme 3.1: Showing the synthesis of **PDI**, **Ref-PDI**, and **Sp-PDI₂**.

confirmed the molecular structure of **Sp-PDI₂** (Figure 3.1). An sp³-hybridized spiro carbon atom connects the two blades of **PDI** subunits to form a Greek cross (+)-architecture (edge-to-edge arrangement) with a rotational angle (θ) of 87.43° between the chromophores (CCDC number 2086823 & Table A3.2). Geometry optimization of **PDI**, **Ref-PDI**, and **Sp-PDI₂** was performed at the B97D3/def2-TZVP level of theory.^{62,63} The geometrical features of **Sp-PDI₂** are essentially the same in vacuum, and θ was found to be 90° between the spiro fused **PDI** units (Figure A3.1). As a response to the increased steric constraint of the five-membered cyclic carbon ring in the **PDI** core's bay region, a small inward bent along the long axis of the perylenediimide chromophore of **Ref-PDI** and **Sp-PDI₂** is observed (Figure A3.2).

3.2.2. Optical properties. The ground state electronic properties of **Sp-PDI₂** along with the reference compounds (**Ref-PDI** and **PDI**) were explored by means of steady-state absorption spectroscopy in toluene ($c_0 = 0.1\text{-}0.5\mu\text{M}$) at room temperature (Figure 3.2 & Figure A3.3). The UV-visible absorption spectrum of **Ref-PDI** shows characteristic spectral signatures of monomeric **PDI** dye with a 10 nm bathochromic shift (Figure A3.3). The absorption maximum of **Ref-PDI** observed at 533 nm ($\lambda_{max}^{Abs} = 18761.73\text{ cm}^{-1}$) with a molar extinction coefficient (ϵ_{max}) of 95690

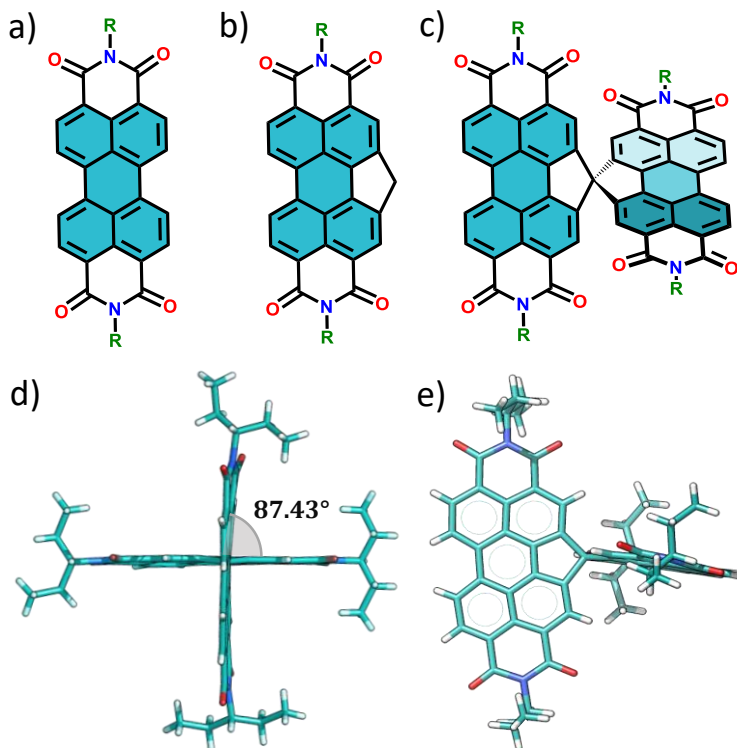


Figure 3.1: Molecular structure of (a) **PDI**, (b) **Ref-PDI**, and (c) **Sp-PDI₂**. (d & e) Single-crystal X-ray structure of **Sp-PDI₂**. “R” represents 3-pentyl group.

$\text{M}^{-1}\text{cm}^{-1}$ corresponds to the S_0-S_1 electronic transition ($f = 0.72$, Table A3.3). The dipole allowed electronic transition of **Ref-PDI** (S_0-S_1 transition) is strongly coupled to the vinyl stretching mode of the perylene core ($\nu_{C=C} \sim 1400 \text{ cm}^{-1}$) resulting in pronounced vibronic progression in the absorption spectrum at 495 nm ($\lambda_{0-0}^{Abs} = 20202.02 \text{ cm}^{-1}$), 464 nm ($\lambda_{0-1}^{Abs} = 21551.72 \text{ cm}^{-1}$) and 435 nm ($\lambda_{0-2}^{Abs} = 22988.51 \text{ cm}^{-1}$). The A_{0-0}/A_{0-1} oscillator strength ratio, as determined by the ratio of the intensities of the 0-0 and 0-1 absorption band, amounts to 1.74 (Table 3.1). In concurrence with the theoretical predictions, UV-visible absorption spectrum of **Sp-PDI₂**, Greek cross-shaped molecule with two π -conjugated perylenediimide rings embraced by spiro linker, reveal virtually unperturbed spectral features as compared to the **Ref-PDI**. Though **Sp-PDI₂** exhibits a monomeric spectral signature, absorption maximum is bathochromically shifted to 549 nm ($\lambda_{max}^{Abs} = 18214.94 \text{ cm}^{-1}$) with an extinction coefficient of $123590 \text{ M}^{-1}\text{cm}^{-1}$. The observed redshift (546.79 cm^{-1}), though not insignificant, arises from the self-energy correction (ΔCT , vide infra).⁴⁸ A minor decrease in the ratio of the absorption band intensities ($A_{0-0}/A_{0-1} = 1.60$ (**Sp-PDI₂**) and 1.74 (**Ref-PDI**)) and minimal absorption band broadening of the ($\Delta\tilde{\nu}_{1/2} = 721.35 \text{ cm}^{-1}$ for **Ref-PDI** and $\Delta\tilde{\nu}_{1/2} = 746.17 \text{ cm}^{-1}$ for **Sp-PDI₂**) suggests negligible exciton coupling among the orthogonally connected **PDI**

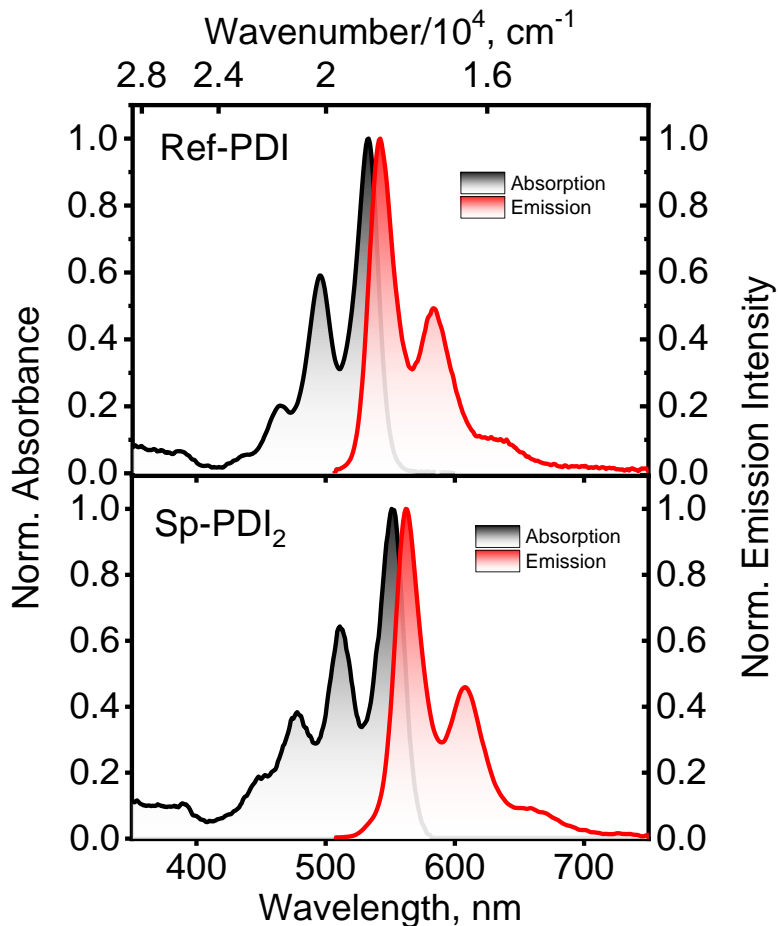


Figure 3.2: Normalized absorption (solid black line) and emission spectra (solid red line) of **Ref-PDI** (top) and **Sp-PDI₂** (bottom) in toluene at room temperature.

units in **Sp-PDI₂**.

To get additional insights into the excitonic coupling of **Sp-PDI₂**, steady-state fluorescence spectroscopy was performed in toluene ($c_0 = 0.1\text{-}0.5 \mu\text{M}$) at room temperature (Figure 3.2 & Figure A3.3). Photoexcitation of **Ref-PDI** shows a characteristic fluorescence emission spectrum with a well-resolved vibronic fine structure of **PDI**. The emission maximum of **Ref-PDI** (λ_{em}) is bathochromically shifted to 542 nm (18450.18 cm^{-1}), and a Stokes shift of 9 nm was observed. The fluorescence quantum yield of **Ref-PDI** is quantified as 97.7%, which is comparable to the reported value of **PDI**.^{33,64} Fascinatingly, the fluorescence emission spectrum of **Sp-PDI₂** reveals a monomer-like spectral signature with well-resolved vibronic bands (Figure 3.2) with the peak maximum (λ_{em}) at 558 nm. Furthermore, high fluorescence quantum yield ($\phi_{Fl} = 90.20\%$) and identical Stokes shift ($\Delta\tilde{\nu}_{Stokes} = 9 \text{ nm}$) reconfirm the exiguous exciton communication between the **PDI** monomers and rules out the other possible deactivation channels (Table 3.1).

Table 3.1: *UV/vis and fluorescence spectroscopic data of Ref-PDI and Sp-PDI₂ were measured in toluene at room temperature.*

| | Ref-PDI | Sp-PDI ₂ |
|--|--------------|---------------------|
| $\lambda_{abs}(A_{0-0}), nm/cm^{-1}$ | 533/18761.73 | 549/18214.94 |
| $\lambda_{abs}(A_{0-1}), nm/cm^{-1}$ | 495/20202.02 | 509/19646.37 |
| $\lambda_{em}, nm/cm^{-1}$ | 542/18450.18 | 558/17921.15 |
| $\epsilon_{max}, M^{-1}/cm^{-1}$ | 95690 | 123590 |
| A_{0-0}/A_{0-1} | 1.74 | 1.60 |
| $\Delta\tilde{\nu}_{Stokes}, nm/cm^{-1}$ | 9/311.50 | 9/293.79 |
| $\phi_{FL}, \%$ | 97.7 | 90.20 |
| τ_{FL}, ns | 4.17 | 6.62 |

3.2.3. Theoretical Investigation. Having rationalized the presence of null exciton coupling of **Sp-PDI₂** in toluene, we explored the nature of excitonic interactions arising from relative interchromophoric orientations by employing theoretical methods. The excitonic coupling (J) of the **Sp-PDI₂** was scrutinized by evaluating the contributions from both long-range and short-range effects^{20,48} (during the theoretical calculation, the spiro carbon atom of the DFT optimized **Sp-PDI₂** molecule were replaced by four H atoms). The long-range Coulombic coupling between any two chromophores arises from the interaction between their transition charge distribution which is often calculated using point-dipole approximation.^{65,66} Herein, we have employed the TrEsp (Transition Charge from Electrostatic Potential) method for calculating Coulombic coupling energy (J_{coul}) between the interacting molecules.⁶⁷ The method provides a good result when the interchromophore distance is shorter than the chromophores size, where dipole-dipole approximation overestimates the exciton coupling energy. In the TrESP method, the transition electrostatic potential is fitted to atomic partial charges. The Coulomb interaction between the transition charges of the different chromophores equal to long-range Coulombic coupling (J_{coul}) and can be efficiently calculated using Eq.1:

$$J_{coul} = \frac{1}{4\pi\epsilon_0} \sum_i \sum_j \frac{q_i^{(1)} q_j^{(2)}}{|r_i^{(1)} - r_j^{(2)}|} \quad (\text{Eq 1})$$

Here, $q_i^{(m)}$ represents the transition charge on i^{th} atom of chromophore m , $r_i^{(m)}$ corresponds to the position vector of the respective transition charge and ϵ_0 is the vacuum permittivity (Appendix, Section 3.7.3). **Sp-PDI₂** shows a negligible long-range Coulombic coupling (J_{coul}) value of 3.34

cm^{-1} reinforcing the hypothesis of minimum Coulombic coupling between orthogonally (edge-to-edge) arranged transition dipole vectors of **PDI** molecules (Figure 3.3 and Table 3.2).

The charge-mediated short-range coupling stemming from the wave function overlap between neighboring molecules has a significant role in defining the effective excitonic interaction.^{17,20,48} The LUMO–LUMO and HOMO–HOMO orbital overlap, which can be substantial in the short inter-chromophoric distance, enables a virtual high energy charge-transfer state between the molecules. The short-range exciton coupling energy can be calculated by Eq. 2.^{68,69}

$$J_{CT} = -2 \frac{t_e t_h}{E_{CT} - E_{S_1}} \quad (\text{Eq 2})$$

Where t_e and t_h represent the electron and hole-transfer integrals which depend on the LUMO–LUMO and HOMO–HOMO orbital overlap of the monomer respectively; E_{CT} is the energy of the virtual charge-transfer state; and E_{S_1} is the energy of the local Frenkel exciton state. Equation 2 holds under the assumption that diabatic Frenkel and CT states are energetically well separated.

The net exciton coupling (J) between neighboring molecules derived from the interference between the long-range Coulombic coupling (J_{Coul}) and the short-range charge transfer mediated

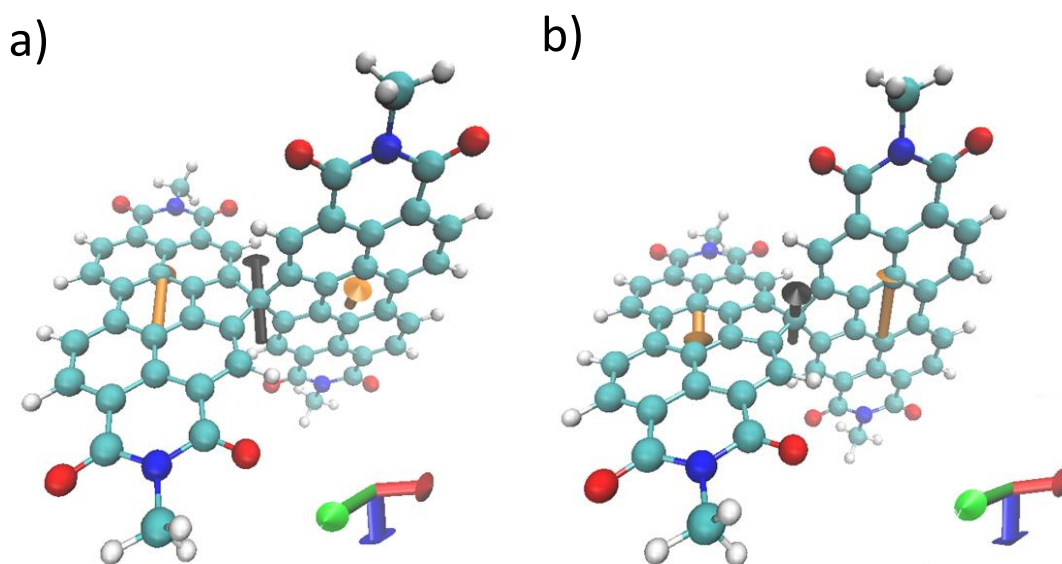


Figure 3.3: Transition dipole vectors (m) of **Sp-PDI**₂ for (a) $S_0 \rightarrow S_1$ transition and (b) $S_0 \rightarrow S_2$ transition. (Transition dipole moment for $S_0 \rightarrow S_1$ and $S_0 \rightarrow S_2$ transition is the same and calculated as 7.79 D).

coupling (J_{CT}) is given by: ^{68,69}

$$J = J_{coul} + J_{CT} \quad (\text{Eq 3})$$

The hole and electron-transfer integral were calculated using the energy splitting dimer method (Table 3.2, Figures 3.4a and 3.4b).^{70,71}

Sp-PDI₂ impart a selective hole-transfer coupling ($t_h = -1185.63 \text{ cm}^{-1}$, Figure 3.4b) owing to the constructive interference between the HOMO of the monomeric **PDI** molecule. Whereas, destructive LUMO-LUMO orbital interaction of the **PDI** unit resulted in the minimal value of electron transfer coupling ($t_e = -8.06 \text{ cm}^{-1}$, Figure 3.4a). Constructive and destructive interference of the P_z orbital around the spiro-linkage is depicted in Figure 3.4a & Figure 3.4b (P_z orbitals of these four carbon atoms are close enough to interact through space). We further proceeded to calculate the J_{CT} value using eq 2. The energy difference between the charge-transfer state (E_{CT}) and the local Frenkel exciton state (E_{S_1}) for **Sp-PDI₂** ($E_{CT} - E_{S_1} = 0.875 \text{ eV}$) was calculated using TheoDORÉ (vide infra) which is in good agreement with the recent literature.⁷² The minimal magnitude of CT coupling ($J_{CT} = -2.79 \text{ cm}^{-1}$) obtained upholds the insignificant nature of the charge-transfer coupling between the orthogonally arranged PDI units ($\Theta = 90^\circ$) of **Sp-PDI₂** (Table 3.2). Thus, spiro-conjugated perylene diimide dimer exhibits null exciton coupling ($J = -0.55 \text{ cm}^{-1}$) due to negligible contributions from Coulombic and CT-mediated couplings.

Table 3.2: Experimentally and theoretically calculated excitonic coupling and hole/electron transfer integrals of **Sp-PDI₂**.

| | (eV) | (cm^{-1}) |
|--------------|------|---------------------------------|
| J^a | | 1.72×10^{-2} 139.13 |
| J^b | | 0.64×10^{-4} 0.55 |
| J_{coul}^c | | 4.10×10^{-4} 3.34 |
| t_e | | -1.03×10^{-3} -8.06 |
| t_h | | -1.47×10^{-1} -1185.63 |
| J_{CT}^d | | -3.46×10^{-4} -2.79 |

^aEstimated from the intensity ratio of the A_{0-0} and A_{0-1} absorption bands in the UV-vis spectra. ^bDetermined based on eq 3. ^cCalculated by the transition charge method based on eq 1. ^dDetermined based on eq 2.

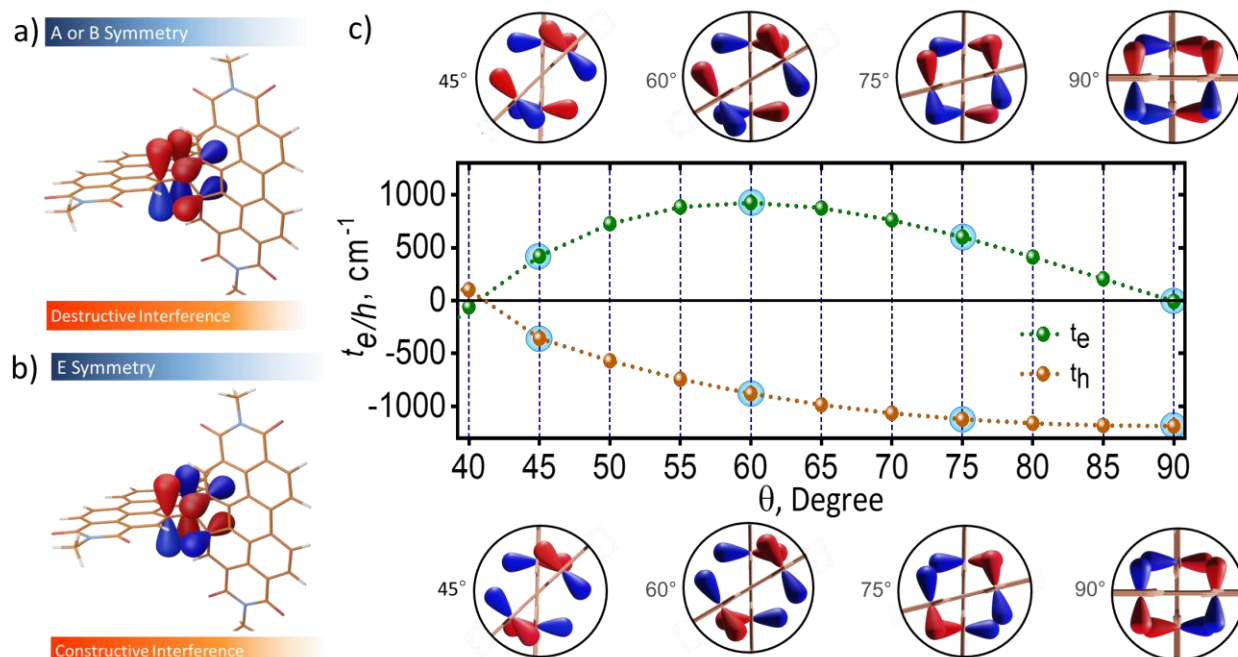


Figure 3.4: Schematic of the $Sp-PDI_2$ molecule with the P_z orbitals around the spiro-link showing (a) destructive interference between LUMOs and (b) constructive interference between HOMOs of PDI molecule. (c) Top: schematic of the LUMO-LUMO orbital interaction of PDI dimer responsible for the electron transfer integral in different rotational angles. Middle: the electron and hole transfer integrals as a function of the rotational angle between two orthogonally arranged PDI molecules. Bottom: schematic of the HOMO-HOMO orbital interaction of PDI dimer responsible for hole transfer integral in different rotational angles (representation of HOMO and LUMO molecular orbitals of PDI molecule is restricted to the P_z orbitals that are close enough to interact through space).

We further calculated the excitonic coupling of $Sp-PDI_2$ by employing a method developed by Spano and co-workers based on the 0-0 and 0-1 absorption band intensities that show exciton-vibrational coupling (Appendix, Section 3.7.4).^{72,73} Excitonic coupling energy obtained by the method is comparable with the one obtained by equation 3 (Table 3.2). The marginal disparity in excitonic coupling energy could be a consequence of exciton coupling stemming from the small rotational degree of freedom around the spiro-linkage of Greek cross (+)-arranged $Sp-PDI_2$ under the experimental conditions (Figure 3.5).^{41,74,75} Therefore, the exciton coupling calculated by the ratio of the intensity of the 0-0 and 0-1 absorption band observed in the UV-visible absorption spectra and theoretical methods restate the null excitonic coupling between the orthogonally (edge-to-edge) arranged **PDI** chromophores.

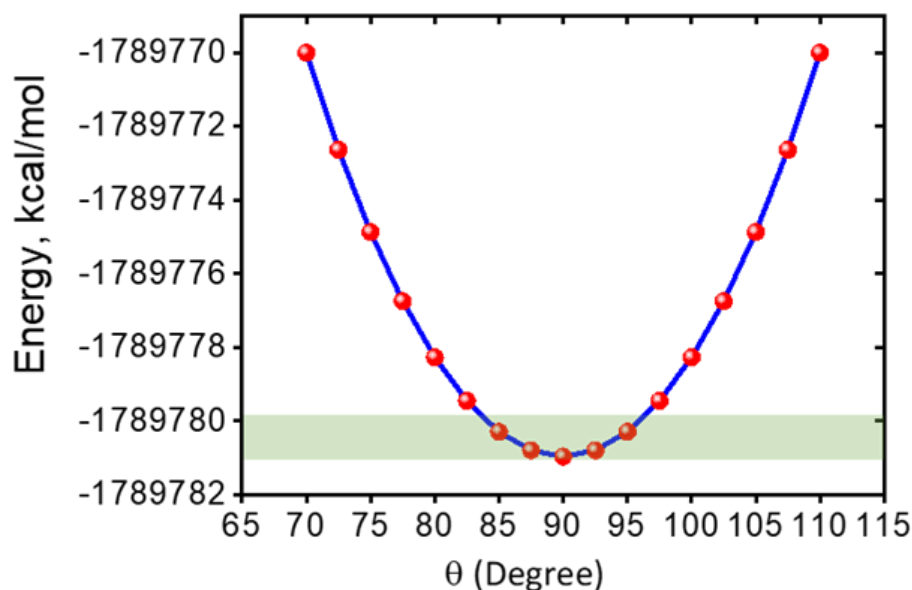


Figure 3.5: The ground-state potential energy surface of **Sp-PDI₂** computed at the *wb97xd/def2svp* level of theory in a vacuum.

To obtain further insight into the nature of different excited states of **Sp-PDI₂**, fragment-based excited state analysis developed by Plasser, implemented in TheoDORE was performed (Appendix, Section 3.7.5).^{76,77} **Sp-PDI₂** has two nearly degenerate localized Frenkel states S_1 and S_2 with equal oscillator strengths ($f=0.79$). While the degenerate S_3 and S_4 states ($f=0.06$) possess pure CT states character (S_3 and S_4 states with $CT = 0.82$), where the hole is localized on one fragment, and the electron is localized on the other. The higher energy virtual CT state (S_3 and S_4) and local Frenkel exciton state (S_1 and S_2) are energetically well-separated, and $E_{CT} - E_{S_1} = 0.87$ eV is calculated for **Sp-PDI₂** in toluene. The description is pictorially represented using an electron-hole correlation plot (Table 3.3 & Figure 3.6).

Table 3.3. Energy (ΔE), oscillator strength (f), mean position (POR), participation ratio (PR) of initial orbital (hole) and final orbital (electron) and charge transfer character (CT) of excited singlet states in **Sp-PDI₂**.

| State | ΔE (eV) | f | POR | PR | CT |
|-------|-----------------|-------|-------|-------|------|
| S_1 | 2.505 | 0.787 | 1.913 | 1.190 | 0.08 |
| S_2 | 2.505 | 0.787 | 1.090 | 1.196 | 0.06 |
| S_3 | 3.380 | 0.064 | 1.001 | 1.574 | 0.82 |
| S_4 | 3.380 | 0.064 | 1.001 | 1.429 | 0.82 |

Further, natural transition orbitals (NTO)⁷⁸ and hole–electron isosurface analyses⁷⁹ of the S_0 to S_n transition ($n = 1, 2, 3,$ and 4) of **Sp-PDI₂** are portrayed in Figures 3.6, A3.4 and 3.7. Localization of hole–electron distribution in one of the **PDI** monomers of **Sp-PDI₂** is observed for $S_0 \rightarrow S_1$ and $S_0 \rightarrow S_2$ transition. In contrast, hole–electron distribution isosurface of $S_0 \rightarrow S_3$ and $S_0 \rightarrow S_4$ electronic transitions show that hole and electron are localized on different **PDI** units of **Sp-PDI₂**. The excited state characteristics of **Sp-PDI₂** in its ground state geometry resembles the bianthryl molecules reported in the literature, where all excited states reflect the symmetry of the molecular structure. However, transition dipole vectors are arranged parallelly in bianthryl and orthogonally in **Sp-PDI₂** (Figure 3.3).^{80,81}

The short-range CT-mediated exciton coupling, or superexchange coupling, J_{CT} , represent an energy-transfer process that proceeds through a high-energy virtual CT state, as depicted in

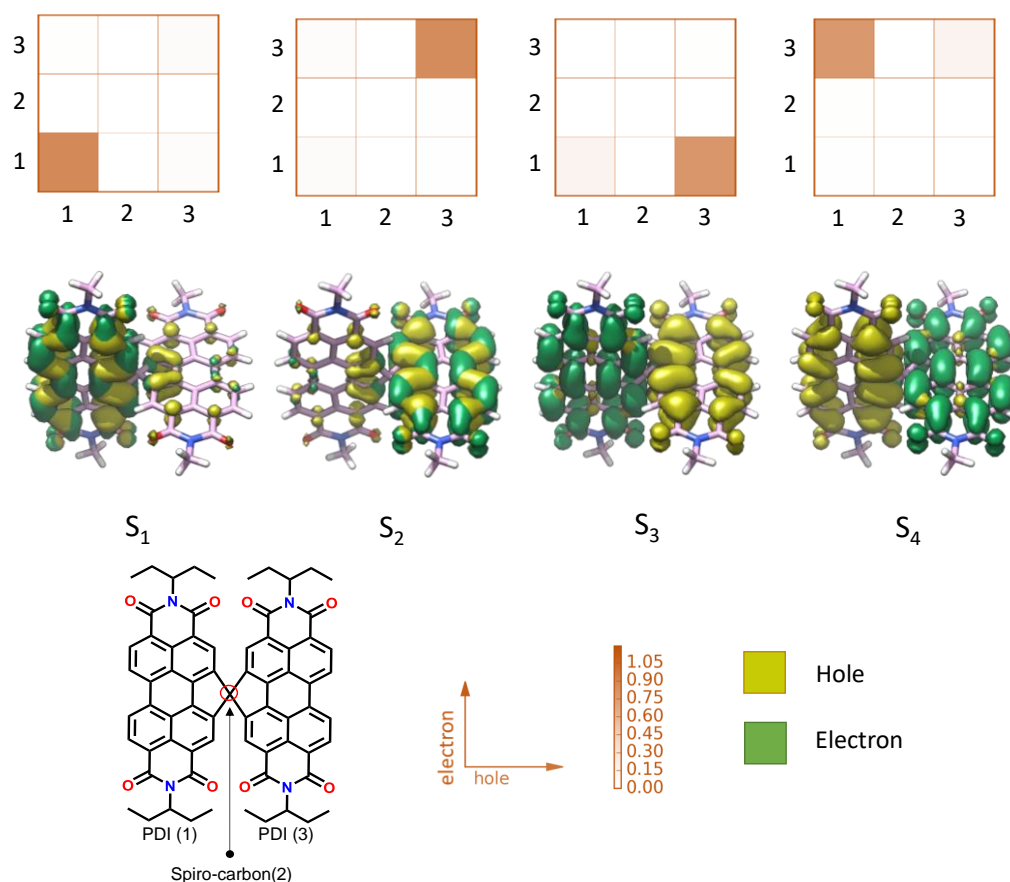


Figure 3.6: (Top) Electron-hole correlation plots of **Sp-PDI₂** for the S_1 , S_2 , S_3 , and S_4 states (fragment 1: PDI A, fragment 2: spiro-carbon, and fragment 3: PDI B). (Bottom) Distribution of hole (yellow) and electron (green) for first four excited states of **Sp-PDI₂** obtained from hole–electron isosurface analyses.

Figure 3.7.²⁰ In **Sp-PDI₂**, the exciton localized initially on a single PDI molecule dissociates by transferring a hole ($t_h = -1185.63 \text{ cm}^{-1}$) to its neighbor PDI molecule resulting in creating the higher energy CT state. Electron transfer is forbidden due to negligible electron transfer coupling $t_e = -8.06 \text{ cm}^{-1}$. In order to have energy transfer to the neighboring molecule (J_{CT}), the created CT state has to decay by transferring an electron to the neighboring molecule. In contrast, because of the minimal magnitude of t_e , the CT state decay to initial local Frenkel exciton state by the back-transfer of hole, resulted in self-energy correction (ΔCT).^{20,48}

$$\Delta CT = -2 \frac{(t_e^2 + t_h^2)}{E_{CT} - E_{S_1}} \quad (\text{Eq 4})$$

ΔCT is universally negative whenever the virtual CT state is higher in energy than the local Frenkel exciton. Calculated self-energy correction ($\Delta CT = -396.34 \text{ cm}^{-1}$) successfully accounts for the spectral absorption shift of 546.94 cm^{-1} observed for the **Sp-PDI₂** in toluene. Interestingly, the spectral absorption shift stemmed from ΔCT complicates Kasha's conventional classification of H- and J-aggregates.

To assess the effect of relative spatial orientation on the Coulombic and charge transfer coupling, rotational angle-dependent J_{Coul} , t_e , t_h and J_{CT} were probed for orthogonally arranged **PDI** monomers of **Sp-PDI₂** (spiro carbon of the optimized structure was replaced by four H atoms, Figure 3.4c, Figure 3.8, and Tables A3.4-A3.5). The **PDI** dimer with a rotational angle of 90° has J_{Coul} value of 3.34 cm^{-1} . J_{Coul} drastically increased to 76.90 cm^{-1} for rotation of a **PDI** monomer

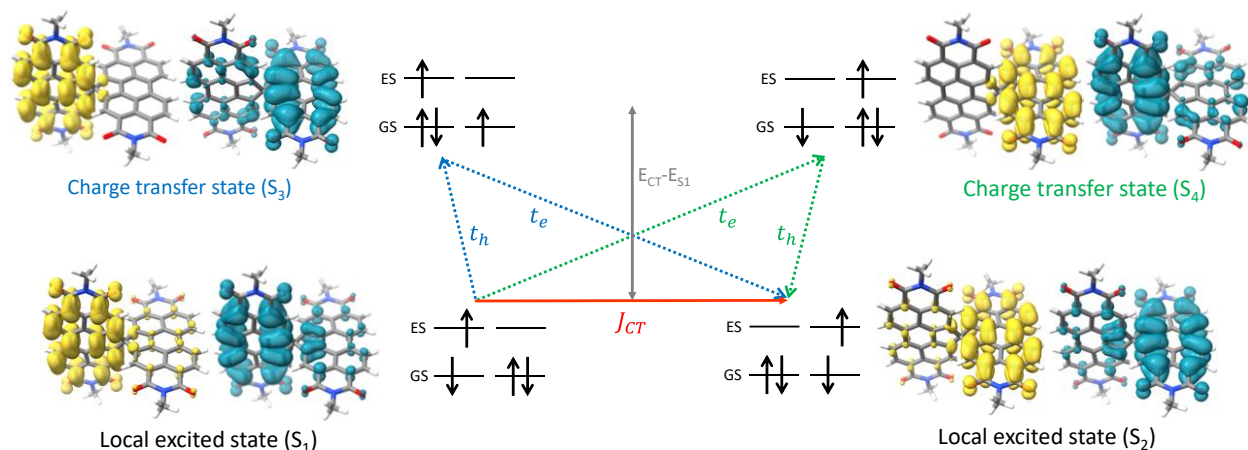


Figure 3.7: Energy level diagram of different singlet excited states of **Sp-PDI₂**, depicting hole and electron transfer between neighboring PDI molecule and corresponding isosurface of hole (blue) and electron (yellow) distribution.

with respect to the other about an angle of 5° from the initial 90° cross-architecture. A linear increase of J_{Coul} with the decrease of rotational angle is observed, and a maximum value of 798.59 cm^{-1} reached at the rotational angle of 40° , indicating the relatively more robust Coulomb-coupled regime. On the other hand, the behavior of t_e , t_h and J_{CT} will depend on the nodal pattern of the molecular orbitals involved. The hole transfer integral shows a significant value ($t_h = -1185.63 \text{ cm}^{-1}$) at the rotational angle of 90° , while the electron transfer integral exhibits minimal magnitude ($t_e = -8.06 \text{ cm}^{-1}$), reflecting the charge filtering effect in **Sp-PDI₂**.

A linear decrease in t_h as a function of θ was observed and resulted in $t_h=0$ at $\sim 41^\circ$. The constructive interference between HOMOs of **PDI** at 90° is gradually transforming to destructive interference as θ reduces (Figure 3.4c). In contrast, t_e depicts inverted-parabolic behavior as a function of intramolecular rotational angle (θ). As the θ decreases from 90° , the electron transfer coupling increases from $t_e = -8.06 \text{ cm}^{-1}$ to reach a maximum value of $t_e = 924.21 \text{ cm}^{-1}$ at 60° (destructive interference between LUMOs of **PDI** changes to constructive interference). Similarly, rotational angle-dependence of short-range CT coupling, J_{CT} , follows inverted-parabola behavior

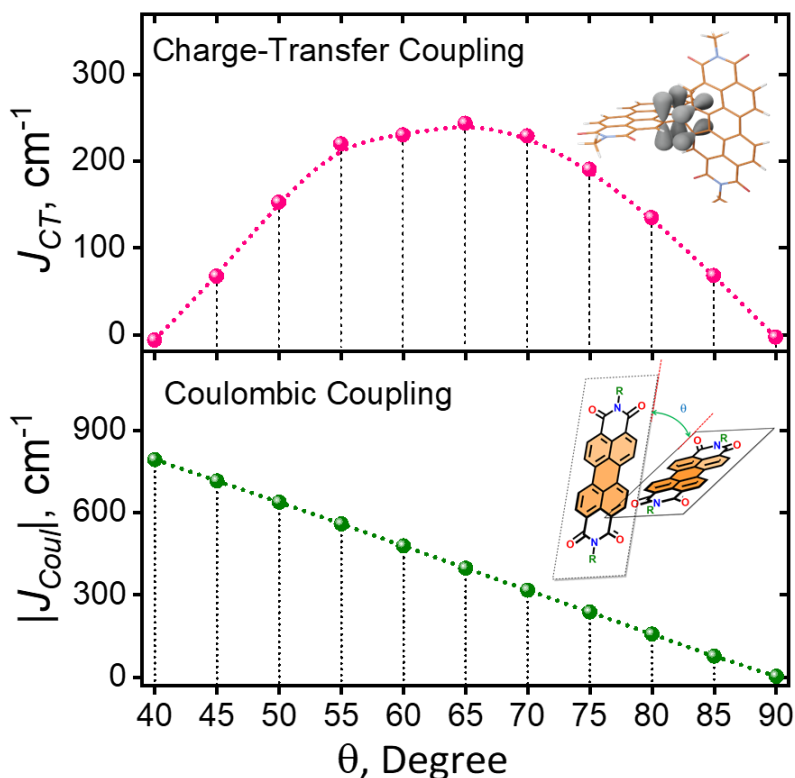


Figure 3.8: Variation of the modulus of Coulombic coupling $|J_{Coul}|$ and charge-transfer coupling (J_{CT}) as a function of rotation angle (θ) between the perylenediimide monomers (for evaluating J_{CT} , $E_{CT} - E_{S_1} = 0.875 \text{ eV}$ was used as constant).

and attain a maximum at $\sim 65^\circ$ (Figure 3.8). At the angle of $\sim 41^\circ$, both t_h , and t_e , becomes zero, effectively shutting off charge-transfer coupling and creating an aggregate driven solely by Coulombic couplings, i.e., an ideal Kasha aggregate.

To shed light on the solvent polarity modulated photophysical properties of null exciton coupled **Sp-PDI₂**, we carried out solvent-dependent absorption and fluorescence measurements in solvents of different dielectric constants, i.e., toluene ($\epsilon = 2.4$), tetrahydrofuran (THF, $\epsilon = 7.6$), and acetonitrile (ACN, $\epsilon = 37.50$) (Figures 3.9, A3.5-A3.6 and Table 3.4).⁸² The line shapes of the absorption spectra of **Sp-PDI₂** in different solvents have a strong resemblance. However, fluorescence quantum yield decreases substantially and the fluorescence lifetime decay exhibits biexponential lifetimes as the solvent polarity increases (Figure 3.9 and Table 3.4), which indicates the existence of additional decay pathways such as SB-CS. In high-polar solvents, such as ACN, the fluorescence is almost quenched ($\Phi_{Fl} < 1\%$) and biexponential emission lifetimes are observed ($\tau_{Fl}^1 = 1.63$ ns (15.75%) and $\tau_{Fl}^2 = 6.87$ ns (84.25%)). Whereas in THF, moderately polar solvent, **Sp-PDI₂** exhibits considerable fluorescence emission ($\Phi_{Fl} = 24\%$) and biexponential

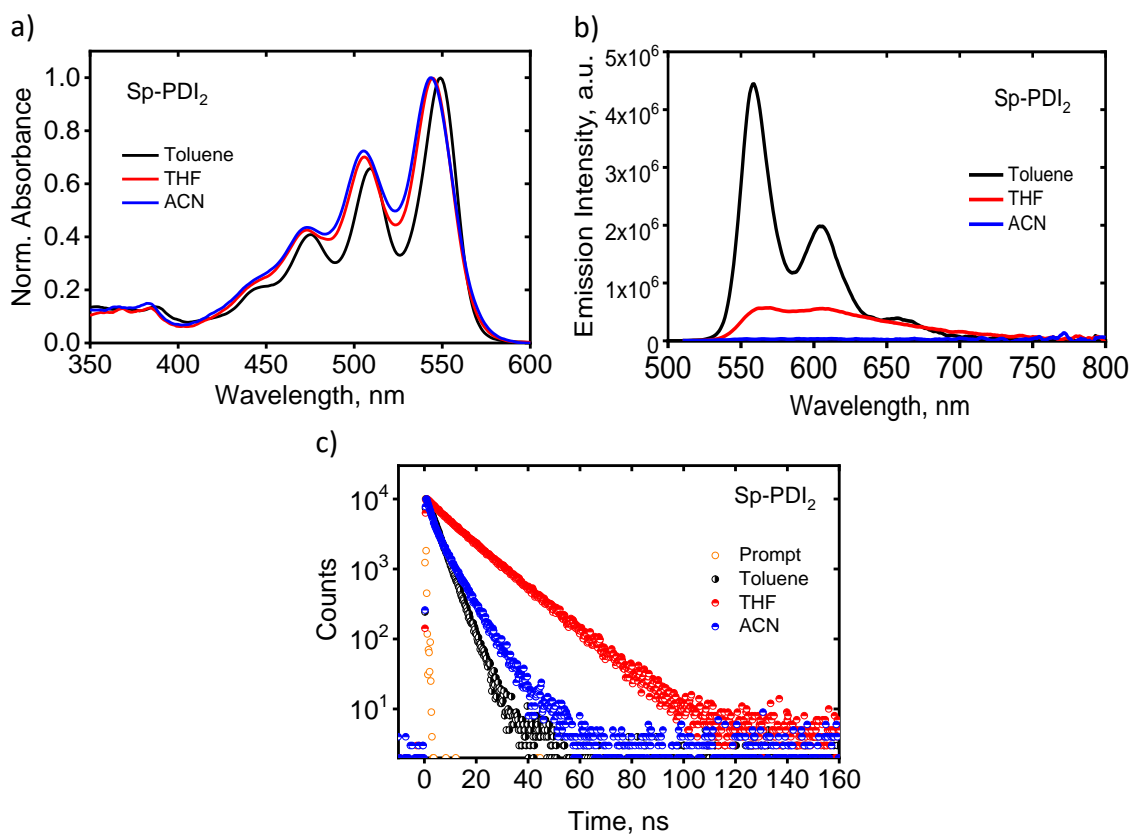


Figure 3.9: (a) Absorption and (b) emission spectra for **Sp-PDI₂** in different solvents. (c) Fluorescence lifetime decay profile of **Sp-PDI₂** in different solvents.

Table 3.4: Photophysical properties of **Ref-PDI** and **Sp-PDI₂** in different solvents.

| Solvent | Ref-PDI | | Sp-PDI ₂ | |
|-----------------|-------------------|------------------|---------------------|------------------------------|
| | Quantum yield (%) | τ_{Fl} (ns) | Quantum yield (%) | τ_{Fl} (ns) |
| Toluene | 97.78 | 4.23 | 90.20 | 6.62 |
| Tetrahydrofuran | 95.00 | 4.241 | 24.00 | 14.2(90.20%) 6.87(9.8%) |
| Acetonitrile | 97.0 | 4.43 | <1 | 1.63(15.74%) 6.80(84.25%) |

decay profile ($\tau_{Fl}^1 = 14.2$ ns (90.20%) and $\tau_{Fl}^2 = 6.80$ ns (9.80%)). The normalized emission spectrum of **Sp-PDI₂** in polar solvents (Figure A3.5) is observed as broad and distinct from that in toluene and not exhibiting any Stokes shift, implying that the emission may have originated from newly formed states. By virtue of the orthogonal arrangement of PDI molecules and restricted rotation around the spiro linkage, the presence of emission from low-lying excimer and relaxed singlet states can be ruled out.^{33,35} The nature of the emissive states in THF and ACN has to be further explored employing transient absorption and emission measurements (vide infra).

The rate constants (k) for SB-CS and charge recombination (CR) were calculated through the classical expression of Marcus electron transfer theory:^{83,84}

$$k = \frac{2\pi}{\hbar} \frac{V_{DA}^2}{\sqrt{4\pi\lambda k_b T}} \exp\left(-\frac{(\Delta G + \lambda)^2}{4\lambda k_b T}\right) \quad (\text{Eq 5})$$

According to eq 5, the nonadiabatic electron transfer rate depends on the three variables that can be computed or determined experimentally. The first Marcus parameter is the Gibbs free energy change (ΔG) between the equilibrium reactant and product states; the other Marcus parameters are total reorganization energy (λ), which is the total energy required to distort the equilibrium geometry of the reactant state to the product state, and electronic coupling (V_{DA}). The magnitude of the electronic coupling matrix element indicates the coupling strength between the initial and the final state. The region in which the V_{DA} is small is commonly referred to as nonadiabatic electron transfer. The most profound feature of the Marcus theory for charge separation is the so-called inverted region effect; that is, the charge recombination kinetics gets slowed down given that the free energy changes are more significant than the reorganization energy (λ).^{30,85}

3.2.4. Energetics. The feasibility of the photoinduced symmetry-breaking charge transfer is determined with the Rehm-Weller formulation⁸⁶ based on the Born dielectric continuum model, which estimates the energy gap between the optically excited state (E_{00}) and the ion pair using the redox potentials (E_{redox}) and the Coulomb penalty for holding the charges at a fixed distance. The optical bandgap (E_{00}) was determined by the crossing points of the normalized absorption and emission spectra. Electrochemical bandgap (E_g) of **Sp-PDI₂** was calculated by cyclic voltammetry (CV) and differential pulse voltammetry (DPV) with the ferrocene/ferrocenium (Fc/Fc^+) couple as a reference in dry CH_2Cl_2 under nitrogen atmosphere (Figure 3.10 & Table 3.5). As previously reported,^{60,61} the **Ref-PDI** exhibits two distinct reversible reduction waves ($E_{1(red)} = -1.15$ and $E_{2(red)} = -1.35$ V) and one quasi-reversible oxidation wave ($E_{1(ox)} = 1.20$ V), like PDI.³³ Whereas **Sp-PDI₂** shows four consecutive redox waves ($E_{1(red)} = -0.99$, $E_{2(red)} = -1.02$, $E_{3(red)} = -1.21$ and $E_{4(red)} = -1.33$ V) and a single oxidation wave at 1.23 V. The distinct redox properties of **Sp-PDI₂** confirms the electronic communication between the orthogonally arranged PDI chromophores. The near degeneracy of first and second reduction potentials (-0.99 , -1.02 V) of

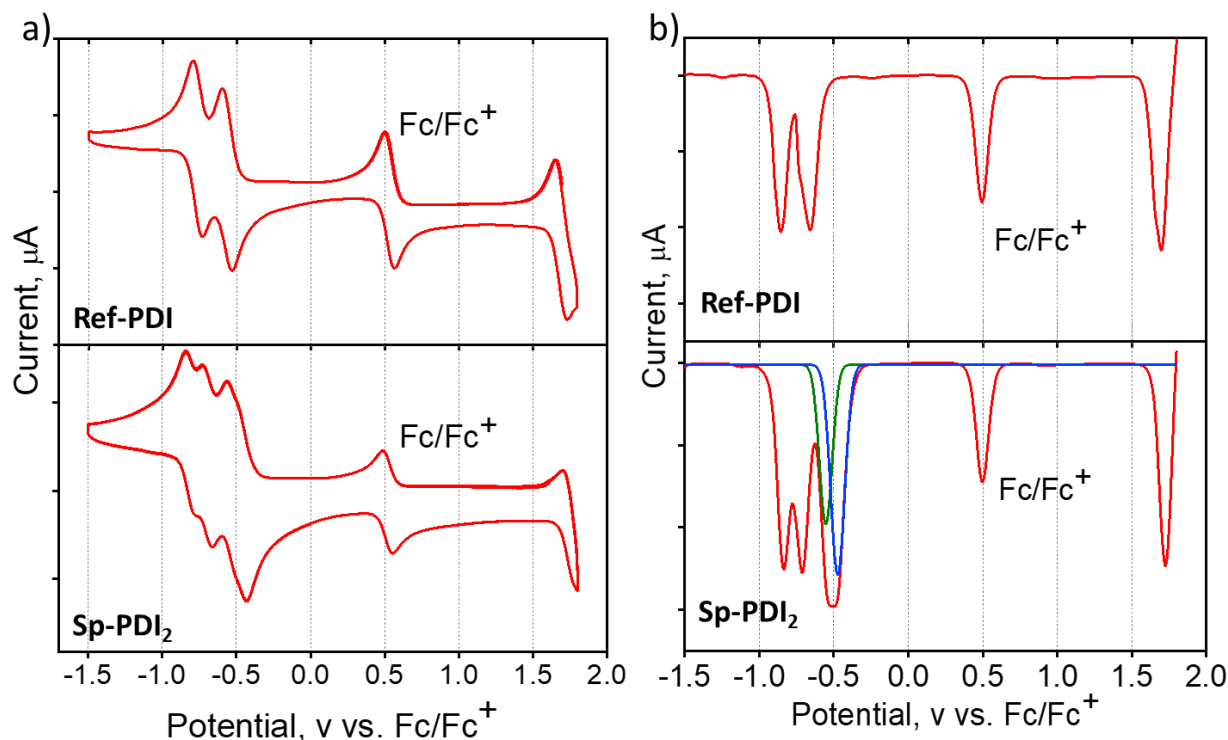


Figure 3.10: (a) Cyclic voltammetry data and (b) differential pulse voltammograms of **Ref-PDI** and **Sp-PDI₂** in CH_2Cl_2 . (Tetrabutylammonium hexafluorophosphate (0.1 M) as the supporting electrolyte, scan rate 200 mV s^{-1} . Fc/Fc^+ =ferrocene/ferrocenium couple).

Table 3.5: Summary of redox potentials and HOMO/LUMO calculations of **Ref-PDI** and **Sp-PDI₂** (CH_2Cl_2 , 298 K, $\epsilon_S = 8.93$).

| | ^a $E_{1(ox)}$ (V) | ^b $E_{1(red)}$ (V) | ^b $E_{2(red)}$ (V) | ^b $E_{3(red)}$ (V) | ^b $E_{4(red)}$ (V) | HOMO (eV) | LUMO (eV) | E_g (eV) | E_{00} (eV) |
|---------------------------|---------------------------------|----------------------------------|----------------------------------|----------------------------------|----------------------------------|--------------|--------------|---------------|------------------|
| Ref-PDI | 1.20 | -1.15 | -1.35 | - | - | -6.00 | -3.65 | 2.35 | 2.31 |
| Sp-PDI₂ | 1.23 | -0.99 | -1.02 | -1.21 | -1.33 | -6.03 | -3.81 | 2.22 | 2.24 |

^a $E_{ox} = -(E'_{ox} - E_{Fc/Fc+})$ eV, ^b $E_{red} = -(E'_{red} - E_{Fc/Fc+})$ eV, E'_{ox} and E'_{red} is the oxidation and reduction potential vs. Ag, E_{ox} and E_{red} is the oxidation and reduction potential vs. Fc/Fc⁺.

Sp-PDI₂ can be attributed to the destructive interference between LUMO of the **PDI** monomers and is consistent with calculated t_e value (Figures A3.7 and A3.8). Thus, Rehm-Weller treatment gives $\Delta G_{CS} \approx +0.37, -0.16, -0.30$ eV for **Sp-PDI₂** in toluene, THF, and ACN, respectively. The estimated positive free energy change of charge separation ($\Delta G_{CS} \approx +0.37$) in toluene would render SB-CS infeasible in non-polar solvents (vide infra). Calculated ΔG_{CS} in toluene seems to be a bit higher than expected which could be due to the overestimation of polarity of nonpolar solvents by the Born dielectric continuum model.⁸⁷

3.2.5. SB-CS dynamics. To unravel the excited-state dynamics responsible for its efficient non-radiative decay, we carried out solvent-dependent femtosecond transient absorption (fsTA) measurement of **Sp-PDI₂** in toluene, THF, and ACN solvents. The fsTA spectra of **Sp-PDI₂** (optical density = 0.2 to 0.3) are shown in Figure 3.11. Upon photoexcitation at 440 nm, using a ~100 fs laser pulse, the fsTA spectra of **Sp-PDI₂** in nitrogen-purged toluene solution (Figure 3.11a) exhibit the characteristic features of the singlet excited state of perylenediimide chromophore (Figure A3.9).^{33,35} The fsTA spectra display negative ground-state bleach (GSB)/stimulated emission bands (SE) ~465 to 626 nm, alongside the positive broad excited-state absorption (ESA) features are also observed, with peaks at 651, 733, and 755 nm. The SB-CS process is switched off in toluene because the charge-separated state has higher energy than the excited singlet state ($\Delta G_{CS} \approx +0.37$ eV). On the other hand, **Sp-PDI₂** in THF ($\epsilon_S = 7.6, \Delta G_{CS} \approx -0.16$ eV) shows remarkably different excited-state dynamics, as shown in Figure 3.11b, characterized by fast decay of the ¹**Sp-PDI₂*** local singlet state (GSB was seen as a negative band extending from ~465 to 585 nm, accompanied by a positive ESA band in the ~608-770 nm range) with the evolution of a broad new transient species characterized by positive features in the visible region at ~590, 699 and 731 nm. The newly emerging ESA signature serves as a direct measure of the SB-CS in THF; however, the

characteristic signature of PDI radical cation peak ~ 730 nm is not evident in ESA as compared to radical anion peak of PDI at ~ 587 nm.^{35,88} The intensity of ESA band ~ 650 -750 nm is almost intact during the SB-CS, which could be due to the presence of an equilibrium between the singlet excited state and CS state. The solvation of **Sp-PDI₂** by moderately polar THF reduces the energy of the CS state close to the local singlet excited state. A similar equilibrium between excited singlet state and SB-CS state of zinc dipyrins, 9,9'-bianthryl and PDI dimers were documented in the literature in weakly polar solvents.^{35,40,41}

Further, we performed fsTA measurements of **Sp-PDI₂** in more polar ACN ($\epsilon_s = 37.50$) to probe the effect of solvent polarity on charge separation, where SB-CS is more energetically feasible $\Delta G_{CS} \approx -0.30$ eV (Figure 3.11c). The dynamics of the photoexcited dimers in ACN were similar to that observed in THF, display a broad positive band (ESA) around ~ 657 nm and pronounced negative bands after photoexcitation at the initial time (~ 465 -567 nm). Subsequently, these bands decay rapidly by a concomitant growth of two new absorption bands at around ~ 581 and ~ 727 nm corresponding to the spectral features of **PDI** radical cation and radical anion, respectively.^{35,88}

To extract the kinetic components responsible for these transformations in the total spectra, a singular value decomposition (SVD) followed by target analysis (using an $A \rightarrow GS$ or $A \rightarrow B \rightarrow GS$ or $A \rightleftharpoons B \rightarrow GS$ kinetic models, Figure A3.13) of the time versus wavelength-based three-dimensional map of fsTA spectra was executed.^{89,90} Selected kinetic traces superimposed target analysis fitted curves at different wavelengths are chosen to display the fitting qualities as shown in Figures A3.10-A3.12. In the case of **Sp-PDI₂** in toluene, species associated spectra (SAS) shows a single principal component corresponding to locally excited singlet state (A) ($S_1 - S_n$ electronic transitions). The lowest singlet excited state (**¹Sp-PDI₂***) does not decay entirely to the ground state (GS) within the given experimental time scale, plausibly due to the long singlet lifetime (fitted lifetime, $\tau_A = 6.95$ ns), consistent with the fluorescence decay of **Sp-PDI₂** in toluene ($\tau_{Fl} = 6.62$ ns). However, in polar solvents, THF and ACN, species associated spectra (SAS) of **Sp-PDI₂** showed two principal components that are ascribed to the locally excited singlet state (A) and the SB-CS state (B, Figure A3.14). The fs-TA data of **Sp-PDI₂** in THF was fitted with a target model ($A \rightleftharpoons B \rightarrow GS$) to account for an equilibrium process between LE state and CS state, whereas in ACN sequential target model ($A \rightarrow B \rightarrow GS$) were employed. The forward and backward charge transfer rate constants ($k_{A \rightarrow B}$ and $k_{A \leftarrow B}$) between the locally excited state and CS states **Sp-PDI₂** in THF are $(2.96 \text{ ps})^{-1}$

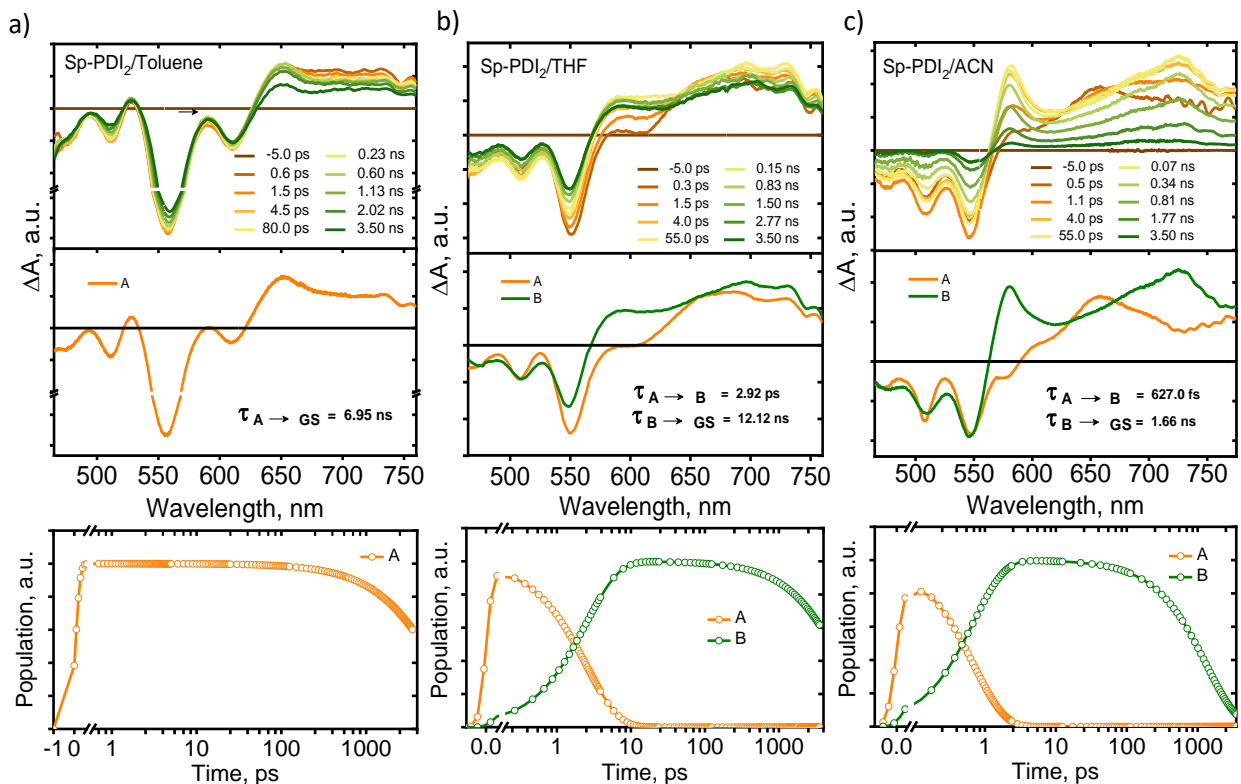


Figure 3.11: (Top) Femtosecond transient absorption spectra of **Sp-PDI₂** in (a) toluene, (b) THF, and (c) ACN showing the excited-state dynamics after photoexcitation. (Middle) Species associated spectra reconstructed from target analysis of $A \rightarrow GS$ model for toluene, $A \rightleftharpoons B \rightarrow GS$ model for THF and $A \rightarrow B \rightarrow GS$ model for ACN, respectively, where A is $^1*\text{Sp-PDI}_2$, B is the SB-CS state and GS is the ground state ($\lambda_{ex}=440$ nm). (Bottom) Relative population profiles of the excited state are fitted by kinetic models.

and $(132 \text{ ps})^{-1}$, respectively. In ACN, the excited singlet state (A) of **Sp-PDI₂** decays within a rate constant of $k_{A \rightarrow B} = (627 \text{ fs})^{-1}$, which initiates the ultrafast growth of a new species characterized by positive features in the visible region (~ 565 to 775 nm). The spectroscopic signature of the newly formed species in ACN and THF persists across the entire time window of the transient absorption measurement (3.5 ns). Subsequently, these charge-separated states decay by charge recombination (CR) to the ground state with rate constants of $k_{B \rightarrow GS} = (1.66 \text{ ns})^{-1}$ and $(12.20 \text{ ns})^{-1}$ for ACN and THF, respectively, with no evidence of triplet excited state. An isosbestic point observed at ~ 625 and 634 nm for ACN and THF, respectively, indicates the transformation of a singlet state to the prolonged charge-separated state. The observed ultrafast transient dynamics show photoinduced intramolecular SB-CS behavior of **Sp-PDI₂** in a polar solvent, consistent with its quenched fluorescence in polar solvents (THF and ACN). The CS and CR rate constants (k) and

Table 3.6: Time constants (τ), rate constants (k), driving forces (ΔG), reorganization energy (λ) and activation barrier (ΔG^\ddagger) for symmetry-breaking charge separation (SB-CS), back charge transfer (BCT) and charge recombination (CR) in **Sp-PDI₂**.

| Symmetry-breaking charge separation (SB-CS) and back charge transfer (BCT) of Sp-PDI₂ | | | | | | |
|---|---------------------|---|--------------------------------------|------------------------|----------------------|---|
| Solvent | τ_{CS} (ps) | $k_{CS} \times 10^{10}$ (s ⁻¹) | ΔG_{CS} (eV) ^a | λ_{CS} (eV) | τ_{BCT} (ps) | $k_{BCT} \times 10^8$ (s ⁻¹) |
| Toluene | - | - | +0.37 | 0.24 | - | - |
| THF | 2.96 | 33.78 | -0.16 | 0.57 | 132 | 75.75 |
| ACN | 0.627 | 159.48 | -0.30 | 0.96 | - | - |

τ and $k = 1/\tau$ from target fits of visible fsTA spectra. ΔG for CS from Rehm-weller. λ for CS calculated based on equations 6,7 and 8.

| Charge recombination (CR) in Sp-PDI₂ | | | | | | |
|--|---------------------|--|--------------------------------------|--------------------------------------|------------------------|-----------------------------|
| Solvent | τ_{CR} (ns) | $k_{CR} \times 10^8$ (s ⁻¹) | ΔG_{CR} (eV) ^a | ΔG_{CR} (eV) ^b | λ_{CR} (eV) | ΔG^\ddagger (eV) |
| Toluene | - | - | -2.60 | -2.70 | 0.48 | 0.38 |
| THF | 12.20 | 0.82 | -2.08 | -2.41 | 0.81 | 0.18 |
| ACN | 1.66 | 6.02 | -1.94 | -2.30 | 1.20 | 0.11 |

τ and $k = 1/\tau$ from target fits of visible fsTA spectra. ΔG for CR from Rehm-weller analysis^a and constrained density functional computation.^b λ for CR calculated based on equations 6,7 and 8.

time constants (τ) for **Sp-PDI₂** in different solvents are summarised in Table 3.6. The target fitted time constants of charge separation and recombination are $\tau_{CS} = \sim 2.96$ ps and $\tau_{CR} = \sim 12.20$ ns in THF, respectively, while the corresponding time constants are somewhat shorter in more polar ACN ($\tau_{CS} = 0.627$ ps and $\tau_{CR} = \sim 1.66$ ns).

τ_{CR} obtained from target analysis can be employed for explaining fluorescence emission profile and fluorescence lifetime decay of **Sp-PDI₂** in THF and ACN. In polar solvents, **Sp-PDI₂** display biexponential decay (Figure 3.9 and Table 3.4) and fluorescence lifetime of the first component ($\tau_{Fl}^1 = 1.63$ ns and 14.2 ns for ACN and THF, respectively) is comparable with the

charge recombination lifetime of **Sp-PDI₂** ($\tau_{CR} = 1.66$ ns and 12.20 ns for ACN and THF, respectively). Thus, the fluorescence emission of the first component can be assigned to emission originated from SB-CS state \rightarrow ground state (GS) transition. Analogous radiative emissions from SB-CS to GS transition are reported for DIPYR dimers, 9,9'-bianthryl, and 10,10'-dicyano-9,9'-bianthryl molecules.^{38,41} Since the locally excited state of **Sp-PDI₂** in polar solvents decays within few picoseconds (627 fs and 2.96 ps in ACN and THF, respectively), the absence of a short lifetime component in the TCSPC lifetime measurements suggest the non-emissive nature of locally excited state (Figure 3.9). The symmetry-breaking charge separation of **Sp-PDI₂** in polar solvents results from the asymmetric distribution of polarizabilities around the Greek cross-arranged molecule. The origin of emissive second species having $\tau_{Fl}^2 = 6.87$ ns and 6.80 ns for ACN and THF, respectively, can be explained by the presence of different microenvironments around the photoexcited molecules; i.e., photoexcited donor/acceptor dyad undergo charge separation in some environments and in another microenvironment, it may not undergo the charge separation.^{91,92}

The emissive nature of the charge-separated state of **Sp-PDI₂** in THF can further be substantiated by the picosecond time-resolved emission spectra (TRES) measurement, followed by global analysis (GA) of the kinetic traces (Figures 3.12 and 3.13, Appendix, section 3.7.10). The GA of time versus wavelength plots gave a DAS-based deconvolution of the temporal components in fluorescence emission. The DAS and population profile of **Sp-PDI₂** in THF reveal the presence

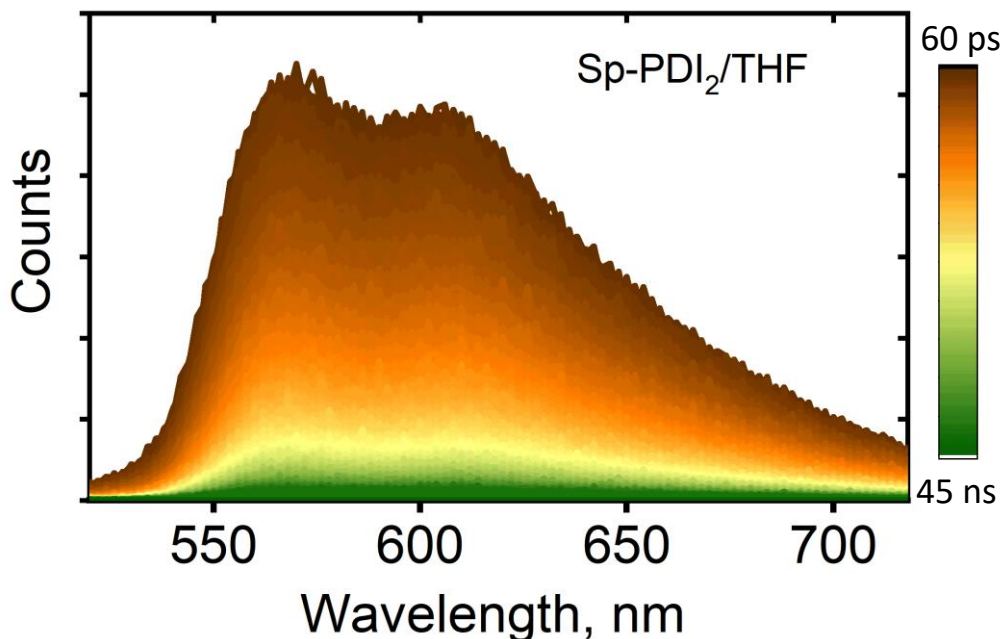


Figure 3.12: Time-resolved emission spectra (TRES, $\lambda_{ex} = 478$ nm) of **Sp-PDI₂** in THF at room temperature.

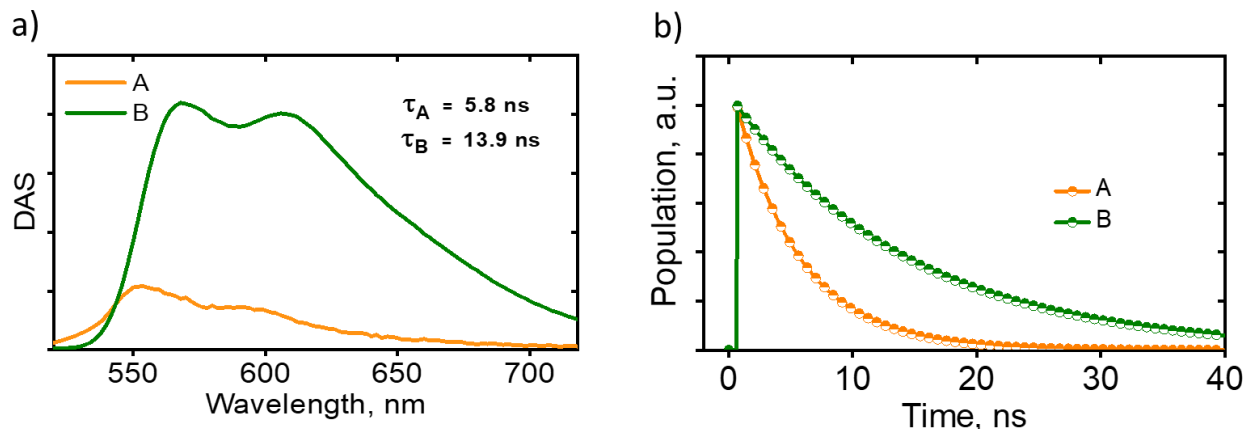


Figure 3.13: (a) Decay associated spectra (DAS) and (b) the relative population profiles of the Sp-PDI₂ in THF. The orange (A) and green (B) colored spectrum and decay profiles correspond to CS→GS emission and LE→GS emission, where microenvironmental does not favour CS, respectively.

of two independent emissive species ($\tau_A = 5.8$ ns and $\tau_B = 13.9$ ns). The spectral character of the long-lived species ($\tau_B = 13.9$ ns) is assigned to CS→GS emission which is red-shifted to LE→GS emission feature ($\tau_A = 5.8$ ns) in THF where the microenvironmental effect does not favour the charge separation.

3.2.6. Evaluation using electron transfer theory. Since the nature of Sp-PDI₂ excited states is different in the diverse solvent environment (Toluene, THF and ACN), discussion of SB-CS and CR dynamics in terms of classical Marcus theory is not straightforward.^{80,81} Though SB-CS is a part of the general electron transfer reaction and realizations of electron transfer theory can be embraced to describe the dynamics of SB-CS and CR.^{26,30,93} More quantitative analysis of CS and CR kinetics requires estimation of Marcus parameters (ΔG , λ , and V) and activation barrier (ΔG^\ddagger) of Sp-PDI₂. Driving forces (i.e., Gibbs free energy changes) of charge separation (ΔG_{CS}) and charge recombination (ΔG_{CR}) were estimated by the Weller approximation (Table 3.6 & Appendix, Section 3.7.8).⁸⁶ The Gibbs free-energy change of charge separation with negative values show that SB-CS is thermodynamically allowed for Sp-PDI₂ in both THF and ACN solvents, which agrees with the fluorescence quenching behavior. For Sp-PDI₂, in moderate polar aprotic solvent THF, the value of ΔG_{CS} is -0.16 eV, and in polar solvent acetonitrile, Gibbs free energy changes of SB-CS becomes more negative ($\Delta G_{CS} = -0.30$ eV). i.e., the driving forces for charge separation are more prominent with the increasing solvent polarity. In contrast, Gibbs free energy changes of CR in ACN ($\Delta G_{CR} = -1.94$ eV) is less negative than THF ($\Delta G_{CR} = -2.08$ eV); the driving forces for

charge recombination are smaller with the increasing solvent polarity. From the Marcus equation 5, it is evident that the reorganization energy (λ) plays a crucial role in charge separation kinetics. Reorganization energy is composed of the solvent shell reorganization energy (λ_s) and the solute molecular structure reorganization energy upon charge separation ($\lambda_{i(CS)}$) and charge recombination $\lambda_{i(CR)}$.⁹⁴⁻⁹⁶ Internal reorganization energy (λ_i) was calculated by employing constraint DFT for charge-separated state and DFT for ground-state calculation.⁹⁷

$$\lambda_{i(CS)} = E_{CS}(R_{eq}^{GS}) - E_{CS}(R_{eq}^{CS}) \quad (\text{Eq 6})$$

The first term is the energy calculated at the optimized ground state (GS) geometry in the CS redox state. While the second term is the energies of the CS at their equilibrium geometries. This calculation provides $\lambda_{i(CS)} = 0.20$ eV.

$$\lambda_{i(CR)} = E_{GS}(R_{eq}^{CS}) - E_{GS}(R_{eq}^{GS}) \quad (\text{Eq 7})$$

The first term corresponds to the energy calculated at the optimized CS geometry in the GS state and the second term is the energies of the GS at their equilibrium geometries. Calculated $\lambda_{i(CR)} = 0.44$ eV (Figure 3.14, Table 3.7 & Appendix, Section 3.7.11). The solvent reorganization energy is computed using the dielectric continuum theory and depends on the radii of the donor (r_D) and acceptor (r_A), the center-to-center distance (r_{DA}), and the optical (ϵ_{op}) and static (ϵ_s) dielectric constants of the solvent as given in Eq. 8:⁸³

$$\lambda_s = \frac{e^2}{4\pi\epsilon_0} \left(\frac{1}{2r_A} + \frac{1}{2r_D} - \frac{1}{r_{DA}} \right) \left(\frac{1}{\epsilon_{op}} - \frac{1}{\epsilon_s} \right) \quad (\text{Eq 8})$$

Sp-PDI₂ is a rigid organic molecule for which theoretically calculated low internal reorganization energy ($\lambda_{i(CS)} = 0.20$ eV and $\lambda_{i(CR)} = 0.44$ eV) is reasonable.³⁰ Thus, the total reorganization energy for the charge recombination (λ_{CR}) process would be 1.20 eV for ACN, which is approximately 0.74 eV lower than $-\Delta G_{CR}$. The charge recombination of **Sp-PDI₂** in ACN fall under the inverted region (where $-\Delta G_{CR} > \lambda_{CR}$). Whereas, in THF, total reorganization energy ($\lambda_{CR} = 0.81$ eV) is 1.27 eV lower than $-\Delta G_{CR}$ (2.08 eV), pushing the system into the deep inverted region than ACN (Table 3.6). This could rationalize the slow charge recombination of **Sp-PDI₂** in moderately polar THF ($\tau_{CR} = 12.20$ ns) than more polar solvent ACN ($\tau_{CR} = 1.66$ ns). Several research groups unequivocally established the presence of inverted region in charge recombination kinetics.⁹⁸⁻¹⁰¹ Theoretically calculated ΔG_{CR} for different solvents are in good agreement with the

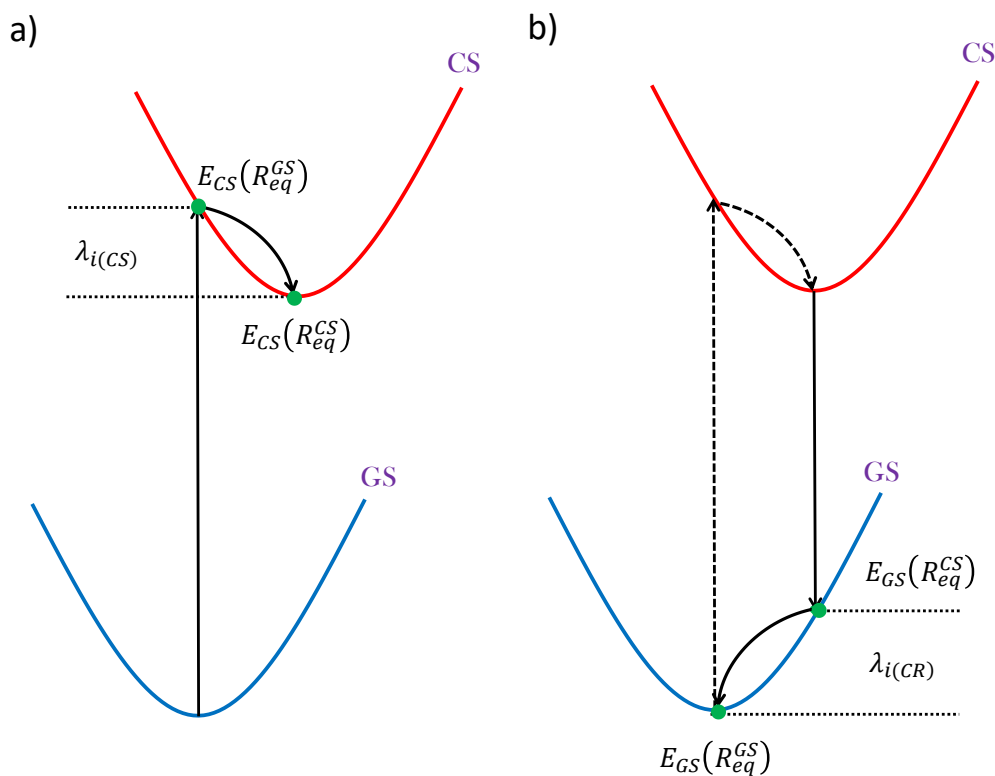


Figure 3.14: Schematic description of the internal reorganization energy calculation for (a) charge separation and (b) charge recombination processes.

Table 3.7: Computed energies of charge-separated state and ground state of **Sp-PDI₂** by employing CDFT and DFT.

| | Vacuum (eV) | Toluene (eV) | THF (eV) | ACN (eV) |
|-----------------------|-------------|--------------|-------------|-------------|
| $E_{CS}(R_{eq}^{GS})$ | -77690.7817 | - | - | - |
| $E_{CS}(R_{eq}^{CS})$ | -77690.9763 | -77692.1187 | -77692.7693 | -77693.0294 |
| $E_{GS}(R_{eq}^{CS})$ | -77693.7387 | - | - | - |
| $E_{GS}(R_{eq}^{GS})$ | -77694.1782 | -77694.8172 | -77695.1814 | -77695.3263 |

magnitude estimated by Weller analysis (Table 3.6 and Appendix, Section 3.7.11). Another factor controlling the k_{CS} and k_{CR} is the electronic coupling matrix element (V). This term is used to quantify the mixing of two states, or more intuitively, the electronic communication between the electron/hole donor and acceptor. Theoretically calculated charge transfer integrals provide an estimation of effective electronic coupling (V). The magnitude of hole transfer coupling ($t_h = -0.147$ eV) is significantly higher than that of electron transfer coupling ($t_e = -0.001$ eV), facilitating the excited state SB-CS of **Sp-PDI₂** in polar solvents via hole transfer (Figure 3.15).

The effective hole transfer electronic coupling ($V_{CS} = -0.147$ eV) can explain the origin of the significantly accelerated charge separation rate in THF and ACN. Calculated electronic coupling of CR ($V_{CR} = -0.018$ eV) is much lower than CS ($V_{CS} = -0.147$ eV), support the decelerated CR processes over CS of **Sp-PDI**₂ in THF and ACN. Since the $2V < \lambda$, SB-CS in **Sp-PDI**₂ falls under a weak coupling regime.¹⁰² A remarkable feature of Marcus theory is the relation between the kinetic barrier of charge transfer and the reaction thermodynamics. When the reaction is more exergonic in nature, the barrier for electron transfer reduces. The activation barrier for the SB-CS calculated by Eq. 9:

$$\Delta G^\ddagger = \frac{(\Delta G_{CS} + \lambda)^2}{4\lambda} \quad (\text{Eq 9})$$

The reorganization energy has a strong effect on the ΔG^\ddagger . The estimated activation barrier in different solvents is given in Table 3.6. The ultrafast charge separation of **Sp-PDI**₂ in ACN ($k_{CS} = 159.48 \times 10^{10} \text{ s}^{-1}$) than THF ($k_{CS} = 33.78 \times 10^{10} \text{ s}^{-1}$) solvent stem from the low activation energy for a nonadiabatic reaction. ΔG^\ddagger for the more polar ACN solvent has amounted to 0.11 eV, and moderate polar THF is 0.18 eV. Estimated Marcus parameters and activation barrier are given in Table 3.6. The potential energy surfaces are shown schematically in Figure 3.16.

Chemical redox titration experiments using cobaltocene and antimony pentachloride were performed to confirm the charge-separated state features of **Sp-PDI**₂ observed in the femtosecond transient absorption spectroscopy. Upon addition of reducing agent cobaltocene (CoCp₂), a decrease in the neutral-state absorption he neutral-state absorption by the appearance of new bands at ~ 715 nm (Figure 3.17). On the other hand, partial oxidation of **Sp-PDI**₂ with antimony pentachloride (SbCl₅) results in positive features at ~ 574 nm (Figure 3.18).

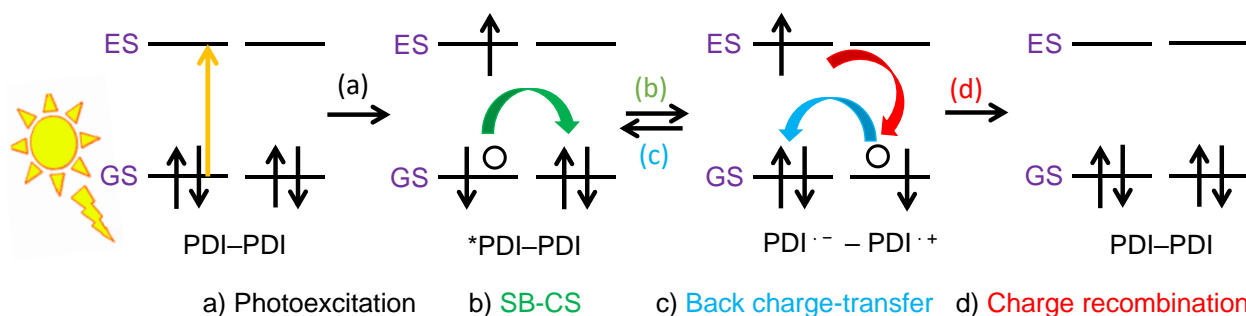


Figure 3.15: Mechanism of symmetry-breaking charge separation, back charge transfer and charge recombination of **Sp-PDI**₂ in polar solvents.

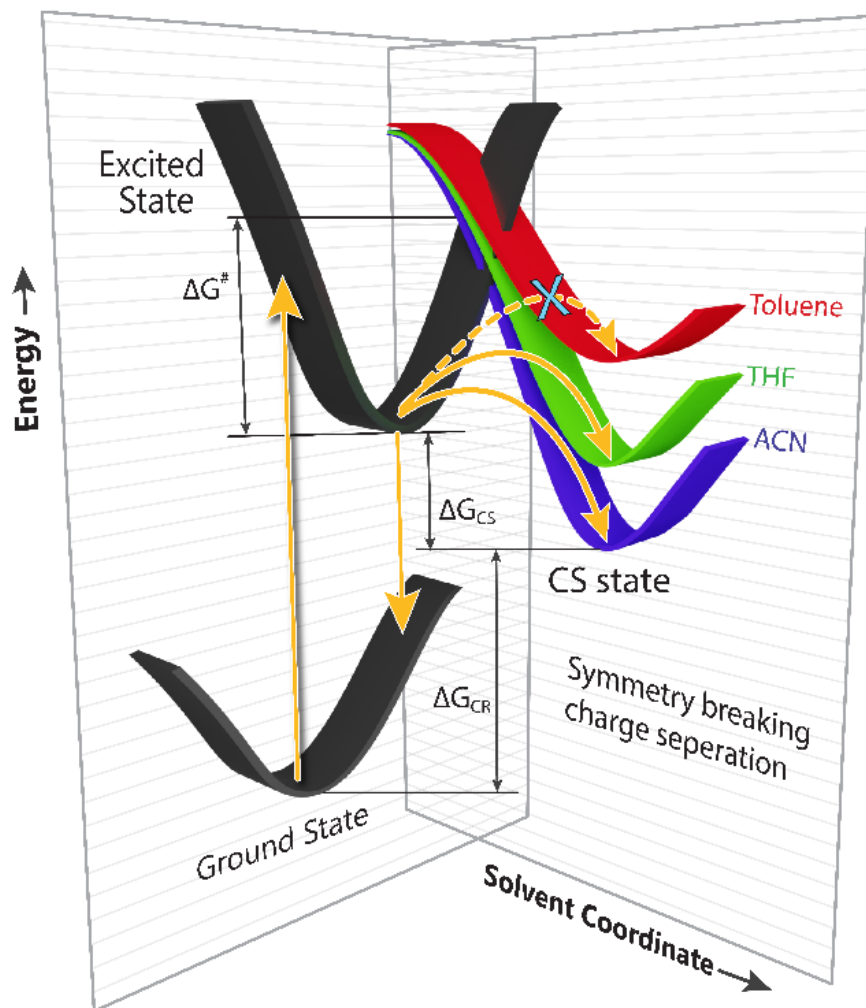


Figure 3.16: Schematic potential energy diagrams for SB-CS of *Sp*-PDI₂ in different solvents.

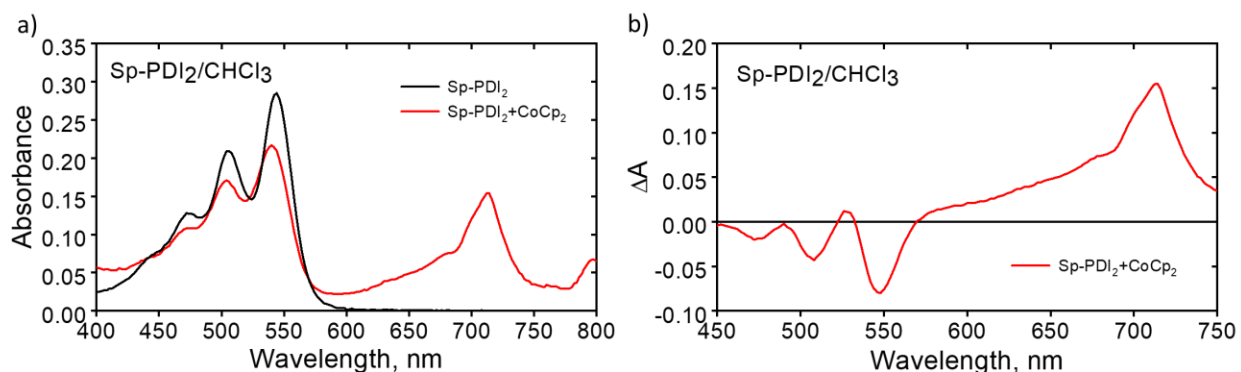


Figure 3.17: (a) UV-vis absorption changes of *Sp*-PDI₂ upon the addition of cobaltocene (CoCp₂) and (b) difference absorption spectra of *Sp*-PDI₂ obtained by subtracting ground state absorption from that of chemically reduced anions radicals.

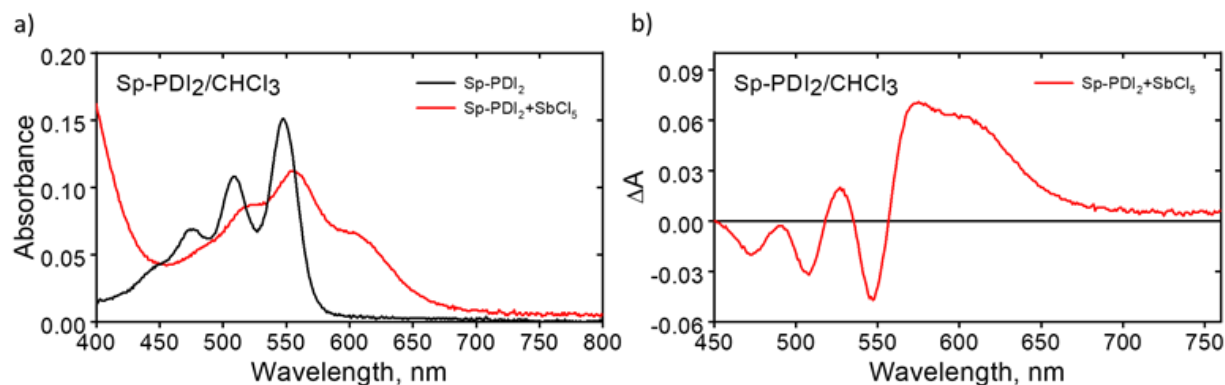


Figure 3.18: (a) UV-vis absorption changes of **Sp-PDI₂** upon the addition of antimony pentachloride (**SbCl₅**) and (b) difference absorption spectra of **Sp-PDI₂** obtained by subtracting ground state absorption from that of chemically oxidized cation radicals.

3.3. Conclusions

To conclude, we report the unequivocal evidence for the prolonged SB-CS state ($k_{CS}/k_{CR} = 2,647$ in ACN, Table A3.1) in null exciton coupled spiro-conjugated perylene diimide dimer (**Sp-PDI₂**). Single crystal structure examination of **Sp-PDI₂** confirms the Greek cross (+)-shaped molecule with two π -conjugated perylene diimide chromophores linked by an sp^3 hybridized carbon atom. The monomer-like steady-state absorption spectrum and photoexcited state properties of **Sp-PDI₂** in toluene advocate negligible exciton coupling among the orthogonally arranged **PDI** molecules. The interference between the theoretically calculated negligible contributions of J_{Coul} and J_{CT} resulted in null exciton coupling of an edge-to-edge arranged perylene diimide dimer possessing orthogonal orientation of transition dipoles. **Sp-PDI₂** impart selective hole-transfer coupling owing to the constructive and destructive interaction between the HOMOs and LUMOs of **PDI** molecules, respectively. The fragment-based excited state analysis of **Sp-PDI₂** exhibited localized Frenkel exciton in the first two degenerate excited states (S_1 and S_2) and charge transfer (CT) character in the degenerate S_3 and S_4 states. The rotational angle-dependent Coulombic and charge transfer coupling calculations provided significant values for lower rotational angles, manifesting impeccable evidence for the ability of Greek cross (+)-architecture in lowering excitonic coupling. The solvent-dependent fsTA measurement of **Sp-PDI₂** demonstrated the SB-CS in polar solvents. The charge separation reactions of **Sp-PDI₂** in polar solvents are in the Marcus normal region ($\Delta G_{CS} < \lambda$) and k_{CS} values follow the expected quadratic dependence on ΔG_{CS} . i.e., k_{CS} increases with increment in CS driving forces. The lower activation

barrier (ΔG^\ddagger) for CS in ACN than THF further supported the $k_{CS}(\text{ACN}) > k_{CS}(\text{THF})$. The CR reactions of **Sp-PDI**₂ lie far into the Marcus inverted region ($\Delta G_{CS} > \lambda$). Solvent-dependent studies demonstrate the rate of CR in polar solvents following the order ACN > THF, CR becoming slower at higher driving forces. The current work integrates two fundamental concepts of photophysics, null exciton splitting and symmetry-breaking charge separation, as an innovative strategy to generate an efficient long-lived charge-separated state. Greek cross (+)-arrangement of **Sp-PDI**₂ can be considered as an ideal system that highlights the explicit correlation between the relative orientation of the chromophoric system and its orbital interaction in dictating complex excited-state dynamics. Further efforts are underway to achieve a more prolonged charge-separated state in near-orthogonal arranged **PDI** dimers.

3.4. Experimental Section

3.4.1. Synthesis of PDI

The compound was synthesized according to the literature procedure.¹⁰³ 5 g PTCDA was accurately weighed out in a 250 ml round bottom flask. Then about 125 g of Imidazole was also added and mixed well. Then the temperature was raised from room temperature to 140° C. When imidazole melts entirely and forms a homogeneous solution with PTCDA, 2.5 equivalents (3.7 g) of 3-amino pentane were added slowly under the N₂ atmosphere. Continue this reflux for about 6 hr. After the completion of the reaction, wash with a mixture of 1N HCl and Ethanol (40:60). Filter the precipitated product and purified using column chromatography using DCM: PET ether. Yield is noted (5.75 g, 85 % yield).

M.p. > 300 °C.

¹H NMR (500 MHz, CDCl₃, ppm) δ = 8.66 (d, J = 8.0 Hz, 4H), 8.60 (d, J = 8.1 Hz, 4H), 5.11 – 5.03 (m, 2H), 2.34 – 2.17 (m, 4H), 1.95 (m, 4H), 0.93 (t, 12H).

¹³C NMR (500 MHz, CDCl₃, ppm) δ = 134.7, 131.7, 129.8, 126.7, 123.7, 123.2, 57.9, 25.2, 11.6.

HRMS (APCI) m/z calculated for C₃₄H₃₁N₂O₄ [(M+H)⁺]: 531.2283; found 531.2271.

IR (KBr): cm⁻¹ = 2966, 2934, 2876, 1699, 1659, 1595, 1578, 1456, 1434, 1406, 1339, 1252, 1198, 1090, 852, 809, 746.

3.4.2. Synthesis of Br-PDI

The compound was synthesized according to the literature procedure.¹⁰³ To a solution of PDI (2.00 g, 3.77 mmol) in CH₂Cl₂ (100 mL) Br₂ solution was added (9.97 mL, 0.19 mol) and the mixture was stirred at room temperature for 1-4 days. The excess bromine was removed by air bubbling, and the solvent was removed under vacuum. The crude product was purified by a silica gel column chromatography, using hexane: CHCl₃=6:4 as eluent. Yield is noted (1.2 g, 52 % yield).

M.p. > 300 °C.

¹H NMR (500 MHz, CDCl₃, ppm) δ = 9.80 (d, J = 8.0 Hz, 1H), 8.93 (s, J = 8.1 Hz, 1H), 8.75 – 8.67 (m, 3H), 8.63 (dd, 2H), 5.13 – 4.97 (m, 2H), 2.40 – 2.13 (m, 4H), 2.03 – 1.83 (m, 4H), 0.94 (t, J = 7.5 Hz, 6H), 0.91 (t, 6H).

¹³C NMR (500 MHz, CDCl₃, ppm) δ = 139.4, 134.1, 133.8, 133.8, 131.3, 130.8, 129.2, 129.0, 128.4, 128.3, 127.3, 124.0, 123.2, 121.2, 58.1, 58.0, 29.9, 25.2, 25.2, 11.5, 11.5.

HRMS (APCI) m/z calculated for C₃₄H₃₀BrN₂O₄ [(M+H)⁺]; 609.1388; found 609.1367.

IR (KBr): cm^{-1} = 2966, 2932, 2876, 1703, 1661, 1593, 1469.76, 1402, 1335, 1246, 1201, 1162, 1088, 810, 746.

3.4.3. Synthesis of Sp-PDI₂

The compound was synthesized according to the literature procedure.¹⁰⁴ To a 10 mL Schlenk-type tube equipped with a magnetic stir bar was charged with Br-PDI (200 mg, 1 mmol), Pd(OAc)₂ (30 mg), KHCO₃ (0.526 g, 18 mmol), KOAc (0.88 g, 9 mmol), the mixture was deoxygenated with argon for 10 min followed by adding CH₂Br₂ (0.8 mg, 14 mmol), i-PrOH (0.1 ml, 4 mmol), and then 1,4-dioxane (7 mL) as the mixed solvent. The Schlenk-type tube was backfilled with argon and sealed, then heated to 75 °C with vigorous stirring for 10 hr. The reaction mixture was cooled to ambient temperature, poured into water (500 mL) and stirred for another 2 hr. The resulting red solid was collected by vacuum filtration. The filter cake was washed neutral with distilled water, afterwards dried in vacuum at 60 °C. The solids were further purified by column chromatography on silica gel eluted with CH₂Cl₂/petroleum ether (1:1) to afford Sp-PDI₂ as red solids. Yield is noted (110 mg, 31 % yield).

M.p. > 300 °C.

¹H NMR (500MHz, CDCl₃, 300 K), δ = 8.82-8.80 (d, J = 8.81 Hz, 4H), 8.75-8.73 (d, J = 8.74 Hz 4H), 8.10 (s, 4H), 5.12-5.04 (m, 4H), 2.20-1.84 (m, 8H), 0.91-0.86 (m, 24H).

¹³C NMR (500 MHz, CDCl₃, 300 K): δ = 141.79, 138.67, 135.04, 129.65, 124.95, 75.40, 57.19, 31.59, 24.99, 22.66, 14.12, 11.29.

HRMS (APCI) m/z calculated for C₆₉H₅₇N₄O₈ [(M+H)⁺]: 1069.4176; found, 1069.4156.

IR (KBr): cm^{-1} = 2961, 2930, 2874, 1695, 1661, 1603, 1574, 1435, 1394, 1308, 1246, 1196, 1070, 814, 744.

3.4.4. Synthesis of Cy-PDI

The compound was synthesized according to the literature procedure.⁶⁰ To a 10 mL Schlenk flask containing a magnetic stirring bar was added Br-PDI (233 mg, 0.30 mmol), Mo(CO)₆ (237 mg, 0.90 mmol) and Pd(dppf)Cl₂ (22 mg, 0.03 mmol). The flask was filled with argon, and then toluene (6 mL) and DBU (0.5 mL) were added to the tube. The mixture was heated at 60 °C for 12 hr, and then was cooled to room temperature. The crude solution was concentrated in vacuo. The residue

was purified by column chromatography on silica gel (petroleum ether/CH₂Cl₂, 2:1 v/v) to give the product Cy-PDI as a blue solid. Yield is noted (95 mg, 46 % yield).

M.p. > 300 °C.

¹H NMR (400 MHz, CDCl₃) δ = 8.56-8.53 (m, 4H), 8.30-8.28 (d, J = 8.3 Hz, 2H), 5.08-5.03 (m, 2H), 2.29-2.20 (m, 4H), 1.99-1.90 (m, 4H), 0.94-0.97 (m, 12H).

¹³C NMR (500 MHz, CDCl₃) δ = 189.5, 144.7, 135.1, 132.7, 129.2, 125.5, 123.2, 125.6, 58.5, 57.9, 29.7, 24.9, 18.4, 14. 13,11.3.

HRMS (APCI) m/z calculated for C₃₅H₃₁N₂O₅ [(M+H)⁺]: 557.2076; found, 557.2061.

IR (KBr): cm⁻¹ = 2963, 2926, 2876, 1738, 1703, 1661, 1603, 1574, 1456, 1394, 1312, 1236, 1099, 812, 733.

3.4.5. Synthesis of Ref-PDI

The compound was synthesized according to the literature procedure.⁶⁰ To a 25 mL two-neck round-bottom flask fitted with a condenser and a dropping funnel containing a magnetic stirring bar was added iodine (254 mg, 1.0 mmol). The flask was filled with argon, and then hypophosphorous acid (50% aq., 1 mL, 11.2 mmol) and acetic acid 0.5 mL were added to the flask. The mixture was heated to reflux for 0.5 hr, and then a solution of Cy-PDI (150 mg, 0.2 mmol) in 5 mL acetic acid was added over a period of 0.5 h. The mixture was then stirred and refluxed for 1 hr and then was cooled to room temperature. The mixture was diluted with water and extracted with DCM. The organic phase was dried over Na₂SO₄, filtered, and evaporated. The residue was purified by column chromatography on silica gel (petroleum ether/CH₂Cl₂, 2:1 v/v) to give product Ref-PDI as a red solid. Yield is noted (125 mg, 86 % yield).

M.p. > 300 °C.

¹H NMR (400 MHz, CDCl₃) δ = 8.89 (s, 2H), 8.73-8.72 (d, J = 8.72 Hz, 2H), 8.61-8.59 (d, J = 8.61 Hz 2H), 5.20-5.14 (m, 2H), 4.39 (s, 2H), 2.37-2.28 (m, 4H), 2.04-1.96 (m, 4H), 0.99-0.96 (m, 12H).

¹³C NMR (100 MHz, CDCl₃) δ = 164.9, 139.6, 139.0, 133.9, 127.4, 122.7, 121.9, 56.7, 39.9, 28.7, 24.13, 10.4.

HRMS (APCI) m/z calculated for C₃₅H₃₁N₂O₄ [(M+H)⁺]: 543.2283; found, 543.2271. **IR** (KBr): cm⁻¹ = 2965, 2934, 2876, 1695, 1655, 1601, 1570, 1472, 1420, 1394, 1313, 1269, 1240, 1192, 1078, 797, 752.

3.5. Additional Tables

Table A3.1: A comparison of the rate of charge separation and charge recombination in multi-chromophoric perylene diimide derivatives in literature.

| Contributed by | Molecule | Solvent | $1/k_{CS}$ | $1/k_{CR}$ | k_{CS}/k_{CR} |
|--|---|-------------------|------------|------------|-----------------|
| Present work | Sp-PDI₂ | Acetonitrile | 627 fs | 1.66 ns | 2647 |
| Wasielewski and co-workers | cof-5PDI₂ J. Am. Chem. Soc. 2002 , 124, 8530 | Toluene | 520 fs | 222 ps | 427 |
| Wasielewski, Young, and co-workers | m-PDI₂ J. Phys. Chem. C 2020 , 124, 10408–10419 | Chloroform | 33.2 ps | 7.3 ns | 220 |
| Xia, Wang, and co-workers | p-BDNP J. Am. Chem. Soc. 2019 , 141, 12789–12796 | Tetrahydrofuran | 12.4 ps | 1.94 ns | 156 |
| Kim, Würthner, and co-workers | rPBI-CP J. Phys. Chem. Lett. 2019 , 10, 1919–1927 | benzonitrile | 23 ps | 2.5 ns | 109 |
| Xia, Tang, Wan, and co-workers | PM-PDI₄ J. Phys. Chem. Lett. 2020 , 11, 10329–10339 | Dimethylformamide | 44.7 ps | 4.8 ns | 107 |
| Wasielewski, Stoddart, Würthner and co-workers | PDI-Δ J. Am. Chem. Soc. 2015 , 137, 13236 | Chloroform | 12.0 ps | 1.12 ns | 93 |
| Wasielewski and co-workers | H-tpPDI J. Am. Chem. Soc. 2020 , 142, 18243–18250 | Tin film | 17.6 ps | 1.04 ns | 59 |
| Würthner, Wasielewski, and co-workers | Cy-PBI Chem. Sci., 2016 , 7, 5428 | Chloroform | 161 ps | 8.9 ns | 55 |
| Adams and co-workers | Do J. Am. Chem. Soc. 2004 , 126, 16126–16133 | Dimethylformamide | 59 ps | 2.26 ns | 38 |
| Würthner, Kim, and co-workers | PBI-CP J. Am. Chem. Soc. 2016 , 138, 29, 9029–9032 | Chloroform | 36 ps | 1.1 ns | 31 |
| Yu, Goodson and co-workers | PDI dimer Chem. Mater. 2018 , 30, 4263–4276 | Chloroform | na | na | na |

Table A3.2: Crystallographic data and refinement parameters for *Sp-PDI*₂ crystal.

| Parameters | |
|--|---|
| Formula | C ₆₉ H ₅₆ N ₄ O ₈ |
| Formula wt. | 1069.17 |
| dimens, mm ³ | 0.250 x 0.100 x 0.080 |
| crystal system | Monoclinic |
| space group, Z | P 21/c |
| a, Å | 22.316(8) |
| b, Å | 34.530(11) |
| c, Å | 18.305(6) |
| α, deg | 90 |
| β, deg | 95.384(10) |
| γ, deg | 90 |
| V, Å ³ | 14043(8) |
| temp, K | 150(2) |
| d _{calcd} , mg/m ³ | 1.011 |
| no. of reflections collected | 185287 |
| no. of unique reflections | 24724 |
| no. of parameters | 1460 |
| R1, wR2 (I > 2s(I)) | R1 = 0.1160, wR2 = 0.2849 |
| R1, wR2 (all data) | R1 = 0.3107, wR2 = 0.4365 |
| goodness of fit | 0.971 |
| CCDC Deposition number | 2086823 |

Table A3.3: Oscillator strength for different transitions of *Ref-PDI* and *Sp-PDI*₂ calculated at TD-ωB97XD/ def2svp level of theory.

| Molecule | Excitation | | Energy (eV) | Wavelength (nm) | Main Transition Orbital |
|----------------|----------------|---------------------|-------------|-----------------|-------------------------|
| | State | Oscillator Strength | | | |
| Ref-PDI | S ₁ | 0.7273 | 2.6761 | 463.31 | HOMO → LUMO |
| | S ₂ | 0.0043 | 3.8191 | 324.64 | HOMO-3 → LUMO |
| | S ₃ | 0.0691 | 3.8556 | 321.57 | HOMO-7 → LUMO+3 |

| | | | | | |
|---------------------------|----------------|--------|--------|--------|--|
| | S ₄ | 0.0006 | 3.9163 | 316.58 | HOMO-1 → LUMO HOMO-8 → LUMO HOMO-2 → LUMO HOMO → LUMO+2 |
| | S ₁ | 0.5937 | 2.7790 | 446.15 | HOMO → LUMO |
| | S ₂ | 0.5937 | 2.7790 | 446.15 | HOMO-1 → LUMO+1 HOMO → LUMO+1 |
| Sp-PDI₂ | S ₃ | 0.0565 | 3.5879 | 345.56 | HOMO-1 → LUMO HOMO → LUMO HOMO → LUMO+4 |
| | S ₄ | 0.0565 | 3.5879 | 345.56 | HOMO-2 → LUMO+1 HOMO-1 → LUMO+1 HOMO → LUMO+5 |

Table A3.4: Rotation angle (θ) dependent hole and electron coupling integral of PDI dimer.

| Rotational angle (θ) Degree | Hole transfer coupling (t_h) | | Electron transfer coupling (t_e) | |
|--|----------------------------------|------------------|--------------------------------------|------------------|
| | eV | cm ⁻¹ | eV | cm ⁻¹ |
| 90 | -0.1470 | -1185.634 | -0.0010 | -8.0655401 |
| 85 | -0.1464 | -1180.7951 | 0.0253 | 204.0582 |
| 80 | -0.1438 | -1159.8247 | 0.0510 | 411.3425 |
| 75 | -0.1391 | -1121.9166 | 0.0744 | 600.0762 |
| 70 | -0.1320 | -1064.6513 | 0.0942 | 759.7739 |
| 65 | -0.1222 | -985.609 | 0.1083 | 873.498 |
| 60 | -0.1091 | -879.95043 | 0.1146 | 924.3109 |
| 55 | -0.0922 | -743.6428 | 0.1095 | 883.1766 |
| 50 | -0.0707 | -570.23369 | 0.08989 | 725.0114 |
| 45 | -0.0443 | -357.30343 | 0.0519 | 418.6015 |
| 40 | 0.0126 | 101.6258 | -0.0075 | -60.491551 |

Table A3.5: Rotation angle (θ) dependent Coulombic and charge-transfer coupling of PDI dimer.

| Rotational angle (θ) degree | Coulombic coupling (J_{coul}) | | Charge-transfer coupling (J_{CT}) | |
|---|-----------------------------------|------------------|---------------------------------------|------------------|
| | eV | cm ⁻¹ | eV | cm ⁻¹ |
| 90 | 0.000415 | 3.344 | -0.000346 | -2.792 |
| 85 | -0.009535 | -76.906 | 0.008466 | 68.284 |
| 80 | -0.019485 | -157.160 | 0.016754 | 135.131 |
| 75 | -0.029435 | -237.369 | 0.023661 | 190.837 |

Chapter 3: Null Exciton Coupled Chromophoric Dimer Exhibits Symmetry-Breaking Charge Separation

| | | | | |
|----|-----------|----------|-----------|---------|
| 70 | -0.039380 | -317.621 | 0.028435 | 229.346 |
| 65 | -0.049334 | -397.873 | 0.030251 | 243.988 |
| 60 | -0.059387 | -479.013 | 0.028570 | 230.435 |
| 55 | -0.069337 | -559.265 | 0.027304 | 220.219 |
| 50 | -0.079183 | -638.630 | 0.018946 | 152.814 |
| 45 | -0.088822 | -716.382 | 0.008382 | 67.608 |
| 40 | -0.098461 | 794.590 | -0.000761 | -6.137 |

3.6. Additional Figures

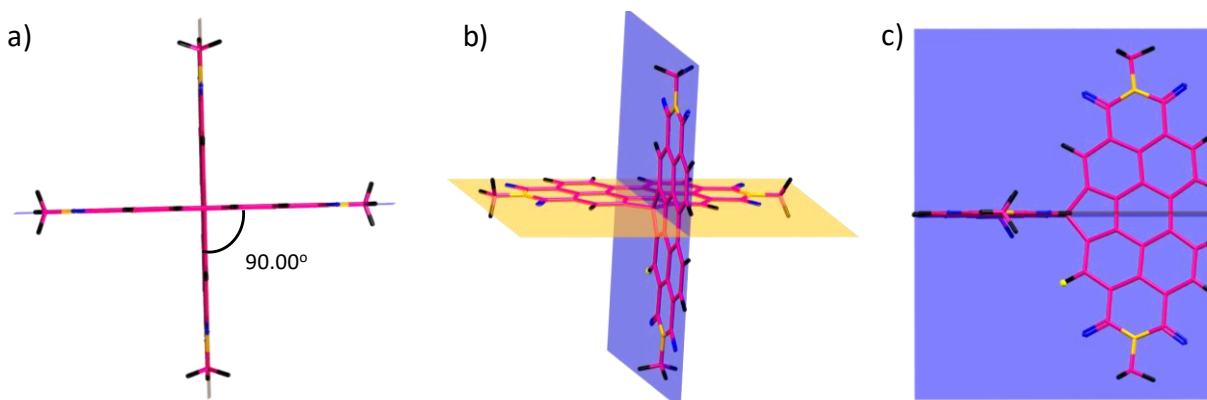


Figure A3.1: Optimized structure of *Sp*-PDI₂ with the rotational angle (θ) of 90°.

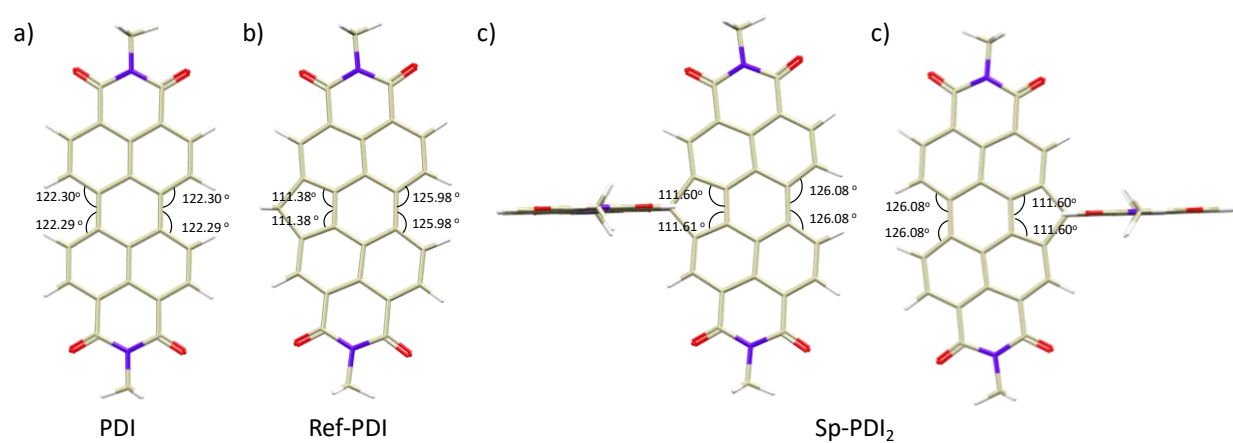


Figure A3.2: Optimized structure of *PDI*, *Ref-PDI*, and *Sp-PDI*₂ showing selected dihedral angles.

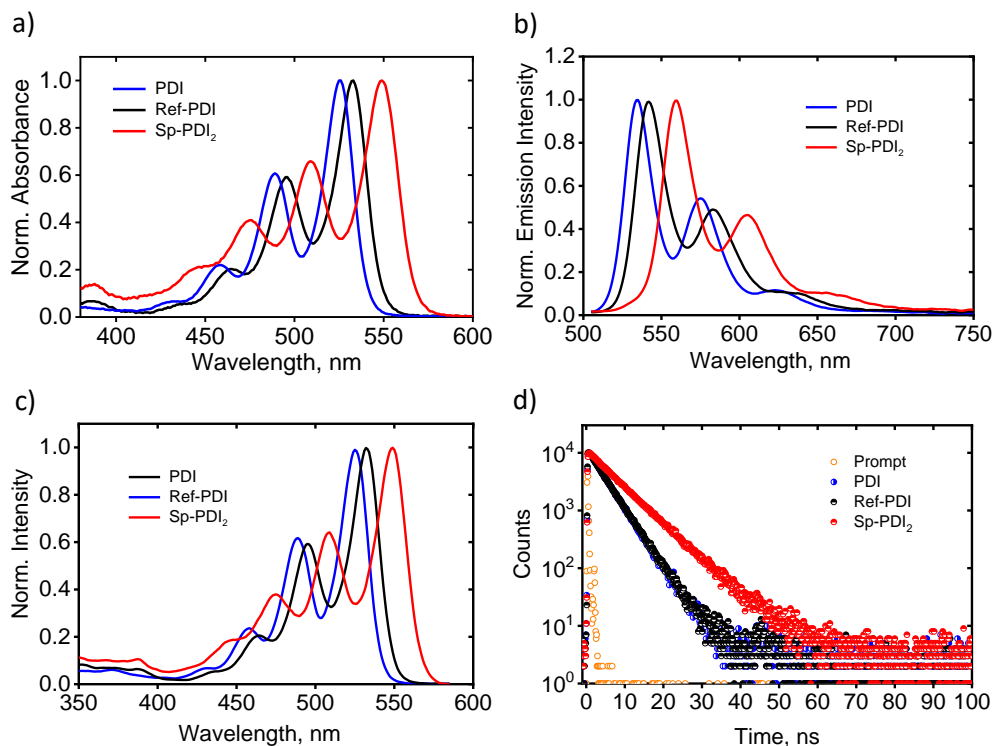


Figure A3.3: (a) Absorption, (b) fluorescence emission, (c) fluorescence excitation spectra and (d) fluorescence decay profile of **PDI**, **Ref-PDI** and **Sp-PDI₂** in toluene.

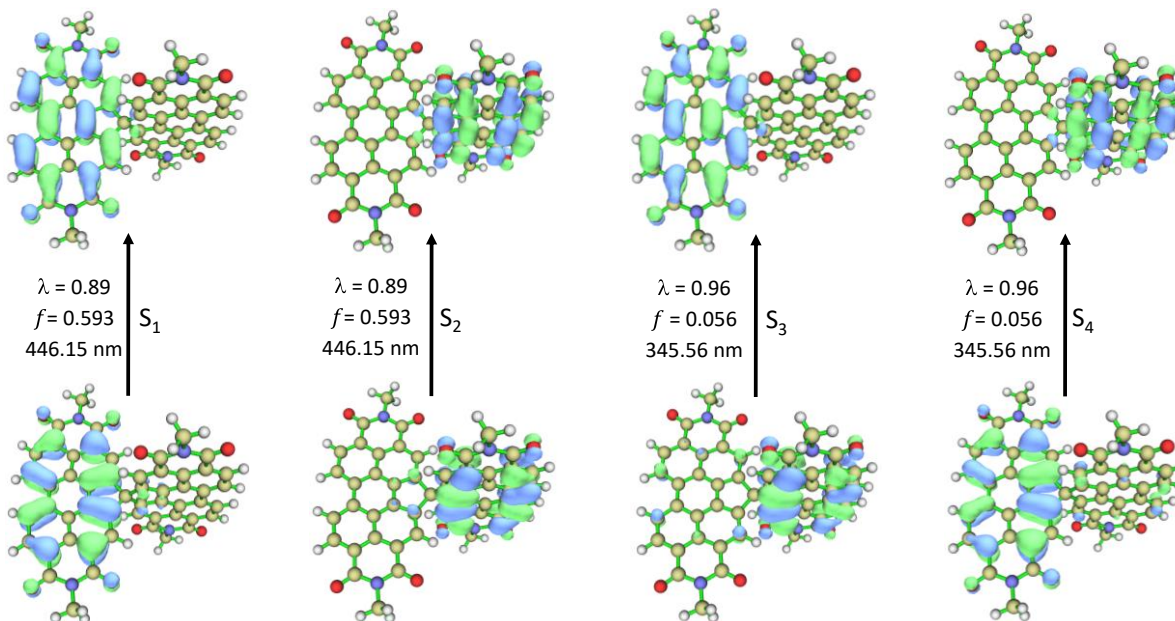


Figure A3.4: TD-DFT calculated natural transition orbitals (NTO) of the four lowest excited singlet states of **Sp-PDI₂**. The corresponding weightage of NTO (λ), oscillator strength (f) and wavelength are mentioned.

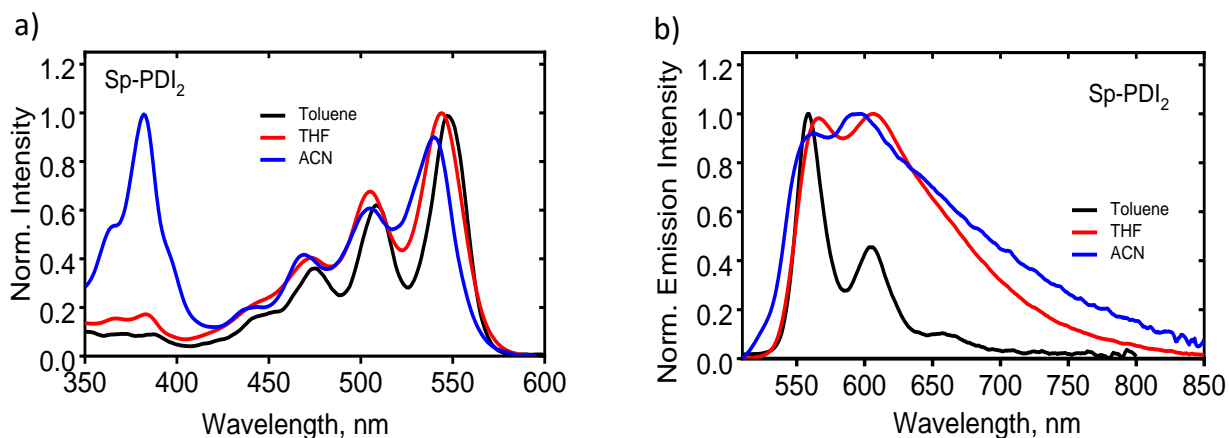


Figure A3.5: Normalized (a) excitation and (b) emission spectra for *Sp-PDI*₂ in different solvents.

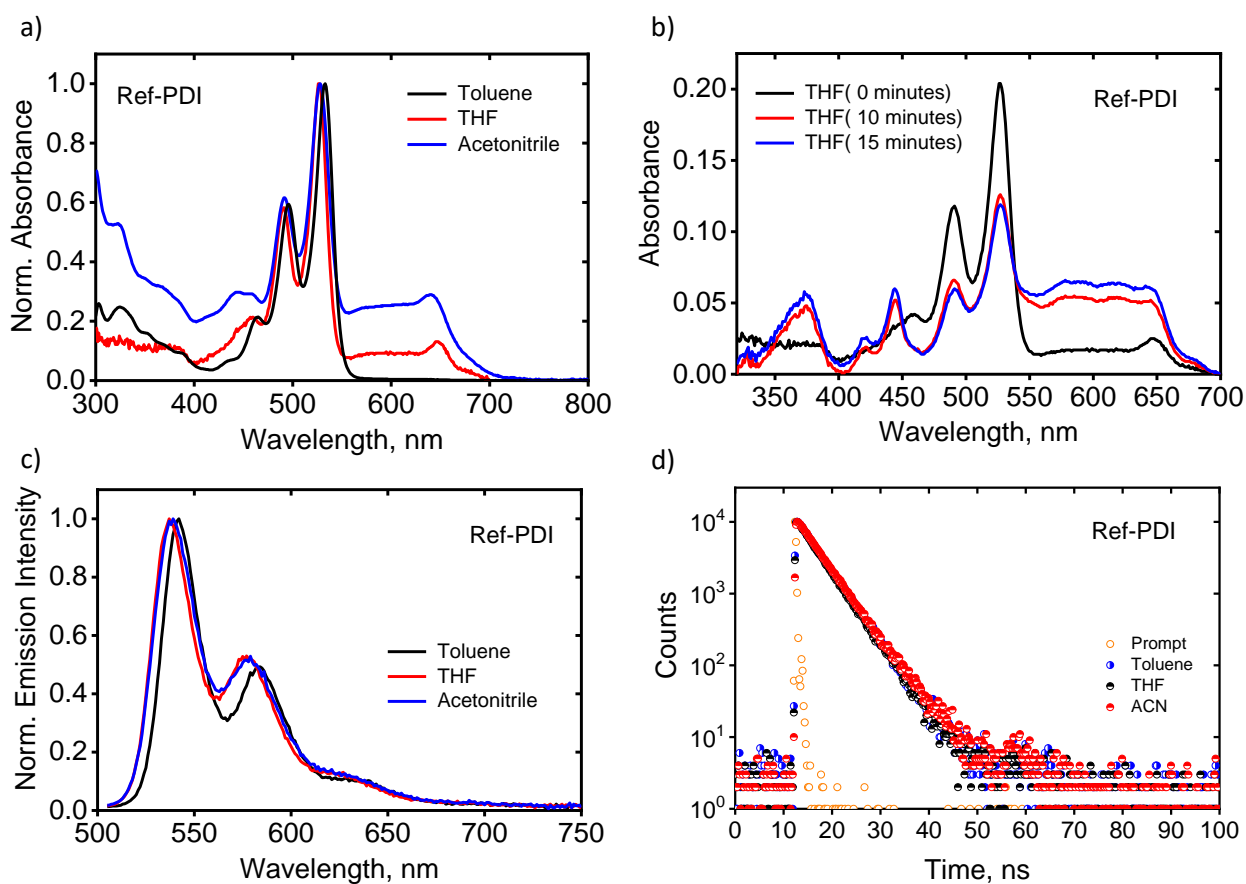


Figure A3.6: (a) Absorption spectra of *Ref-PDI* in different solvents, (b) time-dependent absorption spectra of *Ref-PDI* in THF, (c) fluorescence emission spectra of *Ref-PDI* in different solvents recorded by exciting at 490 nm, (d) and fluorescence decay profile of *Ref-PDI* in different solvents.

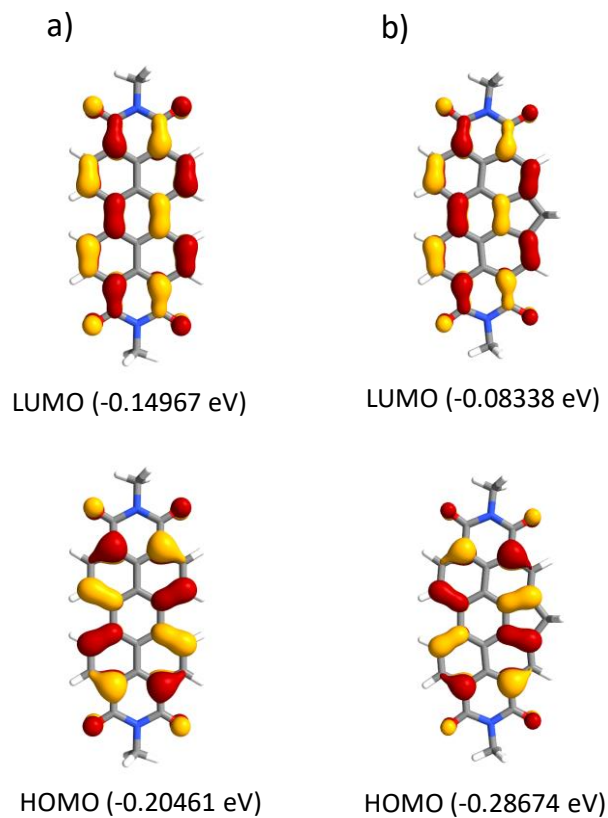


Figure A3.7: Frontier molecular orbitals (HOMO and LUMO) of (a) *PDI* and (b) *Ref-PDI* (isovalue 0.02).

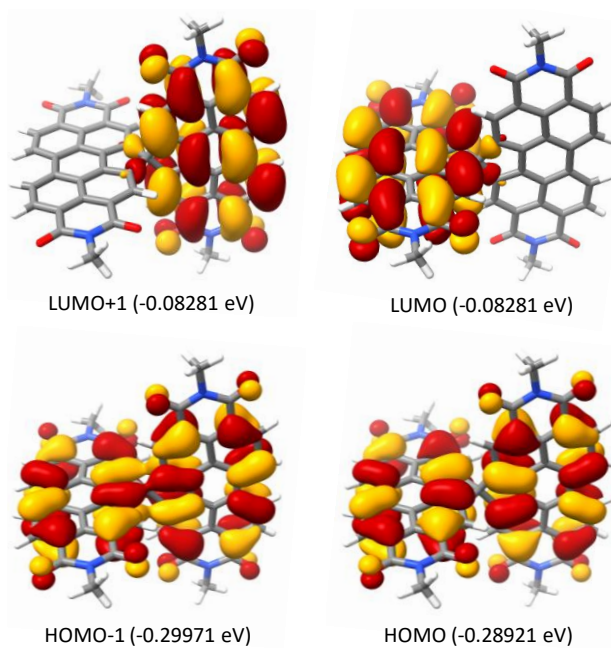


Figure A3.8: Frontier molecular orbitals of *Sp-PDI₂* (Degenerated HOMO-1, HOMO, and Nearly-degenerated LUMO, LUMO+1).

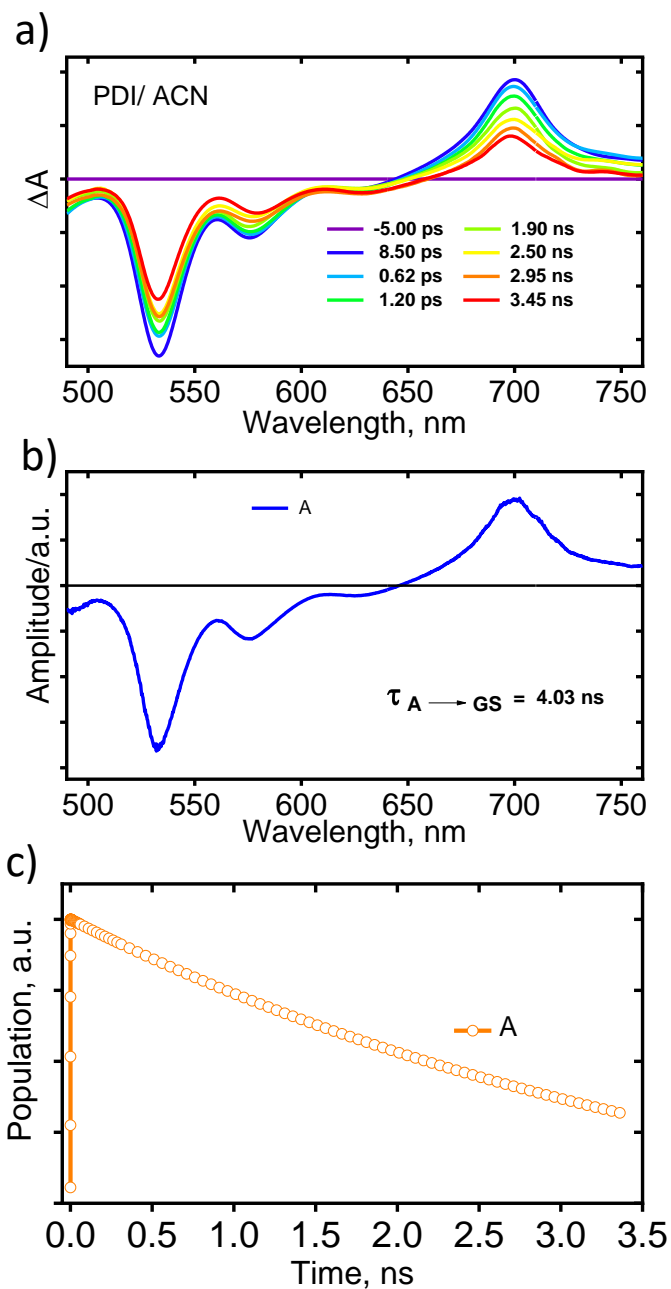


Figure A3.9: (a) Femtosecond transient absorption spectra ($\lambda_{\text{ex}}=440 \text{ nm}$), (b) Evolution associated spectra, and (c) the relative population profiles of the excited states of **PDI** in ACN.

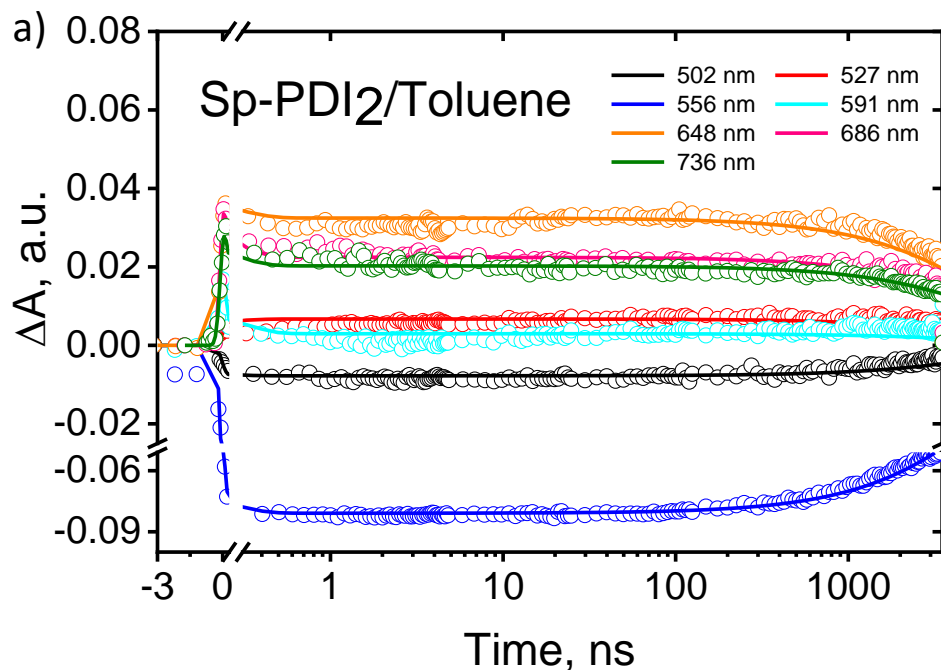


Figure A3.10: Target analysis fits for selected fsTA wavelengths of *Sp-PDI*₂ ($\lambda_{\text{ex}} = 440 \text{ nm}$) in toluene to $A \rightarrow \text{GS}$ (ground state) kinetic model. Fits are shown as solid lines.

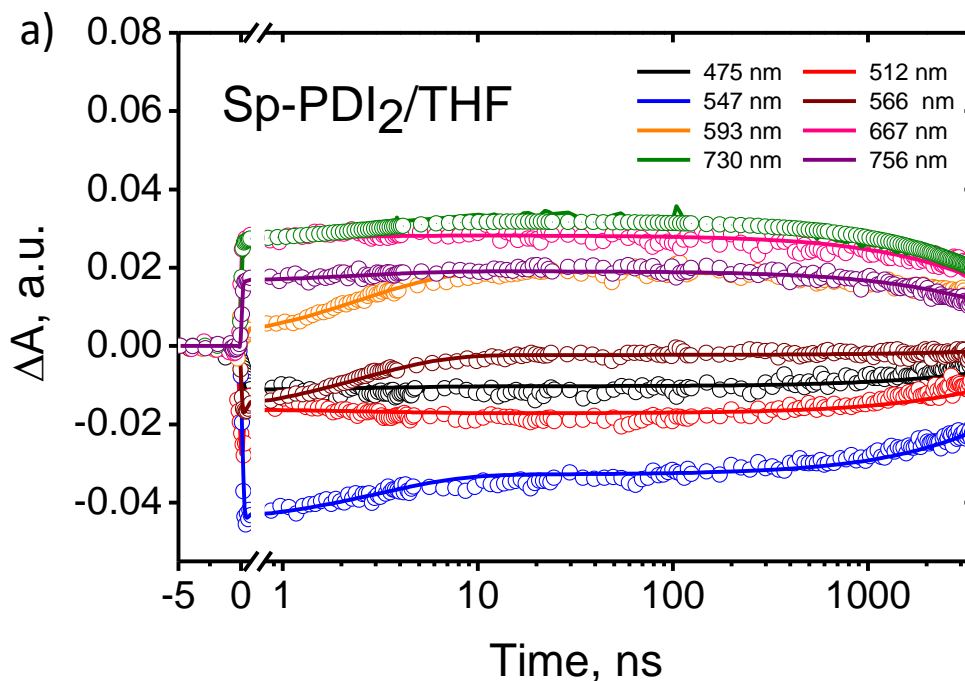


Figure A3.11: Target analysis fits for selected fsTA wavelengths of *Sp-PDI*₂ ($\lambda_{\text{ex}} = 440 \text{ nm}$) in THF to $A \rightleftharpoons B \rightarrow \text{GS}$ (ground state) kinetic model. Fits are shown as solid lines.

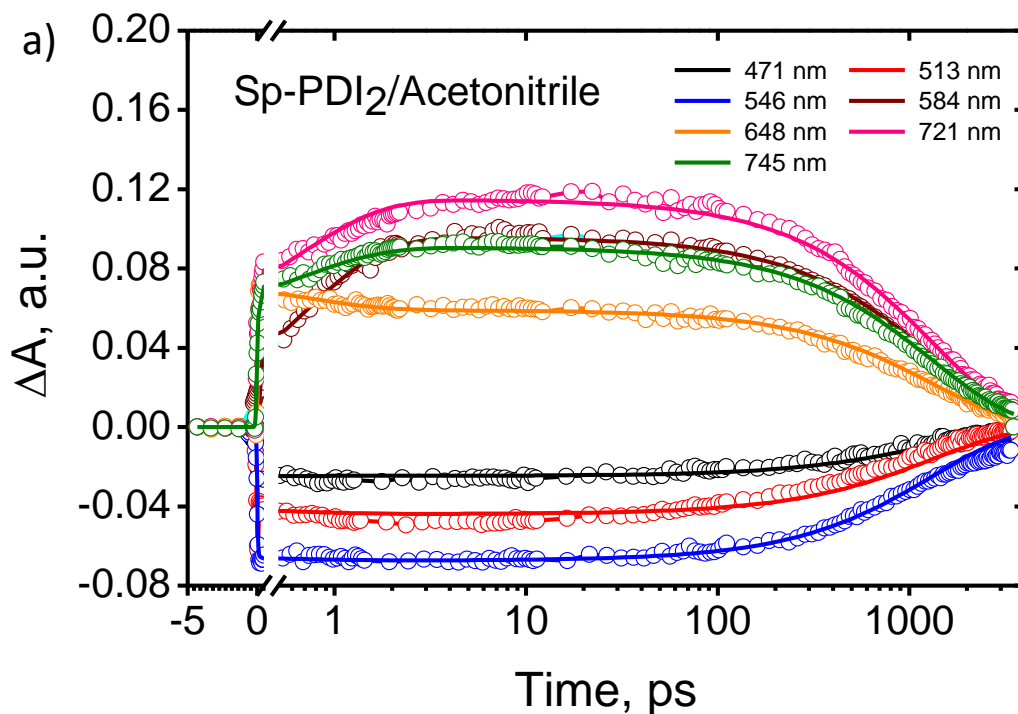


Figure A3.12: Target analysis fits for selected fsTA wavelengths of *Sp-PDI*₂ ($\lambda_{ex} = 440$ nm) in ACN to $A \rightarrow B \rightarrow GS$ (ground state) kinetic model. Fits are shown as solid lines

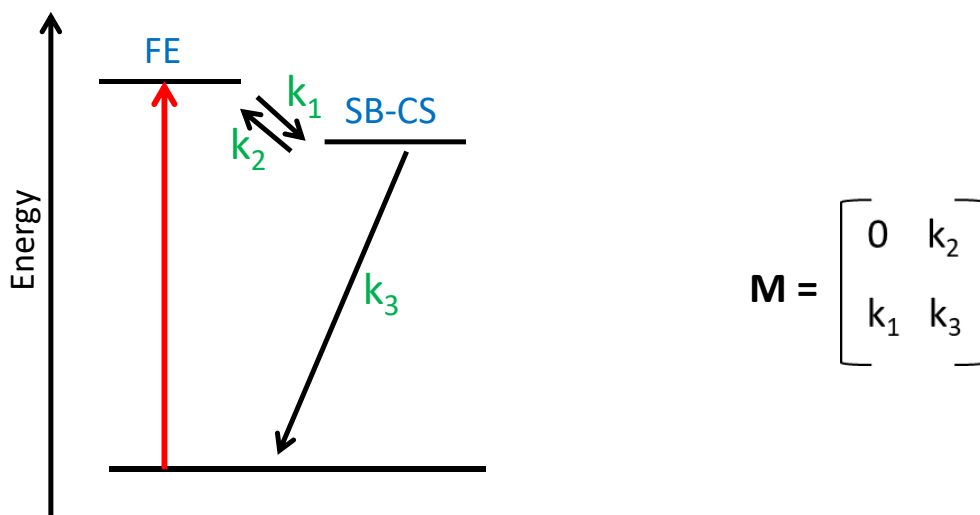


Figure A3.13. Energy level diagram describing equilibrium between FE and SB-CS states and rate matrix.

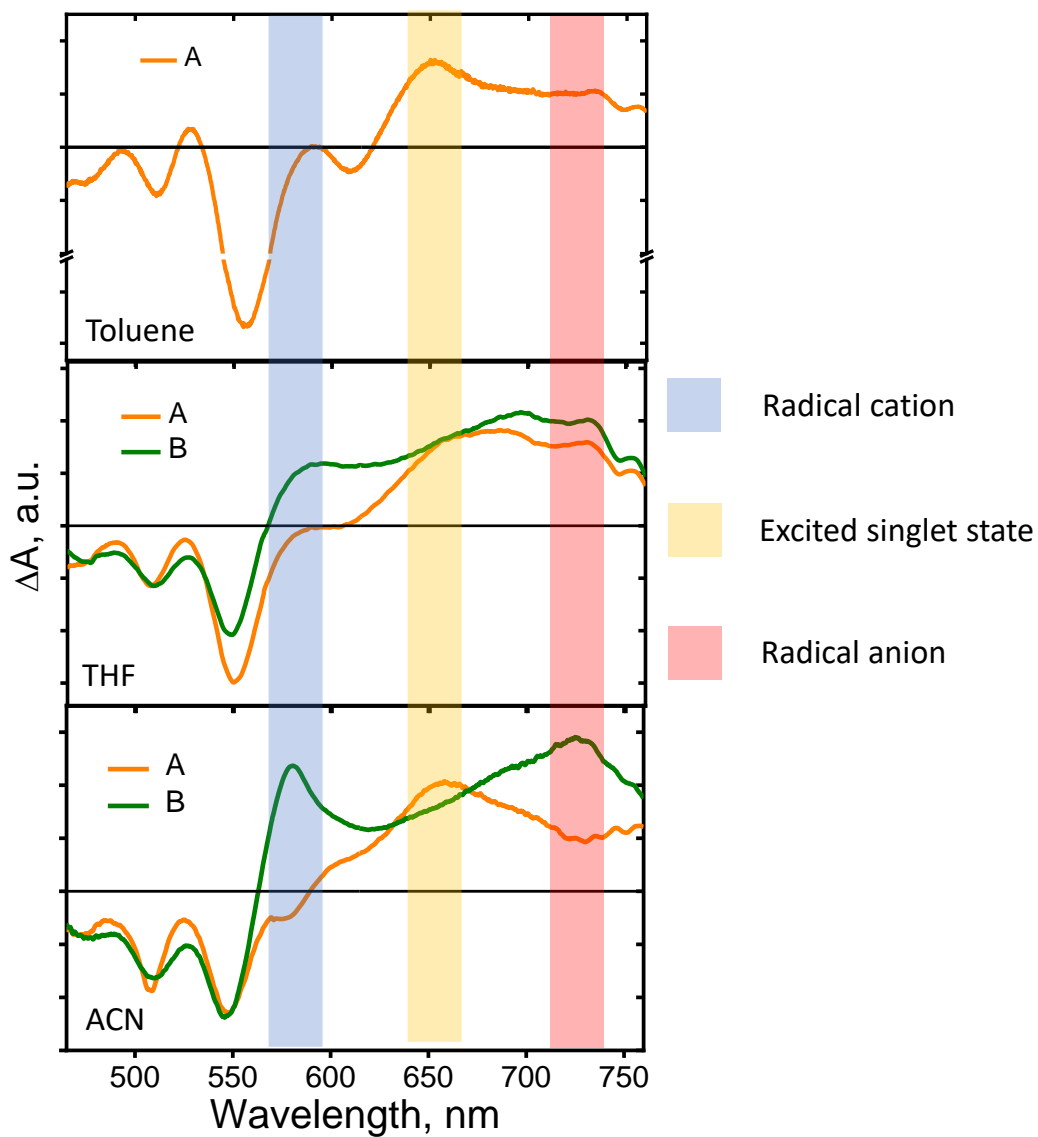


Figure A3.14: Species associated spectra (SAS) of *Sp*-PDI₂ in toluene (top), THF (middle) and ACN (bottom) resulted from target analysis.

3.7. Appendix

3.7.1: Materials and Methods

Similar to that discussed in section 2.7.1 (Chapter 2)

Lifetime measurements were carried out in an IBH picosecond time-correlated single-photon counting (TCSPC) system. The pulse width of the excitation ($\lambda_{exci} = 439$ nm) source is determined to be <100 ps, and 455 nm long-pass filter (Newport) was used to minimize the scatter arising from the laser source.

3.7.2: X-ray Crystallography

Similar to that discussed in section 2.7.2 (Chapter 2)

3.7.3: Computational Analysis

All the calculations are carried out in Gaussian 16 employing the ω B97XD functional and def2svp basis set at the DFT level of theory in vacuum unless stated otherwise. Vertical excitation energies and oscillator strengths were calculated employing time-dependent DFT (TD-DFT) at the ω B97XD functional and def2svp level of theory. The frontier molecular orbitals (FMO) of **Ref-PDI** and **Sp-PDI₂** were obtained from the generated cube files of energy calculations. In order to compute long-range Coulombic coupling, Transition Charge from Electrostatic Potential (TrEsp) method¹⁰⁵ available Multiwfn version 3.7.8 program is utilized.¹⁰⁶ Hole-electron analysis and natural transition orbitals (NTO) generation were carried out using Multiwfn version 3.7.8. Electron and hole transfer coupling values were calculated by employing the CATNIP Tool version 1.9.9.¹⁰⁷ Both multiwfn and CATNIP use post-processed Gaussian 16 output files for the respective analyses.¹⁰⁵ The transition dipoles for **Sp-PDI₂** were calculated and plotted using Multiwfn and VMD, respectively. 3-pentane alkane chain of **Sp-PDI₂** and **Ref-PDI** were replaced with methane group during the computation calculation in order to reduce the computational cost.

3.7.4: Calculation of the Exciton Coupling Energies from UV-vis Absorption Spectra

The ratio of the intensities of the 0–0 and 0–1 absorption band of a dimer aggregate exhibiting exciton vibrational coupling in the perturbative limit can be calculated by Eq.10:^{108,109}

$$\frac{I_A^{0-0}}{I_A^{1-0}} = \frac{1}{\lambda^2} \left[\frac{1 - G(0; \lambda^2) e^{-\lambda^2 J / \omega_0}}{1 - G(1; \lambda^2) e^{-\lambda^2 J / \omega_0}} \right]^2 \quad (\text{Eq 10})$$

where λ^2 is the Huang-Rhys factor, J represents the exciton coupling energy and ω_0 stands for the vibrational frequency. The vibrational function $G(\nu_t; \lambda^2)$ is defined as

$$G(\nu_t; \lambda^2) = \sum_{\substack{u=0,1,\dots \\ (u \neq \nu_t)}} \frac{\lambda^{2u}}{u!(u-\nu_t)!} \quad \nu_t = 0,1,2, \dots \quad (\text{Eq 11})$$

The Huang-Rhys factor can be determined from the UV-vis absorption spectrum of the monomeric dye, i.e., **Ref-PDI**. For this, the absorption spectrum was fitted by Gaussian functions assuming a one-effective mode model. We took the absorption spectrum in the range of 17000 to 24000 cm^{-1} . The Huang-Rhys factor was then calculated from the height of the 0–1 and 0–0 Gaussian peaks:¹⁰⁸

$$\lambda^2 = \frac{I_{\text{Gaussian}}^{0-1}}{I_{\text{Gaussian}}^{0-0}} \quad (\text{Eq 12})$$

With this, we obtain $\lambda^2 = 0.625$, in good agreement with previously reported values for PDI dyes.²⁵ The frequency ω_0 was set to 1398 cm^{-1} and equals the energy difference between the maxima of the Gaussian functions of the 0–0 and 0–1 absorption bands used for the fitting of the absorption spectrum. This value fits well with the C–C stretching mode of the perylene core of $\sim 1400 \text{ cm}^{-1}$.

3.7.5: TheoDORE Analysis

The excitations of orthogonally arranged spiro-conjugated perylenediimide dimer at the DFT optimized structure were analyzed using TheoDORE.^{110,111} We study dimer systems, where each PDI monomer and spiro carbon is considered as a fragment (Figure 3.6). The parameters used to investigate the excited state characteristics are participation ratio (PR), mean position (POS) of initial orbital (hole) and final orbital (electron), and charge transfer character (CT). The magnitude of PR relates to the number of fragments participating in the excitation; hence, in our investigation, the PR ranges from 1 to 2. POS provides the mean position of hole and electron for a particular excitation. Charge transfer states and delocalized Frenkel states show POS = 1.5. If the Frenkel state is localized on monomer A, then POS = 1, and if localized on monomer B, POS = 2, for a dimer AB. Finally, CT is related to the total weight of configurations where initial and final orbitals are situated on different fragments. A CT value of 1 denotes the presence of a charge-separated state, and CT = 0 refers to Frenkel states. Further, electron-hole correlation plots were generated for analyzing the excitonic character for the perylenediimide dimer systems. If the shade is present only in the off-diagonal parts, the excitonic character is Frenkel. Diagonal shades refer to a CT state.

3.7.6: Femtosecond transient absorption (fsTA) measurement

A Spectra-Physics Mai Tai SP mode-locked laser (86 MHz, 800 nm) was used as a seed for a Spectra-Physics Spitfire ace regenerative amplifier (1 kHz, 5.5 mJ). A fraction of the amplified output was used to produce a 440 nm pump pulse by TOPAS. A residual pulse of 800 nm was sent through an optical delay line inside an ExciPro pump-probe spectrometer to produce a white light continuum by employing a sapphire crystal. The white light continuum was split into two, and the streams were used as a probe and reference pulses. The femtosecond transient absorption spectra of the sample were recorded using a dual diode array detector, having a 200 nm detection window and 3.5 ns optical delay. Sample solutions were prepared in a rotating cuvette with a 1.2 mm path length. Determination of an appropriate instrument response function (IRF) is needed for accurate deconvolution of recorded transient absorption data. The IRF was determined by a solvent (10% benzene in methanol) two-photon absorption and was found to be ~110 fs at about 530 nm. A neutral density filter (80%) was used for controlling the incident flux on the sample. fsTA measurement of **Sp-PDI₂** in different solvents and PDI in ACN was recorded by photoexciting the sample with 440 nm, 200 nJ, and 100 fs pulses to moderate singlet–singlet annihilation that often arises in multi-chromophoric assemblies.¹¹² The observed kinetic components were laser intensity-independent, ruling out the chance of singlet–singlet annihilation.

3.7.7: Global Analysis

Target analyses of the fsTA spectra were performed using the Glotaran software.¹¹³ The procedure evaluates the instrument time response function and the group velocity dispersion of the white continuum and allows one to compute decay time constants and dispersion-compensated spectra. All the wavelengths were analyzed in target analysis concurrently, employing a target model to give species-associated spectra (SAS). The SAS indicates that the evolution of the spectra in time does not necessarily denote a real physical/chemical species. SAS designates the spectral changes that occur with their associated time constants.

3.7.8: Weller Analysis

The change in free energy for the charge separation and charge recombination (ΔG) were estimated employing the followed relations¹¹⁴ based on the Born dielectric continuum model.

$$\Delta G_{CS} = e[E_{ox} - E_{red}] - E_{00} + C + S \quad (\text{Eq 13})$$

$$C = \frac{-e^2}{4\pi\epsilon_0} \left(\frac{1}{\epsilon_S r_{AD}} \right) \quad (\text{Eq 14})$$

$$S = \frac{e^2}{8\pi\epsilon_0} \left(\frac{1}{r_D} + \frac{1}{r_A} \right) \left(\frac{1}{\epsilon_S} - \frac{1}{\epsilon_{opt}} \right) \quad (\text{Eq 15})$$

$$\Delta G_{CR} = -(E_{00} + \Delta G_{CS}) \quad (\text{Eq 16})$$

Where e is the charge of the electron, E_{ox} and E_{red} are the oxidation and reduction potentials, respectively, ϵ_0 is the permittivity of free space, ϵ_S is the static dielectric constant of the solvent, and ϵ_{SP} is the static dielectric constant of the solvent used for electrochemical measurements, r_{AD} is the donor-acceptor distance, r_D and r_A are the cation and anion hard-sphere radii, respectively (were approximated as $\frac{r_{AD}}{2}$) and E_{00} is the energy of the excited singlet (donor) state. At finite distances, the Coulombic attraction energy between(C) the radical ion-is given by a point-charge model as $\left(\frac{1}{\epsilon_S r_{AD}} \right)$.

3.7.9: Electrochemistry

Cyclic voltammograms and differential pulse voltammograms were acquired on CH instruments, inc electrochemical workstation at room temperature, employing a three-electrode single-compartment cell: glassy carbon electrode as working electrode, a Pt wire as the counter electrode, and silver wire as the reference electrode. Working and reference electrodes were polished on a felt pad with 0.05 μm Al_2O_3 suspension, sonicated in acetone for about 3 minutes, and dried before each experiment; the Pt wire was flame-cleaned. The supporting electrolyte, tetrabutylammonium hexafluorophosphate (TBAPF), was previously dried under vacuum, dichloromethane was degassed prior to use, and all measurements were performed under a nitrogen atmosphere. The concentration of TBAPF used was typically 100 times of the analyte. Calibration of the instrument was performed using the ferrocene/ferrocenium (Fc/Fc^+) redox couple as an external standard and measured under the same condition before and after the measurement of samples. $E_{\text{Fc}/\text{Fc}^+}$ is the potential of Fc/Fc^+ vs. Ag (0.496 V, as measured by cyclic voltammetry). The energy level of Fc/Fc^+ was assumed to be -4.8 eV with respect to vacuum.¹¹⁵ HOMO and LUMO energies were calculated using the following equation.

$$E_{HOMO} = -(E'_{ox} + 4.8 - E_{\text{Fc}/\text{Fc}^+}) \text{ eV} \quad (\text{Eq 17})$$

$$E_{LUMO} = -(E'_{red} + 4.8 - E_{\text{Fc}/\text{Fc}^+}) \text{ eV} \quad (\text{Eq 18})$$

respectively, where E'_{ox} and E'_{red} are the experimentally measured oxidation and reduction potentials vs. Ag.

The electrochemical energy gap (E_g) is estimated as follows:

$$E_g = (E_{LUMO} - E_{HOMO}) \text{ eV} \quad (\text{Eq 19})$$

Where E_{LUMO} and E_{HOMO} are the corresponding to LUMO and HOMO energy levels.

3.7.10: Time-Resolved Emission Spectra (TRES) Analysis:

Time-resolved emission spectral (TRES) measurements followed by global analysis (GA) of the kinetic traces (at all wavelengths) were performed in an IBH picosecond time-correlated single-photon counting (TCSPC) system and glotaran¹¹³ software, respectively. The singular value decomposition (SVD) followed by the GA of the time vs. wavelength plots furnished a decay associated spectra (DAS) based deconvolution of the temporal components in the fluorescence emission. Time-resolved emission spectral (TRES) investigation of **Sp-PDI₂** in THF was carried out by exciting at 478 nm (DD-470L; pulse width <60 ps) and the fluorescence decay profiles were collected in the spectral range of 515-713 nm (2 nm interval). Decay at each wavelength was collected with an identical acquisition time and the emission observed immediately after the laser excitation pulse was assigned as zero time.

3.7.11: Calculation of Marcus Parameters

We are interested in two charge transfer rates: excited PDI to the symmetry-broken charge-separated state, $k_{A \rightarrow SB-CS}$ and SB-CS to the ground state, $k_{SB-CS \rightarrow GS}$. Hence, three electronic states are of particular interest: the excited PDI singlet state, $^1\text{PDI}^* - \text{PDI}$; the charge transfer state, $\text{PDI}^{\cdot+} - \text{PDI}^-$ and the ground state $\text{PDI} - \text{PDI}$. The rate of SB-CS and CR depends on three Marcus parameters. The first Marcus parameter is the Gibbs free energy change (ΔG); the other Marcus parameters are total reorganization energy (λ) and electronic coupling (V_{DA}).

Driving force charge recombination; The reaction free energies between the ground state (GS) and the charge-separated state (CSS) were estimated using density functional theory (DFT). The GS geometry was optimized with conventional DFT, and the CSS geometry was optimized with constrained DFT¹¹⁶ (CDFT) implemented in Qchem 5.0.1.¹¹⁷ For the calculations, the geometries were optimized in the gas phase using the B3LYP functional and the 6-31G** basis set, followed by the solvation free energy using the conductor-like polarizable continuum model (C-PCM). The

reaction-free energy for CR was determined to be the difference in free energies between the product GS and the reactant CSS.

$$\Delta G_{CR} = E_{CS}(R_{eq}^{CS}) - E_{GS}(R_{eq}^{GS}) \quad (\text{Eq 20})$$

The first term is the energy calculated at the optimized charge-separated state (CS) geometry in the CS redox state using CDFT. While the second term is the energies of the ground state (GS) at their equilibrium geometries. The resulting reaction-free energies are given in Table 3.7.

Internal reorganization energy (λ_i); The total reorganization energy λ is the sum of the inner-sphere (solute) and outer-sphere (solvent) reorganization energies. The inner-sphere reorganization energy for CS and CR were calculated using CDFT for the CSS and standard DFT for the GS using the B3LYP functional and the 6-31G** basis set implemented in Qchem 5.0.1.¹¹⁷

Electronic coupling; The electronic coupling matrix element for charge separation and charge recombination were calculated using the energy splitting in dimer method implemented in the Catnip tool. The coupling strength between the orbitals involved in the hole/electron transfer processes is estimated by using HOMOs (for hole transfer calculations) or the LUMOs (for electron transfer). At the same time, charge recombination electronic coupling is calculated by the transfer integral between HOMO of the first PDI and LUMO of the second PDI. Input files were generated in Gaussian 16 suite.¹⁰⁵

3.8 REFERENCES

- (1) Jelley, E. E. Spectral Absorption and Fluorescence of Dyes in the Molecular State. *Nature*. **1936**, 1009–1010.
- (2) Wasielewski, M. R. Photoinduced Electron Transfer in Supramolecular Systems for Artificial Photosynthesis. *Chem. Rev.* **1992**, *92*, 435–461.
- (3) Gust, D.; Moore, T. A.; Moore, A. L. Solar Fuels via Artificial Photosynthesis. *Acc. Chem. Res.* **2009**, *42*, 1890–1898.
- (4) Frischmann, P. D.; Mahata, K.; Würthner, F. Powering the Future of Molecular Artificial Photosynthesis with Light-Harvesting Metallo-supramolecular Dye Assemblies. *Chem. Soc. Rev.* **2013**, *42*, 1847–1870.
- (5) Ward, M. D. Photo-Induced Electron and Energy Transfer in Non-Covalently Bonded Supramolecular Assemblies. *Chem. Soc. Rev.* **1997**, *26*, 365–375.
- (6) Würthner, F.; Kaiser, T. E.; Saha-Möller, C. R. J-Aggregates: From Serendipitous Discovery to Supramolecular Engineering of Functional Dye Materials. *Angew. Chem., Int. Ed.* **2011**, *50*, 3376–3410.
- (7) Proppe, A. H.; Li, Y. C.; Aspuru-Guzik, A.; Berlinguette, C. P.; Chang, C. J.; Cogdell, R.; Doyle, A. G.; Flick, J.; Gabor, N. M.; van Grondelle, R.; Hammes-Schiffer, S.; Jaffer, S. A.; Kelley, S. O.; Leclerc, M.; Leo, K.; Mallouk, T. E.; Narang, P.; Schlau-Cohen, G. S.; Scholes, G. D.; Vojvodic, A.; Yam, V. W. W.; Yang, J. Y.; Sargent, E. H. Bioinspiration in Light Harvesting and Catalysis. *Nat. Rev. Mater.* **2020**, 828–846.
- (8) El-Khouly, M. E.; El-Mohsnawy, E.; Fukuzumi, S. Solar Energy Conversion: From Natural to Artificial Photosynthesis. *Journal of Photochemistry and Photobiology C: Photochemistry Reviews*. **2017**, 36–83.
- (9) Fukuzumi, S.; Ohkubo, K.; D'souza, F.; Sessler, J. L. Supramolecular Electron Transfer by Anion Binding. *Chem. Commun.* **2012**, *48*, 9801–9815.
- (10) Weil, T.; Vosch, T.; Hofkens, J.; Peneva, K.; Müllen, K. The Rylene Colorant Family-Tailored Nanoemitters for Photonics Research and Applications. *Angew. Chem., Int. Ed.* **2010**, *49*, 9068–9093.
- (11) Luechai, A.; Gasiorowski, J.; Petsom, A.; Neugebauer, H.; Sariciftci, N. S.; Thamyongkit, P. Photosensitizing Porphyrin-Triazine Compound for Bulk Heterojunction Solar Cells. *J. Mater. Chem.* **2012**, *22*, 23030–23037.
- (12) Davydov, A. S. The Theory of Molecular Excitons. *Sov. Phys. Uspekhi* **1964**, *7*, 145–178.
- (13) Kasha, M. Energy Transfer Mechanisms and The Molecular Exciton Model for Molecular Aggregate. *Radiat. Res.* **1963**, *20*, 55–70.
- (14) McRae, E. G.; Kasha, M. The Molecular Exciton Model. In *Physical Processes in Radiation Biology*; **1964** 23–42.
- (15) Kasha, M.; Rawls, H. R.; El-Bayoumi, M. A. The Exciton Model In Molecular Spectroscopy. *Pure Appl. Chem.* **1965**, *11*, 371–392.
- (16) Eisfeld, A.; Briggs, J. S. The J- and H-Bands of Organic Dye Aggregates. *Chem. Phys.* **2006**, *324*, 376–384.
- (17) Spano, F. C.; Silva, C. H- and J-Aggregate Behavior in Polymeric Semiconductors. *Annu.*

- Rev. Phys. Chem.* **2014**, *65*, 477–500.
- (18) Felter, K. M.; Grozema, F. C. Singlet Fission in Crystalline Organic Materials: Recent Insights and Future Directions. *J. Phys. Chem. Lett.* **2019**, *10*, 7208–7214.
- (19) Jean-Luc Brédas; David Beljonne; Veaceslav Coropceanu; Jérôme Cornil. Charge-Transfer and Energy-Transfer Processes in π -Conjugated Oligomers and Polymers: A Molecular Picture. *Chem. Rev.* **2004**, *104*, 4971–5003.
- (20) Hestand, N. J.; Spano, F. C. Expanded Theory of H- and J-Molecular Aggregates: The Effects of Vibronic Coupling and Intermolecular Charge Transfer. *Chem. Rev.* **2018**, 7069–7163.
- (21) Deutsch, M.; Wirsing, S.; Kaiser, D.; Fink, R. F.; Tegeder, P.; Engels, B. Geometry Relaxation-Mediated Localization and Delocalization of Excitons in Organic Semiconductors: A Quantum Chemical Study. *J. Chem. Phys.* **2020**, *153*, 224104.
- (22) Cornil, J.; Dos Santos, D. A.; Beljonne, D.; Brédas, J. L. Electronic Structure of Phenylene Vinylene Oligomers: Influence of Donor/Acceptor Substitutions. *J. Phys. Chem.* **1995**, *99*, 5604–5611.
- (23) Yamagata, H.; Maxwell, D. S.; Fan, J.; Kittilstved, K. R.; Briseno, A. L.; Barnes, M. D.; Spano, F. C. HJ-Aggregate Behavior of Crystalline 7,8,15,16-Tetraazaterrylene: Introducing a New Design Paradigm for Organic Materials. *J. Phys. Chem. C* **2014**, *118*, 28842–28854.
- (24) Bae, Y. J.; Shimizu, D.; Schultz, J. D.; Kang, G.; Zhou, J.; Schatz, G. C.; Osuka, A.; Wasielewski, M. R. Balancing Charge Transfer and Frenkel Exciton Coupling Leads to Excimer Formation in Molecular Dimers: Implications for Singlet Fission. *J. Phys. Chem. A* **2020**, *124*, 8478–8487.
- (25) Kaufmann, C.; Bialas, D.; Stolte, M.; Würthner, F. Discrete π -Stacks of Perylene Bisimide Dyes within Folda-Dimers: Insight into Long- and Short-Range Exciton Coupling. *J. Am. Chem. Soc.* **2018**, *140*, 9986–9995.
- (26) Vauthey, E. Photoinduced Symmetry-Breaking Charge Separation. *ChemPhysChem* **2012**, *13*, 2001–2011.
- (27) Rettig, W. Charge Separation in Excited States of Decoupled Systems? TICT Compounds and Implications Regarding the Development of New Laser Dyes and the Primary Process of Vision and Photosynthesis. *Angew. Chem., Int. Ed.* **1986**, *25*, 971–988.
- (28) Kellogg, M.; Akil, A.; Muthiah Ravinson, D. S.; Estergreen, L.; Bradforth, S. E.; Thompson, M. E. Symmetry Breaking Charge Transfer as a Means to Study Electron Transfer with No Driving Force. *Faraday Discuss.* **2019**, *216*, 379–394.
- (29) Grabowski, Z. R.; Rotkiewicz, K.; Rettig, W. Structural Changes Accompanying Intramolecular Electron Transfer: Focus on Twisted Intramolecular Charge-Transfer States and Structures. *Chem. Rev.* **2003**, *103*, 3899–4031.
- (30) Coleman, A. F.; Chen, M.; Zhou, J.; Shin, J. Y.; Wu, Y.; Young, R. M.; Wasielewski, M. R. Reversible Symmetry-Breaking Charge Separation in a Series of Perylenediimide Cyclophanes. *J. Phys. Chem. C* **2020**, *124*, 10408–10419.
- (31) Hou, Y.; Zhang, X.; Chen, K.; Liu, D.; Wang, Z.; Liu, Q.; Zhao, J.; Barbon, A. Charge Separation, Charge Recombination, Long-Lived Charge Transfer State Formation and
-

- Intersystem Crossing in Organic Electron Donor/Acceptor Dyads. *J. Mater. Chem. C* **2019**, *7*, 12048–12074.
- (32) Röhr, M. I. S.; Marciniak, H.; Hoche, J.; Schreck, M. H.; Ceymann, H.; Mitric, R.; Lambert, C. Exciton Dynamics from Strong to Weak Coupling Limit Illustrated on a Series of Squaraine Dimers. *J. Phys. Chem. C* **2018**, *122*, 8082–8093.
- (33) Wu, Y.; Young, R. M.; Frasconi, M.; Schneebeil, S. T.; Spent, P.; Gardner, D. M.; Brown, K. E.; Würthner, F.; Stoddart, J. F.; Wasielewski, M. R. Ultrafast Photoinduced Symmetry-Breaking Charge Separation and Electron Sharing in Perylenediimide Molecular Triangles. *J. Am. Chem. Soc.* **2015**, *137*, 13236–13239.
- (34) Guo, Y.; Ma, Z.; Niu, X.; Zhang, W.; Tao, M.; Guo, Q.; Wang, Z.; Xia, A. Bridge-Mediated Charge Separation in Isomeric N-Annulated Perylene Diimide Dimers. *J. Am. Chem. Soc.* **2019**, *141*, 12789–12796.
- (35) Kong, J.; Zhang, W.; Li, G.; Huo, D.; Guo, Y.; Niu, X.; Wan, Y.; Tang, B.; Xia, A. Excited-State Symmetry-Breaking Charge Separation Dynamics in Multibranched Perylene Diimide Molecules. *J. Phys. Chem. Lett.* **2020**, *11*, 10329–10339.
- (36) Aster, A.; Licari, G.; Zinna, F.; Brun, E.; Kumpulainen, T.; Tajkhorshid, E.; Lacour, J.; Vauthey, E. Tuning Symmetry Breaking Charge Separation in Perylene Bichromophores by Conformational Control. *Chem. Sci.* **2019**, *10*, 10629–10639.
- (37) Markovic, V.; Villamaina, D.; Barabanov, I.; Lawson Daku, L. M.; Vauthey, E. Photoinduced Symmetry-Breaking Charge Separation: The Direction of the Charge Transfer. *Angew. Chemie Int. Ed.* **2011**, *50*, 7596–7598.
- (38) Golden, J. H.; Estergreen, L.; Porter, T.; Tadler, A. C.; Sylvinson, D. M. R.; Facendola, J. W.; Kubiak, C. P.; Bradforth, S. E.; Thompson, M. E. Symmetry-Breaking Charge Transfer in Boron Dipyrldimethene (DIPYR) Dimers. *ACS Appl. Energy Mater.* **2018**, *1*, 1083–1095.
- (39) Kim, T.; Kim, J.; Mori, H.; Park, S.; Lim, M.; Osuka, A.; Kim, D. Symmetry-Breaking Charge Transfer in the Excited State of Directly Linked Push-Pull Porphyrin Arrays. *Phys. Chem. Chem. Phys.* **2017**, *19*, 13970–13977.
- (40) Trinh, C.; Kirlikovali, K.; Das, S.; Ener, M. E.; Gray, H. B.; Djurovich, P.; Bradforth, S. E.; Thompson, M. E. Symmetry-Breaking Charge Transfer of Visible Light Absorbing Systems: Zinc Dipyrins. *J. Phys. Chem. C* **2014**, *118*, 21834–21845.
- (41) Jacob J. Piet; Wouter Schuddeboom; Bastiaan R. Wegewijs; Ferdinand C. Grozema;; Warman, J. M. Symmetry Breaking in the Relaxed S1 Excited State of Bianthryl Derivatives in Weakly Polar Solvents. *J. Am. Chem. Soc.* **2001**, *123*, 5337–5347.
- (42) Roy, P.; Bressan, G.; Gretton, J.; Cammidge, A. N.; Meech, S. R. Ultrafast Excimer Formation and Solvent Controlled Symmetry Breaking Charge Separation in the Excitonically Coupled Subphthalocyanine Dimer. *Angew. Chem., Int. Ed.* **2021**, *60*, 10568–10572
- (43) Zhao, X.; O'Connor, J. P.; Schultz, J. D.; Bae, Y. J.; Lin, C.; Young, R. M.; Wasielewski, M. R. Temperature Tuning of Coherent Mixing between States Driving Singlet Fission in a Spiro-Fused Terrylenediimide Dimer. *J. Phys. Chem. B* **2021**, *125*, 6945–6954.
-

- (44) Powers-Riggs, N. E.; Zuo, X.; Young, R. M.; Wasielewski, M. R. Symmetry-Breaking Charge Separation in a Nanoscale Terrylenediimide Guanine-Quadruplex Assembly. *J. Am. Chem. Soc.* **2019**, *141*, 17512–17516.
- (45) Ramirez, C. E.; Chen, S.; Powers-Riggs, N. E.; Schlesinger, I.; Young, R. M.; Wasielewski, M. R. Symmetry-Breaking Charge Separation in the Solid State: Tetra(Phenoxy)Perylenediimide Polycrystalline Films. *J. Am. Chem. Soc.* **2020**, *142*, 18243–18250.
- (46) Kim, W.; Nowak-Król, A.; Hong, Y.; Schlosser, F.; Würthner, F.; Kim, D. Solvent-Modulated Charge-Transfer Resonance Enhancement in the Excimer State of a Bay-Substituted Perylene Bisimide Cyclophane. *J. Phys. Chem. Lett.* **2019**, *10*, 1919–1927.
- (47) Cornil, J. Influence of Interchain Interactions in the Absorption and Luminescence of Conjugated Oligomers and Polymers: A Quantum-Chemical Characterization. *J. Am. Chem. Soc.* **1998**, *120*, 1289–1299.
- (48) Hestand, N. J.; Spano, F. C. Interference between Coulombic and CT-Mediated Couplings in Molecular Aggregates: H- to J-Aggregate Transformation in Perylene-Based π -Stacks. *J. Chem. Phys.* **2015**, *143*, 244707.
- (49) Nayak, N.; Gopidas, K. R. Self-Assembly of a β -Cyclodextrin Bis-Inclusion Complex into a Highly Crystalline Fiber Network. An Effective Strategy for Null Aggregate Design. *J. Phys. Chem. B* **2019**, *123*, 8131–8139.
- (50) Zhou, J.; Zhang, W.; Jiang, X. F.; Wang, C.; Zhou, X.; Xu, B.; Liu, L.; Xie, Z.; Ma, Y. Magic-Angle Stacking and Strong Intermolecular π - π Interaction in a Perylene Bisimide Crystal: An Approach for Efficient Near-Infrared (NIR) Emission and High Electron Mobility. *J. Phys. Chem. Lett.* **2018**, *9*, 596–600.
- (51) Sebastian, E.; Philip, A. M.; Benny, A.; Hariharan, M. Null Exciton Splitting in Chromophoric Greek Cross (+) Aggregate. *Angew. Chem., Int. Ed.* **2018**, *57*, 15696–15701.
- (52) Lijina, M. P.; Benny, A.; Ramakrishnan, R.; Nair, N. G.; Hariharan, M. Exciton Isolation in Cross-Pentacene Architecture. *J. Am. Chem. Soc.* **2020**, *142*, 17393–17402.
- (53) Benny, A.; Ramakrishnan, R.; Hariharan, M. Mutually Exclusive Hole and Electron Transfer Coupling in Cross Stacked Acenes. *Chem. Sci.* **2021**, *12*, 5064–5072.
- (54) Hong, Y.; Kim, J.; Kim, W.; Kaufmann, C.; Kim, H.; Würthner, F.; Kim, D. Efficient Multiexciton State Generation in Charge-Transfer-Coupled Perylene Bisimide Dimers via Structural Control. *J. Am. Chem. Soc.* **2020**, *142*, 7845–7857.
- (55) Mallia, A. R.; Salini, P. S.; Hariharan, M. Nonparallel Stacks of Donor and Acceptor Chromophores Evade Geminate Charge Recombination. *J. Am. Chem. Soc.* **2015**, *137*, 15604–15607.
- (56) Philip, A. M.; Mallia, A. R.; Hariharan, M. Prolonged Charge Separated States in Twisted Stacks of All-Carbon Donor and Acceptor Chromophores. *J. Phys. Chem. Lett.* **2016**, *7*, 4751–4756.
- (57) Khandelwal, H.; Mallia, A. R.; Cheriya, R. T.; Hariharan, M. Effect of Temperature on Symmetry Breaking Excited State Charge Separation: Restoration of Symmetry at Elevated Temperature. *Phys. Chem. Chem. Phys.* **2012**, *14*, 15282–15285.

- (58) Nagarajan, K.; Mallia, A. R.; Muraleedharan, K.; Hariharan, M. Enhanced Intersystem Crossing in Core-Twisted Aromatics. *Chem. Sci.* **2017**, *8*, 1776–1782.
- (59) Song, H.; Zhao, H.; Guo, Y.; Philip, A. M.; Guo, Q.; Hariharan, M.; Xia, A. Distinct Excited-State Dynamics of Near-Orthogonal Perylenimide Dimer: Conformational Planarization versus Symmetry Breaking Charge Transfer. *J. Phys. Chem. C* **2019**, *124*, 237–245.
- (60) Zhang, A.; Jiang, W.; Wang, Z. Fulvalene-Embedded Perylene Diimide and Its Stable Radical Anion. *Angew. Chem., Int. Ed.* **2020**, *59*, 752–757.
- (61) Gao, G.; Liang, N.; Geng, H.; Jiang, W.; Fu, H.; Feng, J.; Hou, J.; Feng, X.; Wang, Z. Spiro-Fused Perylene Diimide Arrays. *J. Am. Chem. Soc.* **2017**, *139*, 15914–15920.
- (62) Grimme, S.; Antony, J.; Ehrlich, S.; Krieg, H. A Consistent and Accurate Ab Initio Parametrization of Density Functional Dispersion Correction (DFT-D) for the 94 Elements H-Pu. *J. Chem. Phys.* **2010**, *132*, 10089.
- (63) Weigend, F.; Ahlrichs, R. Balanced Basis Sets of Split Valence, Triple Zeta Valence and Quadruple Zeta Valence Quality for H to Rn: Design and Assessment of Accuracy. *Phys. Chem. Chem. Phys.* **2005**, *7*, 3297–3305.
- (64) Mohan, A.; Sebastian, E.; Gudem, M.; Hariharan, M. Near-Quantitative Triplet State Population via Ultrafast Intersystem Crossing in Perbromoperylene diimide. *J. Phys. Chem. B* **2020**, *124*, 6867–6874.
- (65) Beljonne, D.; Cornil, J.; Silbey, R.; Millié, P.; Brédas, J. L. Interchain Interactions in Conjugated Materials: The Exciton Model versus the Supermolecular Approach. *J. Chem. Phys.* **2000**, *112*, 4749.
- (66) Chang, J. C. Monopole Effects on Electronic Excitation Interactions between Large Molecules. I. Application to Energy Transfer in Chlorophylls. *J. Chem. Phys.* **1977**, *67*, 3901–3909.
- (67) Madjet, M. E.; Abdurahman, A.; Renger, T. Intermolecular Coulomb Couplings from Ab Initio Electrostatic Potentials: Application to Optical Transitions of Strongly Coupled Pigments in Photosynthetic Antennae and Reaction Centers. *J. Phys. Chem. B* **2006**, *110*, 17268–17281.
- (68) Scholes, G. D.; Ghiggino, K. P. Electronic Interactions and Interchromophore Excitation Transfer. *J. Phys. Chem.* **1994**, *98*, 4580–4590.
- (69) Hestand, N. J.; Spano, F. C. Molecular Aggregate Photophysics beyond the Kasha Model: Novel Design Principles for Organic Materials. *Acc. Chem. Res.* **2017**, *50*, 341–350.
- (70) Valeev, E. F.; Coropceanu, V.; Da Silva Filho, D. A.; Salman, S.; Brédas, J. L. Effect of Electronic Polarization on Charge-Transport Parameters in Molecular Organic Semiconductors. *J. Am. Chem. Soc.* **2006**, *128*, 9882–9886.
- (71) Kirkpatrick, J. An Approximate Method for Calculating Transfer Integrals Based on the ZINDO Hamiltonian. *Int. J. Quantum Chem.* **2008**, *108*, 51–56.
- (72) Kistler, K. A.; Pochas, C. M.; Yamagata, H.; Matsika, S.; Spano, F. C. Absorption, Circular Dichroism, and Photoluminescence in Perylene Diimide Bichromophores: Polarization-Dependent H- and J-Aggregate Behavior. *J. Phys. Chem. B* **2012**, *116*, 77–86.
- (73) Spano, F. C. The Spectral Signatures of Frenkel Polarons in H- And J-Aggregates. *Acc.*

- Chem. Res.* **2010**, *43*, 429–439.
- (74) Heimel, G.; Daghofer, M.; Gierschner, J.; List, E. J. W.; Grimsdale, A. C.; Müllen, K.; Beljonne, D.; Brédas, J.-L.; Zojer, E. Breakdown of the Mirror Image Symmetry in the Optical Absorption/Emission Spectra of Oligo(Para-Phenylene)S. *J. Chem. Phys.* **2005**, *122*, 54501.
- (75) Shang, C.; Wang, G.; Liu, K.; Jiang, Q.; Liu, F.; Chou, P.; Fang, Y. Perylene Bisimide and Naphthyl-Based Molecular Dyads: Hydrogen Bonds Driving Co-planarization and Anomalous Temperature-Response Fluorescence. *Angew. Chem., Int. Ed.* **2020**, *132*, 8657–8663.
- (76) Plasser, F. TheoDORE: A Toolbox for a Detailed and Automated Analysis of Electronic Excited State Computations. *J. Chem. Phys.* **2020**, *152*, 084108.
- (77) Plasser, F.; Lischka, H. Analysis of Excitonic and Charge Transfer Interactions from Quantum Chemical Calculations. *J. Chem. Theory Comput.* **2012**, *8*, 2777–2789.
- (78) Martin, R. L. Natural Transition Orbitals. *J. Chem. Phys.* **2003**, *118*, 4775.
- (79) Liu, Z.; Lu, T.; Chen, Q. An Sp-Hybridized All-Carboatomic Ring, Cyclo[18]Carbon: Electronic Structure, Electronic Spectrum, and Optical Nonlinearity. *Carbon N. Y.* **2020**, *165*, 461–467.
- (80) Ferdinand C. Grozema,; Marcel Swart,; Robert W. J. Zijlstra,; Jacob J. Piet,; Laurens D. A. Siebbeles,; Duijnen, P. T. van. QM/MM Study of the Role of the Solvent in the Formation of the Charge Separated Excited State in 9,9'-Bianthryl. *J. Am. Chem. Soc.* **2005**, *127*, 11019–11028.
- (81) Scholes, G. D.; Fournier, T.; Parker, A. W.; Phillips, D. Solvation and Intramolecular Reorganization in 9,9'-Bianthryl: Analysis of Resonance Raman Excitation Profiles and Ab Initio Molecular Orbital Calculations. *J. Chem. Phys.* **1999**, *111*, 5999.
- (82) Solvent-Dependent Steady-State and Time-Resolved Photophysical Studies of Ref-PDI Are Avoided in the Manuscript Due to the Degrading Nature of Ref-PDI under the Polar Solvent Condition (Figure S13).
- (83) Marcus, R. A. On the Theory of Oxidation-Reduction Reactions Involving Electron Transfer. I. *J. Chem. Phys.* **1956**, *24*, 966–978.
- (84) Marcus, R. A. On the Theory of Electron-Transfer Reactions. VI. Unified Treatment for Homogeneous and Electrode Reactions. *J. Chem. Phys.* **1965**, *43*, 679–701.
- (85) Han, Y.; Hamada, M.; Chang, I. Y.; Hyeon-Deuk, K.; Kobori, Y.; Kobayashi, Y. Fast T-Type Photochromism of Colloidal Cu-Doped ZnS Nanocrystals. *J. Am. Chem. Soc.* **2021**, *143*, 2239–2249.
- (86) Weller, A. Photoinduced Electron Transfer in Solution: Exciplex and Radical Ion Pair Formation Free Enthalpies and Their Solvent Dependence. *Z. Phys. Chem.* **1982**, *133*, 93–98.
- (87) Hiroshi Imahori; Kiyoshi Hagiwara,; Masanori Aoki; Tsuyoshi Akiyama; Seiji Taniguchi,; Tadashi Okada,; Masahiro Shirakawa,; Sakata, Y. Linkage and Solvent Dependence of Photoinduced Electron Transfer in Zincporphyrin-C60 Dyads. *J. Am. Chem. Soc.* **1996**, *118*, 11771–11782.
-

- (88) Wu, Y.; Young, R. M.; Frasconi, M.; Schneebeli, S. T.; Spenst, P.; Gardner, D. M.; Brown, K. E.; Würthner, F.; Stoddart, J. F.; Wasielewski, M. R. Ultrafast Photoinduced Symmetry-Breaking Charge Separation and Electron Sharing in Perylenediimide Molecular Triangles. *J. Am. Chem. Soc.* **2015**, *137*, 13236–13239.
- (89) Snellenburg, J. J.; Laptanok, S.; Seger, R.; Mullen, K. M.; van Stokkum, I. H. M. Glotaran: A Java-Based Graphical User Interface for the R Package TIMP. *J. Stat. Softw.* **2012**, *49*, 1–22.
- (90) Van Stokkum, I. H. M.; Larsen, D. S.; Van Grondelle, R. Global and Target Analysis of Time-Resolved Spectra. *Biochim. Biophys. Acta - Bioenerg.* **2004**, *1657*, 82–104.
- (91) Wu, H.; Wang, H.; Xue, L.; Shi, Y.; Li, X. Hindered Intramolecular Electron Transfer in Room-Temperature Ionic Liquid. *J. Phys. Chem. B* **2010**, *114*, 14420–14425.
- (92) B. Ramachandram.; Samanta, A. Transition Metal Ion Induced Fluorescence Enhancement of 4-(N,N-Dimethylethylenediamino)-7-Nitrobenz-2-Oxa-1,3-Diazole. *J. Phys. Chem. A* **1998**, *102*, 10579–10587.
- (93) Nazarov, A. E.; Ivanov, A. I. Nonstationary Theory of Excited State Charge Transfer Symmetry Breaking Driven by Polar Solvent. *J. Phys. Chem. B* **2020**, *124*, 10787–10801.
- (94) Nelsen, S. F.; Blackstock, S. C.; Kim, Y. Estimation of Inner Shell Marcus Terms for Amino Nitrogen Compounds by Molecular Orbital Calculations. *J. Am. Chem. Soc.* **1987**, *109*, 677–682.
- (95) Balawi, A. H.; Stappert, S.; Gorenflot, J.; Li, C.; Müllen, K.; Andrienko, D.; Laquai, F. Direct and Energy-Transfer-Mediated Charge-Transfer State Formation and Recombination in Triangulene-Spacer-Perylenediimide Multichromophores: Lessons for Photovoltaic Applications. *J. Phys. Chem. C* **2019**, *123*, 16602–16613.
- (96) Cupellini, L.; Wityk, P.; Mennucci, B.; Rak, J. Photoinduced Electron Transfer in 5-Bromouracil Labeled DNA. A Contrathermodynamic Mechanism Revisited by Electron Transfer Theories. *Phys. Chem. Chem. Phys.* **2019**, *21*, 4387–4393.
- (97) Wu, Q.; Van Voorhis, T. Direct Calculation of Electron Transfer Parameters through Constrained Density Functional Theory. *J. Phys. Chem. A* **2006**, *110*, 9212–9218.
- (98) Umeyama, T.; Imahori, H. Electron Transfer and Exciplex Chemistry of Functionalized Nanocarbons: Effects of Electronic Coupling and Donor Dimerization. *Nanoscale Horizons* **2018**, *3*, 352–366.
- (99) Smitha, M. A.; Prasad, E.; Gopidas, K. R. Photoinduced Electron Transfer in Hydrogen Bonded Donor - Acceptor Systems. Free Energy and Distance Dependence Studies and an Analysis of the Role of Diffusion. *J. Am. Chem. Soc.* **2001**, *123*, 1159–1165.
- (100) Parada, G. A.; Goldsmith, Z. K.; Kolmar, S.; Rimgard, B. P.; Mercado, B. Q.; Hammarström, L.; Hammes-Schiffer, S.; Mayer, J. M. Concerted Proton-Electron Transfer Reactions in the Marcus Inverted Region. *Science* **2019**, *364*, 471–475.
- (101) Gould, I. R.; Moser, J. E.; Armitage, B.; Farid, S.; Goodman, J. L.; Herman, M. S. Electron-Transfer Reactions in the Marcus Inverted Region-Charge Recombination versus Charge Shift Reactions. *J. Am. Chem. Soc.* **1989**, *111*, 1917–1919.
- (102) D'alessandro, D. M.; Keene, F. R. Current Trends and Future Challenges in the

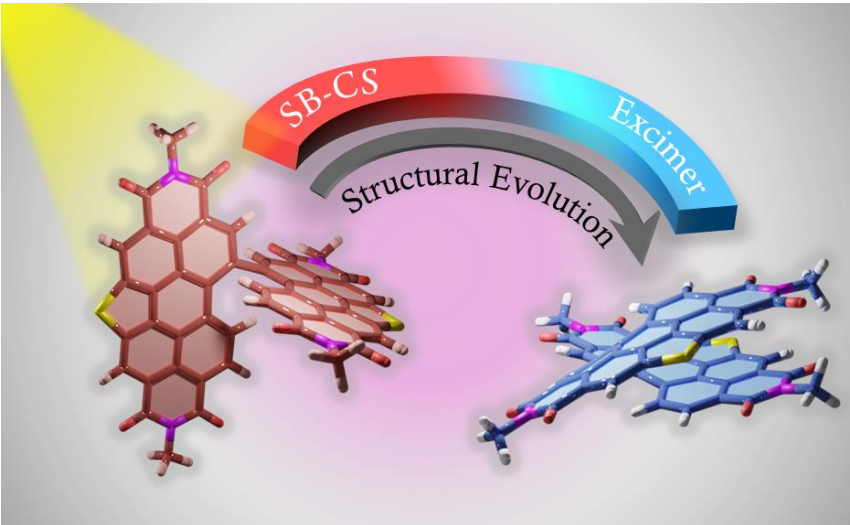
- Experimental, Theoretical and Computational Analysis of Intervalence Charge Transfer (IVCT) Transitions. *Chem. Soc. Rev.* **2006**, *35*, 424–440.
- (103) Dordević, L.; Milano, D.; Demitri, N.; Bonifazi, D. O-Annulation to Polycyclic Aromatic Hydrocarbons: A Tale of Optoelectronic Properties from Five- To Seven-Membered Rings. *Org. Lett.* **2020**, *22*, 4283–4288.
- (104) Gao, G.; Liang, N.; Geng, H.; Jiang, W.; Fu, H.; Feng, J.; Hou, J.; Feng, X.; Wang, Z. Spiro-Fused Perylene Diimide Arrays. *J. Am. Chem. Soc.* **2017**, *139*, 15914–15920.
- (105) Citation | Gaussian.com <https://gaussian.com/citation/> (accessed Jun 3, 2021).
- (106) Lu, T.; Chen, F. Multiwfn: A Multifunctional Wavefunction Analyzer. *J. Comput. Chem.* **2012**, *33*, 580–592.
- (107) GitHub - differint/differint: Python package for calculating fractional derivatives. <https://github.com/differint/differint> (accessed Jun 3, 2021).
- (108) Kistler, K. A.; Pochas, C. M.; Yamagata, H.; Matsika, S.; Spano, F. C. Absorption, Circular Dichroism, and Photoluminescence in Perylene Diimide Bichromophores: Polarization-Dependent H- and J-Aggregate Behavior. *J. Phys. Chem. B* **2012**, *116*, 77–86.
- (109) Hestand, N. J.; Spano, F. C. Interference between Coulombic and CT-Mediated Couplings in Molecular Aggregates: H- to J-Aggregate Transformation in Perylene-Based π -Stacks. *J. Chem. Phys.* **2015**, *143*, 244707.
- (110) Plasser, F. TheoDORE: A Toolbox for a Detailed and Automated Analysis of Electronic Excited State Computations. *J. Chem. Phys.* **2020**, *152*, 084108.
- (111) Plasser, F.; Lischka, H. Analysis of Excitonic and Charge Transfer Interactions from Quantum Chemical Calculations. *J. Chem. Theory Comput.* **2012**, *8*, 2777–2789.
- (112) Wu, Y. L.; Brown, K. E.; Wasielewski, M. R. Extending Photoinduced Charge Separation Lifetimes by Using Supramolecular Design: Guanine-Perylenediimide G-Quadruplex. *J. Am. Chem. Soc.* **2013**, *135*, 13322–13325.
- (113) Snellenburg, J. J.; Laptinok, S.; Seger, R.; Mullen, K. M.; van Stokkum, I. H. M. Glotaran: A Java-Based Graphical User Interface for the R Package TIMP. *J. Stat. Softw.* **2012**, *49*, 1–22.
- (114) Weller, A. Photoinduced Electron Transfer in Solution: Exciplex and Radical Ion Pair Formation Free Enthalpies and Their Solvent Dependence. *Z. Phys. Chem.* **1982**, *133*, 93–98.
- (115) Deng, P.; Liu, L.; Ren, S.; Li, H.; Zhang, Q. N-Acylation: An Effective Method for Reducing the LUMO Energy Levels of Conjugated Polymers Containing Five-Membered Lactam Units. *Chem. Commun.* **2012**, *48*, 6960–6962.
- (116) Wu, Q.; Van Voorhis, T. Direct Calculation of Electron Transfer Parameters through Constrained Density Functional Theory. *J. Phys. Chem. A* **2006**, *110*, 9212–9218.
- (117) Shao, Y.; Gan, Z.; Epifanovsky, E.; Gilbert, A. T. B.; Wormit, M.; Kussmann, J.; Lange, A. W.; Behn, A.; Deng, J.; Feng, X.; Ghosh, D.; Goldey, M.; Horn, P. R.; Jacobson, L. D.; Kaliman, I.; Khaliullin, R. Z.; Kuš, T.; Landau, A.; Liu, J.; Proynov, E. I.; Rhee, Y. M.; Richard, R. M.; Rohrdanz, M. A.; Steele, R. P.; Sundstrom, E. J.; Woodcock, H. L.; Zimmerman, P. M.; Zuev, D.; Albrecht, B.; Alguire, E.; Austin, B.; Beran, G. J. O.; Bernard,

Y. A.; Berquist, E.; Brandhorst, K.; Bravaya, K. B.; Brown, S. T.; Casanova, D.; Chang, C. M.; Chen, Y.; Chien, S. H.; Closser, K. D.; Crittenden, D. L.; Diedenhofen, M.; Distasio, R. A.; Do, H.; Dutoi, A. D.; Edgar, R. G.; Fatehi, S.; Fusti-Molnar, L.; Ghysels, A.; Golubeva-Zadorozhnaya, A.; Gomes, J.; Hanson-Heine, M. W. D.; Harbach, P. H. P.; Hauser, A. W.; Hohenstein, E. G.; Holden, Z. C.; Jagau, T. C.; Ji, H.; Kaduk, B.; Khistyayev, K.; Kim, J.; Kim, J.; King, R. A.; Klunzinger, P.; Kosenkov, D.; Kowalczyk, T.; Krauter, C. M.; Lao, K. U.; Laurent, A. D.; Lawler, K. V.; Levchenko, S. V.; Lin, C. Y.; Liu, F.; Livshits, E.; Lochan, R. C.; Luenser, A.; Manohar, P.; Manzer, S. F.; Mao, S. P.; Mardirossian, N.; Marenich, A. V.; Maurer, S. A.; Mayhall, N. J.; Neuscammann, E.; Oana, C. M.; Olivares-Amaya, R.; Oneill, D. P.; Parkhill, J. A.; Perrine, T. M.; Peverati, R.; Prociuk, A.; Rehn, D. R.; Rosta, E.; Russ, N. J.; Sharada, S. M.; Sharma, S.; Small, D. W.; Sodt, A.; Stein, T.; Stück, D.; Su, Y. C.; Thom, A. J. W.; Tsuchimochi, T.; Vanovschi, V.; Vogt, L.; Vydrov, O.; Wang, T.; Watson, M. A.; Wenzel, J.; White, A.; Williams, C. F.; Yang, J.; Yeganeh, S.; Yost, S. R.; You, Z. Q.; Zhang, I. Y.; Zhang, X.; Zhao, Y.; Brooks, B. R.; Chan, G. K. L.; Chipman, D. M.; Cramer, C. J.; Goddard, W. A.; Gordon, M. S.; Hehre, W. J.; Klamt, A.; Schaefer, H. F.; Schmidt, M. W.; Sherrill, C. D.; Truhlar, D. G.; Warshel, A.; Xu, X.; Aspuru-Guzik, A.; Baer, R.; Bell, A. T.; Besley, N. A.; Chai, J. Da; Dreuw, A.; Dunietz, B. D.; Furlani, T. R.; Gwaltney, S. R.; Hsu, C. P.; Jung, Y.; Kong, J.; Lambrecht, D. S.; Liang, W.; Ochsenfeld, C.; Rassolov, V. A.; Slipchenko, L. V.; Subotnik, J. E.; Van Voorhis, T.; Herbert, J. M.; Krylov, A. I.; Gill, P. M. W.; Head-Gordon, M. *Advances in Molecular Quantum Chemistry Contained in the Q-Chem 4 Program Package. Mol. Phys.* **2015**, *113*, 184–215.

Chapter 4

Symmetry-Broken Charge Separated State Hampered by Excimer Evolution: Impact of Excited-State Structural Evolution

Abstract: *Achieving a long-lived symmetry-broken charge-separated state in chromophoric assemblies is quintessential for the enhanced performance of artificial photosynthetic mimics. However, the occurrence of energy trap states hinders exciton and charge transport across photovoltaic devices, diminishing power conversion efficiency. Herein, we demonstrate unprecedented excimer formation in the relaxed excited-state geometry of bichromophoric systems impeding the lifetime of symmetry-broken charge-separated states. Core-annulated perylene-3,4,9,10-tetracarboxylic diimide dimers (SC-SPDI₂ and SC-NPDI₂) prefer a near-orthogonal arrangement in the ground state and a π -stacked foldamer structure in the excited state. The prospect of an excimer-like state in the foldameric arrangement of SC-SPDI₂ and SC-NPDI₂ has been rationalized by fragment-based excited state analysis and temperature-dependent photoluminescence measurements. Effective*



electronic coupling matrix element in the Franck-Condon geometry of SC-SPDI₂ and SC-NPDI₂ facilitate solvation-assisted ultrafast symmetry-breaking charge-separation (SB-CS) in a high dielectric environment, in contrast to

unrelaxed excimer formation (Ex) in low dielectric environment. Subsequently, the SB-CS state dissociates into an undesired relaxed excimer state (Ex) due to configuration mixing of Frenkel*

exciton (FE) and charge-separated state in the foldamer structure, downgrading the efficacy of the charge-separated state. The decay rate constant of FE to SB-CS ($k_{FE \rightarrow SB-CS}$) in polar solvents is 8-17 fold faster than direct Ex^ formation ($k_{FE \rightarrow Ex^*}$) in non-polar solvent ($k_{FE \rightarrow SB-CS} \gg k_{FE \rightarrow Ex^*}$), characterized by femtosecond transient absorption (fsTA) spectroscopy. The present investigation establishes the impact of detrimental excimer formation on the persistence of SB-CS state in chromophoric dimers and offers the requisite of conformational rigidity as one of the potential design principles for developing advanced molecular photovoltaics.*

4.1. Introduction

Symmetry-breaking charge separation (SB-CS) is a photoexcited-state process by which a pair of identical chromophores forms a charge-separated state with the electron and hole localized on different chromophoric units.¹⁻⁷ Since discovering their existence in the 9,9-bianthryl and photosynthetic reaction centers, SB-CS processes have received tremendous attention.⁸⁻¹³ Accomplishing SB-CS in a multi-chromophoric system is analogous to exciton formation in silicon semiconductors where exciton binding energy between hole and electron is overcome by thermal energy.³ The fundamental understanding of structure-property correlation and related excited-state dynamics among the molecular architectures has enabled researchers to rationalize the design of organic photovoltaics (OPVs).¹⁴⁻¹⁸ The conventional donor-acceptor based OPVs generally exhibit low open-circuit voltages (V_{OC}) due to the significant energy difference between the optical band gap and charge-separated state at the interface.^{16,19,20} However, the energy loss during SB-CS is low compared to the charge separation (CS) in donor-acceptor systems.^{3,21} Moreover, SB-CS processes in solid-state, transition metal complexes, and polymers are a progressing topic of interest and have been widely explored in weakly coupled multichromophoric systems.^{2-4,22-24} Developing robust organic materials exhibiting optimized SB-CS and recombination dynamics is hence pivotal for the advancement of organic photovoltaics.

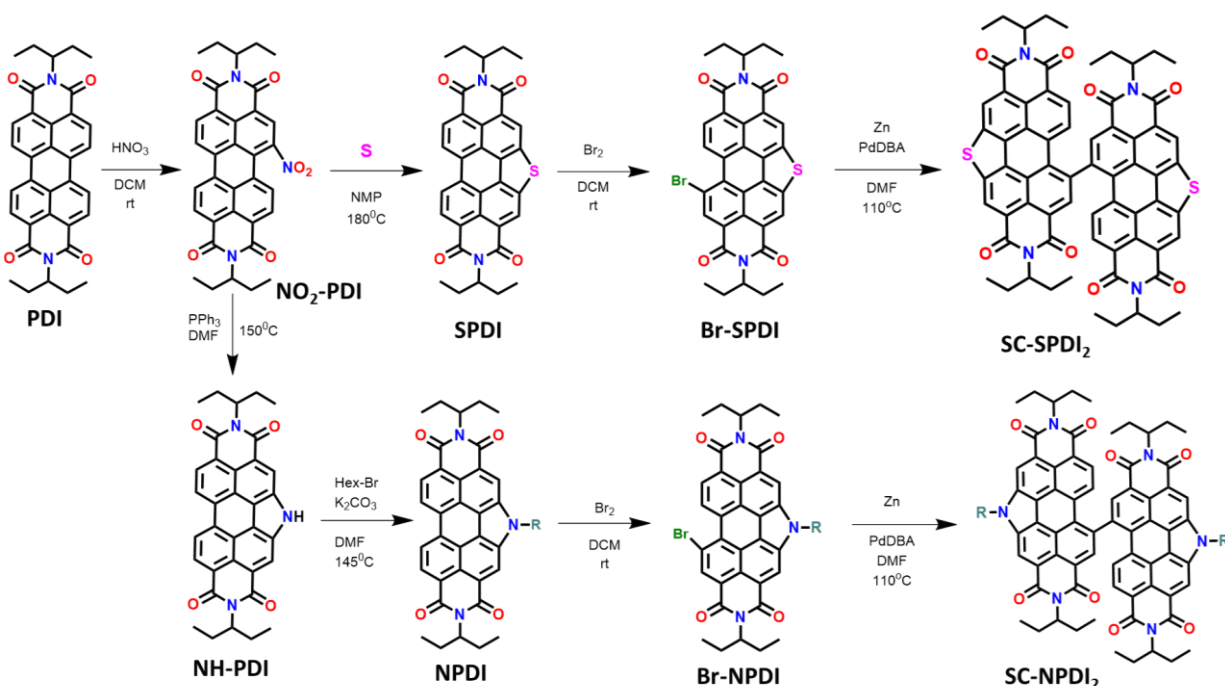
The factors determining the excited-state dynamics of SB-CS in multichromophoric architectures are the relative spatial orientation, distance and strength of electronic interaction between the monomeric units and the surrounding dielectric environment.^{3,25-30} Among the various weakly coupled chromophoric assemblies investigated for SB-CS properties, multichromophoric perylenediimide (**PDI**) architectures are widely explored due to PDI derivatives' exciting optoelectronic properties.^{3,7,24,27,31} Out of the several interesting **PDI** molecular constructs reported

to date, the spiro-conjugated orthogonal arranged **PDI** dimer (**Sp-PDI**₂) reported by our group exhibited a prolonged SB-CS state ($k_{SB-CS}/k_{CR}=2647$ in acetonitrile).³² Ultrafast SB-CS in **PDI** dimers was first experimentally demonstrated by Wasielewski and coworkers in cofacial and head-to-tail stacked **PDI** dimers.³³ Whereas excimer as an intermediated state to SB-CS was recognized by Würthner, Kim and coworkers in cofacial arranged dimer.²⁶ In excimer-mediated excited state processes, the proficiency of the desired state is limited by intermediate parasitic excimer formation.^{26,34} The superposition of Frenkel exciton and the charge-transfer states in a chromophoric assembly populates the excimer state, which is generally considered as an exciton trap state that diminishes the efficacy of OPVs.^{35–39} Structural flexibility in the form of rotational or translational degrees of freedom in multichromophoric systems profoundly affects the population of distinct excited states.^{40–42} Planarization of chromophores in the excited state reported in flexible molecular systems opens up diversified excited state dynamics.^{41,43,44} Hence controlling the conformational flexibility and the concomitant manifestation of undesired radiative and non-radiative deactivation pathways of SB-CS state is vital for long-lived CS state, thereby enhancing photovoltaic efficiency.

The core-annulated near-orthogonal arranged perylenediimide dimers have found extensive applications as non-fullerene acceptors in organic solar cells owing to greater solubility, reduced aggregation and excimer formation.^{45,46} Though vital for photovoltaic application, excited-state dynamics of heteroatom annulated **PDI** dimers remain elusive. Our continuous efforts in understanding the excited-state dynamics of orthogonal/near-orthogonal arranged multichromophoric architectures motivated us to dwell into the realm of excited-state structural rearrangement and the associated deactivation pathways.^{32,43,47–50} Herein, we showcase the transformation of the initially populated SB-CS state to a detrimental excimer state due to excited-state conformational changes. Near-orthogonal stacked **SC-SPDI**₂ and **SC-NPDI**₂ undergo ultrafast structural relaxation to foldamer structure, leading to a direct population of the excimer state in toluene. However, ultrafast SB-CS is favored over excimer formation in a polar environment due to the effective electronic coupling in Franck-Condon geometry and the thermodynamic feasibility of charge separation. The initially populated SB-CS state decay to an excimer state as the chromophore rearranges to a foldamer structure and the excitation energy gets dissipated as photoluminescence. Rigidification of the near-orthogonal arranged dimers emerges as an elegant strategy for achieving a long-lived charge-separated state and diminishing the unwanted deactivation pathway.

4.2. Results and Discussion

4.2.1. Synthesis, characterization and geometry Optimizations. In this work, sulfur and nitrogen annulated perylene-3,4,9,10-tetracarboxylic diimide dimers, **SC-SPDI₂** and **SC-NPDI₂**, respectively, were synthesized and characterized following the reported and modified procedures (Scheme 4.1 and Figure 4.1).^{45,51,52} **SPDI** and **NPDI** are the monomer units of **SC-SPDI₂** and **SC-NPDI₂**, respectively. In **SC-SPDI₂** and **SC-NPDI₂**, the monomeric units are covalently connected via a carbon-carbon single bond in the bay region of the perylene-3,4,9,10-tetracarboxylic diimide core. The ground-state optimized geometries of **SC-SPDI₂** and **SC-NPDI₂** in vacuum were found to have an edge-to-edge arrangement between the monomeric units with a dihedral angle (ϕ) of 86.5° in **SC-SPDI₂** and 83.6° in **SC-NPDI₂** (Figures 4.1c and 4.1d). The single-crystal X-ray diffraction structure of **SC-NPDI₂** reported by Welch and coworkers exhibited a similar edge-to-edge arrangement with a dihedral angle of 66° , which is significantly lower than that observed in the optimized structure due to the crystal packing forces in the solid-state.⁴⁵ The incorporation of S and N atoms on the perylene core of **PDI** imposed a curved bowl-shape or bowed molecular geometry as a consequence of the ring strain of the fused heteroring (Figure 4.1).^{53,54} The computed carbon-heteroatom bond lengths in the annulated heteroring of **SC-SPDI₂** and **SC-NPDI₂** indicate that the ring strain induced by the thiophene ring (C-S bond length: 1.77 \AA , Figure 4.2) on the **PDI** core is weaker



Scheme 4.1: Showing the synthesis scheme for monomers (**SPDI** and **NPDI**) and dimers (**SC-SPDI₂** and **SC-NPDI₂**).

than that by pyrrole ring (C–N bond length: 1.41 Å, Figure 4.3).

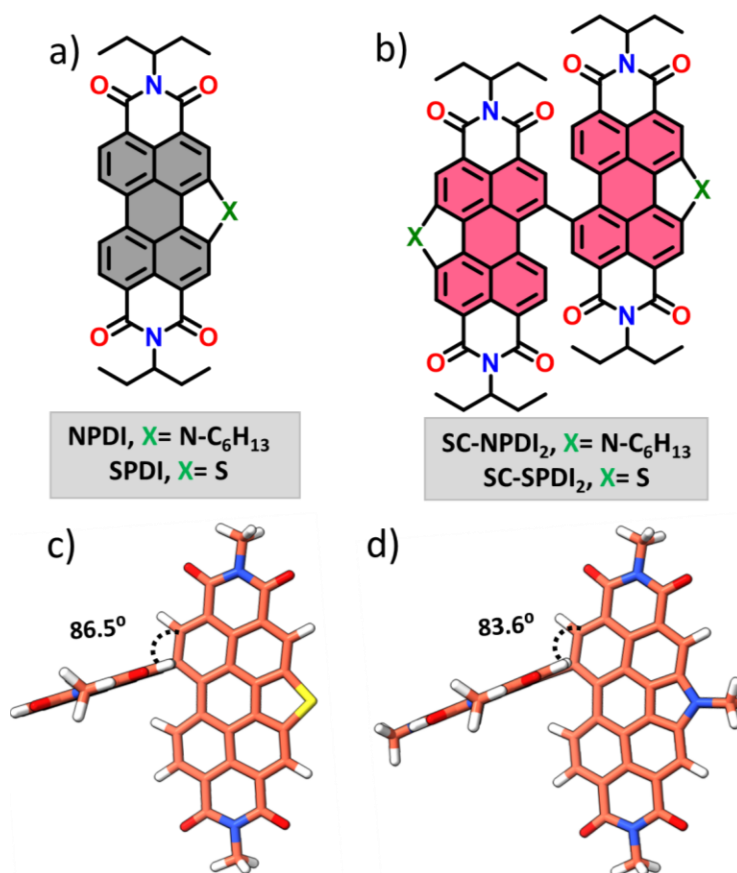


Figure 4.1: Molecular structure of monomeric *SPDI* and *NPDI* (a) and dimeric *SC-SPDI*₂ and *SC-NPDI*₂ (b). Optimized geometries of *SC-SPDI*₂ (c) and *SC-NPDI*₂ (d) with the corresponding dihedral angles between the monomeric planes.

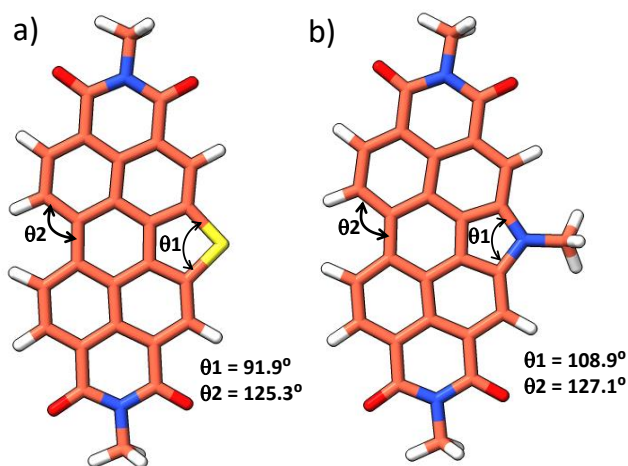


Figure 4.2: Optimised structures of core annulated perylenediimide monomers a) *SPDI* and b) *NPDI* showing the in-plane bend in the perylene core.

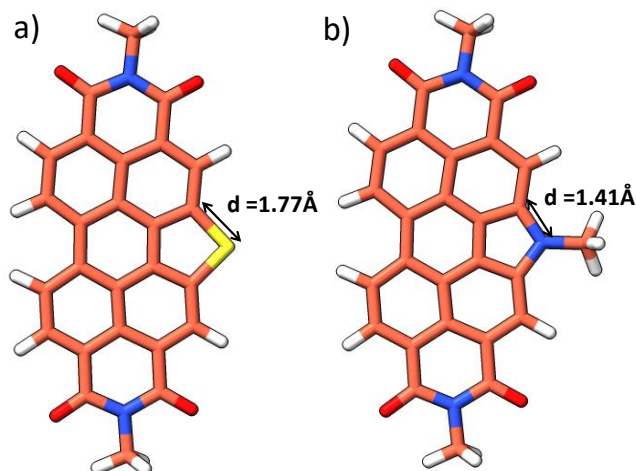


Figure 4.3: Optimised structures of core annulated perylenediimide monomers a) *SPDI* and b) *NPDI* showing the C-S and C-N bond lengths.

4.2.2. Optical properties. The steady-state electronic properties of *SC-SPDI*₂ and *SC-NPDI*₂ along with the reference compounds were explored by electronic absorption and photoluminescence spectroscopy measurements in toluene (TOL, $c_0=0.1-0.3 \mu\text{M}$) at room temperature. The UV-visible absorption spectrum of *NPDI* shows characteristic spectral signatures of perylenediimide (*PDI*) dye with absorption maximum (λ_{max}^{Abs}) at 527 nm, while *SPDI* ($\lambda_{max}^{Abs}=501\text{nm}$) shows a 26 nm hypsochromic shift compared to *PDI* and *NPDI* (Figure 4.4). As a result of the near-orthogonal arrangement, *SC-SPDI*₂ and *SC-NPDI*₂ showcase negligible red-shifted electronic absorption spectra with absorption maximum centered at 503 and 530 nm (Tables A4.1- A4.4).^{32,55}

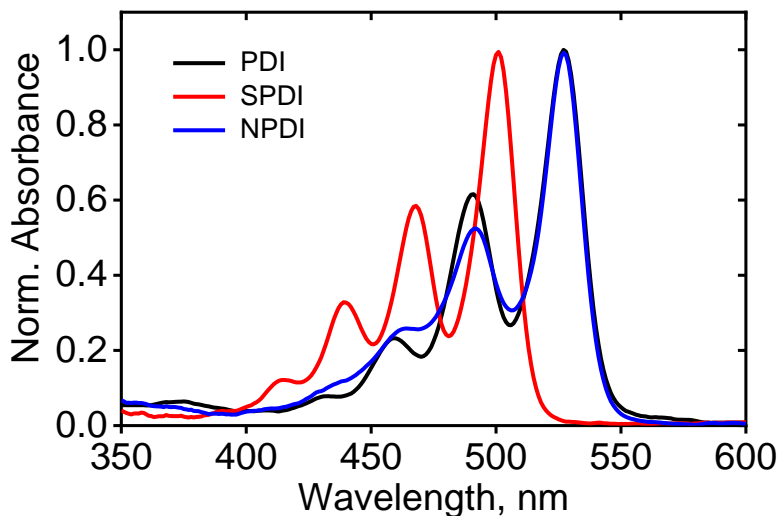


Figure 4.4: Normalized absorption spectra of sulphur annulated (*SPDI*) and nitrogen annulated (*NPDI*) perylenediimide monomers compared to unsubstituted *PDI*.

However, the ratio of the intensity of first and second vibronic bands, I_{0-0}/I_{0-1} , of **SC-SPDI**₂ (1.42) and **SC-NPDI**₂ (1.55) decreased from monomeric **SPDI** (1.70) and **NPDI** (1.92), indicating the weak H-type excitonic coupling among the monomeric units of **SC-SPDI**₂ and **SC-NPDI**₂ (Figure 4.5).⁵⁶ In addition, slight broadening of the 0-0 vibronic absorption band of **SC-SPDI**₂ and **SC-NPDI**₂ as compared to the monomeric unit reiterates the weak excitonic coupling in the near-orthogonal dimers.

As shown in Figure 4.5, photoexcitation of **SPDI** and **NPDI** at 470 nm displays a characteristic **PDI** photoluminescence spectrum with emission maximum (λ_{max}^{Em}) observed at 509 nm and 535 nm, respectively (Stokes shift of ~8 nm). The photoluminescence quantum yield (ϕ_{Fl}) of **SPDI** and **NPDI** is quantified as 0.58 and 0.68 in toluene (Table 4.1). Fascinatingly, **SC-SPDI**₂ and **SC-NPDI**₂ reveal a significantly red-shifted (Stokes shift of ~54 nm) and broadened photoluminescence spectrum relative to the monomeric **SPDI** and **NPDI** in TOL (λ_{max}^{Em} =558 nm for **SC-SPDI**₂ and 584 nm for **SC-NPDI**₂). The broad, featureless, and large Stokes shifted photoluminescence spectra are the characteristic spectral features of an excimer state (Ex) or relaxed singlet state having charge-transfer character ($S_{1(CT)}$).^{29,35,57-59}

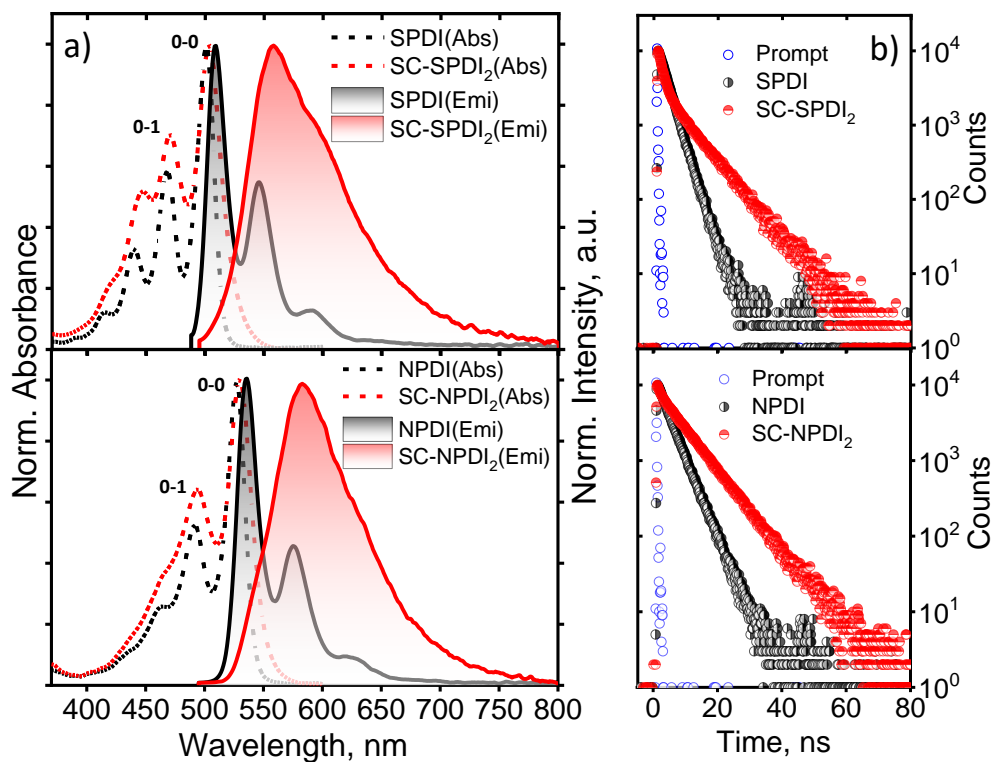


Figure 4.5: Normalized UV-vis absorption, emission spectra (a) and fluorescence decay profile (b) of **SC-SPDI**₂ (Top) and **SC-NPDI**₂ (Bottom) in toluene at room temperature.

Table 4.1: Photoluminescence Quantum Yield (ϕ_{FL}) and Fluorescence Lifetime (τ_{FL}) of **SPDI**, **NPDI**, **SC-SPDI₂**, and **SC-NPDI₂**.

| Solvents | SPDI | | NPDI | | SC-SPDI₂ | | SC-NPDI₂ | |
|----------|-------------|------------------|-------------|-------------|----------------------------|------------------------|----------------------------|------------------------|
| | ϕ_{FL} | τ_{FL} (ns) | ϕ_{FL} | τ_{FL} | ϕ_{FL} | τ_{FL} | ϕ_{FL} | τ_{FL} |
| TOL | 0.58 | 2.73 | 0.68 | 3.34 | 0.60 | 1.42 (42) 8.35 (58) | 0.71 | 0.84 (15) 7.86 (85) |
| ACE | 0.53 | 2.21 | 0.61 | 3.39 | 0.09 | 5.89 | 0.08 | 3.82 |
| ACN | 0.55 | 2.15 | 0.62 | 3.31 | 0.08 | 5.81 | <0.01 | 2.23 |

However, the photoluminescence quantum yield of dimers is not drastically quenched, $\phi_{FL}=0.60$ and 0.71 for **SC-SPDI₂** and **SC-NPDI₂**, respectively, as compared to the reference molecules (Table 4.1).⁶⁰ Ex or $S_{1(CT)}$ states are generally considered as an energy trap state with increased non-radiative decay rate.^{27,54,55}

To further scrutinize the nature of the emissive state of **SC-SPDI₂** and **SC-NPDI₂**, fluorescence lifetime measurements were performed in TOL. **SC-SPDI₂** and **SC-NPDI₂** exhibit biexponential decay of emission with the lifetime of $\tau_{FL}^1=1.42$ ns, $\tau_{FL}^2=8.15$ ns for **SC-SPDI₂** and $\tau_{FL}^1=0.84$ ns, $\tau_{FL}^2=7.86$ ns for **SC-NPDI₂** (Figure 4.5 and Table 4.1), suggesting the presence of dual emissive states in the dimers. Monomeric **SPDI** and **NPDI** in TOL display a monoexponential decay profile with a lifetime of $\tau_{FL}=2.73$ ns and $\tau_{FL}=3.34$ ns, respectively. Since the fluorescence lifetime of the Ex or $S_{1(CT)}$ state is reported to be longer than that of the monomer unit. i.e., the long-lived emissive component of **SC-SPDI₂** ($\tau_{FL}^2=8.15$ ns) and **SC-NPDI₂** ($\tau_{FL}^2=7.86$ ns) might stem from the Ex or $S_{1(CT)}$ states.^{26,35} The dual emissive nature of **SC-SPDI₂** and **SC-NPDI₂** indicates that the dimers in the FC geometry may undergo a structural change in the excited state and form a different state, which can emit photons.^{41,61} However, the most intriguing aspect of the emissive excited-state of **SC-SPDI₂** and **SC-NPDI₂** is that the population of Ex or $S_{1(CT)}$ states does not quench photoluminescence quantum yield. What could be the excited-state structure that promotes the aforementioned optical properties? To address this, theoretical and experimental techniques have been employed to unravel the underlying excited-state phenomena.

4.2.3. Excited-state geometry optimizations and fragment-based analysis. In order to obtain in-depth insight into the excited-state relaxed structure, density functional theory-based geometry optimization has been performed in the excited-state by applying dispersion corrected

functional to account for the π -stacking interactions (TD-B3LYP-D3/def2-svp level of theory).^{62–65} The theoretical calculations propose that the ground state (S_0) near-orthogonal arrangement of **SC-SPDI**₂ and **SC-NPDI**₂ gets transformed to the nearly π -stacked foldamer conformation in the excited state (S_1) (Figures 4.6 and A4.1). Due to excited-state structural relaxation, the electronic interaction between the monomeric units increases as the dihedral angle (φ) between monomeric units lowers from 86.5° to 57.6° in **SC-SPDI**₂ and from 83.6° to 62.5° in **SC-NPDI**₂. Furthermore, the centroid to centroid distance (d) between annulated PDIs decreases from 5.97 Å to 4.50 Å for **SC-SPDI**₂ and 5.80 Å to 4.48 Å for **SC-NPDI**₂ upon excited-state structural relaxation (Figure A4.1). Schwartz and coworkers reported the existence of two conformers (near-orthogonal and nearly π -stacked arrangement) in the ground state of non-annulated bay-linked perylene diimide dimer (**di-PDI**, Figure A4.2).⁶⁶ The absence of two minima in the ground state potential energy surface of **SC-SPDI**₂ and **SC-NPDI**₂ when the dihedral angle changes from 45° to 125°, in contrast to **di-PDI**, could originate from the effect core-annulation has in altering the energy landscapes (Figure 4.7).

The nature of different excited-states of **SC-SPDI**₂ and **SC-NPDI**₂, in its Franck-Condon (FC) near-orthogonal geometry and relaxed excited-state foldamer geometry, were evaluated by fragment-based excited-state analysis (Figure 4.8 and Appendix, Section 4.7.3).^{67,68} The participation ratio (PR) defines the extent of delocalization of the excitation energy in different fragments (each annulated PDI monomer unit of dimers is considered as a fragment) and its magnitude will range from 2 (delocalized on 2 fragments) to 1 (localized on one fragment). The charge-transfer (CT) value describes the nature of the molecule's different excited-states. The CT value can vary from 1 to 0, where the excited-state having $CT < 0.2$ indicates Frenkel exciton and $CT > 0.8$ describes the charge-transfer state. Finally, the excited-state defined by CT values ranging

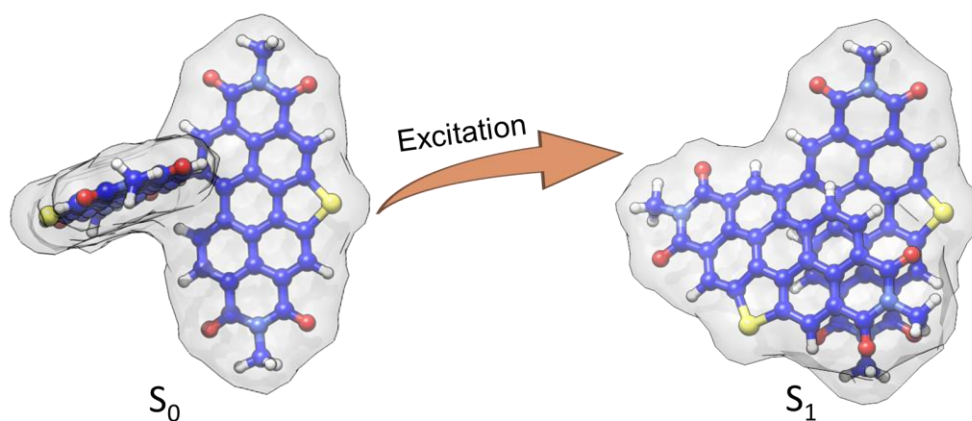


Figure 4.6: Excited-state structural relaxation of **SC-SPDI**₂ dimer upon photoexcitation.

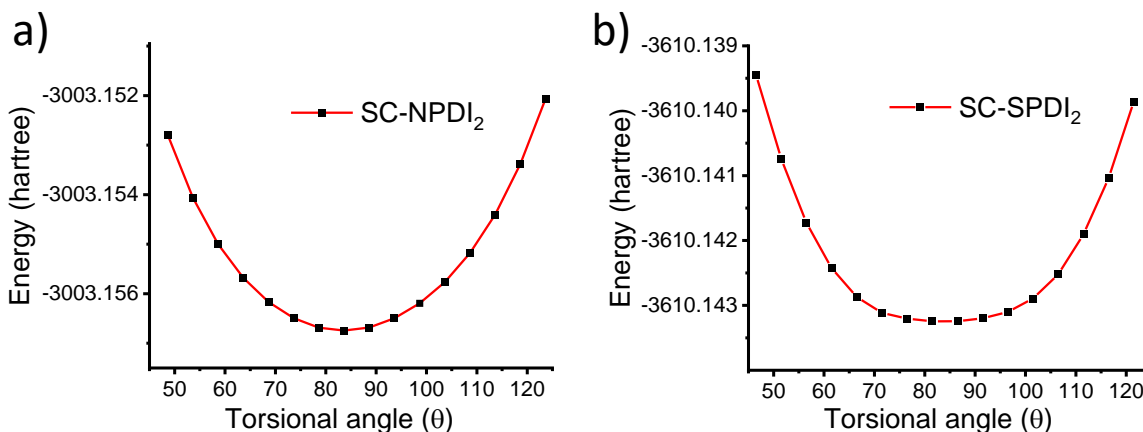


Figure 4.7: Potential energy curve of the dimers a) **SC-NPDI₂** and b) **SC-SPDI₂** in the ground state with varying torsional angles.

from 0.2 to 0.8 ($0.2 < CT < 0.8$, $PR > 1.25$) is assigned to an excimer state.^{67,69} In the FC geometry, **SC-SPDI₂** and **SC-NPDI₂** have four delocalized Frenkel exciton (FE) states, S_1 , S_2 , S_3 , and S_4 ($CT \cong 0$ and $PR = 2$) and two near-degenerate charge-transfer/resonance states, S_5 and S_6 ($CT \cong 0.94$ and $PR = 2$, Figures A4.3-A4.6 and Tables A4.5-A4.6). The charge resonance states (S_5 and S_6 , $CT \approx 1$) and delocalized Frenkel exciton states (S_1 - S_4 , $CT \approx 0$) are energetically well-separated in the FC geometry.

Fascinatingly, configuration mixing between Frenkel exciton state and charge-transfer states occurs when the FC geometry (near-orthogonal arrangement) of **SC-SPDI₂** and **SC-NPDI₂** is transformed to excited-state equilibrium geometry (π -stacked foldamer arrangement). The CT value of the first singlet excited-state (S_1) of relaxed foldamer geometry shows a magnitude of 0.37 for **SC-SPDI₂** and 0.39 for **SC-NPDI₂**, along with a PR value of 2, indicating that the monomer units interact strongly to form the stabilized excimer state.⁷⁰ i.e., the S_1 state of **SC-SPDI₂** and **SC-NPDI₂** in the foldamer arrangement does not remain as pure Frenkel exciton instead gains partial CT character. The description is schematically and pictorially represented in Figure 4.8 and Figure A4.3 using electron-hole correlation plots and isosurfaces of **SC-SPDI₂**. The different excited states of **SC-SPDI₂** and **SC-NPDI₂** in the foldamer configuration are given in Tables A4.7-A4.8 and Figures A4.6-A4.7. In the case of delocalized Frenkel exciton, both electron-hole (hole) and excited-electron densities are localized on the same molecular fragment and these local excitations on monomeric units get coupled to form a delocalized state (Figure 4.8, left side). In the charge resonance state, the electron-hole and excited-electron densities are completely localized on different monomeric units and is a linear combination of two charge-transfer transitions opposing

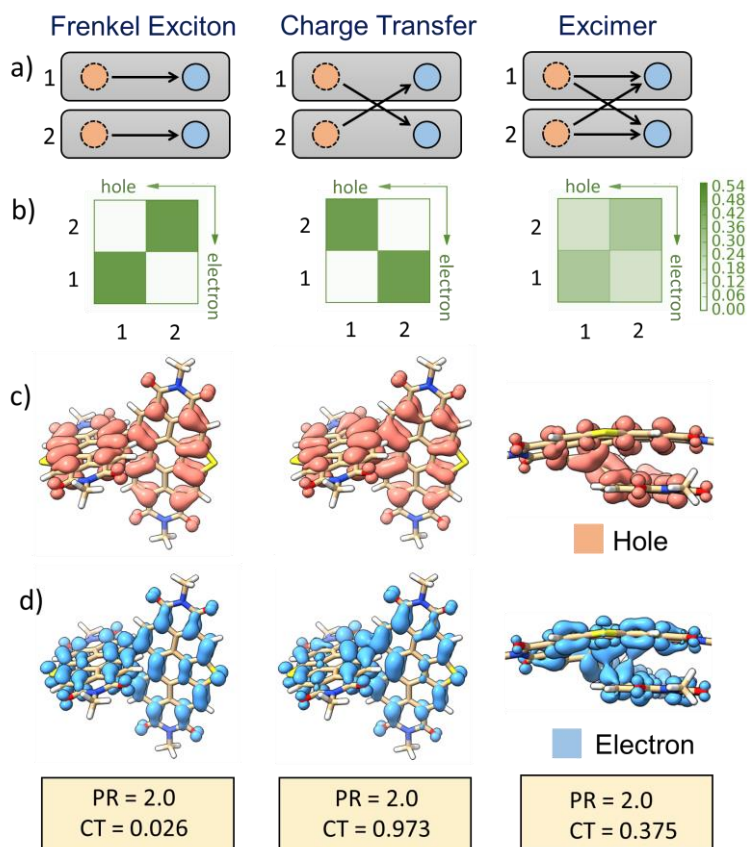


Figure 4.8: Pictorial representation of the delocalized Frenkel exciton (left), charge resonance states (middle) of FC geometry, and excimer state (right) of relaxed foldamer structure of **SC-SPDI₂**. a) Schematic representation of hole-electron distribution in the dimer, the rectangular box represents each fragment; dashed orange circles depict holes, and solid blue circles depict excited electrons. Hole-electron correlation plots (b) and corresponding isosurface of the hole (c, orange) and electron (d, blue) distribution of different excited-states of **SC-SPDI₂**. The CT and PR values are given at the bottom to define the nature of excitations.

each other with no net charge transfer observed (Figure 4.8, middle). Finally, the excimer state implies that electron-hole and excited-electron densities are delocalized over two monomeric units. i.e., both electron-hole and excited-electron of a monomeric unit can be found in the same or different monomeric unit (Figure 4.8, right side).^{67–69}

4.2.4. Solvent-dependent optical properties. To understand the surrounding dielectric constant moderated excited-state properties of **SC-SPDI₂** and **SC-NPDI₂**, we carried out absorption and fluorescence measurements in solvents of different dielectric constants, i.e., toluene (TOL, $\epsilon=2.4$), acetone (ACE, $\epsilon=20.7$), and acetonitrile (ACN, $\epsilon=37.5$). The solvent-dependent UV–vis absorption spectra of **SC-SPDI₂** and **SC-NPDI₂** exhibit virtually unperturbed absorption

line shapes, which is also the case for monomeric **SPDI** and **NPDI** (Figures 4.9, A4.8, A4.9 and Table 4.1). On the other hand, normalized solvent-dependent emission spectra of **SC-SPDI₂** and **SC-NPDI₂** show emission band broadening and red-shift in the emission maximum as the polarity of the solvent increases from TOL to ACE, implying stabilization of the emissive state with increasing solvent polarity (Figure 4.10). Further, the increase in polarity of solvent from ACE to ACN, **SC-NPDI₂** reflects gradual peak broadening and increase in Stokes shifts in normalized emission spectra, characteristics of charge-transfer character of the emissive state.^{29,71} However, normalized emission spectra of **SC-SPDI₂** exhibit negligible changes as the polarity changes from ACE to ACN, suggesting weaker charge-transfer characteristics of an emissive state.

The photoluminescence quantum yield (ϕ_{Fl}) of **SC-SPDI₂** and **SC-NPDI₂** drastically decrease with the increasing solvent polarity from TOL to ACE, presumably due to competitive non-radiative decay channels (ϕ_{Fl} =0.60 in TOL, 0.09 in ACE for **SC-SPDI₂** and ϕ_{Fl} =0.71 in TOL, 0.08 in ACE for **SC-NPDI₂**, Table 4.1). **SC-NPDI₂** exhibits further quenching of photolumi-

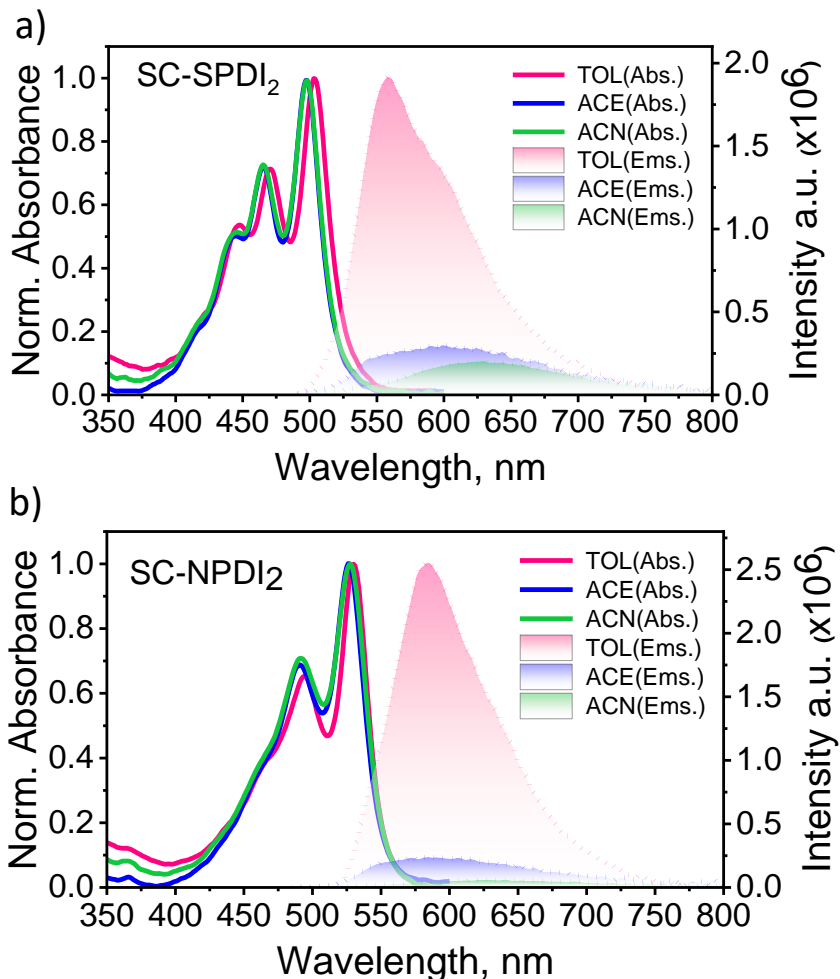


Figure 4.9: Solvent-dependent absorption and emission spectra of a) **SC-NPDI₂** and b) **SC-SPDI₂**.

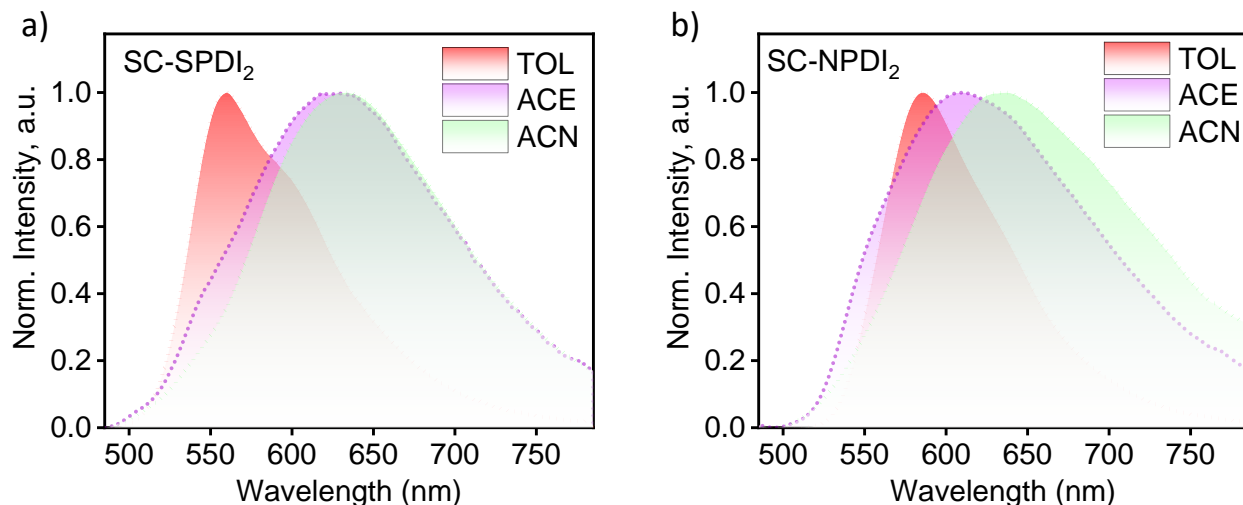


Figure 4.10: Solvent-dependent normalized emission spectra of a) **SC-SPDI₂** and b) **SC-NPDI₂**.

nescence as solvent polarity changes from ACE to ACN; in contrast, **SC-SPDI₂** exhibits negligible effects as the solvent polarity changes from ACE to ACN. The unique dielectric environment-dependent ϕ_{Fl} of **SC-SPDI₂** and **SC-NPDI₂** indicate the variation in the CT nature of the emissive excited-state as the solvent and molecular structure change (ϕ_{Fl} =0.09 in ACE, 0.08 in ACN for **SC-SPDI₂** and ϕ_{Fl} =0.08 in TOL, <0.01 in ACE for **SC-NPDI₂**).

The solvent-dependent fluorescence lifetime measurements of **SC-SPDI₂** and **SC-NPDI₂** show the disappearance of a shorter-lived fluorescence decay component and a decrease in the fluorescence lifetime of the second component as the solvent polarity increases from TOL to ACE (Table 4.1 and Figure 4.11). Additionally, as the dielectric medium changes from ACE to ACN, a negligible difference in the fluorescence lifetime was observed for **SC-SPDI₂** (τ_{Fl} =5.89 ns in ACE and 5.81 ns in ACN). However, **SC-NPDI₂** displays a slight decrease in the fluorescence lifetime as the polarity of the solvent increases (τ_{Fl} =3.82 ns in ACE and 2.23 ns in ACN; Table 4.1 and Figure 4.11). This discrepancy infers the dielectric dependency of the emissive state of **SC-NPDI₂**. The solvent-dependent photoluminescence quenching and decrease in the fluorescence lifetime of **SC-SPDI₂** and **SC-NPDI₂** in more polar solvents (ACE and ACN) implies the existence of an additional non-radiative deactivation channel like SB-CS.⁵⁷ Photoluminescence quantum yield and fluorescence lifetime of monomers **SPDI/NPDI** are nearly-insensitive to solvent polarity (Figure A4.10 and Table 4.1).

4.2.5. Energetics. In order to determine the feasibility of the photoinduced SB-CS in **SC-SPDI₂** and **SC-NPDI₂** in polar solvents, the thermodynamical driving force (ΔG_{CS}) for the SB-CS process has been analyzed using the Weller formulation (Figure 4.12, Tables A4.2 and 4.2, Appe-

ndix, Section 4.6).⁷² The Weller analysis gives $\Delta G_{SB-CS} \approx -0.42$ and -0.46 eV for **SC-SPDI₂**

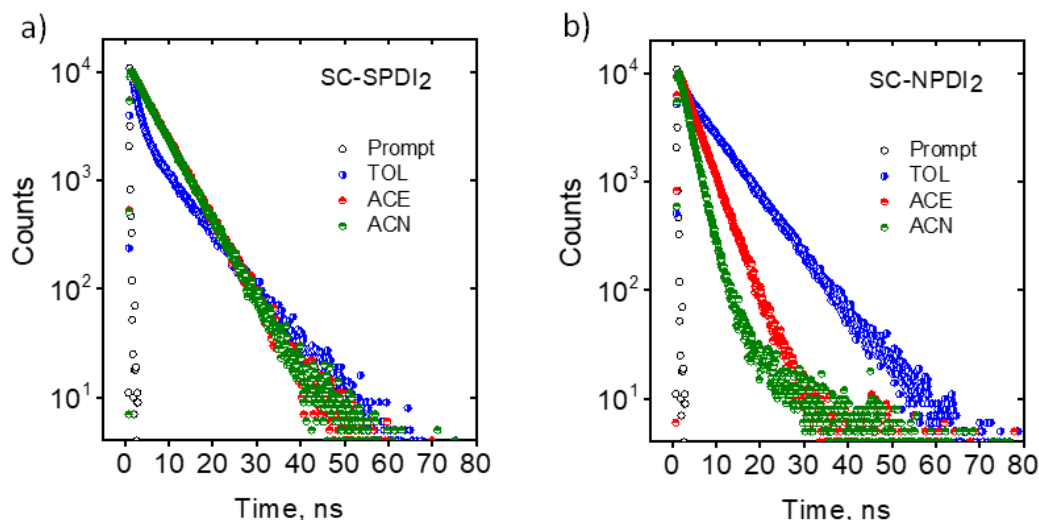


Figure 4.11: Fluorescence decay profiles of a) **SC-SPDI₂** and b) **SC-NPDI₂** in different solvents. The fluorescence decay profile of **SC-NPDI₂** in ACN is biexponentially fitted. The second component is assigned to scattering contribution as **SC-NPDI₂** has very low fluorescence quantum yield in ACN ($<0.1\%$).

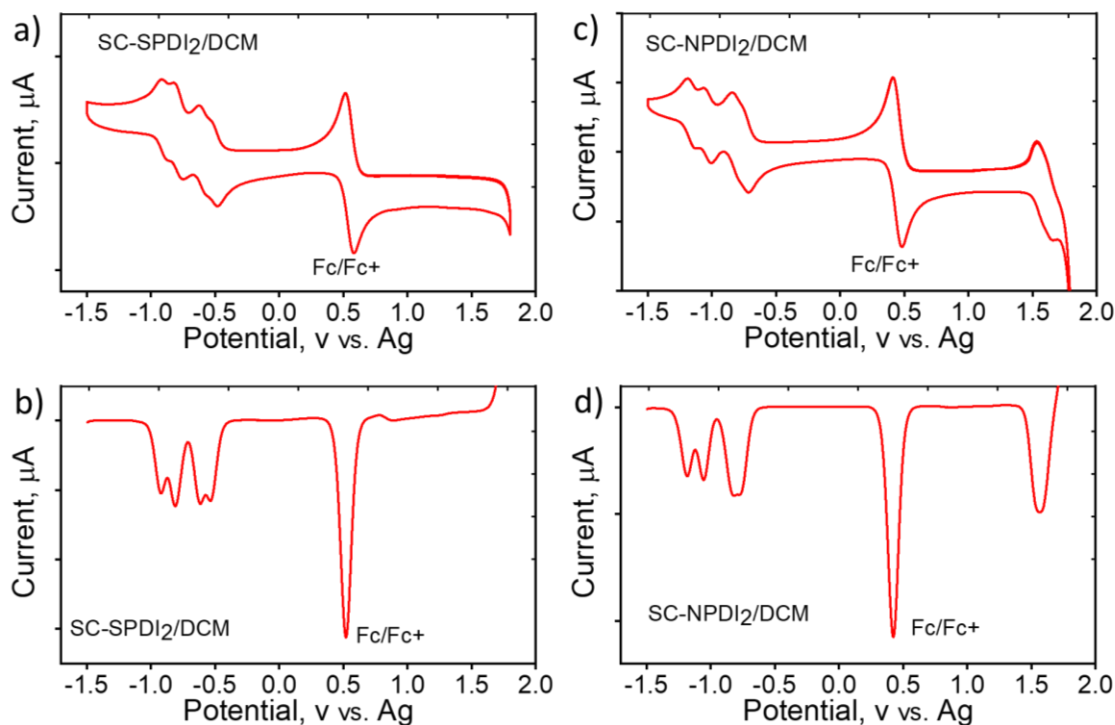


Figure 4.12: (a, c) Cyclic voltammetry data and (b, d) differential pulse voltammograms of **SC-SPDI₂** and **SC-NPDI₂** in CH_2Cl_2 . (Tetrabutylammonium hexafluorophosphate (0.1 M) as the supporting electrolyte, scan rate 100 mV s^{-1} . Fc/Fc^+ =ferrocene/ferrocenium couple).

Table 4.2: Summary of redox potentials and HOMO/LUMO calculations of **SC-SPDI₂** and **SC-NPDI₂** (CH_2Cl_2 , 298 K, $\epsilon_S = 8.93$).

| Compound | $E_{1(\text{red})}$ (v) | $E_{2(\text{red})}$ (v) | $E_{3(\text{red})}$ (v) | $E_{4(\text{red})}$ (v) | λ_{onset} (nm) | E_g^{opt} | HOMO (eV) | LUMO (eV) | E_{00} (eV) |
|--|----------------------------|----------------------------|----------------------------|----------------------------|----------------------------------|--------------------|--------------|--------------|------------------|
| SC-SPDI₂ | -0.54 | -0.62 | -0.81 | -0.92 | 527.00 | 2.35 | -6.10 | -3.74 | -2.48 |
| SC-NPDI₂ | -0.77 | -0.82 | -1.06 | -1.18 | 551.95 | 2.25 | -5.85 | -3.60 | -2.34 |
| E'_{red} is the reduction potential vs. Ag and E_{red} is the reduction potential vs. Fc/Fc ⁺ . | | | | | | | | | |

and $\Delta G_{\text{SB-CS}} \approx -0.40$, and -0.43 eV for **SC-NPDI₂** in ACE and ACN respectively, indicating that SB-CS is thermodynamically favored in ACE and ACN (exergonic process) as compared to non-polar TOL ($\Delta G_{\text{SB-CS}} \approx +0.20$ and $+0.25$ eV respectively, endergonic process).⁷³ The electronic interaction between frontier molecular orbitals of the adjacent monomeric units in the FC geometry of **SC-SPDI₂** and **SC-NPDI₂** provides the required electronic coupling for charge separation (Figures A4.11&A4.12).^{3,32}

4.2.6. Excited-state population dynamics. To shed light on excited-state dynamics accountable for the excimer formation, solvent-dependent fluorescence quenching, and SB-CS in **SC-SPDI₂** and **SC-NPDI₂**, femtosecond transient absorption (fsTA) measurement of the annulated **PDI** dimers were performed (optical density=0.2 to 0.3, excitation at 470 nm, using a ~ 100 fs laser pulse). To extract the temporal and spectral evolutions from the time versus wavelength-based three-dimensional map of the fsTA spectra, a singular value decomposition (SVD) followed by global fitting of the fsTA data using $\text{A} \rightarrow \text{B} \rightarrow \text{C} \rightarrow \text{D}$ sequential models was performed.^{74,75} The solvent-dependent fs-TA spectra of reference molecule, **SPDI** and **NPDI**, exhibit the characteristic spectral features of singlet excited-state (S_1 to S_n transition) of a **PDI** chromophore in the initial time, which decays with the evolution of triplet state of the monomeric unit with a weak spectral signature (Figures 4.13-4.14).^{24,35,54,76}

Upon photoexcitation of the **SC-SPDI₂** in TOL at 470 nm, fsTA spectra exhibit a strong negative ground state bleach (GSB) and weak stimulated emission (SE) between 450 and 563 nm, and excited-state absorption (ESA) maxima at 657 nm in the initial few picoseconds, assigned to singlet excited-state ($^1\text{SC-SPDI}_2$, Figure 4.15 and Figure A4.13). Followed by the rapid broadening of the ESA features between 570-760 nm and the evolution of a small negative SE signal at 538-578 nm region within several hundreds of picoseconds, indicative of the structural relaxation to the unrelaxed excimer (Ex^* ; vide infra). SE signal maximum centered at 558 nm is

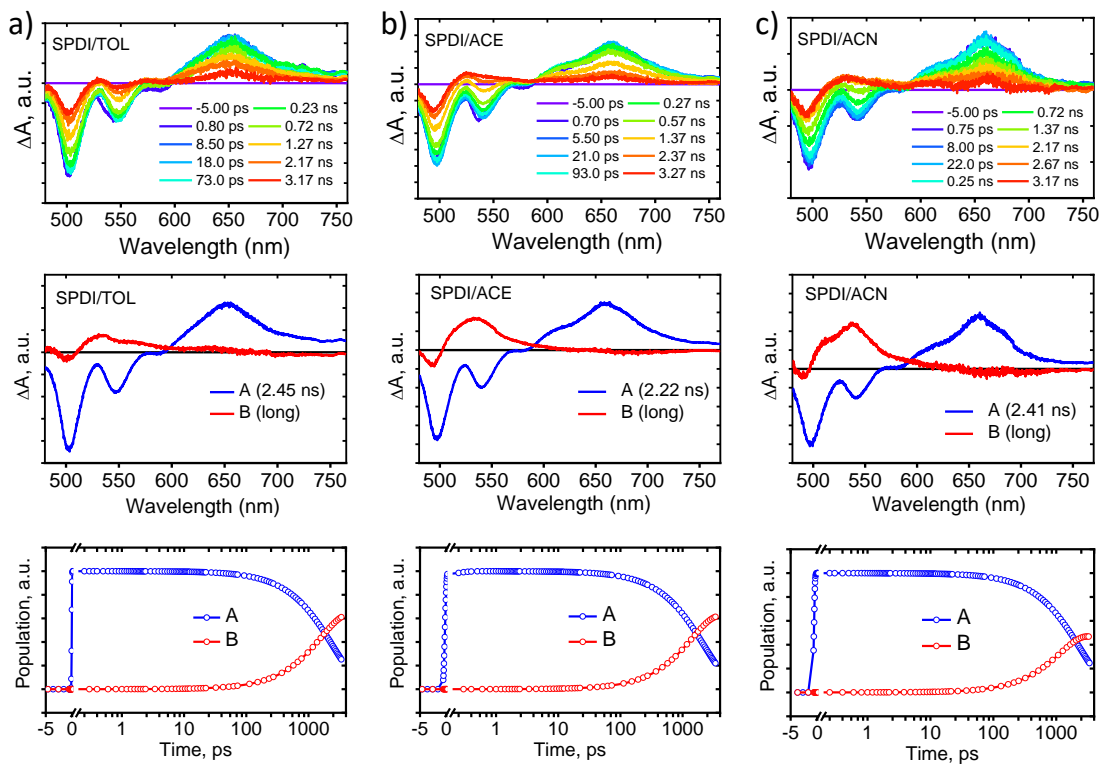


Figure 4.13: Femtosecond transient absorption spectra (top), evolution associated spectra (EAS, middle) and population profiles (bottom) of SPDI in different solvents.

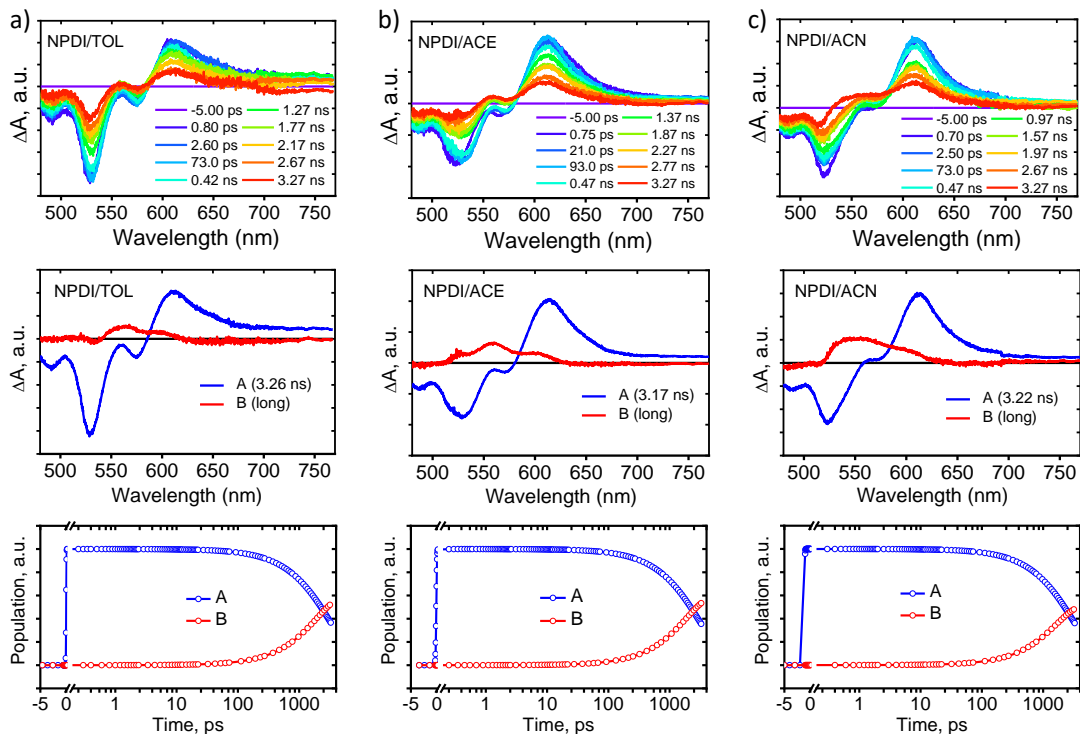


Figure 4.14: Femtosecond transient absorption spectra (top), evolution associated spectra (EAS, middle) and population profiles (bottom) of NPDI in different solvents.

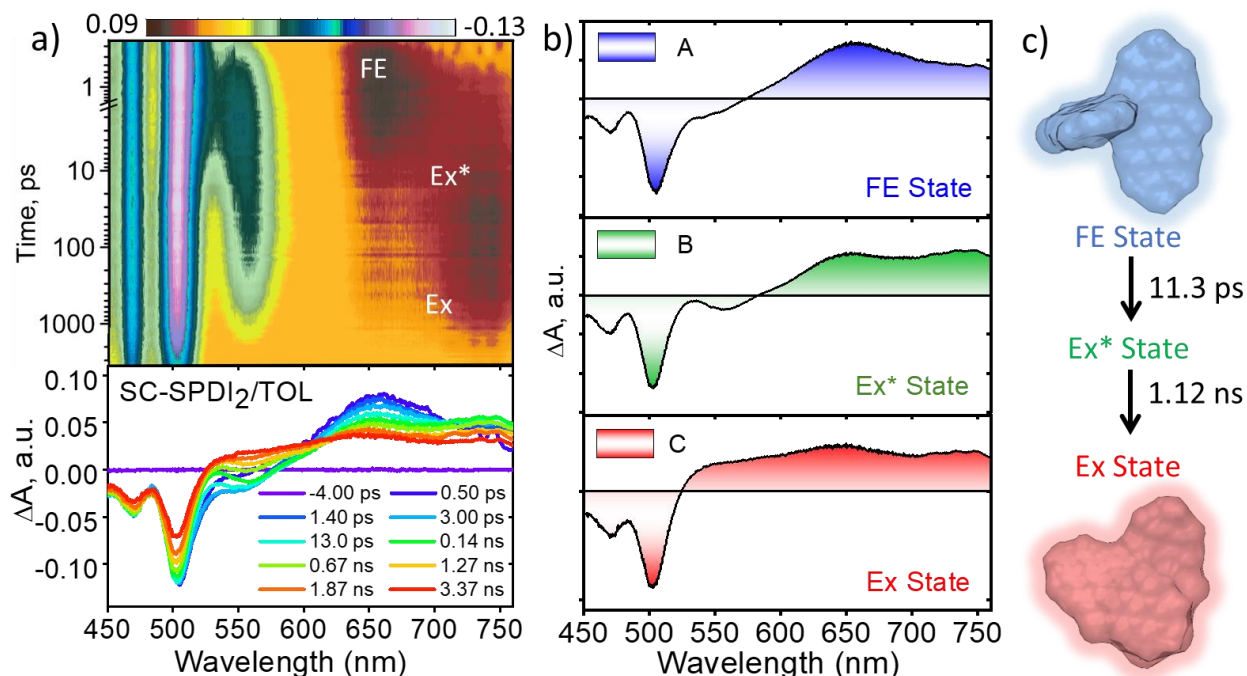


Figure 4.15: (a) Femtosecond transient absorption contour maps (top) and spectra (bottom) of *SC-SPDI*₂ in toluene (TOL) showing the excited-state dynamics after photoexcitation at 470 nm. (b) Evolution associated difference spectra reconstructed from global analysis of $A \rightarrow B \rightarrow C \rightarrow D$ model, where FE is the Frenkel exciton/Singlet excited state; Ex^* is the unrelaxed excimer state; Ex is the relaxed excimer state. (c) Schematic representation of excited-state dynamics of *SC-SPDI*₂ in toluene at room temperature.

comparable with steady-state emission maximum ($\lambda_{max}^{Em} = 558$ nm), suggesting the emissive nature of the corresponding component. Later, singlet ESA disappears with the rise of a new broad and structureless ESA feature between 530 and 760 nm with an isosbestic point at ~ 601 nm, representing the relaxed excimer state (Ex). The presence of two excimer states arises from the structural rearrangement of initially formed high-energy unrelaxed excimer states (Ex^*) to achieve the potential minimum of a stable excimer state.^{25,37,71} Global fitting of the fsTA data shows that singlet excited-state/ FE (A) decay to unrelaxed excimer state (B) with a time constant of $\tau_{A \rightarrow B} = 11.3$ ps, followed by the rise of structurally relaxed excimer state (C) occurring with the lifetime of $\tau_{B \rightarrow C} = 1.12$ ns. Further, the long-lived relaxed excimer state (C) does not decay completely within the experimental time window and which is fitted with a time constant of 8.10 ns.

Similarly, fsTA spectra of *SC-NPDI*₂ in TOL (Figure 4.16 and A4.13) display the singlet excited or FE state features in early times (GSB/SE at 450–560 nm and ESA maxima at 620 nm),

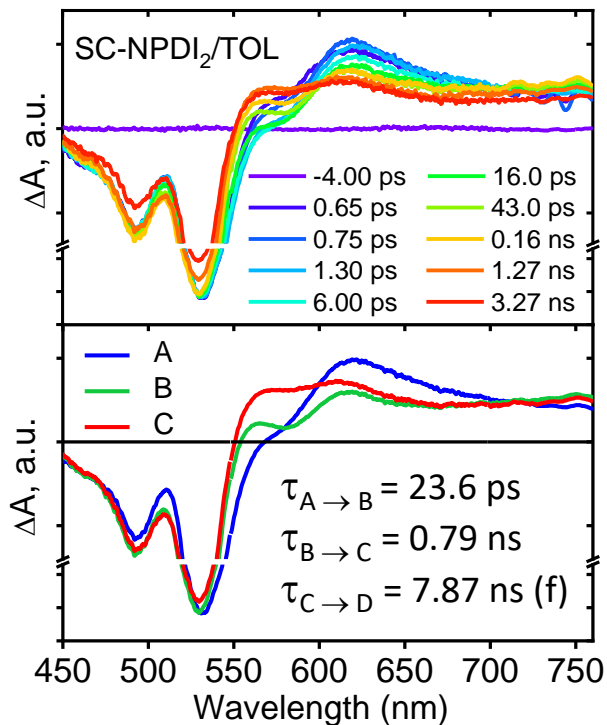


Figure 4.16: Femtosecond transient absorption spectra (top), Evolution associated spectra (bottom) of **SC-NPDI₂** in toluene.

which decays to intermediate unrelaxed excimer state ($\tau_{A \rightarrow B} = 23.6$ ps) characterized by the formation of a new SE band centered at 583 nm ($\lambda_{max}^{Em} = 584$ nm) and broadening of ESA spectral features in the 620–760 nm (the isosbestic point at ~ 580 nm). Furthermore, the unrelaxed high-energy excimer (B) relaxes to form a stable, relaxed excimer state (C, $\tau_{B \rightarrow C} = 0.79$ ns) characterized by featureless and broad ESA, which does not decay within the experimental time window and is fitted with a time constant of 7.87 ns. The two different excimer decay time constants agree with the fluorescence lifetime of **SC-SPDI₂** and **SC-NPDI₂** in TOL, indicating the emissive nature of B and C components (Tables 4.1 and 4.3). The difference in the ESA signature of unrelaxed (B) and relaxed excimer (C) states owes to the higher photoluminescence behavior of the unrelaxed excimer state (Ex*) as compared to the stable excimer state (Ex, vide infra). The approximate twofold increase in the time constant for structural relaxation of **SC-SPDI₂** compared to **SC-NPDI₂** in TOL could have resulted from the difference in the excited-state energy landscapes.

In polar solvents (ACE and ACN), **SC-SPDI₂** shows GSB between 450–538 nm and ESA maxima at ~ 662 nm in the initial time delays (Figures 4.17, 4.18, A4.14 and A4.15). Subsequently, the synchronized evolution of the two transient species is characterized by positive ESA features in the visible region at ~ 575 and 669 nm. The newly evolving ESA signature is attributed to radical

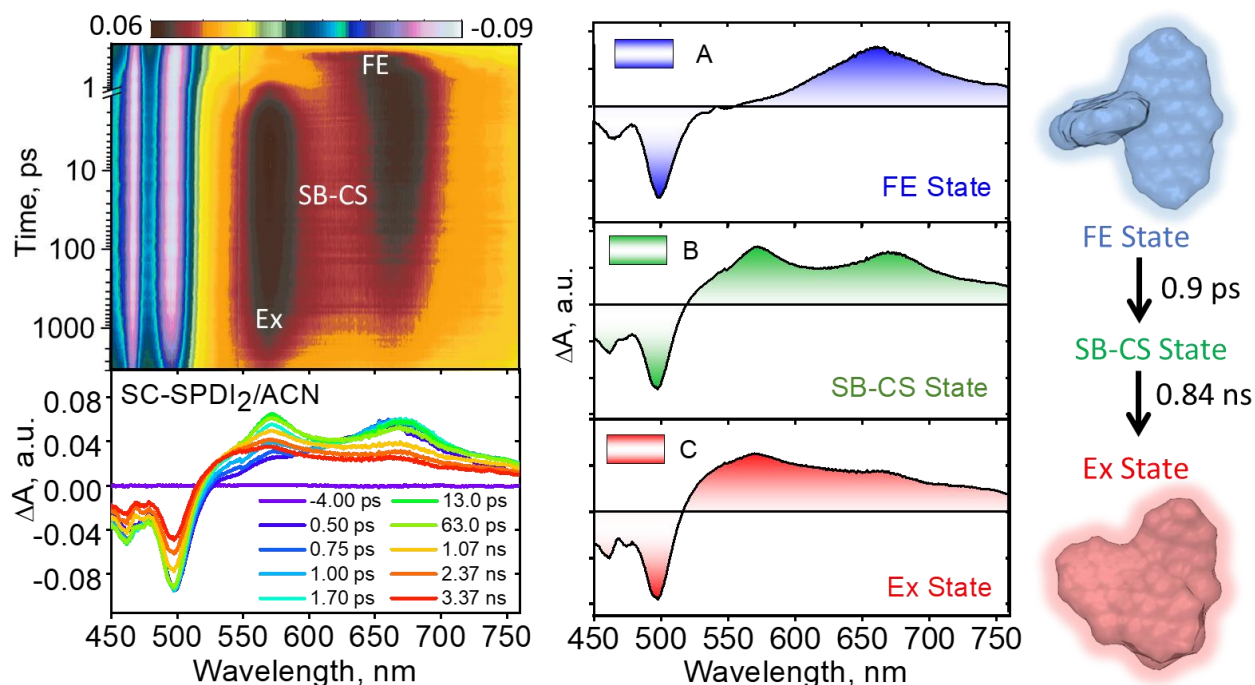


Figure 4.17: (a) Femtosecond transient absorption contour maps (top) and spectra (bottom) of **SC-SPDI₂** in acetonitrile (ACN) showing the excited-state dynamics after photoexcitation at 470 nm. (b) Evolution associated difference spectra reconstructed from global analysis of $A \rightarrow B \rightarrow C \rightarrow D$ model, where FE is the Frenkel exciton/Singlet excited state; SB-CS is the symmetry-breaking charge-separated state; Ex is the excimer state. (c) Schematic representative excited-state dynamics of **SC-SPDI₂** in acetonitrile at room temperature.

cation (ESA~575 nm) and radical anion (EAS~669 nm) of **SC-SPDI₂**, i.e., the SB-CS state (Figure A4.16). The concurrent growth of radical pairs of chromophores is the characteristic signature of intramolecular charge separation occurring between identical chromophores due to the solvent or structural vibration-induced symmetry breaking.^{7,61,77-79} Further, the radical pair of **SC-SPDI₂** decay forms a new transient state with broad spectral signatures resembling the characteristic excimer state features. The sequential fitting of the fsTA data shows ultrafast decay of singlet excited state/Frenkel exciton (A) of **SC-SPDI₂** with the evolution of SB-CS state (B) with a time constant of 1.5 ps and 0.9 ps in ACE and ACN, respectively, which is ~8-13 fold faster than excimer formation in TOL. Afterward, the SB-CS state (B) decays to the relaxed excimer (C) with a time constant of approximately 2.01 ns in ACE and 0.84 ns in ACN (Table 4.4). The long-lived excimer state (C) is fitted with a time constant of 5.89 ns in ACE and 5.81 ns in ACN, assuming that photoluminescence of **SC-SPDI₂** in ACE (τ_{Fl} =5.89 ns) and ACN (τ_{Fl} =5.81 ns) originated from relaxed excimer state (Ex).

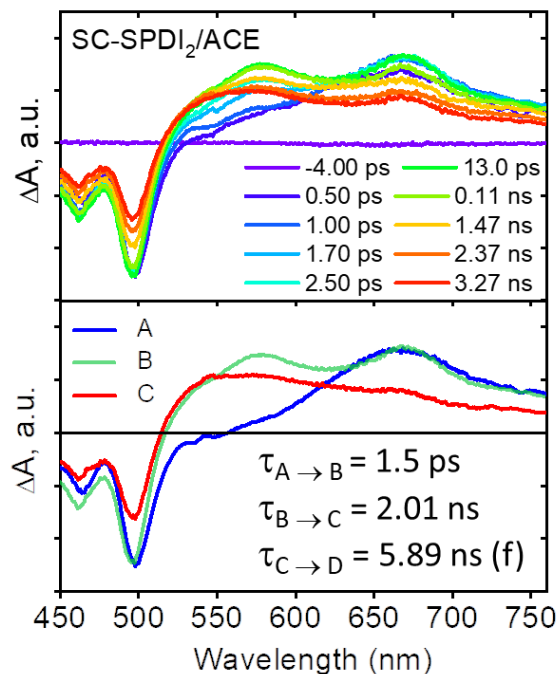


Figure 4.18: Femtosecond transient absorption spectra (top), Evolution associated spectra (EAS, bottom) of **SC-SPDI₂** in acetone.

Table 4.3: Time constants for the different excited processes as observed from the fsTA measurements of **SC-SPDI₂** and **SC-NPDI₂** in different solvents.

| | | SC-NPDI ₂ | SC-SPDI ₂ |
|--|---------------|----------------------|----------------------|
| TOL | FE→Ex* | 23.6 ps | 11.3 ps |
| | Ex*→Ex | 0.79 ns | 1.12 ns |
| | Ex→Triplet/GS | 7.87 ns | 8.10 ns |
| ACE | FE →SB-CS | 2.7 ps | 1.5 ps |
| | SB-CS →Ex | 1.66 ns | 2.01 ns |
| | Ex→Triplet | 3.82 ns | 5.89 ns |
| ACN | FE → SB-CS | 1.4 ps | 0.9 ps |
| | SB-CS →Ex | 0.71 ns | 0.84 ns |
| | Ex→Triplet | 2.30 ns | 5.81 ns |
| FE: Frenkel exciton, Ex*: Unrelaxed excimer, Ex: Relaxed excimer, SB-CS: Symmetry-Breaking Charge Separation | | | |

The excited-state dynamics of **SC-NPDI₂** in ACE and ACN are similar to **SC-SPDI₂** in ACE and ACN, as shown in Figures 4.19, A4.17 and A4.18. The fsTA spectra at 0.5 ps show

singlet excited-state/Frenkel exciton (A) features of **SC-NPDI₂** (ESA=555–760 nm /GSB=<555 nm), which decays to SB-CS state (B, $\tau_{A \rightarrow B}$ =2.7 ps for ACE and 1.4 ps for ACN). ESA centered at ~561 nm (radical cation of **SC-NPDI₂**) and 673 nm (radical anion of **SC-NPDI₂**) appear in the initial few picoseconds, indicating the ultrafast SB-CS state formation.^{24,54} Later, the SB-CS state (B) decays with the formation of a new excimer state (C) having a charge-transfer character ($\tau_{B \rightarrow C}$ =1.66 ns for ACE and 0.71 ns for ACN). As observed in a previous report by Kim, Wurthner and coworkers, this broad spectral feature can be assigned to an excimer state with a strong charge-transfer (CT) resonance character.⁵⁷ On the contrary, the excimer state of **SC-SPDI₂** in polar solvents exhibits a weak CT resonance nature. The lifetime of the long-lived CT resonance excimer state is fitted with ($\tau_{C \rightarrow D}$ =3.82 ns in ACE and 2.3 ns in ACN) the fluorescence lifetime decay component observed. The decrease in the ratio of 0-0 and 0-1 vibronic bands intensity in the GSB may be an indication of excited-state structural relaxation of **SC-SPDI₂** and **SC-NPDI₂** dimers from near-orthogonal arrangement to relaxed foldamer structure (Figure A4.19).³⁷ Energy level diagrams showing the solvent-dependent distinct excited-state decay processes occurring in **SC-SPDI₂** and **SC-NPDI₂** along with the geometries of the dimers in the ground state and relaxed excited-state are shown in Figure 4.20.

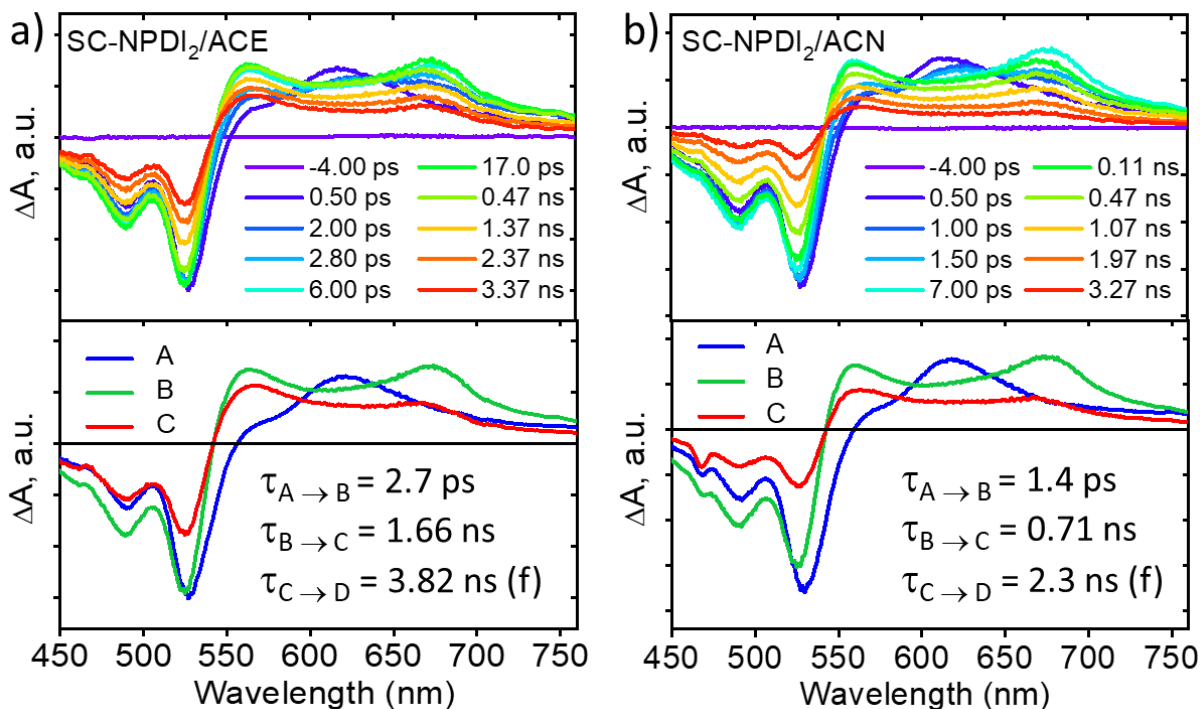


Figure 4.19: Femtosecond transient absorption spectra (top), Evolution associated spectra (EAS, bottom) of **SC-NPDI₂** in a) acetone and b) acetonitrile.

Table 4.4: Driving forces (ΔG), Time Constants (τ), Rate Constants (k) for Symmetry-Breaking Charge Separation (SB-CS) of **SC-SPDI₂** and **SC-NPDI₂** in different solvents.

| | Solvents | ΔG_{CS} (eV) | τ_{CS} (ps) | $k_{CS} \times 10^{11}$ (s ⁻¹) |
|----------------------------|----------|----------------------|------------------|--|
| SC-SPDI₂ | TOL | +0.20 | - | - |
| | ACE | -0.42 | 1.5 | 6.67 |
| | ACN | -0.46 | 0.9 | 11.1 |
| SC-NPDI₂ | TOL | +0.25 | - | - |
| | ACE | -0.40 | 2.7 | 3.70 |
| | ACN | -0.43 | 1.4 | 7.14 |

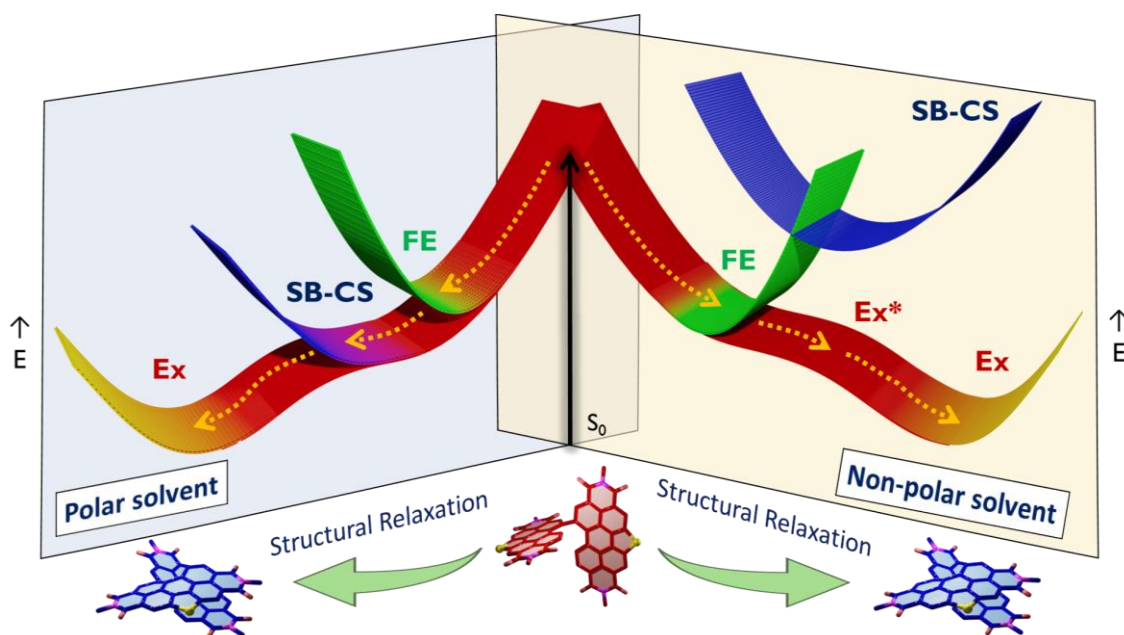


Figure 4.20: The potential energy diagram summarizes the excited-state dynamics of **SC-SPDI₂** and **SC-NPDI₂** undergoes structural relaxation in polar solvents (ACE and ACN) and non-polar solvent (TOL), where FE is the Frenkel exciton, Ex* is the unrelaxed excimer state, Ex is the stable excimer state and SB-CS is the symmetry-breaking charge-separated state. The x-axis represents the reaction coordinate and E on the y-axis indicates the potential energy.

To obtain further evidence on the late events of **SC-SPDI₂** and **SC-NPDI₂**, nanosecond transient absorption (nsTA) spectroscopy measurements were performed in different solvents (Figures 4.21, 4.22, A4.20, and A4.21). In TOL, nsTA spectra of **SC-SPDI₂** show a positive ESA band at around 550 nm corresponding to the $T_1 \rightarrow T_n$ transition and negative GSB below 515 nm,

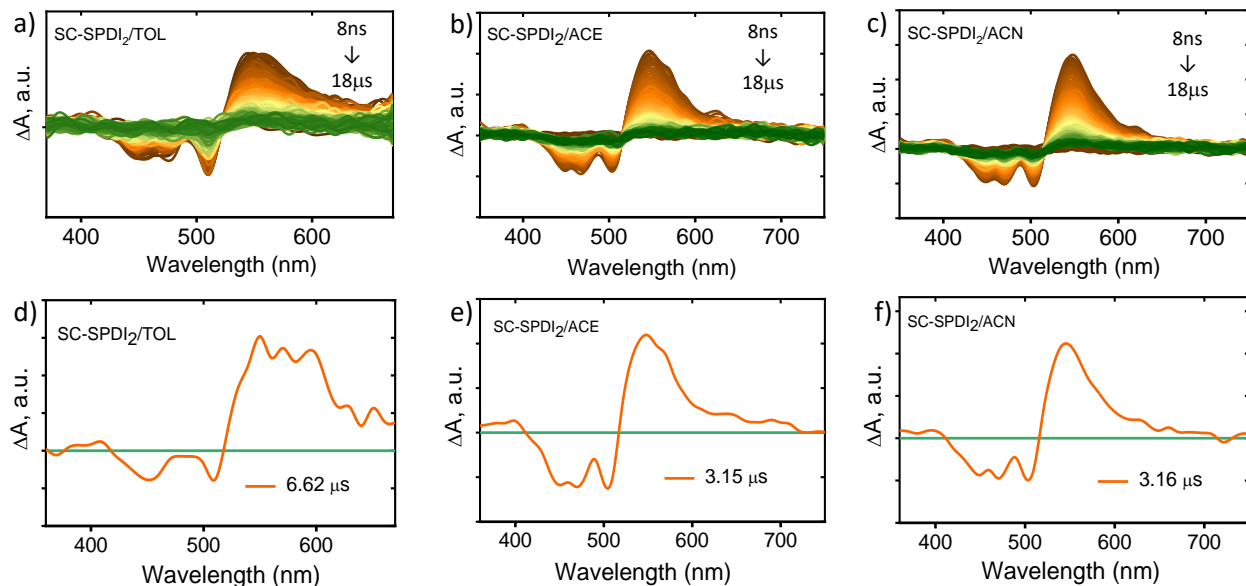


Figure 4.21: (Top) Nanosecond transient absorption spectra of **SC-SPDI₂** in (a) TOL, (b) ACE and (c) ACN showing the excited-state dynamics after photoexcitation in N₂ atmosphere. (Bottom) Evolution-associated spectra were reconstructed from global analysis of the $A \rightarrow GS$ model in all solvents.

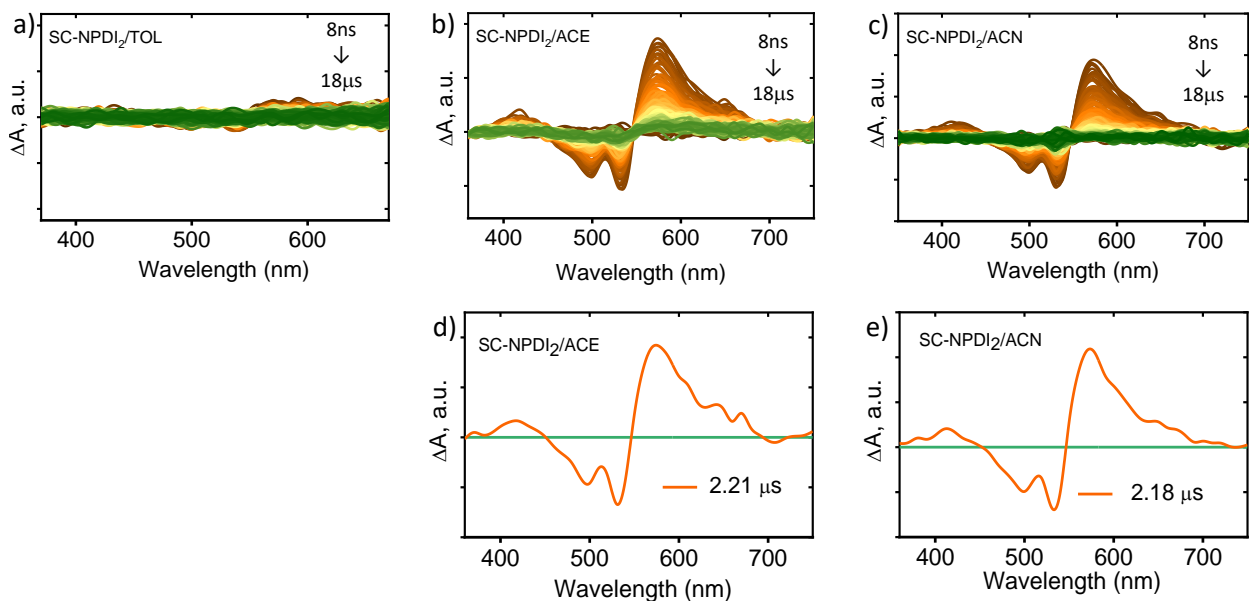


Figure 4.22: (Top) Nanosecond transient absorption spectra of **SC-NPDI₂** in (a) TOL, (b) ACE and (c) ACN showing the excited-state dynamics after photoexcitation in N₂ atmosphere. (Bottom) Evolution associated spectra were reconstructed from global analysis of the $A \rightarrow GS$ model in all solvents.

which decay with a lifetime of 6.62 μs. At the same time, **SC-NPDI₂** in TOL does not show any

spectral signature of the triplet state. Conversely, **SC-SPDI₂** and **SC-NPDI₂** in polar solvents (ACE and ACN) show the characteristic of a triplet manifold (GSB/ESA=515 nm/550 nm for **SC-SPDI₂** and GSB/ESA=535 nm/585 nm for **SC-NPDI₂**), which decay to ground state with a lifetime of 3.15 μ s and 3.16 μ s for **SC-SPDI₂** and 2.21 μ s and 2.18 μ s for **SC-NPDI₂**, respectively. Overall excited state dynamics of **SC-SPDI₂** and **SC-NPDI₂** in different solvents are shown in Figures A4.22-A4.25. The population of excimer state through two different pathways in cofacially arranged perylene dimer have also been reported by Wasielewski and coworkers.²⁵ In polar solvent, partial excimer formation through an SB-CS intermediate state as well as direct excimer population are favored in the weakly coupled cofacial perylene dimer. In our case, effective electronic coupling between FE state and SB-CS state in the near-orthogonal FC geometry of **SC-SPDI₂** and **SC-NPDI₂** facilitates the ultrafast SB-CS and suppresses the excimer formation in the initial time. This is supported by the rate constant of SB-CS in polar solvents being 8-17 folds greater than the rate constant of Ex* formation or excited state structural relaxation in toluene (Table 4.3).

4.2.7. Interplay of FE and CT contribution on excimer state. The excited-state structural relaxation of **SC-SPDI₂** and **SC-NPDI₂** leads to the foldamer structure in the delayed timescales, which renders the excimer state having varying CT and FE character. The excimer state is an adiabatic admixture of Frenkel exciton (FE) and the charge-transfer state (CT).⁸⁰ The relative contributions of the FE and the CT states are dependent on the distance and relative orientation between the chromophore and dielectric medium around the chromophore.^{4,57,69,81,82} In a non-polar solvent, TOL, the energy of the CS/CT state of **SC-SPDI₂** and **SC-NPDI₂** is higher than that of the singlet state/FE state; as a result, efficient mixing of FE state with CT/CS is less probable. Consequently, excimer having more prominent FE character than CT character is observed in the fsTA spectra of **SC-SPDI₂** and **SC-NPDI₂** in TOL, which could be the reason for high ϕ_{FL} of dimers in TOL (Figure 4.15 and Figure A4.16). However, excimer state spectral signatures of **SC-SPDI₂** and **SC-NPDI₂** in polar solvents nearly resemble the SB-CS state, with the positions of the radical pair bands being the same with broader ESA. This observation can be rationalized by fact that energy of CS state is more stabilized than the FE state in polar solvents, facilitating the efficient mixing of FE and CS state in the relaxed excited-state foldamer structure. Charge-transfer contribution to the excimer state of **SC-NPDI₂** is higher than **SC-SPDI₂** in polar solvents, which could stem from the reduced centroid to centroid distance (d) between monomers in the excited-state foldamer structure and the reduced energy difference between the FE and the CS state of **SC-**

NPDI₂ compared to **SC-SPDI₂** (Figure A4.1 and Table 4.4). Photoluminescence quenching and decrease in the fluorescence lifetime of **SC-NPDI₂** as the dielectric medium changes from ACE to ACN is attributed to the enhanced charge-transfer (CT) resonance character of the emissive excimer state. Due to the weak CT resonance nature of the emissive excimer state in **SC-SPDI₂**, the photoluminescence quantum yield and fluorescence lifetimes are nearly unperturbed by a change in solvent polarity, i.e., ACE to ACN (Table 4.1).

4.2.8. Time-resolved emission spectroscopy measurements. To obtain deep insights into the energy landscape of excited-state structural relaxation and excimer formation of **SC-SPDI₂** and **SC-NPDI₂** in TOL, we have performed picosecond time-resolved emission spectroscopy (TRES) measurements (Figures 4.23 and 4.24, Appendix, Section 4.8). The global analysis of TRES data of **SC-SPDI₂** and **SC-NPDI₂** using sequential model A→B indicate two dependent emissive states are present. Evolution associated spectra of the first species (EAS_A) show an intense emission band that resembles the steady-state emission spectra of **SC-SPDI₂** with λ_{max}^{Em} at 559 nm, which is assigned to unrelaxed excimer (Ex*, Figure A4.26). The Ex* state decays to a weakly emissive

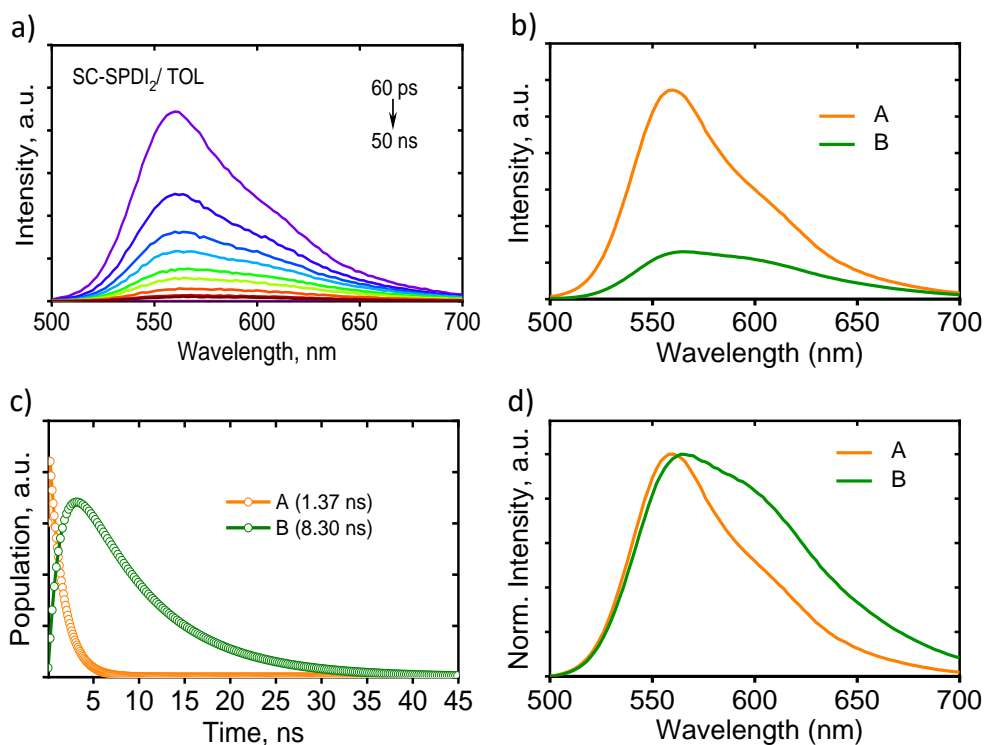


Figure 4.23: a) Time-resolved emission spectra (TRES, $\lambda_{ex}=478$ nm) of **SC-SPDI₂** in TOL, b) decay associated spectra (DAS), c) the relative population profiles of **SC-SPDI₂** in TOL and d) normalised decay associated spectra. The orange (A) and green (B) colored spectrum and decay profiles correspond to emission from the unrelaxed and relaxed excimer states.

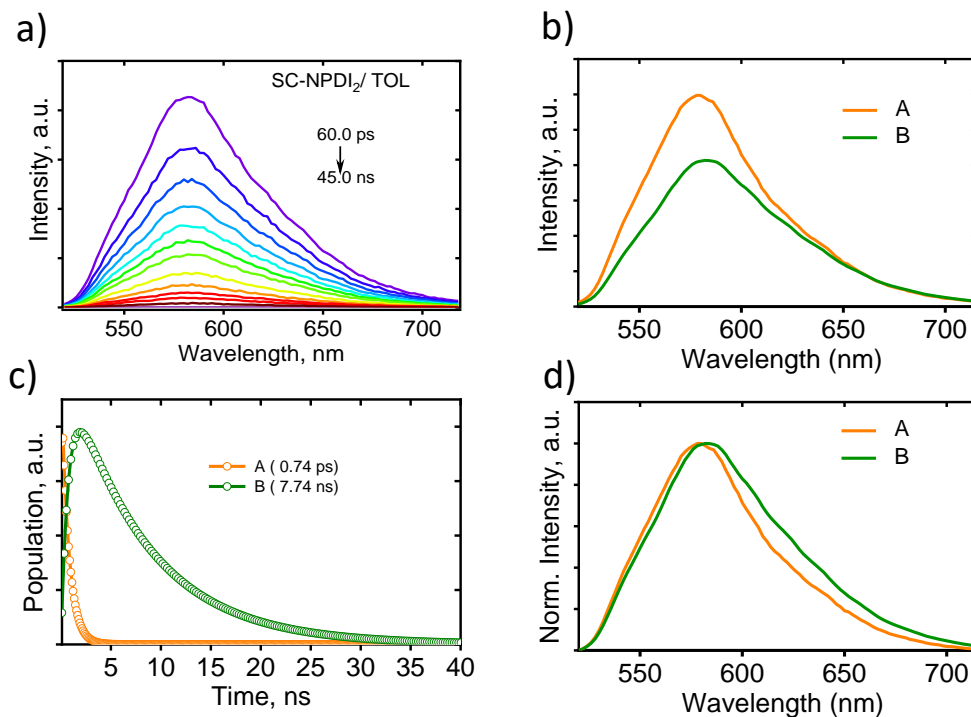


Figure 4.24: *a) Time-resolved emission spectra (TRES, $\lambda_{ex}=478$ nm) of SC-NPDI₂ in TOL, b) decay associated spectra (DAS), c) the relative population profiles of SC-NPDI₂ in TOL and d) normalised decay associated spectra. The orange (A) and green (B) colored spectrum and decay profiles corresponds to emission from the unrelaxed and relaxed excimer states.*

stable excimer state (Ex) with a time constant of $\tau_{Ex^* \rightarrow Ex}=1.37$ ns, which is comparable with the lifetime of Ex* observed in fsTA measurement ($\tau_{Ex^* \rightarrow Ex}=1.12$ ns). Weakly emissive, broadened, and red-shifted ($\lambda_{max}^{Em}=564$ nm) photoluminescence features are characteristics of excimer state (EAS_B) with a lifetime of 8.30 ns coinciding with the long-lived relaxed excimer observed in fsTA measurement. The evolution of the stimulated emission feature in fsTA of SC-SPDI₂ in TOL (Species B) can be rationalized by the intense emissive nature of Ex* (EAS_A) as compared to Ex (EAS_B, Figure A4.27). Similarly, SC-NPDI₂ in TOL exhibits emissive unrelaxed and relaxed excimer states (EAS_A and EAS_B), which decays with time constants of 0.74 ns and 7.42 ns. The relaxed excimer state (Ex) observed is weakly emissive in nature with red-shifted ($\lambda_{max}^{Em}=584$ nm) and broader spectral properties than that of strongly emissive unrelaxed excimer state ($\lambda_{max}^{Em}=579$ nm). Both decay time constants are coincidental with fsTA decay values, and the evolution of the new SE maximum matches the unrelaxed state emission maximum (Figure A4.24). TRES measurement unambiguously confirms that the structural relaxation energetically stabilizes the excimer state and gradually reduces the photoluminescence property.

4.2.9. Temperature-dependent photoluminescence measurements. Further insight into the excited-state structural relaxation of **SC-SPDI₂** and **SC-NPDI₂** dimers in TOL were provided by steady-state temperature-dependent photoluminescence (PL) measurements from 90K to 250K (Figure 4.25).^{40,83,84} Interestingly, at 90K, **SC-SPDI₂** and **SC-NPDI₂** show PL spectra with well-resolved vibronic progression and hypsochromic shifted emission maximum as compared to PL characteristics of dimers observed at room temperature ($\lambda_{max}^{Em}=540$ nm for **SC-SPDI₂** and $\lambda_{max}^{Em}=557$ nm for **SC-NPDI₂**, Figure A4.28). Moreover, the 0-0 transition approximately matches with the corresponding absorption spectrum onset and is assigned to emission from the Frenkel exciton (FE) state. The observed PL spectra of **SC-SPDI₂** and **SC-NPDI₂** at 90K resemble emission features of a monomeric unit with a decrease in the 0-0 to 0-1 PL line strength ratio, which confirms the delocalization of excitation energy among both monomeric unit in the Franck-Condon geometry (Figure A4.29).⁸⁵ As the temperature increases, a gradual reduction in the PL intensity and inversion in the vibronic peak ratio is observed, indicating the transformation of FC geometry to an H-type foldamer conformation.^{86,87}

In the warming temperature of TOL between 140K and 170K, vibronically resolved PL features from the FE disappear and broader, less featured, and red-shifted PL spectra evolves ($\lambda_{max}^{Em}=552$ nm and 582 nm for **SC-SPDI₂** and **SC-NPDI₂**, respectively). The observed PL spectra (140K-170K) resemble the time-resolved emission spectral signatures of the unrelaxed excimer (Ex*) state and emission from Ex* state is more predominant with an overlapping component of a

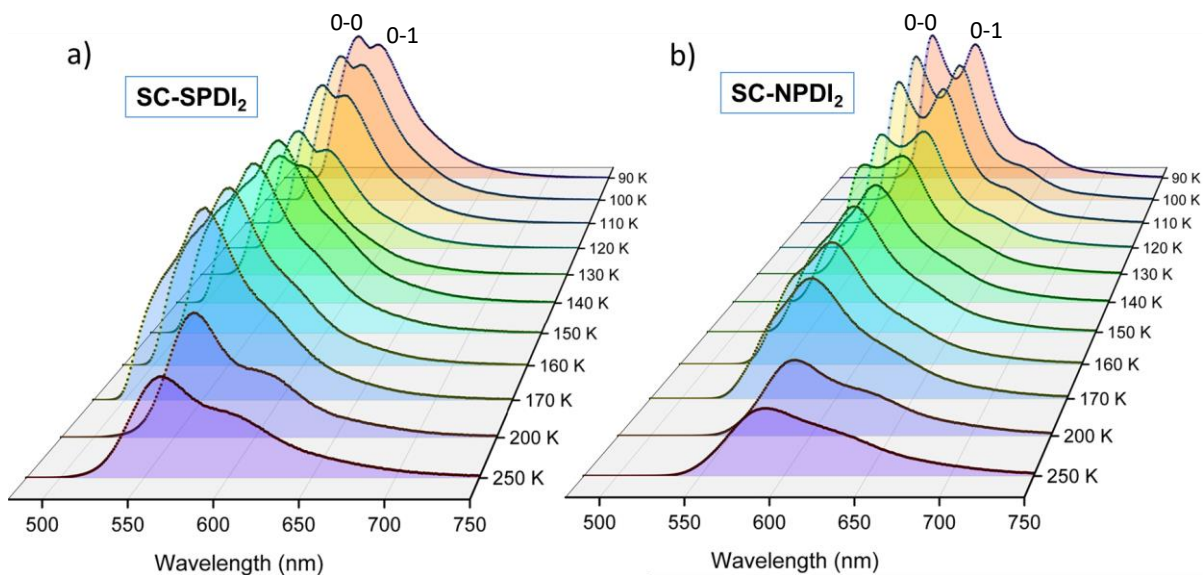


Figure 4.25. The temperature-dependent photoluminescence spectra of (a) **SC-SPDI₂** and (b) **SC-NPDI₂** in toluene.

minor amount of emission from FE state (Figure 4.26). The PL intensity of **SC-SPDI₂** in warming temperature is slightly higher than that at 130K, indicating the higher transition strength of the Ex* state than the FE state. At the same time, PL intensity of **SC-NPDI₂** decreases gradually as the temperature increases from 90K to 170K. Finally, at high temperatures (>170K), PL spectra are further broadened, red-shifted ($\lambda_{max}^{Em} = 560$ and 587 nm for **SC-SPDI₂** and **SC-NPDI₂**, respectively) and PL intensity decreases dramatically, representing the formation of a relaxed excimer state (Ex), which resembles the room temperature PL spectra. The overlapping emission of unrelaxed excimer state (Ex*) and energy stabilized excimer state (Ex) define the PL emission spectra in this region (>170 K), and FE state emission is virtually absent due to the ultrafast structural reorganization as observed in fsTA measurements. The temperature-dependent PL measurement demonstrates the transformation of FC geometry of **SC-SPDI₂** and **SC-NPDI₂** to relaxed foldamer structure by excited-state structural relaxation at room temperature.

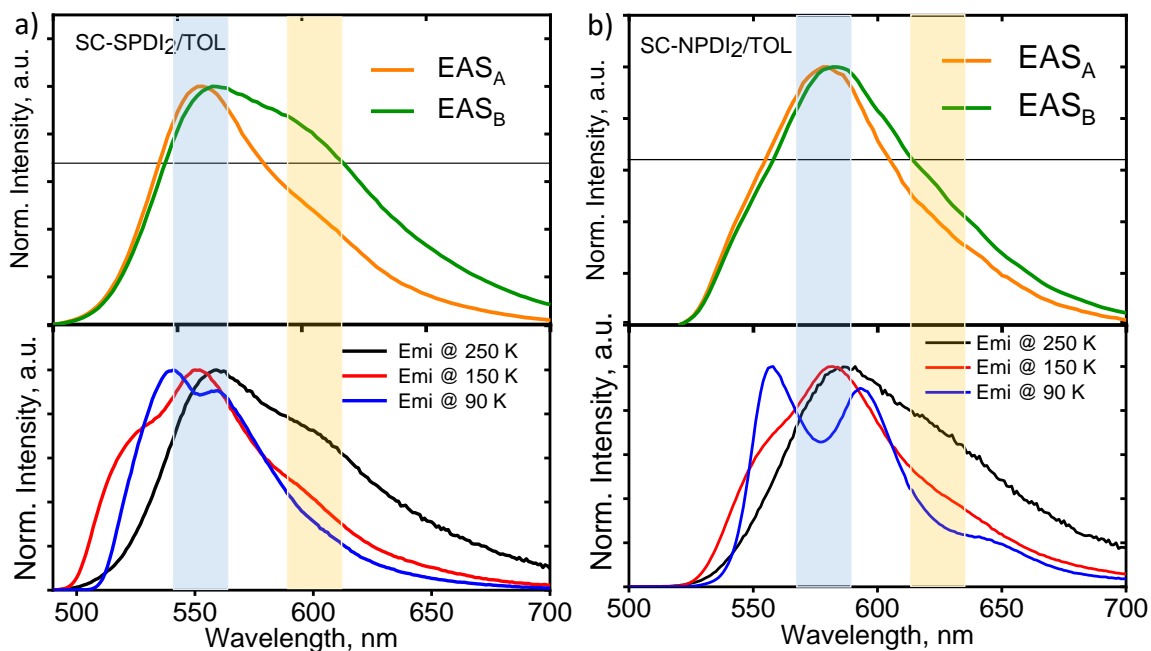


Figure 4.26: Comparison of time-resolved emission spectra with steady-state emission spectra at different temperatures for a) **SC-SPDI₂** and b) **SC-NPDI₂** in TOL.

4.3. Conclusions

In conclusion, we report the unequivocal evidence for the excited-state structural relaxation of **SC-SPDI₂** and **SC-NPDI₂** hampering the efficiency of the SB-CS state. Conjoint spectroscopic and theoretical investigations have rationalized the structural dynamics in the excited state and the

manifestation of an excimer-like state in the π -stacked foldamer structure. The solvent polarity-dependent fsTA measurements of **SC-SPDI₂** and **SC-NPDI₂** reveal ultrafast SB-CS in polar solvents, in contrast to direct excimer formation observed in non-polar TOL. Molecular rearrangement of **SC-SPDI₂** and **SC-NPDI₂** in the excited-state transforms the initially populated SB-CS state into a CT resonance-enhanced excimer state, limiting the SB-CS state lifetime. These observations reinstate the importance of rigid molecular architectures, reminiscent of conformationally rigid special pair of photosynthetic reaction centers embedded in protein scaffold, exhibiting efficient SB-CS as non-fullerene acceptors in OPVs. Further insight into the complex and unprecedented excited state dynamics of **SC-SPDI₂** and **SC-NPDI₂** in different dielectric environments can be obtained from 2D electronic spectroscopy measurements.

4.4. Experimental Section

4.4.1. Synthesis of NPDI

The synthesis of **NPDI** was carried out following reported procedures.¹⁰ **NH-PDI**, 0.50 g, 0.92 mmol) and potassium carbonate (0.25 g, 1.8 mmol) were added to a round-bottom flask. Approximately 20 mL Dry N,N'-dimethylformamide was added, followed by the addition of 1-bromo-hexane (0.27 g, 1.7 mmol). The reaction mixture was purged with nitrogen followed by heating at 170 °C for 1 hour. After the completion of the reaction, the reaction mixture was cooled to room temperature. The compound was extracted using water and dichloromethane. The organic phase was collected and the solvent was removed using a rotary evaporator to give a crude solid. The crude product was purified using column chromatography. The product fraction was collected and the solvent was removed in vacuo to give a red solid. **Yield:** 65%

NPDI: 1H NMR (500 MHz, CDCl₃, ppm) δ = 8.91 (s, 2H), 8.87-8.84 (m, 2H), 8.82-8.76 (m, 2H), 5.30-5.21 (m, 2H), 4.80 (t, 2H), 2.46-2.34 (m, 4H), 2.20-2.12 (m, 2H), 2.11-2.01 (m, 4H), 1.45-1.28 (m, 6H), 1.03 (t, 12H), 0.87 (t, 3H)

13C NMR (500 MHz, CDCl₃, ppm) δ = 133.71, 131.57, 123.59, 122.76, 120.72, 118.42, 56.77, 45.91, 30.47, 30.30, 25.81, 24.22, 21.42, 12.90, 10.47

HRMS (APCI) m/z calculated for C₄₀H₄₂N₃O₄ [(M+H)⁺]: 628.3175, Observed: 628.3164

4.4.2. Synthesis of SPDI

The synthesis of **SPDI** was carried out following modified reported procedures.¹¹ Sulfur (160 mg, 4.9 mmol) was dissolved in N-methylpyrrolidone (12 mL, 70°C). Compound **NO₂-PDI** (0.50 g, 0.62 mmol) was added under nitrogen to the round-bottom flask. The mixture was heated (130°C, ca. 75 min, until the starting material could not be detected by TLC). After the completion of the reaction, the reaction mixture was poured into water (150 mL) and the precipitate was collected by vacuum filtration followed by washing with water. The mixture is dried and purified by column chromatography. **Yield:** 52%

SPDI: 1H NMR (500 MHz, CDCl₃, ppm) δ = 9.204 (d, 2H), 8.826 (d, 4H), 5.144 (m, 2H), 2.286-2.53 (m, 4H), 1.96-1.932 (m, 4H), 0.915 (t, 12H)

13C NMR (500 MHz, CDCl₃, ppm) δ = 137.20, 132.18, 130.46, 125.26, 122.54, 122.16, 76.25, 75.99, 56.97, 24.11, 10.41

HRMS (APCI) m/z calculated for $C_{34}H_{29}N_2O_4S [(M+H)^+]$: 561.1848, Observed: 561.1842.

4.4.3. Synthesis of SC-NPDI₂

The synthesis of **SC-NPDI₂** was carried out following the reported procedures.¹⁰ **Br-NPDI** (0.37 g, 0.52 mmol) and zinc dust (170 mg, 2.6 mmol) were added to a 20 mL roundbottom flask. Approximately 40 mg of bis(dibenzylideneacetone)palladium (0) was added to the mixture. The flask was sealed under a nitrogen atmosphere and 20 mL of N,N-dimethylformamide was added. The reaction mixture was purged with nitrogen for 10 minutes and was heated to ~100 °C for 2.5 hours. After the completion of the reaction, the crude solid obtained after removing the solvent in vacuo was purified using column chromatography. A dark red solid was obtained after the initial purification. For further purification, the red solid was boiled in 100 mL of isopropanol with vigorous stirring for approximately 1 hour followed by cooling to room temperature and filtration using a Buchner funnel, resulting in a bright red solid. **Yield**: 38%.

SC-NPDI₂: **1H NMR** (500 MHz, CDCl₃, ppm) δ = 9.30 (s, 2H), 9.12 (s, 2H), 8.91 (s, 2H), 7.99 (s, 2H), 7.74-7.72 (m, 2H), 5.35-5.16 (m, 4H), 5.07-5.04 (m, 4H), 2.42-2.31 (m, 8H), 2.28-2.16 (m, 4H), 2.07-2.00 (m, 4H), 1.93-1.84 (m, 4H), 1.64-1.56 (m, 4H), 1.50-1.45 (m, 4H), 1.42-1.37 (m, 4H), 1.06-0.82 (m, 30H).

13C NMR (500 MHz, CDCl₃, ppm) δ = 139.87, 134.25, 134.03, 131.89, 129.37, 125.81, 123.94, 123.69, 122.55, 121.73, 119.08, 118.81, 56.98, 56.59, 46.12, 30.66, 30.43, 25.99, 24.02, 21.52, 13.00, 10.49, 10.22

HRMS (APCI) m/z calculated for $C_{80}H_{81}N_6O_8 [(M+H)^+]$: 1253.6115, Observed: 1253.6112.

4.4.4. Synthesis of SC-SPDI₂

The synthesis of **SC-SPDI₂** was carried out following the modified procedures (Scheme 1).¹¹ **Br-SPDI** (0.33 g, 0.52 mmol) and zinc dust (170 mg, 2.6 mmol) were added to a 20 mL roundbottom flask. Approximately 40 mg of bis(dibenzylideneacetone)palladium(0) was added to the mixture. The flask was sealed under a nitrogen atmosphere and 20 mL of N,N-dimethylformamide was added. The reaction mixture was purged with nitrogen for 10 minutes and was heated to ~100 °C for 2.5 hours. After the completion of the reaction, the crude solid obtained after removing the solvent in vacuo was purified using column chromatography. A dark red solid was obtained after the initial purification. For further purification, the red solid was boiled in 100 mL of isopropanol

with vigorous stirring for approximately 1 hour followed by cooling to room temperature and filtration using a Buchner funnel, resulting in a bright red solid. **Yield:** 48%

SC-SPDI₂: **¹H NMR** (500 MHz, CDCl₃, ppm) δ = 9.61 (s, 2H), 9.45 (s, 2H), 8.81 (s, 2H), 8.18-8.10 (m, 4H), 5.30-4.93 (m, 4H), 2.38-2.30 (m, 4H), 2.27-2.16 (m, 4H), 2.04-1.96 (m, 4H), 1.94-1.85 (m, 4H), 1.04-0.83 (m, 24H).

¹³C NMR (500 MHz, CDCl₃, ppm) δ = 140.81, 138.99, 138.42, 133.30, 131.95, 131.63, 130.86, 129.04, 128.23, 126.96, 126.52, 126.36, 125.26, 124.19, 58.23, 57.87, 31.94, 29.71, 29.38, 24.98, 24.93, 22.71, 14.14, 11.47, 11.23.

HRMS (APCI) *m/z* calculated for C₆₈H₅₅N₄O₈S₂ [(M+H)⁺]: 1119.3461, Observed: 1119.3452.

4.5. Additional Tables

Table A4.1: Oscillator strength for different transitions of **SPDI** calculated at TD- ω B97XD/def2svp level of theory.

| Molecule | State | Oscillator Strength | Energy (eV) | Wavelength (nm) | Major Orbital Transition |
|----------|----------------|---------------------|-------------|-----------------|--------------------------------|
| SPDI | S ₁ | 0.7381 | 2.929 | 423.4 | HOMO → LUMO |
| | S ₂ | 0.1113 | 3.432 | 361.3 | HOMO-1 → LUMO |
| | S ₃ | 0.0023 | 4.010 | 309.2 | HOMO-3 → LUMO |
| | S ₄ | 0.0004 | 4.106 | 302.0 | HOMO-4 → LUMO |
| | S ₅ | 0 | 4.109 | 301.7 | HOMO-5 → LUMO |
| | S ₆ | 0.0009 | 4.119 | 301.0 | HOMO → LUMO+2 HOMO-2 → LUMO |

Table A4.2: Oscillator strength for different transitions of **NPDI** calculated at TD- ω B97XD/def2svp level of theory.

| Molecule | State | Oscillator Strength | Energy (eV) | Wavelength (nm) | Major Orbital Transition |
|----------|----------------|---------------------|-------------|-----------------|--------------------------------|
| NPDI | S ₁ | 0.7381 | 2.872 | 431.7 | HOMO → LUMO |
| | S ₂ | 0.1138 | 3.282 | 377.8 | HOMO-1 → LUMO |
| | S ₃ | 0.0091 | 4.009 | 309.3 | HOMO-2 → LUMO |
| | S ₄ | 0.0003 | 4.126 | 300.5 | HOMO-4 → LUMO |
| | S ₅ | 0 | 4.132 | 300.0 | HOMO-5 → LUMO |
| | S ₆ | 0.0001 | 4.139 | 299.6 | HOMO-3 → LUMO HOMO → LUMO+2 |

Table A4.3: Oscillator strength for different transitions of **SC-SPDI₂** calculated at TD- ω B97XD/def2svp level of theory.

| Molecule | State | Oscillator Strength | Energy (eV) | Wavelength (nm) | Major Orbital Transition |
|----------------------|----------------|---------------------|-------------|-----------------|--------------------------------|
| SC-SPDI ₂ | S ₁ | 0.6818 | 2.906 | 426.6 | HOMO → LUMO HOMO-1 → LUMO+1 |
| | S ₂ | 0.6179 | 2.929 | 423.3 | HOMO → LUMO+1 HOMO-1 → LUMO |

| | | | | |
|-------|--------|-------|-------|--|
| S_3 | 0.3322 | 3.388 | 365.9 | HOMO-2 \rightarrow LUMO HOMO-3 \rightarrow LUMO+1 |
| S_4 | 0.0106 | 3.426 | 361.9 | HOMO-3 \rightarrow LUMO HOMO-2 \rightarrow LUMO+1 |
| S_5 | 0.0007 | 3.621 | 342.4 | HOMO-1 \rightarrow LUMO HOMO \rightarrow LUMO+1 |
| S_6 | 0.0050 | 3.622 | 342.3 | HOMO \rightarrow LUMO HOMO-1 \rightarrow LUMO+1 |

Table A4.4: Oscillator strength for different transitions of *SC-NPDI*₂ calculated at TD- ω B97XD/def2svp level of theory.

| Molecule | State | Oscillator Strength | Energy (eV) | Wavelength (nm) | Major Orbital Transition |
|----------------------|-------|---------------------|-------------|-----------------|--|
| SC-NPDI ₂ | S_1 | 0.6211 | 2.826 | 438.7 | HOMO \rightarrow LUMO HOMO-1 \rightarrow LUMO+1 |
| | S_2 | 0.6466 | 2.866 | 432.5 | HOMO \rightarrow LUMO+1 HOMO-1 \rightarrow LUMO |
| | S_3 | 0.3330 | 3.240 | 382.6 | HOMO-2 \rightarrow LUMO HOMO-3 \rightarrow LUMO+1 |
| | S_4 | 0.0189 | 3.286 | 377.3 | HOMO-3 \rightarrow LUMO HOMO-2 \rightarrow LUMO+1 |
| | S_5 | 0.0013 | 3.585 | 345.9 | HOMO-1 \rightarrow LUMO HOMO \rightarrow LUMO+1 |
| | S_6 | 0.0170 | 3.595 | 344.9 | HOMO \rightarrow LUMO HOMO-1 \rightarrow LUMO+1 |

Table A4.5: Energy (ΔE), oscillator strength (f), mean position (POR), participation ratio (PR) of initial orbital (hole) and final orbital (electron) and charge transfer character (CT) and other excited state parameters of singlet states in *SC-SPDI*₂ in the FC geometry.

| State | ΔE (eV) | f | Om | POS | PR | CT | COH | CTnt | PRNTO | Z_HE | RMSeh |
|-------|-----------------|-------|-------|-----|----|-------|-------|------|-------|-------|-------|
| S_1 | 2.906 | 0.682 | 1.009 | 1.5 | 2 | 0.026 | 1.053 | 0 | 2.126 | 2.471 | 4.803 |
| S_2 | 2.929 | 0.618 | 1.01 | 1.5 | 2 | 0.019 | 1.039 | 0 | 2.158 | 2.499 | 4.799 |
| S_3 | 3.388 | 0.332 | 1.006 | 1.5 | 2 | 0.023 | 1.047 | 0 | 2.481 | 3.204 | 4.43 |
| S_4 | 3.426 | 0.011 | 1.007 | 1.5 | 2 | 0.028 | 1.057 | 0 | 2.636 | 3.461 | 4.439 |
| S_5 | 3.621 | 0.001 | 1 | 1.5 | 2 | 0.937 | 1.134 | 0 | 2.015 | 2.07 | 7.201 |
| S_6 | 3.622 | 0.005 | 1 | 1.5 | 2 | 0.937 | 1.133 | 0 | 2 | 2.058 | 7.202 |

Table A4.6: Energy (ΔE), oscillator strength (f), mean position (POR), participation ratio (PR) of initial orbital (hole) and final orbital (electron) and charge transfer character (CT) and other excited state parameters of singlet states in **SC-NPDI₂** in the FC geometry.

| State | ΔE (eV) | f | Om | POS | PR | CT | COH | CTnt | PRNTO | Z_HE | RMSch |
|----------------|-----------------|------|-------|-------|-------|-------|-------|-------|-------|-------|-------|
| S ₁ | 2.826 | 0.61 | 1.009 | 1.498 | 2 | 0.038 | 1.079 | 0 | 2.028 | 2.4 | 4.863 |
| S ₂ | 2.867 | 0.64 | 1.01 | 1.502 | 2 | 0.017 | 1.035 | 0 | 2.162 | 2.501 | 4.822 |
| S ₃ | 3.24 | 0.33 | 1.006 | 1.5 | 2 | 0.021 | 1.043 | 0 | 2.35 | 2.969 | 4.451 |
| S ₄ | 3.286 | 0.02 | 1.007 | 1.499 | 2 | 0.018 | 1.036 | 0 | 2.523 | 3.235 | 4.429 |
| S ₅ | 3.585 | 0.00 | 1 | 1.501 | 1.971 | 0.947 | 1.109 | 0.122 | 1.975 | 2.041 | 7.33 |
| S ₆ | 3.595 | 0.02 | 1 | 1.499 | 1.971 | 0.927 | 1.153 | 0.122 | 1.925 | 2.019 | 7.276 |

Table A4.7: Energy (ΔE), oscillator strength (f), mean position (POR), participation ratio (PR) of initial orbital (hole) and final orbital (electron) and charge transfer character (CT) and other excited state parameters of singlet states in **SC-SPDI₂** in the relaxed foldamer geometry.

| State | ΔE (eV) | f | Om | POS | PR | CT | COH | CTnt | PRNTO | Z_HE | RMSch |
|----------------|-----------------|-------|-------|-----|----|-------|-------|------|-------|-------|-------|
| S ₁ | 2.094 | 0.082 | 1.005 | 1.5 | 2 | 0.375 | 1.882 | 0 | 1.084 | 1.24 | 5.149 |
| S ₂ | 2.684 | 0.627 | 1.013 | 1.5 | 2 | 0.058 | 1.123 | 0 | 2.138 | 2.457 | 4.890 |
| S ₃ | 2.788 | 0 | 1.001 | 1.5 | 2 | 0.873 | 1.285 | 0 | 2.045 | 2.149 | 5.977 |
| S ₄ | 3.114 | 0.019 | 1.003 | 1.5 | 2 | 0.419 | 1.948 | 0 | 2.11 | 2.513 | 5.264 |
| S ₅ | 3.145 | 0.405 | 1.006 | 1.5 | 2 | 0.27 | 1.651 | 0 | 2.292 | 2.782 | 4.981 |
| S ₆ | 3.228 | 0.064 | 1.007 | 1.5 | 2 | 0.094 | 1.206 | 0 | 2.134 | 2.975 | 4.585 |

Table A4.8: Energy (ΔE), oscillator strength (f), mean position (POR), participation ratio (PR) of initial orbital (hole) and final orbital (electron) and charge transfer character (CT) and other excited state parameters of singlet states in **SC-NPDI₂** in the relaxed foldamer geometry.

| state | ΔE (eV) | f | Om | POS | PR | CT | COH | CTnt | PRNTO | Z_HE | RMSch |
|----------------|-----------------|-------|-------|-------|----|-------|-------|------|-------|-------|-------|
| S ₁ | 1.938 | 0.063 | 1.005 | 1.5 | 2 | 0.394 | 1.913 | 0 | 1.071 | 1.209 | 5.165 |
| S ₂ | 2.613 | 0.464 | 1.01 | 1.5 | 2 | 0.203 | 1.479 | 0 | 1.359 | 1.758 | 5.095 |
| S ₃ | 2.756 | 0.141 | 1.003 | 1.5 | 2 | 0.731 | 1.647 | 0 | 1.304 | 1.592 | 5.757 |
| S ₄ | 2.932 | 0.213 | 1.006 | 1.5 | 2 | 0.212 | 1.501 | 0 | 1.504 | 2.103 | 4.839 |
| S ₅ | 3.149 | 0.216 | 1.003 | 1.5 | 2 | 0.483 | 1.998 | 0 | 1.326 | 1.743 | 5.338 |
| S ₆ | 3.684 | 0.01 | 1 | 1.501 | 2 | 0.307 | 1.741 | 0 | 2.699 | 3.521 | 4.77 |

4.6. Additional Figures

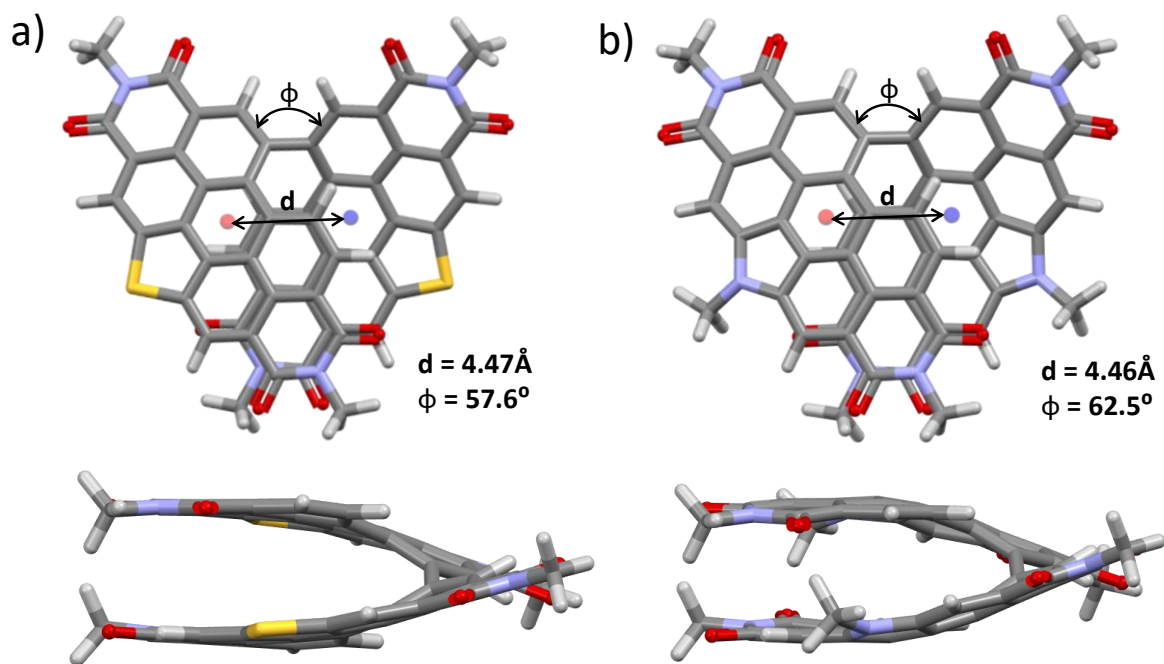


Figure A4.1: Optimized geometries of the dimers a) *SC-SPDI*₂ and b) *SC-NPDI*₂ in the excited state showing the π -stacked foldamer-like geometry viewed from two different axis. The centroid to centroid distance (d) and the torsional/dihedral angles (ϕ) between the chromophores are also indicated in the figure.

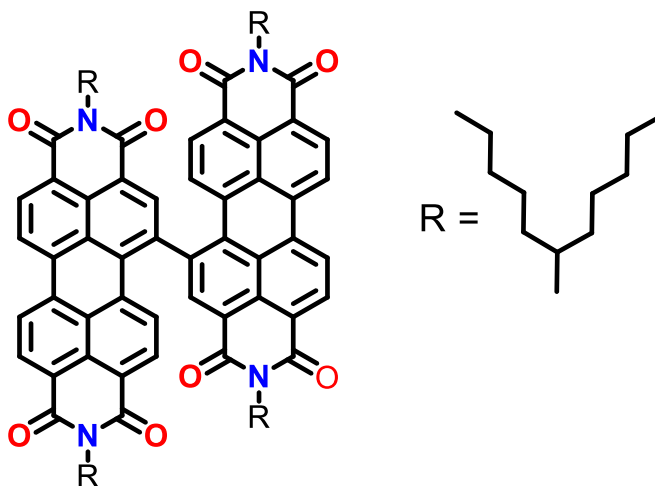


Figure A4.2: Molecular structure of *di-PDI*.

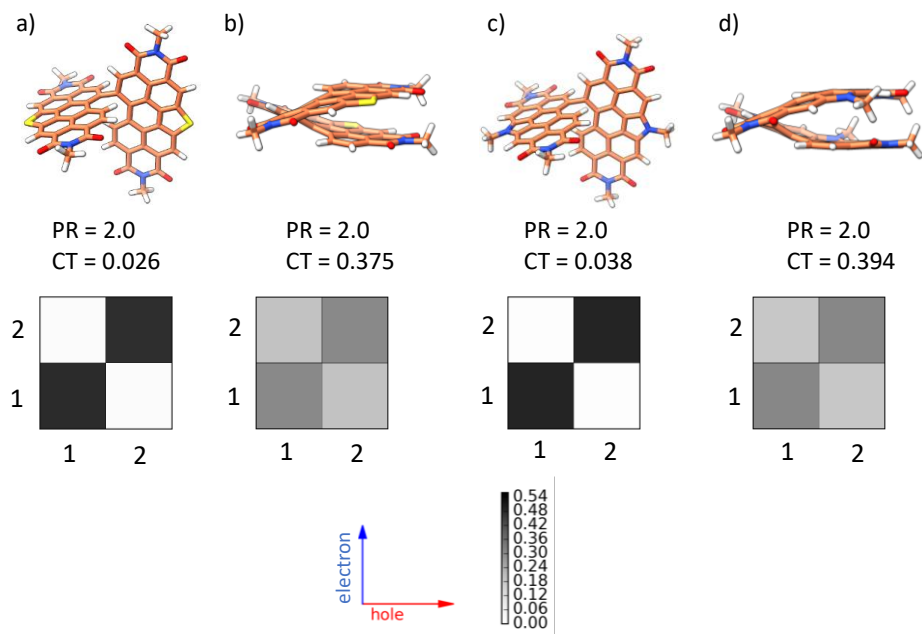


Figure A4.3: Molecular structures of the dimers and the corresponding PR and CT values for the transition to the first singlet excited state along with the electron-hole correlation plots (a,b) *SC-SPDI*₂ and (c,d) *SC-NPDI*₂.

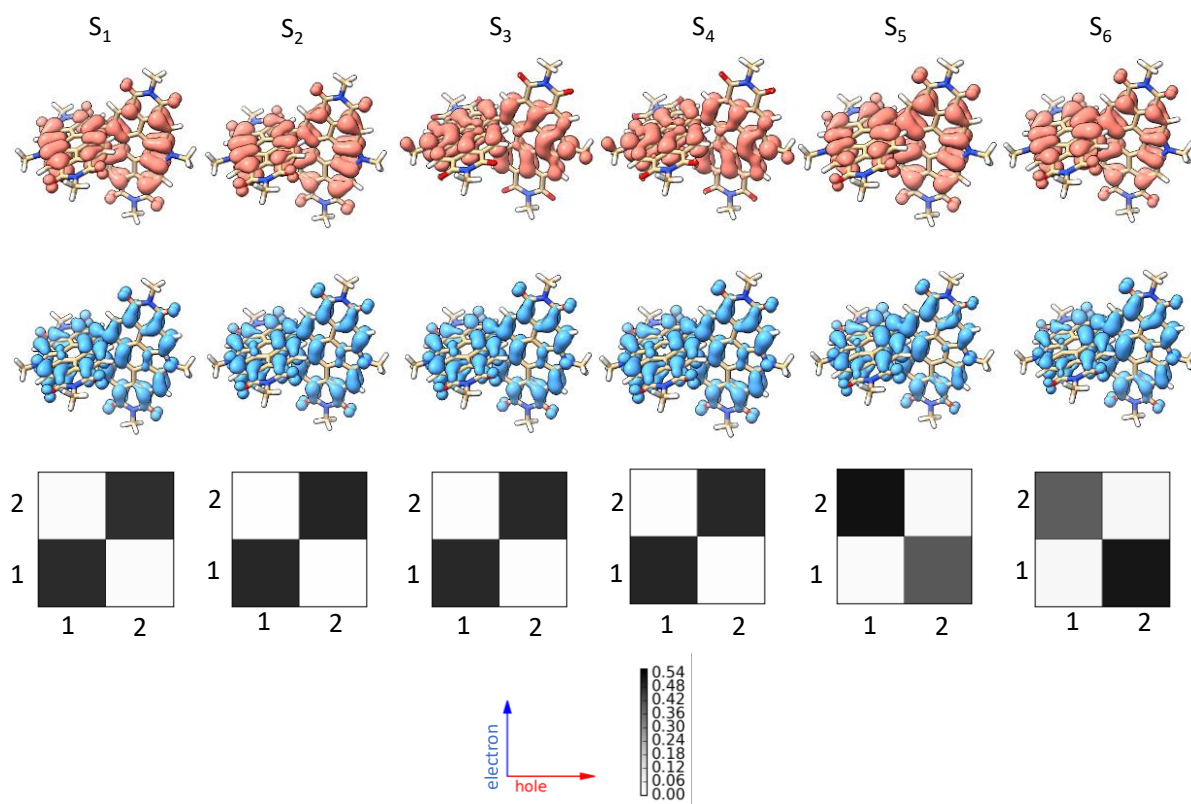


Figure A4.4: Hole and electron isosurfaces for the first six singlet excited state transitions and the corresponding electron-hole correlation plots of *SC-NPDI*₂ in the near-orthogonal geometry.

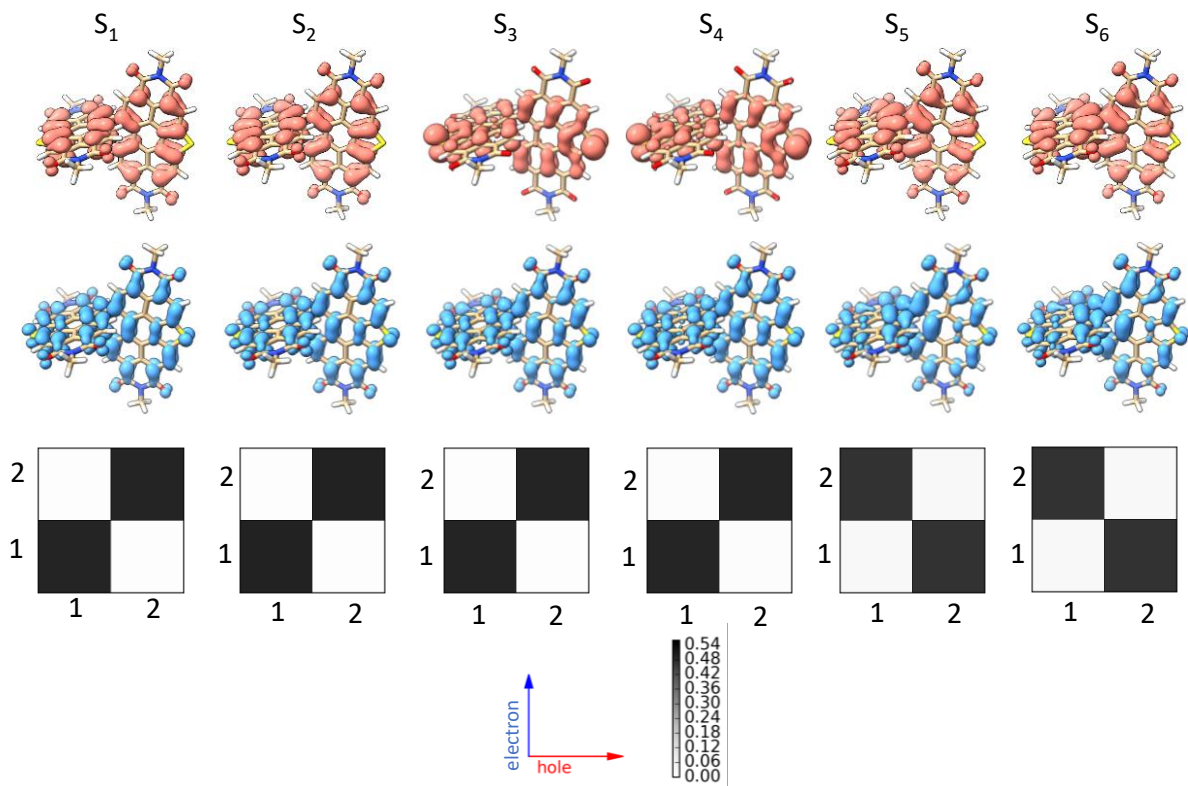


Figure A4.5: Hole and electron isosurfaces for the first six singlet excited state transitions along with the corresponding electron-hole correlation plots of *SC-SPDI*₂ in the near-orthogonal geometry.

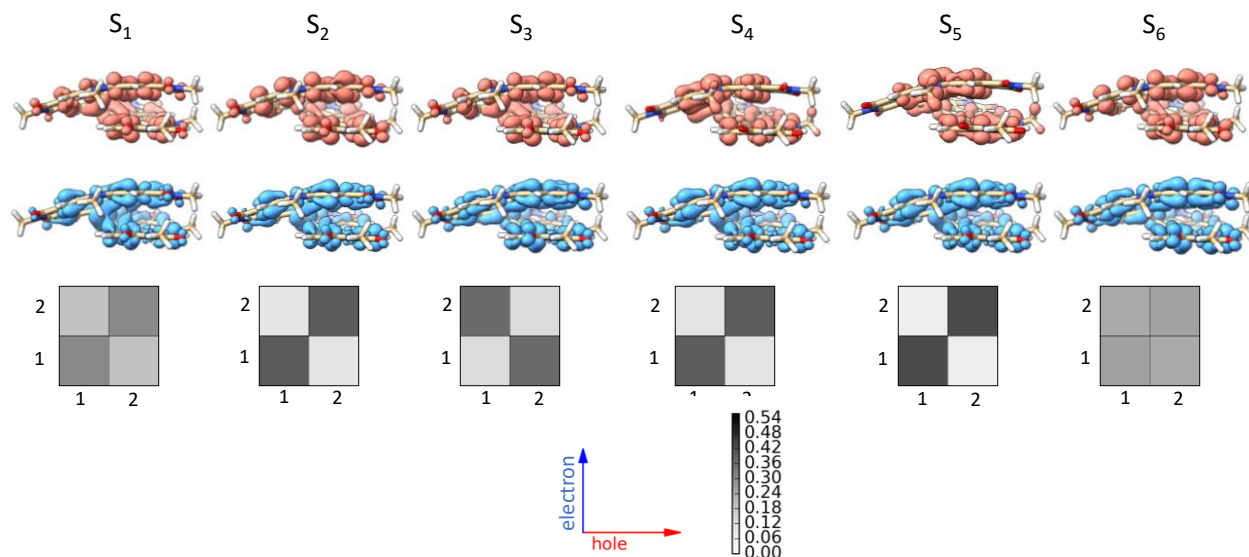


Figure A4.6: Hole and electron isosurfaces for the first six singlet excited state transitions along with the corresponding electron-hole correlation plots of *SC-NPDI*₂ in the foldamer geometry.

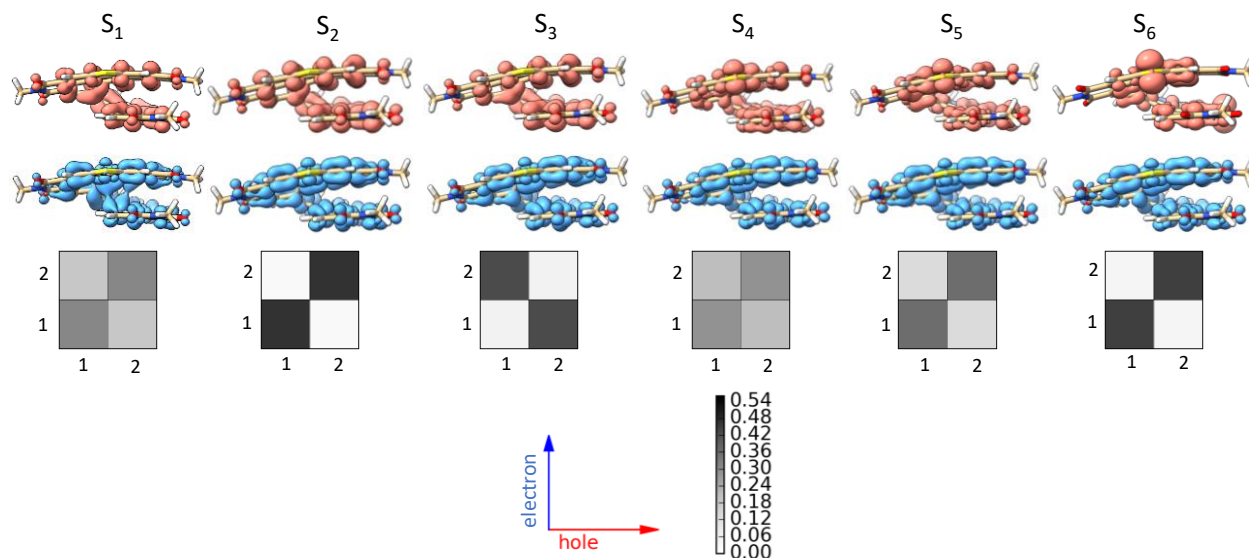


Figure A4.7: Hole and electron isosurfaces for the first six singlet excited state transitions along with the corresponding electron-hole correlation plots of $SC\text{-}SPDI_2$ in the foldamer geometry.

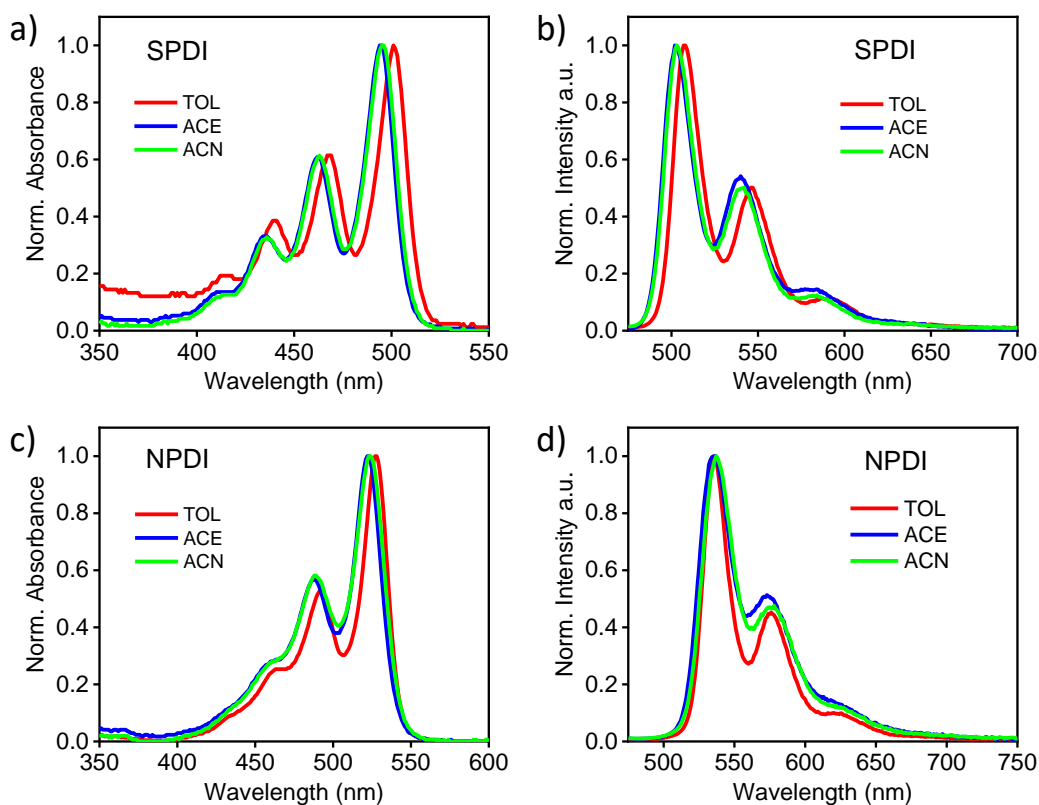


Figure A4.8: Normalised absorption and emission spectra of (a, b) $SPDI$ and (c, d) $NPDI$ in different solvents.

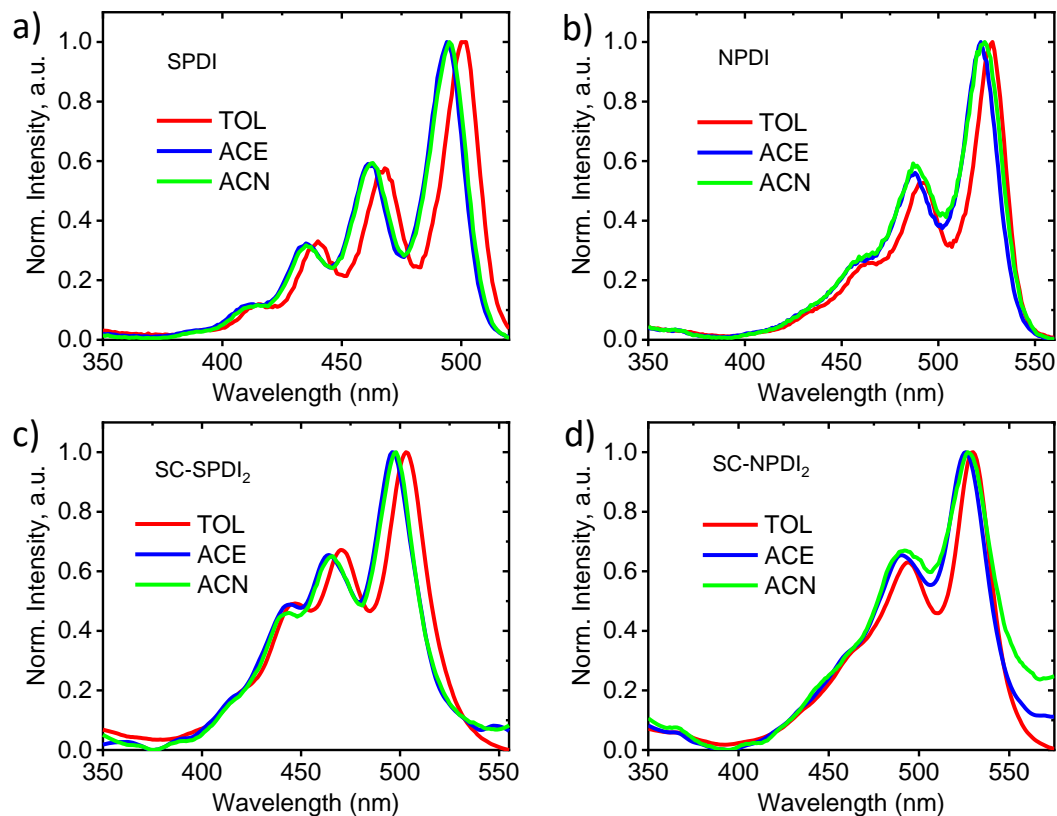


Figure A4.9: Normalised excitation spectra of a) *SPDI*, b) *NPDI*, c) *SC-SPDI*₂ and d) *SC-NPDI*₂ collected at emission maximum in different solvents.

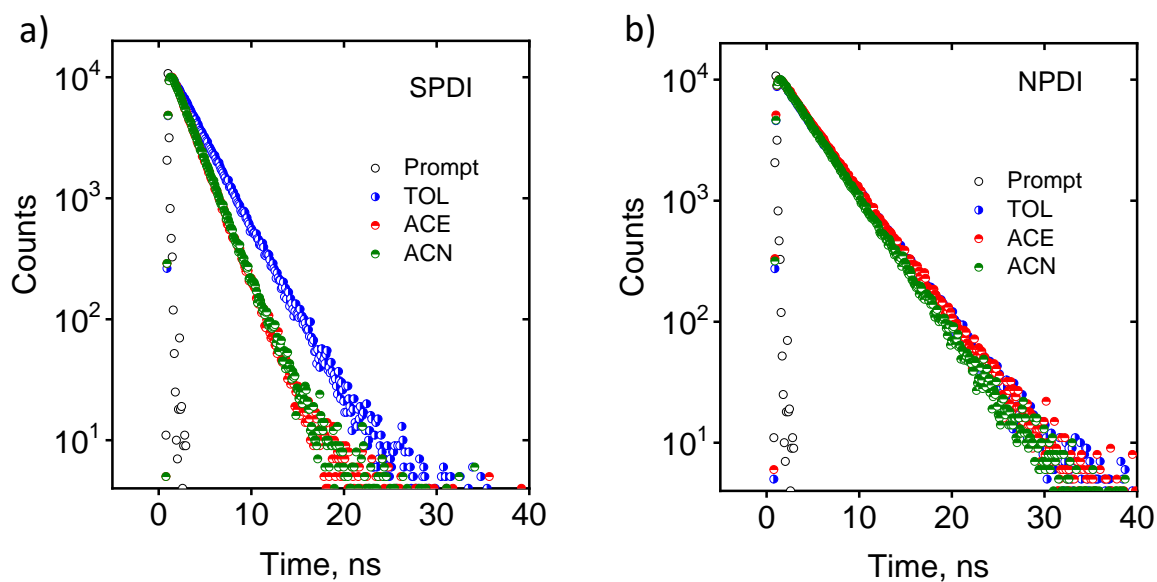


Figure A4.10: Fluorescence decay profiles of (a) *SPDI* and (b) *NPDI* in different solvents.

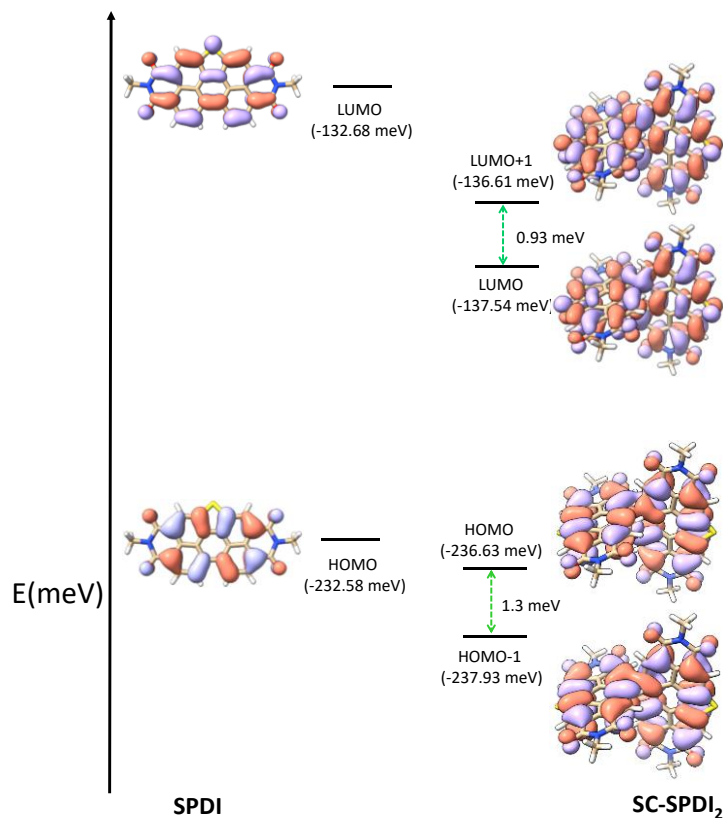


Figure A4.11: Energy level diagram with the frontier molecular orbitals of *SPDI* and *SC-SPDI*₂.

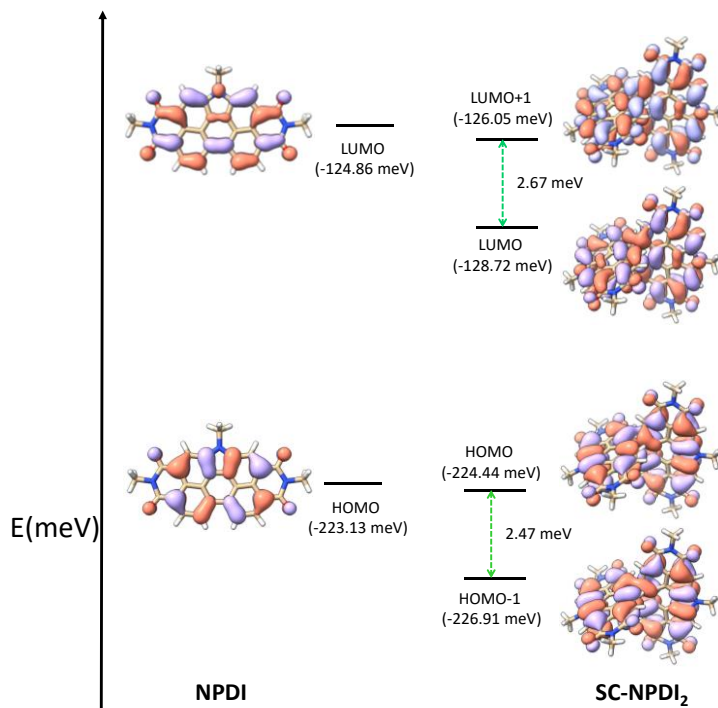


Figure A4.12: Energy level diagram with the frontier molecular orbitals of *NPDI* and *SC-NPDI*₂.

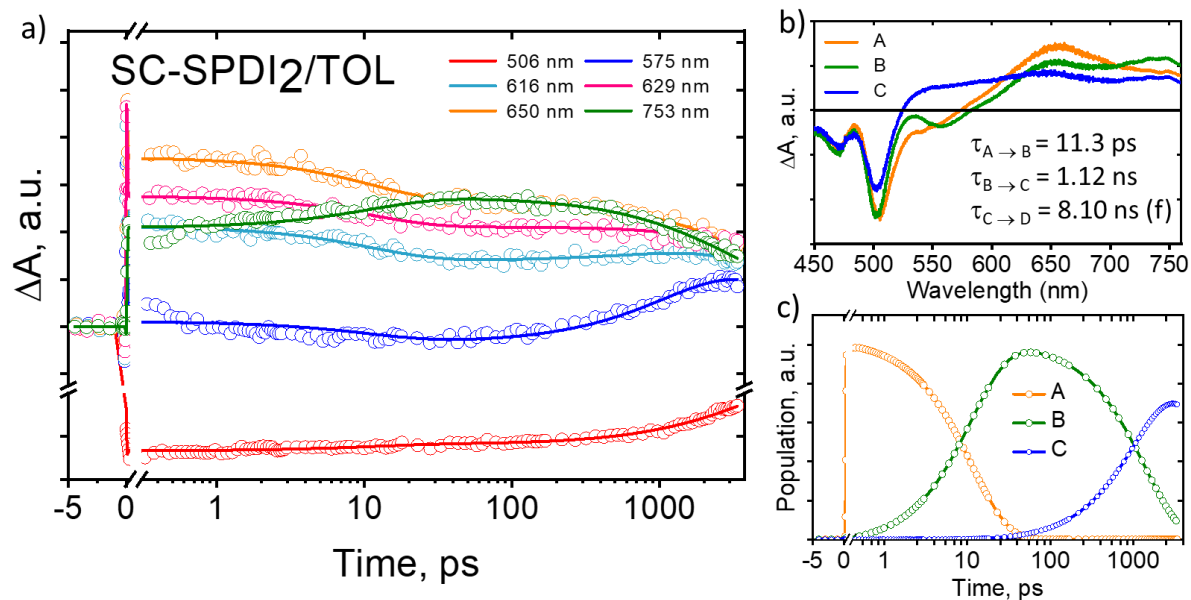


Figure A4.13: Global analysis fits for selected fsTA wavelengths of *SC-SPDI*₂ ($\lambda_{ex} = 470$ nm) in toluene to $A \rightarrow B \rightarrow C \rightarrow D$ kinetic model. Fits are shown as solid lines. Evolution associated spectra (EAS, b) and population profiles (c) of *SC-SPDI*₂ in toluene.

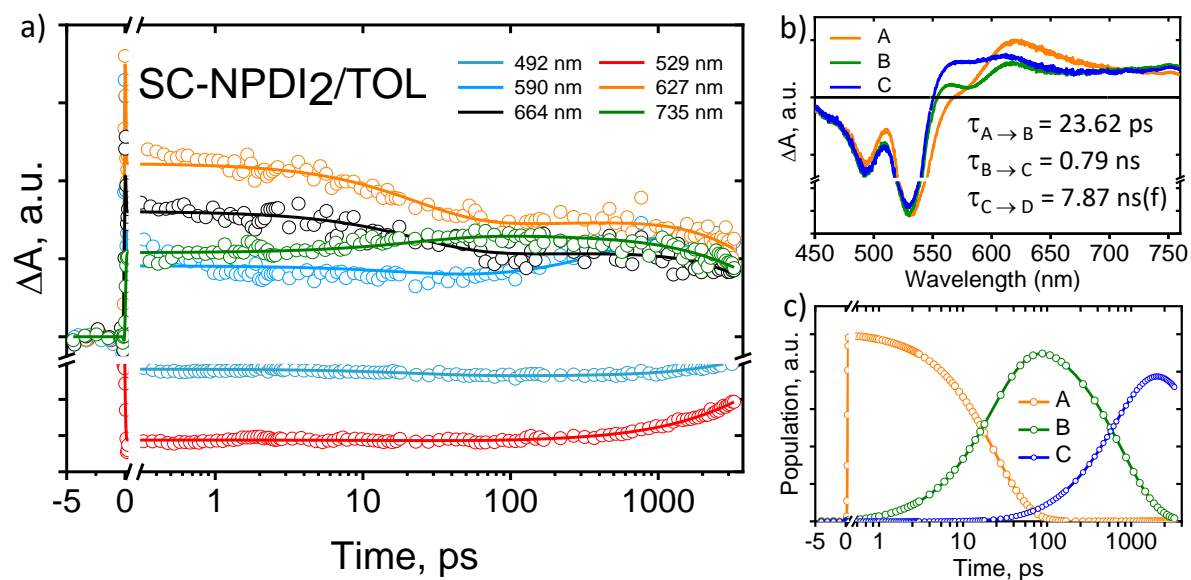


Figure A4.13: Global analysis fits for selected fsTA wavelengths of *SC-NPDI*₂ ($\lambda_{ex} = 470$ nm) in toluene to $A \rightarrow B \rightarrow C \rightarrow D$ kinetic model. Fits are shown as solid lines. Evolution associated spectra (EAS, b) and population profiles (c) of *SC-NPDI*₂ in toluene.

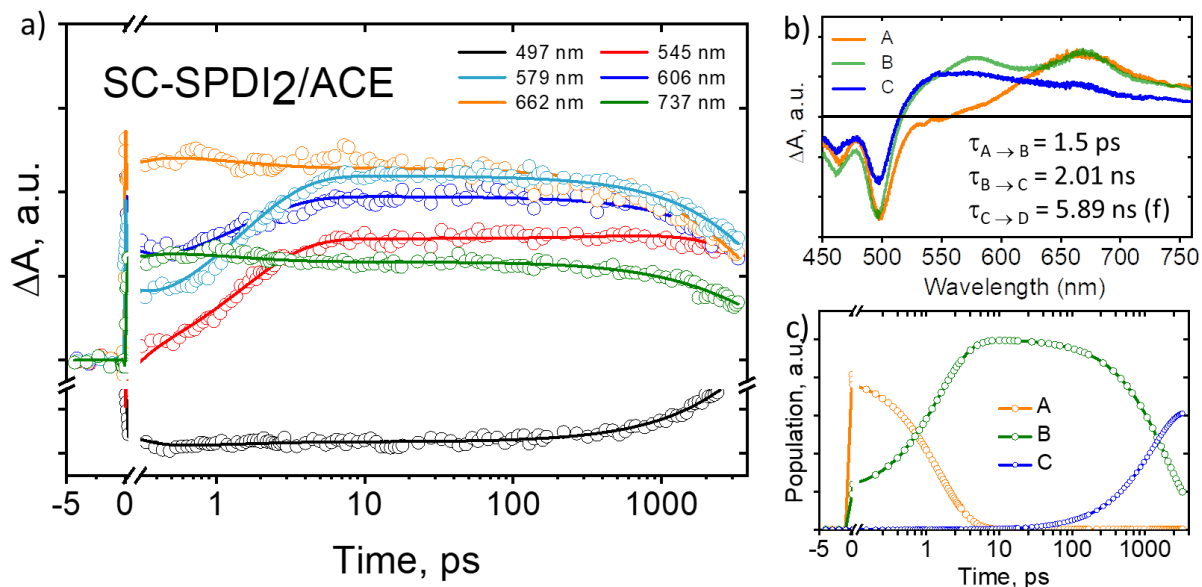


Figure A4.14: Global analysis fits for selected fsTA wavelengths of *SC-SPDI*₂ ($\lambda_{ex}=470$ nm) in acetone to $A \rightarrow B \rightarrow C \rightarrow D$ kinetic model. Fits are shown as solid lines. Evolution associated spectra (EAS, b) and population profiles (c) of *SC-SPDI*₂ in acetone.

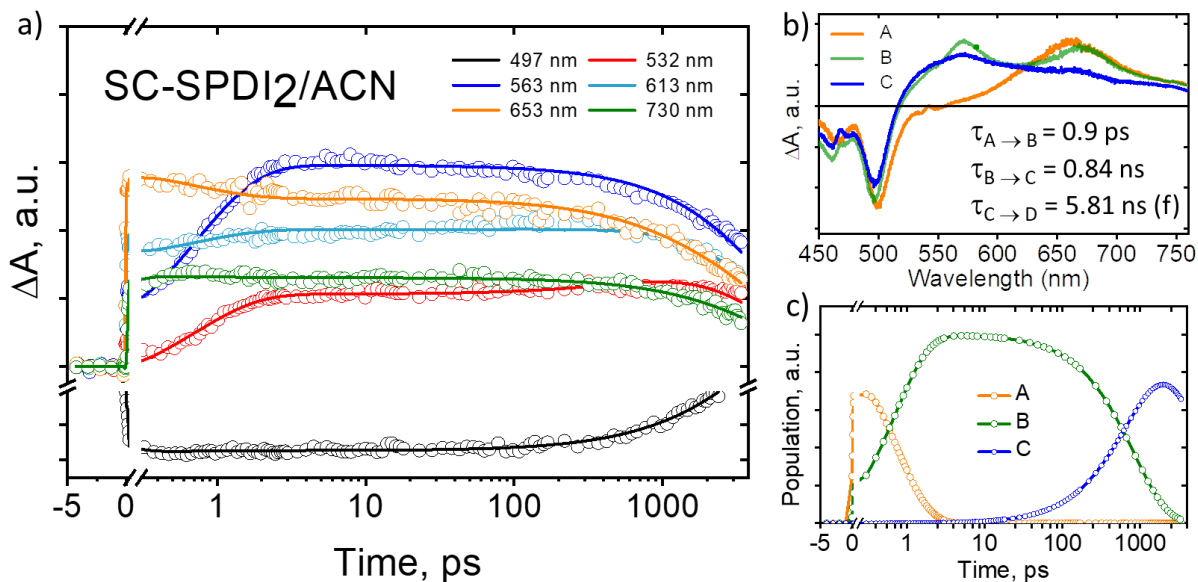


Figure A4.15: Global analysis fits for selected fsTA wavelengths of *SC-SPDI*₂ ($\lambda_{ex}=470$ nm) in acetonitrile to $A \rightarrow B \rightarrow C \rightarrow D$ kinetic model. Fits are shown as solid lines. Evolution associated spectra (EAS, b) and population profiles (c) of *SC-SPDI*₂ in acetonitrile.

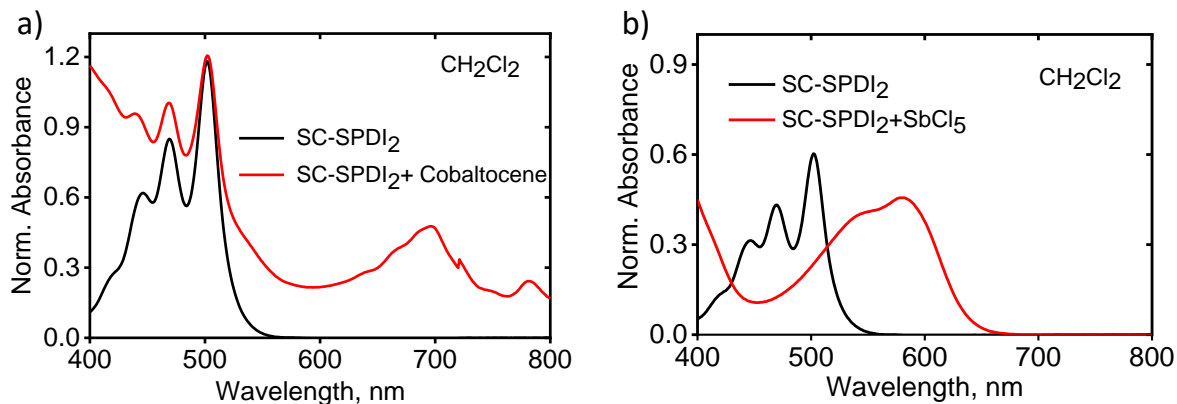


Figure A.16: UV-vis absorption changes of **SC-SPDI₂** upon the addition of a) cobaltocene (CoCp₂) and b) antimony pentachloride (SbCl₅). The small difference in the peaks of anion could be due to solvent effects or conformational changes in the solvent used.

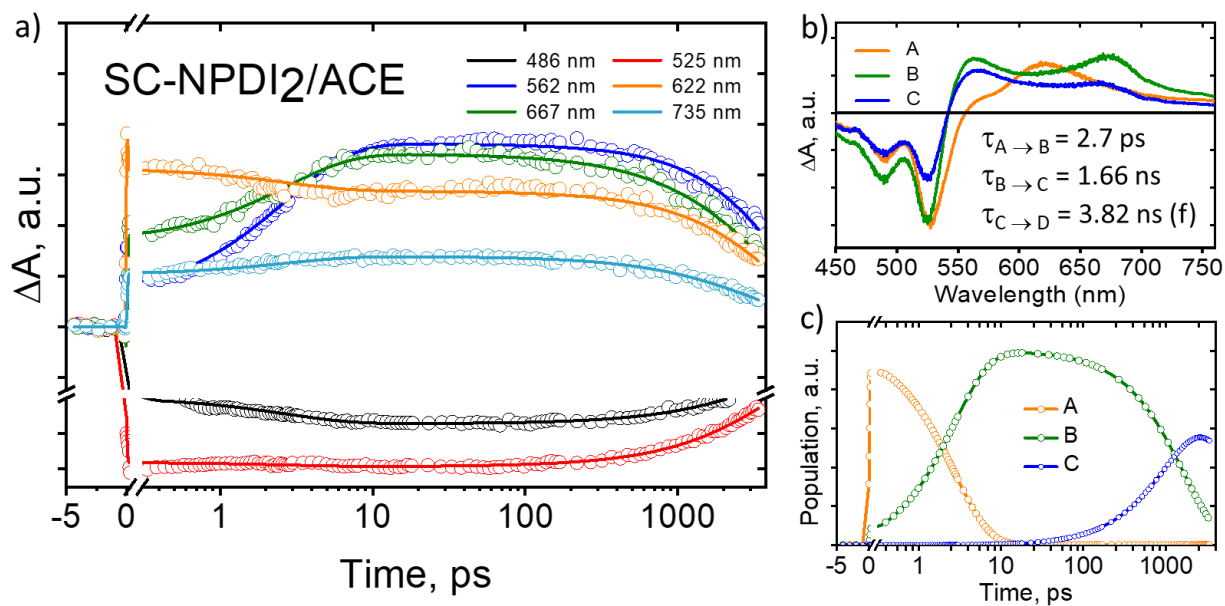


Figure A4.17: Global analysis fits for selected fsTA wavelengths of **SC-SPDI₂** ($\lambda_{ex}=470$ nm) in acetone to $A \rightarrow B \rightarrow C \rightarrow D$ kinetic model. Fits are shown as solid lines. Evolution associated spectra (EAS, b) and population profiles (c) of **SC-NPDI₂** in acetone.

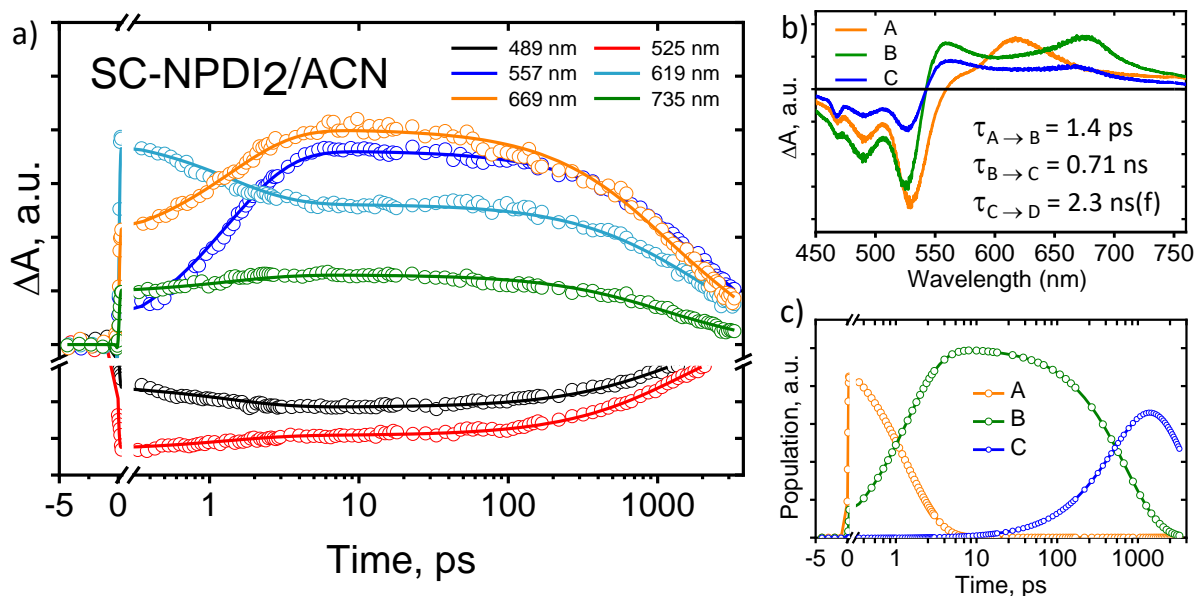


Figure A4.18: Global analysis fits for selected fsTA wavelengths of *SC-SPDI*₂ (λ_{ex} =470 nm) in acetone to $A \rightarrow B \rightarrow C \rightarrow D$ kinetic model. Fits are shown as solid lines. Evolution associated spectra (EAS, b) and population profiles (c) of *SC-NPDI*₂ in acetonitrile.

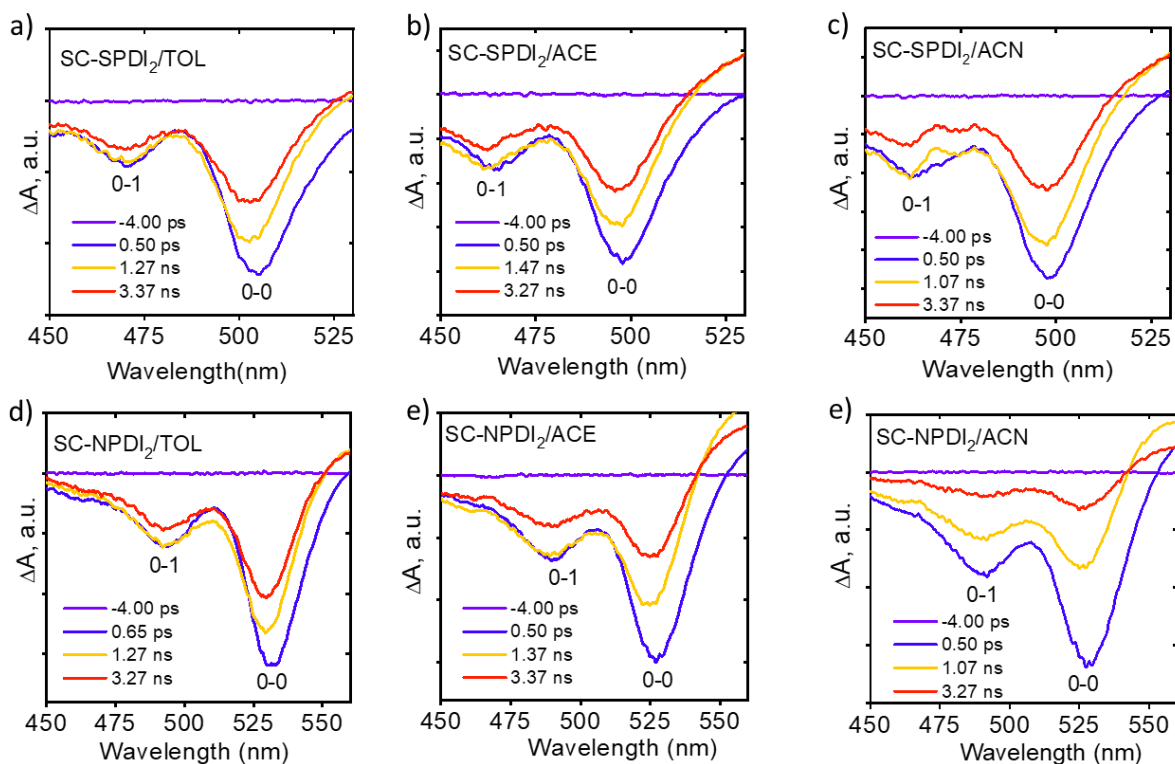


Figure A4.19: fsTA spectra highlighting the change in intensities of 0-0 and 0-1 vibronic bands for *SC-SPDI*₂ and *SC-NPDI*₂ in different solvents.

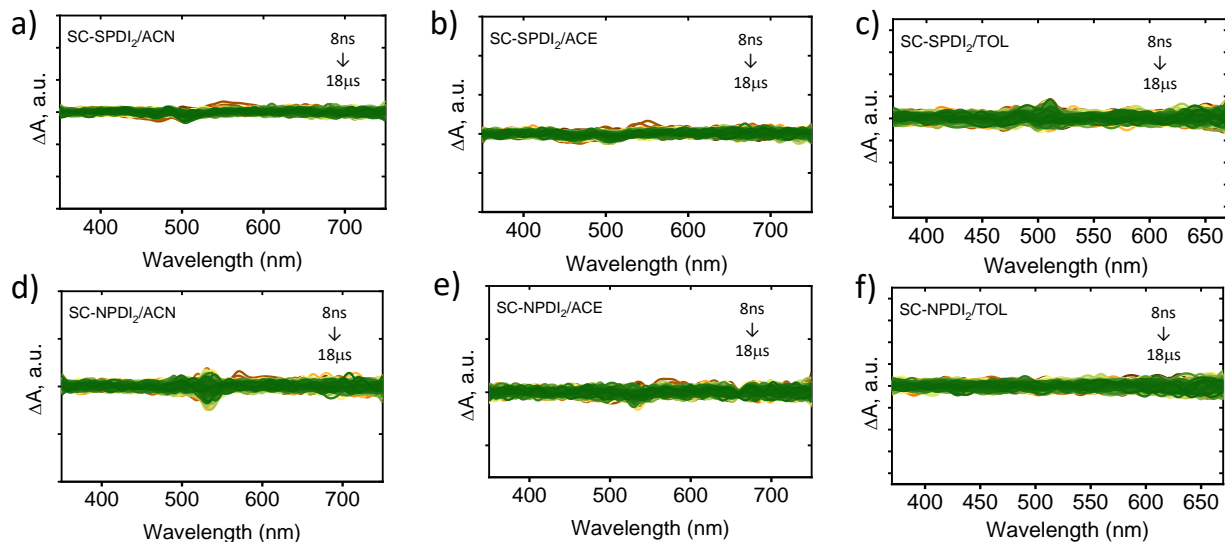


Figure A4.20: Nanosecond transient absorption spectra of *SC-SPDI*₂ in a) ACN, b) ACE, c) TOL and of *SC-NPDI*₂ in d) ACN, e) ACE, f) TOL after O₂ purging.

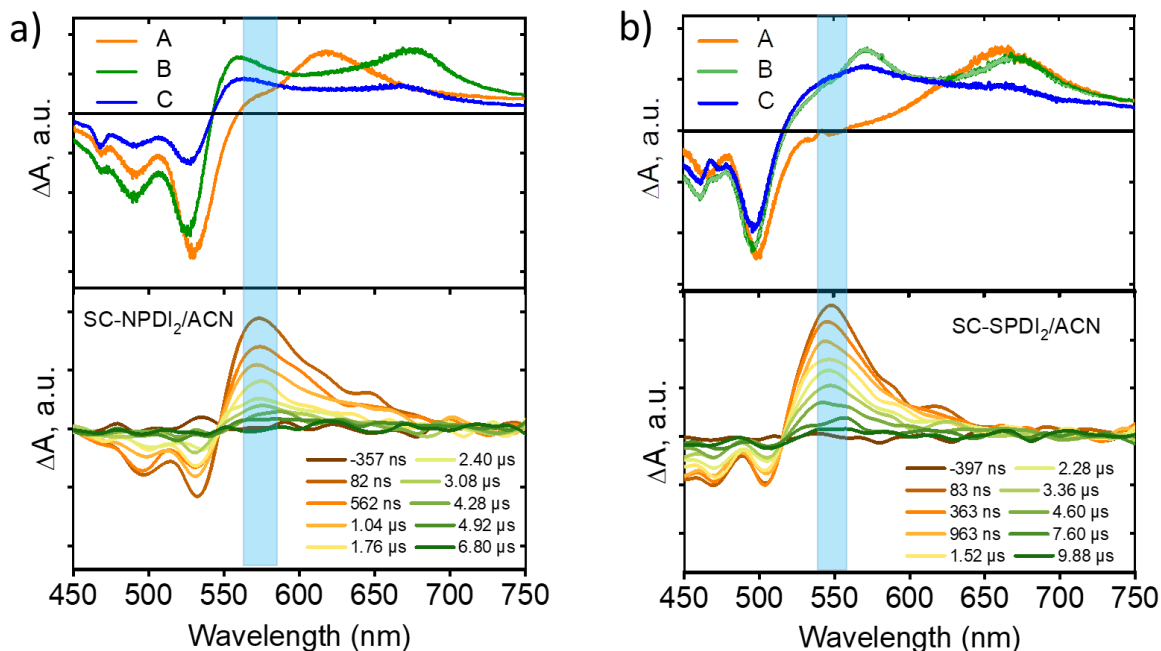


Figure A4.21: Comparison between the EAS from fsTA measurements (top) and nTA spectra (bottom) for a) *SC-NPDI*₂ and b) *SC-SPDI*₂.

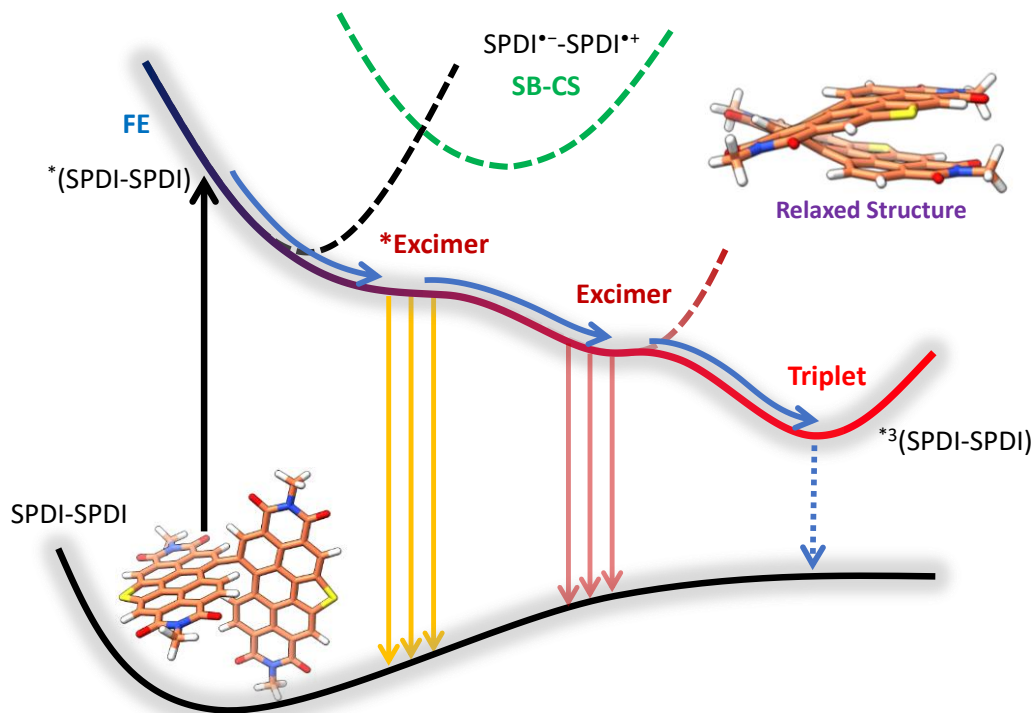


Figure A4.22: Schematic potential energy surface of *SC-SPDI*₂ in TOL summarising the excited state dynamics.

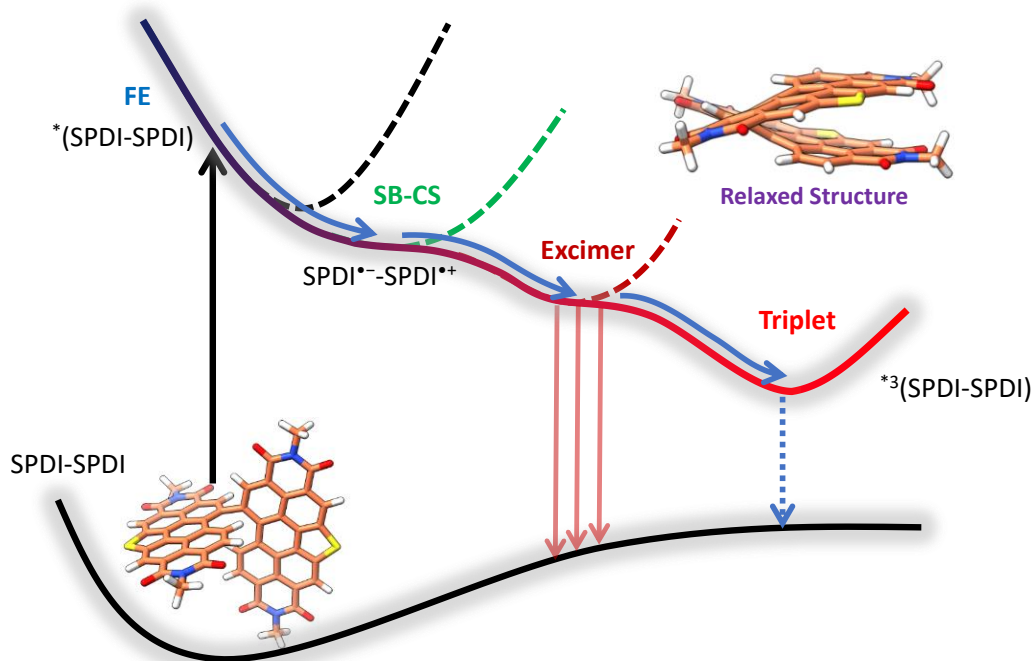


Figure A4.23: Schematic potential energy surface of *SC-SPDI*₂ in ACE and ACN summarising the excited state dynamics.

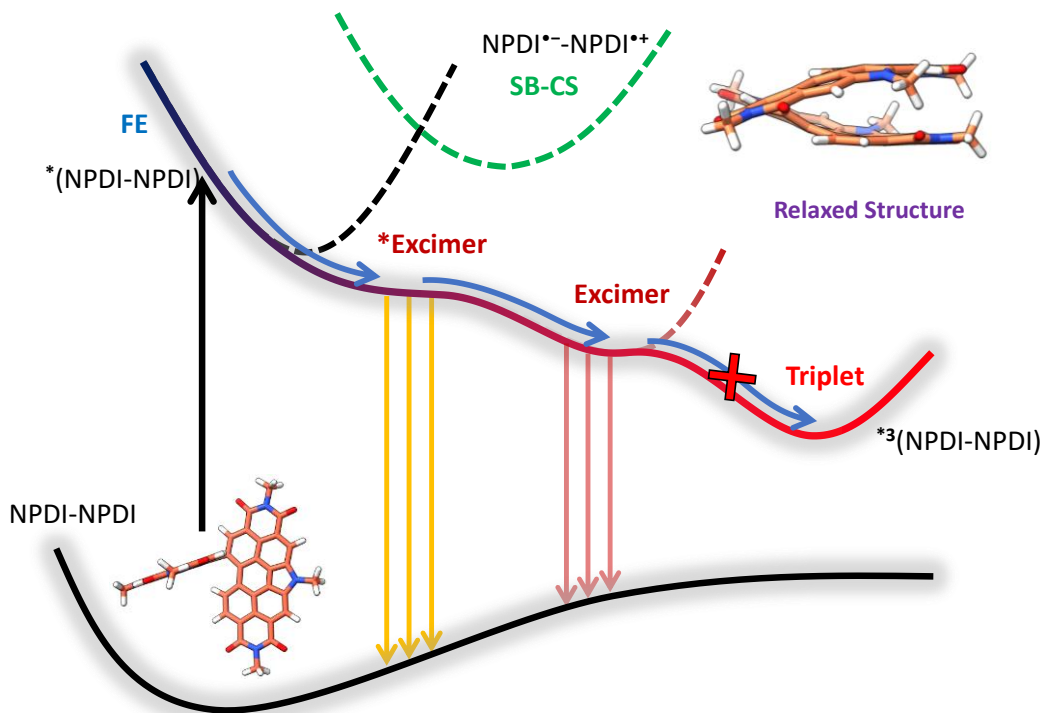


Figure A4.24: Schematic potential energy surface of *SC-NPDI*₂ in TOL summarising the excited state dynamics.

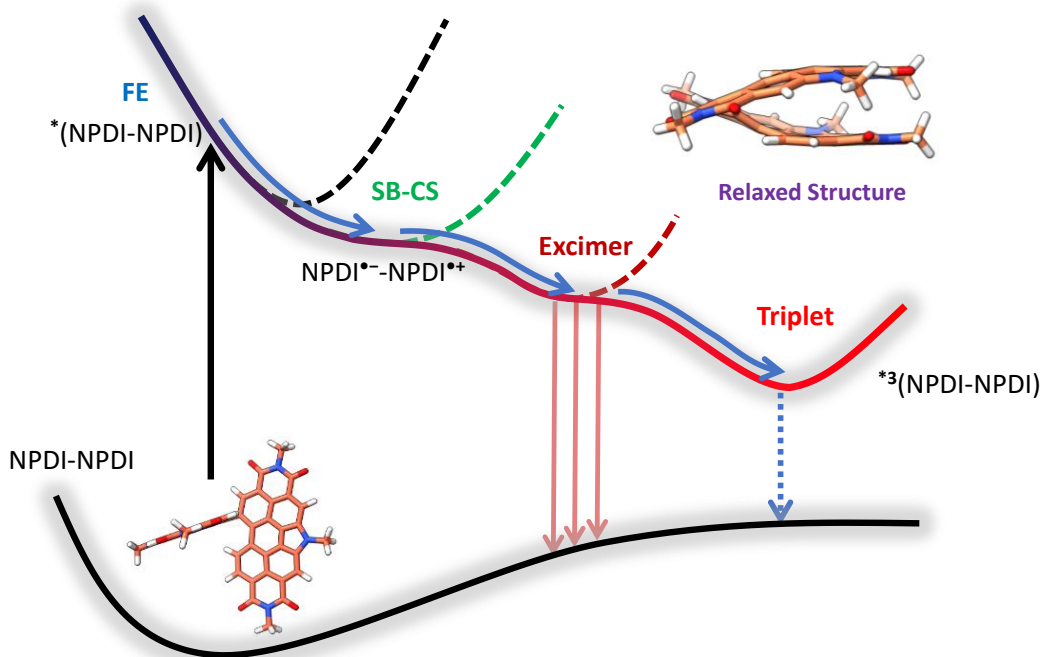


Figure A4.25: Schematic potential energy surface of *SC-NPDI*₂ in ACE and ACN summarising the excited state dynamics.

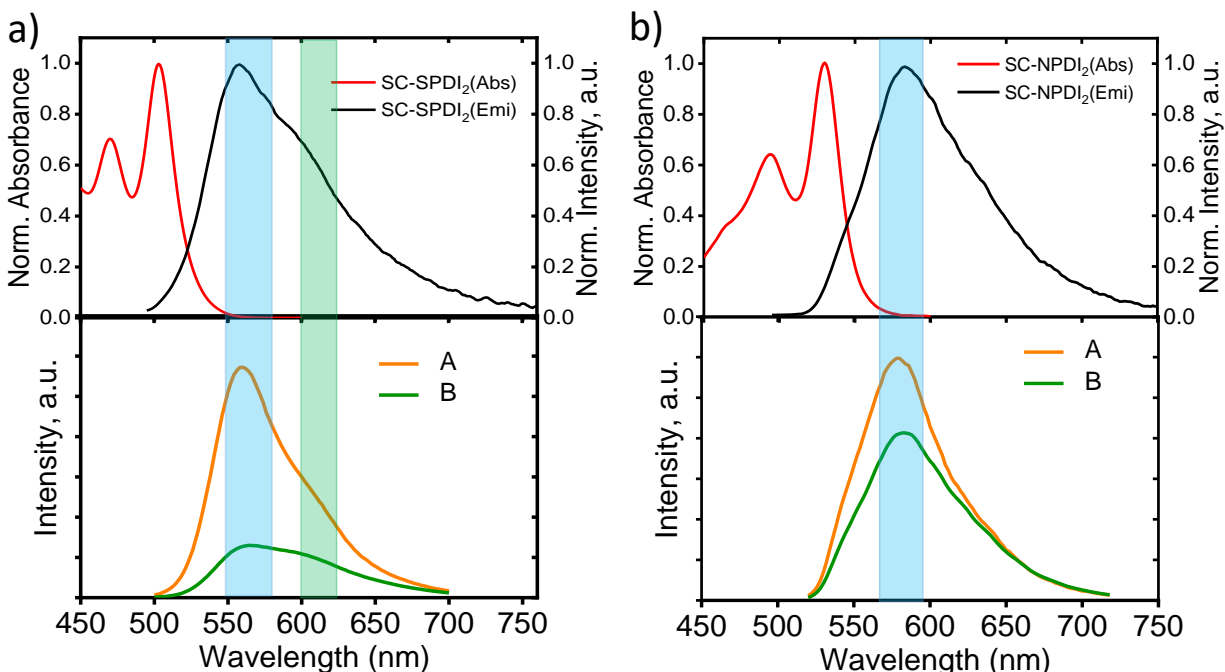


Figure A4.26: Comparison between the steady-state emission spectra (top) with the time-resolved emission spectra (bottom) of a) *SC-SPDI*₂ and b) *SC-NPDI*₂ recorded in TOL.

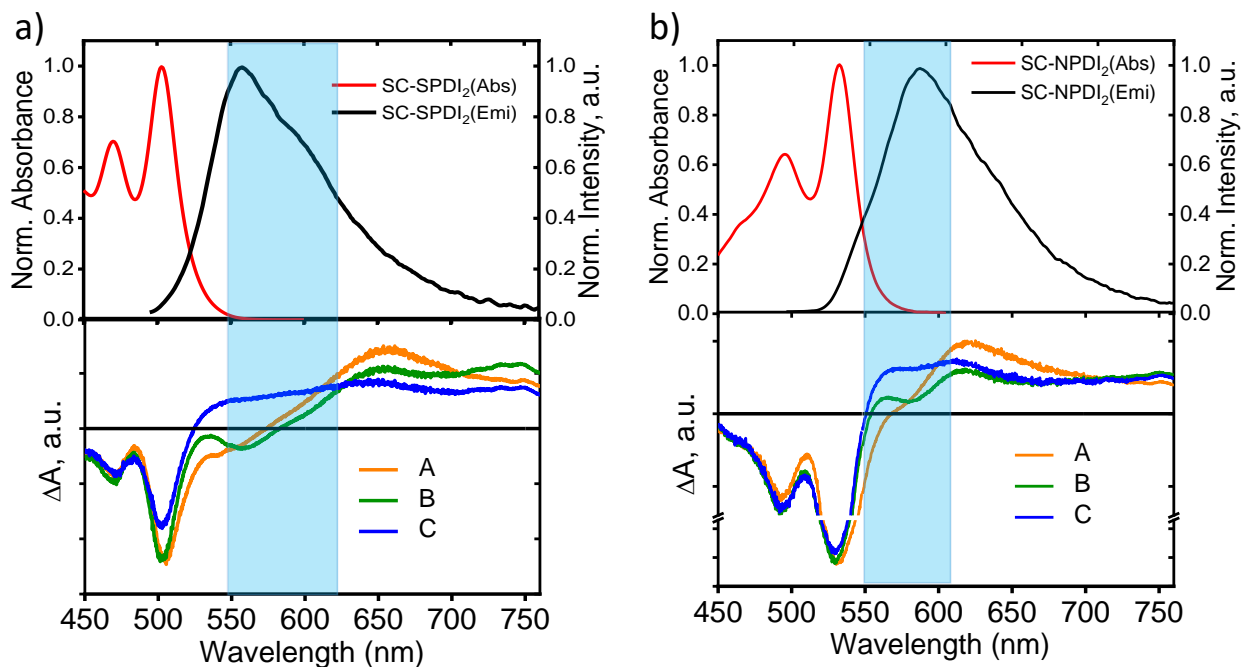


Figure A4.27: Comparison between the steady-state emission spectra (top) with the evolution associated spectra (bottom) of a) *SC-SPDI*₂ and b) *SC-NPDI*₂ recorded in TOL.

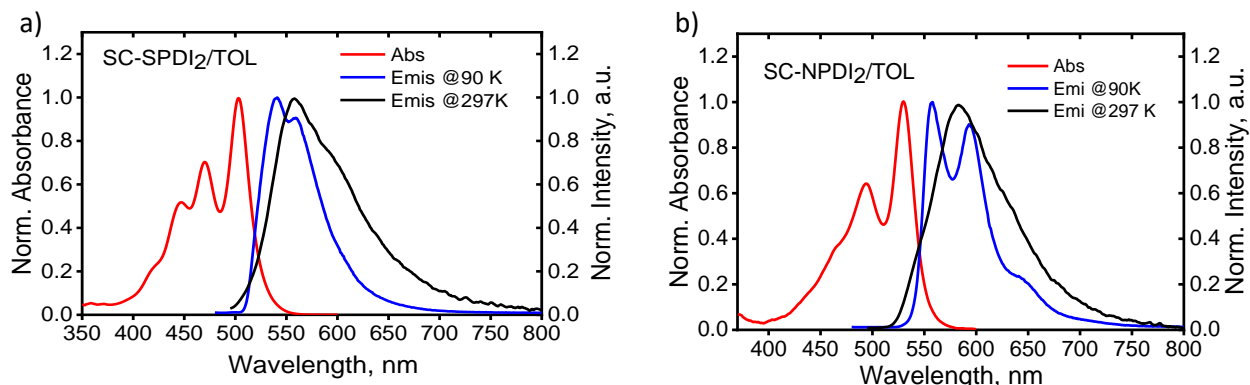


Figure A4.28: Steady-state UV-vis absorption spectra along with emission spectra (recorded at 90K and 297K) of a) **SC-SPDI₂** and b) **SC-NPDI₂** in TOL.

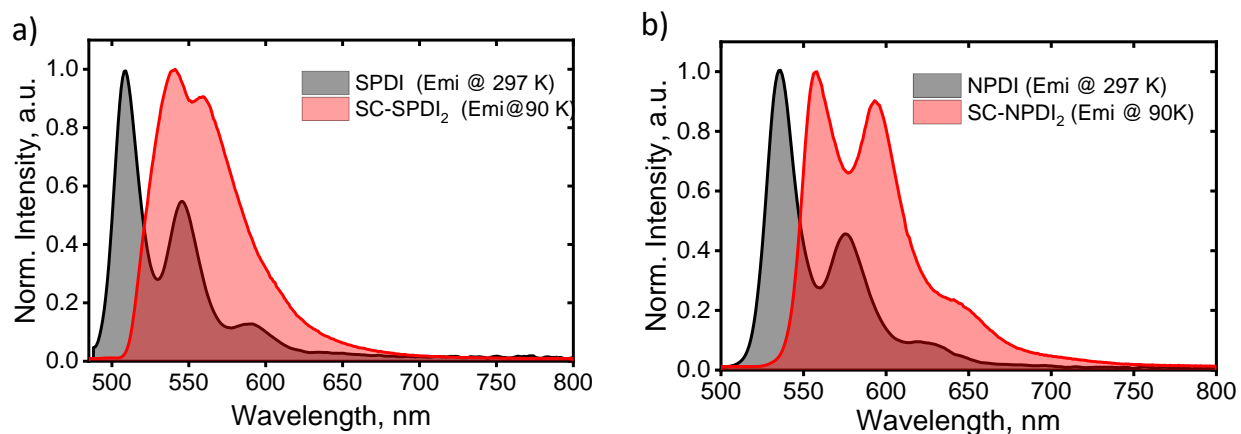


Figure A4.29: a) Emission spectra of **SPDI** at room temperature and **SC-SPDI₂** at 90K and b) Emission spectra of **NPDI** at room temperature and **SC-NPDI₂** at 90K in TOL.

4.7 Appendix

4.7.1: Materials and Methods

Similar to that discussed in section 2.7.1 (Chapter 1).

Lifetime measurements were carried out in an IBH picosecond time-correlated single-photon counting (TCSPC) system. The pulse width of the excitation ($\lambda_{exci} = 478$ nm) source is determined to be <100 ps, and 495 nm long-pass filter (Newport) was used to minimize the scatter arising from the laser source. The fluorescence decay profiles were de-convoluted using DAS6.3 and fitted with exponential decay, minimizing the χ^2 values. Temperature-dependent (90K-250K) photoluminescence measurements were carried out using liquid nitrogen cryostat (Janis VNF-100).

4.7.2: Computational Analysis

Similar to that discussed in section 3.7.3. (Chapter 3)

Ground state and excited state geometry optimization of **SC-SPDI₂** and **SC-NPDI₂** were carried out in Gaussian 16 employing the B3LYP functional with Grimme's D3 dispersion and DEF2VSP 1basis set at the DFT level of theory unless stated otherwise.⁸⁸

4.7.3: TheoDORE Analysis

Similar to that discussed in section 3.7.5. (Chapter 3)

4.7.4: Femtosecond transient absorption (fsTA) measurement

Similar to that discussed in section 3.7.6. (Chapter 3)

4.7.5: Global Analysis

Similar to that discussed in section 3.7.7. (Chapter 3)

All the wavelengths were analyzed in global analysis concurrently, employing a sequential model to give evolution associated spectra (EAS). The EAS indicates that the evolution of the spectra in time does not necessarily denote a real physical/chemical species. EAS designates the spectral changes that occur with their associated time constants.

4.7.6: Weller Analysis

Similar to that discussed in section 3.7.8. (Chapter 3)

Since **SC-SPDI**₂ and **SC-NPDI**₂ exhibit excimer formation in all the solvents, the optical bandgap (E_{00} , the precursor of SB-CS) was determined by the intersection of the normalized absorption and emission spectra of monomeric **SPDI** and **NPDI**.

4.7.7: Electrochemistry

Similar to that discussed in section 3.7.8. (Chapter 3)

HOMO and LUMO energies were calculated using the following equation.⁸⁹

$$E_g^{opt} = 1240 / \lambda_{onset} \quad \text{Eq 1}$$

$$E_{LUMO} = - (E'_{red} + 4.8 - E_{Fc/Fc+}) \text{ eV} \quad \text{Eq 2}$$

$$E_{HOMO} = E_{LUMO} - E_g^{opt} \quad \text{Eq 3}$$

respectively, where E'_{red} are the experimentally measured reduction potentials vs. Ag. E_{LUMO} and E_{HOMO} are the corresponding to LUMO and HOMO energy levels.

4.7.8: Time-Resolved Emission Spectra (TRES) Analysis

Similar to that discussed in section 3.7.10. (Chapter 3)

4.8. REFERENCES

- (1) Wasielewski, M. R. Photoinduced Electron Transfer in Supramolecular Systems for Artificial Photosynthesis. *Chem. Rev.* **2002**, *92*, 435–461.
- (2) Vauthey, E. Photoinduced Symmetry-Breaking Charge Separation. *ChemPhysChem* **2012**, *13*, 2001–2011.
- (3) Sebastian, E.; Hariharan, M. Symmetry-Breaking Charge Separation in Molecular Constructs for Efficient Light Energy Conversion. *ACS Energy Lett.* **2022**, *2022*, 696–711.
- (4) Young, R. M.; Wasielewski, M. R. Mixed Electronic States in Molecular Dimers: Connecting Singlet Fission, Excimer Formation, and Symmetry-Breaking Charge Transfer. *Acc. Chem. Res.* **2020**, *53*, 1957–1968.
- (5) Halperin, H.; Dejong, K.; W Adams, R. E.; Coggins, C. C.; Hammond, N.; Gotufried, D. S.; Steffen, M. A.; Boxer, S. G. Large Protein-Induced Dipoles for a Symmetric Carotenoid in a Photosynthetic Antenna Complex. *Science* **1991**, *251*, 662–665.
- (6) Dereka, B.; Koch, M.; Vauthey, E. Looking at Photoinduced Charge Transfer Processes in the IR: Answers to Several Long-Standing Questions. *Acc. Chem. Res.* **2017**, *50*, 426–434.
- (7) Lin, C.; Kim, T.; Schultz, J. D.; Young, R. M.; Wasielewski, M. R. Accelerating Symmetry-Breaking Charge Separation in a Perylenediimide Trimer through a Vibronically Coherent Dimer Intermediate. *Nat. Chem.* **2022**, 1–8.
- (8) Cherepanov, D. A.; Shelaev, I. V.; Gostev, F. E.; Petrova, A.; Aybush, A. V.; Nadtochenko, V. A.; Xu, W.; Golbeck, J. H.; Semenov, A. Y. Primary Charge Separation within the Structurally Symmetric Tetrameric Chl2APAPBChl2B Chlorophyll Exciplex in Photosystem I. *J. Photochem. Photobiol. B Biol.* **2021**, *217*, 112154.
- (9) Tamura, H.; Saito, K.; Ishikita, H. Acquisition of Water-Splitting Ability and Alteration of the Charge-Separation Mechanism in Photosynthetic Reaction Centers. *Proc. Natl. Acad. Sci. U. S. A.* **2020**, *117*, 16373–16382.
- (10) Diner, B. A.; Rappaport, F. STRUCTURE, DYNAMICS, AND ENERGETICS OF THE PRIMARY PHOTOCHEMISTRY OF PHOTOSYSTEM II OF OXYGENIC PHOTOSYNTHESIS. *Annu. Rev. Plant Biol.* **2003**, *53*, 551–580.
- (11) Vasil'ev, S.; Shen, J. R.; Kamiya, N.; Bruce, D. The Orientations of Core Antenna Chlorophylls in Photosystem II Are Optimized to Maximize the Quantum Yield of Photosynthesis. *FEBS Lett.* **2004**, *561*, 111–116.
- (12) Grabowski, Z. R.; Rotkiewicz, K.; Rettig, W. Structural Changes Accompanying Intramolecular Electron Transfer: Focus on Twisted Intramolecular Charge-Transfer States and Structures. *Chem. Rev.* **2003**, *103*, 3899–4032,
- (13) Lockhart, D. J.; Boxer, S. G. Magnitude and Direction of the Change in Dipole Moment Associated with Excitation of the Primary Electron Donor in Rhodospseudomonas Sphaeroides Reaction Centers. *Biochemistry* **2002**, *26*, 664–668.
- (14) Hong, J.; Sung, M. J.; Cha, H.; Park, C. E.; Durrant, J. R.; An, T. K.; Kim, Y. H.; Kwon, S. K. Understanding Structure-Property Relationships in All-Small-Molecule Solar Cells

- Incorporating a Fullerene or Nonfullerene Acceptor. *ACS Appl. Mater. Interfaces* **2018**, *10*, 36037–36046.
- (15) Brédas, J. L.; Sargent, E. H.; Scholes, G. D. Photovoltaic Concepts Inspired by Coherence Effects in Photosynthetic Systems. *Nat. Mater.* **2016**, *16*, 35–44.
- (16) Coropceanu, V.; Chen, X. K.; Wang, T.; Zheng, Z.; Brédas, J. L. Charge-Transfer Electronic States in Organic Solar Cells. *Nat. Rev. Mater.* **2019**, *4*, 689–707.
- (17) Gillett, A. J.; Privitera, A.; Dilmurat, R.; Karki, A.; Qian, D.; Pershin, A.; Londi, G.; Myers, W. K.; Lee, J.; Yuan, J.; Ko, S. J.; Riede, M. K.; Gao, F.; Bazan, G. C.; Rao, A.; Nguyen, T. Q.; Beljonne, D.; Friend, R. H. The Role of Charge Recombination to Triplet Excitons in Organic Solar Cells. *Nature* **2021**, *597*, 666–671.
- (18) Usui, R.; Yamamoto, K.; Okajima, H.; Mutoh, K.; Sakamoto, A.; Abe, J.; Kobayashi, Y. Photochromic Radical Complexes That Show Heterolytic Bond Dissociation. *J. Am. Chem. Soc.* **2020**, *142*, 10132–10142.
- (19) Menke, S. M.; Ran, N. A.; Bazan, G. C.; Friend, R. H. Understanding Energy Loss in Organic Solar Cells: Toward a New Efficiency Regime. *Joule* **2018**, *2*, 25–35.
- (20) Benduhn, J.; Tvingstedt, K.; Piersimoni, F.; Ullbrich, S.; Fan, Y.; Tropiano, M.; McGarry, K. A.; Zeika, O.; Riede, M. K.; Douglas, C. J.; Barlow, S.; Marder, S. R.; Neher, D.; Spoltore, D.; Vandewal, K. Intrinsic Non-Radiative Voltage Losses in Fullerene-Based Organic Solar Cells. *Nat. Energy* **2017**, *2*, 1–6.
- (21) Bartynski, A. N.; Gruber, M.; Das, S.; Rangan, S.; Mollinger, S.; Trinh, C.; Bradforth, S. E.; Vandewal, K.; Salleo, A.; Bartynski, R. A.; Bruetting, W.; Thompson, M. E. Symmetry-Breaking Charge Transfer in a Zinc Chlorodipyrrin Acceptor for High Open Circuit Voltage Organic Photovoltaics. *J. Am. Chem. Soc.* **2015**, *137*, 5397–5405.
- (22) Kaul, N.; Lomoth, R. The Carbene Cannibal: Photoinduced Symmetry-Breaking Charge Separation in an Fe(III) N-Heterocyclic Carbene. *J. Am. Chem. Soc.* **2021**, *143*, 10816–10821.
- (23) Ramirez, C. E.; Chen, S.; Powers-Riggs, N. E.; Schlesinger, I.; Young, R. M.; Wasielewski, M. R. Symmetry-Breaking Charge Separation in the Solid State: Tetra(Phenoxy)Perylenediimide Polycrystalline Films. *J. Am. Chem. Soc.* **2020**, *142*, 18243–18250.
- (24) Guo, Y.; Ma, Z.; Niu, X.; Zhang, W.; Tao, M.; Guo, Q.; Wang, Z.; Xia, A. Bridge-Mediated Charge Separation in Isomeric N-Annulated Perylene Diimide Dimers. *J. Am. Chem. Soc.* **2019**, *141*, 12789–12796.
- (25) Cook, R. E.; Phelan, B. T.; Kamire, R. J.; Majewski, M. B.; Young, R. M.; Wasielewski, M. R. Excimer Formation and Symmetry-Breaking Charge Transfer in Cofacial Perylene Dimers. *J. Phys. Chem. A* **2017**, *121*, 1607–1615.
- (26) Sung, J.; Nowak-Król, A.; Schlosser, F.; Fimmel, B.; Kim, W.; Kim, D.; Würthner, F. Direct Observation of Excimer-Mediated Intramolecular Electron Transfer in a Cofacially-Stacked Perylene Bisimide Pair. *J. Am. Chem. Soc.* **2016**, *138*, 9029–9032.
- (27) Spenst, P.; Young, R. M.; Wasielewski, M. R.; Würthner, F. Guest and Solvent Modulated Photo-Driven Charge Separation and Triplet Generation in a Perylene Bisimide Cyclophane.
-

- Chem. Sci.* **2016**, *7*, 5428–5434.
- (28) Roy, P.; Bressan, G.; Gretton, J.; Cammidge, A. N.; Meech, S. R. Ultrafast Excimer Formation and Solvent Controlled Symmetry Breaking Charge Separation in the Excitonically Coupled Subphthalocyanine Dimer. *Angew. Chem., Int. Ed.* **2021**, *60*, 10568–10572.
- (29) Kong, J.; Zhang, W.; Li, G.; Huo, D.; Guo, Y.; Niu, X.; Wan, Y.; Tang, B.; Xia, A. Excited-State Symmetry-Breaking Charge Separation Dynamics in Multibranched Perylene Diimide Molecules. *J. Phys. Chem. Lett.* **2020**, *11*, 10329–10339.
- (30) Aster, A.; Licari, G.; Zinna, F.; Brun, E.; Kumpulainen, T.; Tajkhorshid, E.; Lacour, J.; Vauthey, E. Tuning Symmetry Breaking Charge Separation in Perylene Bichromophores by Conformational Control. *Chem. Sci.* **2019**, *10*, 10629–10639.
- (31) Wu, Y.; Young, R. M.; Frasconi, M.; Schneebeli, S. T.; Spent, P.; Gardner, D. M.; Brown, K. E.; Würthner, F.; Stoddart, J. F.; Wasielewski, M. R. Ultrafast Photoinduced Symmetry-Breaking Charge Separation and Electron Sharing in Perylenediimide Molecular Triangles. *J. Am. Chem. Soc.* **2015**, *137*, 13236–13239.
- (32) Sebastian, E.; Hariharan, M. Null Exciton-Coupled Chromophoric Dimer Exhibits Symmetry-Breaking Charge Separation. *J. Am. Chem. Soc.* **2021**, *143*, 13769–13781.
- (33) Jovan M. Giaimo; Alexey V. Gusev, and; Wasielewski*, M. R. Excited-State Symmetry Breaking in Cofacial and Linear Dimers of a Green Perylenediimide Chlorophyll Analogue Leading to Ultrafast Charge Separation. *J. Am. Chem. Soc.* **2002**, *124*, 8530–8531.
- (34) Dover, C. B.; Gallaher, J. K.; Frazer, L.; Tapping, P. C.; Petty, A. J.; Crossley, M. J.; Anthony, J. E.; Kee, T. W.; Schmidt, T. W. Endothermic Singlet Fission Is Hindered by Excimer Formation. *Nat. Chem.* **2018**, *10*, 305–310.
- (35) Margulies, E. A.; Shoer, L. E.; Eaton, S. W.; Wasielewski, M. R. Excimer Formation in Cofacial and Slip-Stacked Perylene-3,4:9,10-Bis(Dicarboximide) Dimers on a Redox-Inactive Triptycene Scaffold. *Phys. Chem. Chem. Phys.* **2014**, *16*, 23735–23742.
- (36) Kim, W.; Nowak-Król, A.; Hong, Y.; Schlosser, F.; Würthner, F.; Kim, D. Solvent-Modulated Charge-Transfer Resonance Enhancement in the Excimer State of a Bay-Substituted Perylene Bisimide Cyclophane. *J. Phys. Chem. Lett.* **2019**, *10*, 1919–1927.
- (37) Bae, Y. J.; Shimizu, D.; Schultz, J. D.; Kang, G.; Zhou, J.; Schatz, G. C.; Osuka, A.; Wasielewski, M. R. Balancing Charge Transfer and Frenkel Exciton Coupling Leads to Excimer Formation in Molecular Dimers: Implications for Singlet Fission. *J. Phys. Chem. A* **2020**, *124*, 8478–8487.
- (38) Singh, R.; Kim, M.; Lee, J. J.; Ye, T.; Keivanidis, P. E.; Cho, K. Excimer Formation Effects and Trap-Assisted Charge Recombination Loss Channels in Organic Solar Cells of Perylene Diimide Dimer Acceptors. *J. Mater. Chem. C* **2020**, *8*, 1686–1696.
- (39) Wang, R.; Zhang, C.; Li, Q.; Zhang, Z.; Wang, X.; Xiao, M. Charge Separation from an Intra-Moiety Intermediate State in the High-Performance PM6:Y6 Organic Photovoltaic Blend. *J. Am. Chem. Soc.* **2020**, *142*, 12751–12759.
- (40) Yongseok, H. +; Kim, W.; Kim, T.; Kaufmann, C.; Kim, H.; Würthner, F.; Kim, D. Real-Time Observation of Structural Dynamics Triggering Excimer Formation in a Perylene
-

- Bisimide Folda-Dimer by Ultrafast Time-Domain Raman Spectroscopy. *Angew. Chem., Int. Ed.* **2021**, e202114474.
- (41) Yamakado, T.; Takahashi, S.; Watanabe, K.; Matsumoto, Y.; Osuka, A.; Saito, S.; Yamakado, J. T.; Takahashi, J. S.; Atanabe, K. W.; Atsumoto, Y. M.; Osuka, P. R. A.; Saito, S. Conformational Planarization versus Singlet Fission: Distinct Excited-State Dynamics of Cyclooctatetraene-Fused Acene Dimers. *Angew. Chem., Int. Ed.* **2018**, *57*, 5438–5443.
- (42) Jin, X.; Li, S.; Guo, L.; Hua, J.; Qu, D. H.; Su, J.; Zhang, Z.; Tian, H. Interplay of Steric Effects and Aromaticity Reversals to Expand the Structural/Electronic Responses of Dihydrophenazines. *J. Am. Chem. Soc.* **2021**, *2022*, 4883–4896.
- (43) Song, H.; Zhao, H.; Guo, Y.; Philip, A. M.; Guo, Q.; Hariharan, M.; Xia, A. Distinct Excited-State Dynamics of Near-Orthogonal Perylenimide Dimer: Conformational Planarization versus Symmetry Breaking Charge Transfer. *J. Phys. Chem. C* **2020**, *124*, 237–245.
- (44) Piontkowski, Z.; McCamant, D. W. Excited-State Planarization in Donor-Bridge Dye Sensitizers: Phenylene versus Thiophene Bridges. *J. Am. Chem. Soc.* **2018**, *140*, 11046–11057.
- (45) Hendsbee, A. D.; Sun, J. P.; Law, W. K.; Yan, H.; Hill, I. G.; Spasyuk, D. M.; Welch, G. C. Synthesis, Self-Assembly, and Solar Cell Performance of N-Annulated Perylene Diimide Non-Fullerene Acceptors. *Chem. Mater.* **2016**, *28*, 7098–7109.
- (46) Xin, R.; Feng, J.; Zeng, C.; Jiang, W.; Zhang, L.; Meng, D.; Ren, Z.; Wang, Z.; Yan, S. Nonfullerene-Acceptor All-Small-Molecule Organic Solar Cells Based on Highly Twisted Perylene Bisimide with an Efficiency of over 6%. *ACS Appl. Mater. Interfaces* **2017**, *9*, 2739–2746.
- (47) Lijina, M. P.; Benny, A.; Ramakrishnan, R.; Nair, N. G.; Hariharan, M. Exciton Isolation in Cross-Pentacene Architecture. *J. Am. Chem. Soc.* **2020**, *142*, 17393–17402.
- (48) Philip, A. M.; Mallia, A. R.; Hariharan, M. Prolonged Charge Separated States in Twisted Stacks of All-Carbon Donor and Acceptor Chromophores. *J. Phys. Chem. Lett.* **2016**, *7*, 4751–4756.
- (49) Mallia, A. R.; Salini, P. S.; Hariharan, M. Nonparallel Stacks of Donor and Acceptor Chromophores Evade Geminate Charge Recombination. *J. Am. Chem. Soc.* **2015**, *137*, 15604–15607.
- (50) Madhu, M.; Ramakrishnan, R.; Vijay, V.; Hariharan, M. Free Charge Carriers in Homo-Sorted I⁻ Stacks of Donor-Acceptor Conjugates. *Chem. Rev.* **2021**, *121*, 8234–8284.
- (51) Meng, D.; Sun, D.; Zhong, C.; Liu, T.; Fan, B.; Huo, L.; Li, Y.; Jiang, W.; Choi, H.; Kim, T.; Kim, J. Y.; Sun, Y.; Wang, Z.; Heeger, A. J. High-Performance Solution-Processed Non-Fullerene Organic Solar Cells Based on Selenophene-Containing Perylene Bisimide Acceptor. *J. Am. Chem. Soc.* **2016**, *138*, 375–380.
- (52) Sun, D.; Meng, D.; Cai, Y.; Fan, B.; Li, Y.; Jiang, W.; Huo, L.; Sun, Y.; Wang, Z. Non-Fullerene-Acceptor-Based Bulk-Heterojunction Organic Solar Cells with Efficiency over 7%. *J. Am. Chem. Soc.* **2015**, *137*, 11156–11162.
- (53) Qian, H.; Yue, W.; Zhen, Y.; Di Motta, S.; Di Donato, E.; Negri, F.; Qu, J.; Xu, W.; Zhu, D.; Wang, Z. Heterocyclic Annelated Di(Perylene Bisimide): Constructing Bowl-Shaped
-

- Perylene Bisimides by the Combination of Steric Congestion and Ring Strain. *J. Org. Chem.* **2009**, *74*, 6275–6282.
- (54) Madu, I. K.; Jiang, H.; Laventure, A.; Zimmerman, P. M.; Welch, G. C.; Goodson, T. Impact of Ring-Fusion on the Excited State Decay Pathways of N-Annulated Perylene Diimides. *J. Phys. Chem. C* **2021**, *125*, 10500–10515.
- (55) Sebastian, E.; Philip, A. M.; Benny, A.; Hariharan, M. Null Exciton Splitting in Chromophoric Greek Cross (+) Aggregate. *Angew. Chem., Int. Ed.* **2018**, *57*, 15696–15701.
- (56) Kaufmann, C.; Bialas, D.; Stolte, M.; Würthner, F. Discrete π -Stacks of Perylene Bisimide Dyes within Folda-Dimers: Insight into Long- and Short-Range Exciton Coupling. *J. Am. Chem. Soc.* **2018**, *140*, 9986–9995.
- (57) Kim, W.; Nowak-Król, A.; Hong, Y.; Schlosser, F.; Würthner, F.; Kim, D. Solvent-Modulated Charge-Transfer Resonance Enhancement in the Excimer State of a Bay-Substituted Perylene Bisimide Cyclophane. *J. Phys. Chem. Lett.* **2019**, *10*, 1919–1927.
- (58) Bagnich, S. A.; Athanasopoulos, S.; Rudnick, A.; Schroegel, P.; Bauer, I.; Greenham, N. C.; Strohrriegl, P.; Köhler, A. Excimer Formation by Steric Twisting in Carbazole and Triphenylamine-Based Host Materials. *J. Phys. Chem. C* **2015**, *119*, 2380–2387.
- (59) Grozema, F. C.; Swart, M.; Zijlstra, R. W. J.; Piet, J. J.; Siebbeles, L. D. A.; Van Duijnen, P. T. QM/MM Study of the Role of the Solvent in the Formation of the Charge Separated Excited State in 9,9'-Bianthryl. *J. Am. Chem. Soc.* **2005**, *127*, 11019–11028.
- (60) Nazari, M.; Cieplechowicz, E.; Welsh, T. A.; Welch, G. C. A Direct Comparison of Monomeric vs. Dimeric and Non-Annulated vs. N -Annulated Perylene Diimide Electron Acceptors for Organic Photovoltaics. *New J. Chem.* **2019**, *43*, 5187–5195.
- (61) Kim, T.; Kim, J.; Mori, H.; Park, S.; Lim, M.; Osuka, A.; Kim, D. Symmetry-Breaking Charge Transfer in the Excited State of Directly Linked Push–Pull Porphyrin Arrays. *Phys. Chem. Chem. Phys.* **2017**, *19*, 13970–13977.
- (62) Fink, R. F.; Seibt, J.; Engel, V.; Renz, M.; Kaupp, M.; Lochbrunner, S.; Zhao, H. M.; Pfister, J.; Würthner, F.; Engels, B. Exciton Trapping in π -Conjugated Materials: A Quantum-Chemistry-Based Protocol Applied to Perylene Bisimide Dye Aggregates. *J. Am. Chem. Soc.* **2008**, *130*, 12858–12859.
- (63) Chai, J. Da; Head-Gordon, M. Long-Range Corrected Hybrid Density Functionals with Damped Atom–Atom Dispersion Corrections. *Phys. Chem. Chem. Phys.* **2008**, *10*, 6615–6620.
- (64) Weigend, F.; Ahlrichs, R. Balanced Basis Sets of Split Valence, Triple Zeta Valence and Quadruple Zeta Valence Quality for H to Rn: Design and Assessment of Accuracy. *Phys. Chem. Chem. Phys.* **2005**, *7*, 3297–3305.
- (65) Grimme, S.; Antony, J.; Ehrlich, S.; Krieg, H. A Consistent and Accurate Ab Initio Parametrization of Density Functional Dispersion Correction (DFT-D) for the 94 Elements H–Pu. *J. Chem. Phys.* **2010**, *132*, 154104.
- (66) Farr, E. P.; Fontana, M. T.; Zho, C. C.; Wu, P.; Li, Y. L.; Knutson, N.; Rubin, Y.; Schwartz, B. J. Bay-Linked Perylenediimides Are Two Molecules in One: Insights from Ultrafast Spectroscopy, Temperature Dependence, and Time-Dependent Density Functional Theory
-

- Calculations. *J. Phys. Chem. C* **2019**, *123*, 2127–2138.
- (67) Plasser, F.; Lischka, H. Analysis of Excitonic and Charge Transfer Interactions from Quantum Chemical Calculations. *J. Chem. Theory Comput.* **2012**, *8*, 2777–2789.
- (68) Plasser, F. TheoDORE: A Toolbox for a Detailed and Automated Analysis of Electronic Excited State Computations. *J. Chem. Phys.* **2020**, *152*, 084108.
- (69) Ibele, L. M.; Sánchez-Murcia, P. A.; Mai, S.; Nogueira, J. J.; González, L. Excimer Intermediates En Route to Long-Lived Charge-Transfer States in Single-Stranded Adenine DNA as Revealed by Nonadiabatic Dynamics. *J. Phys. Chem. Lett.* **2020**, *11*, 7483–7488.
- (70) East, A. L. L.; Lim, E. C. Naphthalene Dimer: Electronic States, Excimers, and Triplet Decay. *J. Chem. Phys.* **2000**, *113*, 8981.
- (71) Hong, Y.; Kim, J.; Kim, W.; Kaufmann, C.; Kim, H.; Würthner, F.; Kim, D. Efficient Multiexciton State Generation in Charge-Transfer-Coupled Perylene Bisimide Dimers via Structural Control. *J. Am. Chem. Soc.* **2020**, *142*, 7845–7857.
- (72) Weller, A. Photoinduced Electron Transfer in Solution: Exciplex and Radical Ion Pair Formation Free Enthalpies and Their Solvent Dependence. *Zeitschrift für Phys. Chemie* **1982**, *133*, 93–98.
- (73) Imahori, H.; Hagiwara, K.; Aoki, M.; Akiyama, T.; Taniguchi, S.; Okada, T.; Shirakawa, M.; Sakata, Y. Linkage and Solvent Dependence of Photoinduced Electron Transfer in Zincporphyrin-C60 Dyads. *J. Am. Chem. Soc.* **1996**, *118*, 11771–11782.
- (74) Van Stokkum, I. H. M.; Larsen, D. S.; Van Grondelle, R. Global and Target Analysis of Time-Resolved Spectra. *Biochim. Biophys. Acta - Bioenerg.* **2004**, *1657*, 82–104.
- (75) Snellenburg, J. J.; Liptonok, S.; Seger, R.; Mullen, K. M.; van Stokkum, I. H. M. Glotaran: A Java-Based Graphical User Interface for the R Package TIMP. *J. Stat. Softw.* **2012**, *49*, 1–22.
- (76) Mohan, A.; Sebastian, E.; Gudem, M.; Hariharan, M. Near-Quantitative Triplet State Population via Ultrafast Intersystem Crossing in Perbromoperylene diimide. *J. Phys. Chem. B* **2020**, *124*, 6867–6874.
- (77) Markovic, V.; Villamaina, D.; Barabanov, I.; Lawson Daku, L. M.; Vauthey, E. Photoinduced Symmetry-Breaking Charge Separation: The Direction of the Charge Transfer. *Angew. Chem., Int. Ed.* **2011**, *50*, 7596–7598.
- (78) Terenziani, F.; Painelli, A.; Katan, C.; Charlot, M.; Blanchard-Desce, M. Charge Instability in Quadrupolar Chromophores: Symmetry Breaking and Solvatochromism. *J. Am. Chem. Soc.* **2006**, *128*, 15742–15755.
- (79) Amthor, S.; Lambert, C.; Dümmler, S.; Fischer, I.; Schelter, J. Excited Mixed-Valence States of Symmetrical Donor–Acceptor–Donor π Systems. *J. Phys. Chem. A* **2006**, *110*, 5204–5214.
- (80) Young, R. M.; Wasielewski, M. R. Mixed Electronic States in Molecular Dimers: Connecting Singlet Fission, Excimer Formation, and Symmetry-Breaking Charge Transfer. *Acc. Chem. Res.* **2020**, *53*, 1957–1968.
- (81) Sung, J.; Nowak-Król, A.; Schlosser, F.; Fimmel, B.; Kim, W.; Kim, D.; Würthner, F. Direct Observation of Excimer-Mediated Intramolecular Electron Transfer in a Cofacially-Stacked
-

- Perylene Bisimide Pair. *J. Am. Chem. Soc.* **2016**, *138*, 9029–9032.
- (82) Casanova, D. Theoretical Investigations of the Perylene Electronic Structure: Monomer, Dimers, and Excimers. *Int. J. Quantum Chem.* **2015**, *115*, 442–452.
- (83) Osaki, H.; Chou, C.-M.; Taki, M.; Welke, K.; Yokogawa, D.; Irle, S.; Sato, Y.; Higashiyama, T.; Saito, S.; Fukazawa, A.; Yamaguchi, S. A Macrocyclic Fluorophore Dimer with Flexible Linkers: Bright Excimer Emission with a Long Fluorescence Lifetime. *Angew. Chem., Int. Ed.* **2016**, *128*, 7247–7251.
- (84) Veldman, D.; Chopin, S. M. A.; Meskers, S. C. J.; Groeneveld, M. M.; Williams, R. M.; Janssen, R. A. J. Triplet Formation Involving a Polar Transition State in a Well-Defined Intramolecular Perylenediimide Dimeric Aggregate. *J. Phys. Chem. A* **2008**, *112*, 5846–5857.
- (85) Spano, F. C.; Yamagata, H. Vibronic Coupling in J-Aggregates and Beyond: A Direct Means of Determining the Exciton Coherence Length from the Photoluminescence Spectrum. *J. Phys. Chem. B* **2010**, *115*, 5133–5143.
- (86) Van Dijk, L.; Bobbert, P. A.; Spano, F. C. Optical Spectra and Stokes Shift in Double-Stranded Helical Supramolecular Assemblies. *J. Phys. Chem. B* **2009**, *113*, 9708–9717.
- (87) Spano, F. C.; Silva, C. H- and J-Aggregate Behavior in Polymeric Semiconductors. *Annu. Rev. Phys. Chem.* **2014**, *65*, 477–500.
- (88) Citation | Gaussian.com <https://gaussian.com/citation/> (accessed Jun 27, 2022).
- (89) Li, G.; Yang, W.; Wang, S.; Liu, T.; Yan, C.; Zhang, Y.; Li, D.; Wang, X.; Hao, P.; Li, J.; Huo, L.; Yan, H.; Tang, B. Methane-Perylene Diimide-Based Small Molecule Acceptors for High Efficiency Non-Fullerene Organic Solar Cells. *J. Mater. Chem. C* **2019**, *7*, 10901–10907.

5. List of Publications

1. Excimer Evolution Hampers Symmetry-Broken Charge-Separated State, **Ebin Sebastian**†, Jeswin Sunny† and Mahesh Hariharan* *Chem. Sci.*, **2022**,13, 10824-10835.
2. Solvent Dielectric Delimited Nitro to Nitrito Photorearrangement in a Rylenediimide, Aniruddha Mazumder, **Ebin Sebastian**, and Mahesh Hariharan* *Chem. Sci.*, **2022**,13, 8860-8870.
3. Ultrafast Intersystem Crossing in Selenium Annulated Perylenediimide, Jibin Sivanarayanan†, **Ebin Sebastian**†, Kavya Vinod and Mahesh Hariharan* *J. Phys. Chem. C* **2022**, 126, 13319–13326.
4. Symmetry-Breaking Charge Separation in Molecular Constructs for Efficient Light Energy Conversion, **Ebin Sebastian** and Mahesh Hariharan*, *ACS Energy Lett.* **2022**, 7, 696–711. **(Front Cover)**
5. Null Exciton-Coupled Chromophoric Dimer Exhibits Symmetry-Breaking Charge Separation, **Ebin Sebastian** and Mahesh Hariharan*, *J. Am. Chem. Soc.* **2021**, 143, 13769–13781. **(Cover)**
6. Near-Quantitative Triplet State Population via Ultrafast Intersystem Crossing in Perbromoperylenediimide,, Amalu Mohan†, **Ebin Sebastian**† Mahesh Gudem, and Mahesh Hariharan*, *J. Phys. Chem. B* **2020**, 124, 6867– 6874. **(Front Cover)**
7. Anomalous Halogen-Halogen Interaction Assists Radial Chromophoric Assembly, M. A. Niyas†, R. Ramakrishnan†, V. Vishnu, **Ebin Sebastian** and Mahesh Hariharan*, *J. Am. Chem. Soc.* **2019**, 141, 4536–4540. **(Cover)**
8. Decoding the Curious Tale of Atypical Intersystem Crossing Dynamics in Regioisomeric Acetylanthracenes, Abbey M. Philip, Mahesh Gudem, **Ebin Sebastian**, and Mahesh Hariharan*, *J. Phys. Chem. A* **2019**, 123, 29, 6105–6112.
9. Viable Access to the Triplet Excited State in Peryleneimide Based Palladium Complex, Abbey M. Philip, **Ebin Sebastian**, G. Gopan, R. Ramakrishnan and Mahesh Hariharan *, *J.Chem.Sci.* **2018**, 130, 137 **(Prof. M. V. George’s Special Issue)**.

10. Null Exciton Splitting in Chromophoric Greek Cross (+) Aggregate, **Ebin Sebastian**[†], Abbey M. Philip[†], Alfy Benny, and Mahesh Hariharan*, *Angew. Chem. Int. Ed.* **2018**, 57, 15696 – 15701. **(Cover)**
11. Extending the scope of the carbonyl facilitated triplet excited state towards visible light excitation, Shinaj K. Rajagopal, Nagaraj K., Somadrita Deb, Vinayak Bhat, Devika Sasikumar, **Ebin Sebastian** and Mahesh Hariharan*, *Phys. Chem. Chem. Phys.*, **2018**, 20, 19120.
12. Local Phonon Environment as a Design Element for Long-lived Excitonic Coherence: Dithia-anthracenophane Revisited, Govind Sidhardh*, Adithi Ajith, **Ebin Sebastian**, Mahesh Hariharan and Anil Shaji, *J. Phys. Chem. A.* **2022**, 126, 3765–3773.
13. Marcus Inverted Region dependence on Intramolecular Charge Recombination of Near-Orthogonal Chromophoric Dimer, **Ebin Sebastian** and Mahesh Hariharan* (Under preparation).

[†]=These authors contributed equally.

6. Workshops and Conferences

- ❖ **3rd Indian Materials Conclave and 32nd Annual meeting of MRSI Research Society of India Conference 2021** | 17th -23rd Dec, 2021| Indian Institute of Technology Madras, Virtual Symposium |.
- ❖ **12th National Workshop on Fluorescence and Raman Spectroscopy (FCS 2021)** | 29th Nov - 4th Dec, 2021| Virtual Symposium|.
- ❖ **Light-Matter Interactions from Scratch; Theory and Experiments at the Border with Biology** | ICTP | 22nd – 25th Nov, 2021| Virtual Symposium|.
- ❖ **11th Asian Photochemistry Conference 2021 (APC 21)** | 31th Oct-4th Nov, 2021| Virtual Symposium |
- ❖ Virtual Chemistry Course “**Functional Pi-Systems – Organic Materials Design by Molecular and Supramolecular Engineering.**” | 19th-23rd Jul, 2021| University of Würzburg |.
- ❖ **15th JNC Research Conference on Chemistry of Materials** | 30th Sep- 02nd Oct, 2019 | Thiruvananthapuram|.
- ❖ **24th CRSI National symposium in Chemistry** | 8th- 10th Feb, 2019 | CSRI-CLRI, Adyar, Chennai |.
- ❖ **International Conference on Ultrafast Spectroscopy (ICUS2020)** | 21st-22nd Feb, 2020 | IISER TVM, Kerala, India |.
- ❖ **IISERTVM-RSC Symposium on Advances in Chemical Sciences** | 4th Feb, 2020 | IISER TVM, Kerala, India|
- ❖ **Faraday Discussions (2018): Photoinduced Processes in Nucleic Acids and Proteins** | 11th- 13th Jan, 2018 Thiruvananthapuram, Kerala, India|.
- ❖ **Nanobioteck-2017: 2nd Annual Conference of Indian Society of Nanomedicine** | 6th-8th Dec, 2017 | Thiruvananthapuram, Kerala, India|.
- ❖ **8th East Asia Symposium on Functional Dyes and Advanced Materials** | 20th-22nd Sep, 2017| Council of Scientific and Industrial Research -National Institute for Interdisciplinary Science and Technology (CSIR-NIIST) Thiruvananthapuram, Kerala, India |.

- ❖ **Recent Advances in Quantum Mechanics and Computational Chemistry** | 22nd-24th Jul, 2015| Sree Sankara College, Kalady, Kerala, India |.
- ❖ **International Conference on Advances in Material Science** | 23rd-24th Oct, 2013 | Sree Sankara College, Kalady, Kerala, India |.

7. Copyrights and Permissions



Home



Help ▾



Email Support



Ebin Sebastian ▾



Light Absorption and Energy Transfer in the Antenna Complexes of Photosynthetic Organisms

Author: Tihana Mirkovic, Evgeny E. Ostroumov, Jessica M. Anna, et al

Publication: Chemical Reviews

Publisher: American Chemical Society

Date: Jan 1, 2017

Copyright © 2017, American Chemical Society

PERMISSION/LICENSE IS GRANTED FOR YOUR ORDER AT NO CHARGE

This type of permission/license, instead of the standard Terms and Conditions, is sent to you because no fee is being charged for your order. Please note the following:

- Permission is granted for your request in both print and electronic formats, and translations.
- If figures and/or tables were requested, they may be adapted or used in part.
- Please print this page for your records and send a copy of it to your publisher/graduate school.
- Appropriate credit for the requested material should be given as follows: "Reprinted (adapted) with permission from {COMPLETE REFERENCE CITATION}. Copyright {YEAR} American Chemical Society." Insert appropriate information in place of the capitalized words.
- One-time permission is granted only for the use specified in your RightsLink request. No additional uses are granted (such as derivative works or other editions). For any uses, please submit a new request.

If credit is given to another source for the material you requested from RightsLink, permission must be obtained from that source.

[BACK](#)

[CLOSE WINDOW](#)



This is a License Agreement between Ebin SEbastian ("User") and Copyright Clearance Center, Inc. ("CCC") on behalf of the Rightsholder identified in the order details below. The license consists of the order details, the Marketplace Order General Terms and Conditions below, and any Rightsholder Terms and Conditions which are included below.

All payments must be made in full to CCC in accordance with the Marketplace Order General Terms and Conditions below.

| | | | |
|-------------------------|-------------|--------------------|------------------------------------|
| Order Date | 24-Jun-2022 | Type of Use | Republish in a thesis/dissertation |
| Order License ID | 1240466-1 | Publisher | ROYAL SOCIETY |
| ISSN | 1742-5662 | Portion | Chart/graph/table/figure |

LICENSED CONTENT

| | | | |
|--------------------------|--|-------------------------|---|
| Publication Title | Journal of the Royal Society interface | Country | United Kingdom of Great Britain and Northern Ireland |
| Author/Editor | Royal Society (Great Britain) | Rightsholder | The Royal Society (U.K.) |
| Date | 01/01/2004 | Publication Type | e-Journal |
| Language | English | URL | https://royalsociety.org/journals/ |

REQUEST DETAILS

| | | | |
|---|--------------------------|------------------------------------|----------------------------------|
| Portion Type | Chart/graph/table/figure | Distribution | Worldwide |
| Number of charts / graphs / tables / figures requested | 1 | Translation | Original language of publication |
| Format (select all that apply) | Print, Electronic | Copies for the disabled? | No |
| Who will republish the content? | Academic institution | Minor editing privileges? | No |
| Duration of Use | Life of current edition | Incidental promotional use? | No |
| Lifetime Unit Quantity | Up to 499 | Currency | USD |
| Rights Requested | Main product | | |

NEW WORK DETAILS

| | | | |
|------------------------|--|-----------------------------------|------------|
| Title | Orthogonal Bichromophoric Systems: From Null Exciton Coupling to Symmetry-Breaking Charge Separation | Institution name | IISER TVM |
| Instructor name | Prof. Mahesh Hariharan | Expected presentation date | 2022-09-02 |



This is a License Agreement between IISER TVM ("User") and Copyright Clearance Center, Inc. ("CCC") on behalf of the Rightsholder identified in the order details below. The license consists of the order details, the Marketplace Order General Terms and Conditions below, and any Rightsholder Terms and Conditions which are included below.

All payments must be made in full to CCC in accordance with the Marketplace Order General Terms and Conditions below.

| | | | |
|-------------------------|-------------|--------------------------|--|
| Order Date | 24-Jun-2022 | Type of Use | Republish in a thesis/dissertation |
| Order License ID | 1240462-1 | Publisher Portion | IOP Publishing Chart/graph/table/figure |
| ISSN | 2050-6120 | | |

LICENSED CONTENT

| | | | |
|--------------------------|--|-------------------------|--|
| Publication Title | Methods and Applications in Fluorescence | Country | United Kingdom of Great Britain and Northern Ireland |
| Date | 01/01/2013 | Rightsholder | IOP Publishing, Ltd |
| Language | English | Publication Type | e-Journal |

REQUEST DETAILS

| | | | |
|---|--|------------------------------------|----------------------------------|
| Portion Type | Chart/graph/table/figure | Distribution | Worldwide |
| Number of charts / graphs / tables / figures requested | 1 | Translation | Original language of publication |
| Format (select all that apply) | Print, Electronic | Copies for the disabled? | No |
| Who will republish the content? | Academic institution | Minor editing privileges? | No |
| Duration of Use | Life of current edition | Incidental promotional use? | No |
| Lifetime Unit Quantity | Up to 499 | Currency | USD |
| Rights Requested | Main product and any product related to main product | | |

NEW WORK DETAILS

| | | | |
|------------------------|--|-----------------------------------|------------|
| Title | Orthogonal Bichromophoric Systems: From Null Exciton Coupling to Symmetry-Breaking Charge Separation | Institution name | IISER TVM |
| Instructor name | Prof. Mahesh Hariharan | Expected presentation date | 2022-09-02 |



RightsLink



Home



Help ▾



Email Support



Ebin Sebastian ▾

Molecular Aggregate Photophysics beyond the Kasha Model: Novel Design Principles for Organic Materials



Author: Nicholas J. Hestand, Frank C. Spano

Publication: Accounts of Chemical Research

Publisher: American Chemical Society

Date: Feb 1, 2017

Copyright © 2017, American Chemical Society

PERMISSION/LICENSE IS GRANTED FOR YOUR ORDER AT NO CHARGE

This type of permission/license, instead of the standard Terms and Conditions, is sent to you because no fee is being charged for your order. Please note the following:

- Permission is granted for your request in both print and electronic formats, and translations.
- If figures and/or tables were requested, they may be adapted or used in part.
- Please print this page for your records and send a copy of it to your publisher/graduate school.
- Appropriate credit for the requested material should be given as follows: "Reprinted (adapted) with permission from {COMPLETE REFERENCE CITATION}. Copyright {YEAR} American Chemical Society." Insert appropriate information in place of the capitalized words.
- One-time permission is granted only for the use specified in your RightsLink request. No additional uses are granted (such as derivative works or other editions). For any uses, please submit a new request.

If credit is given to another source for the material you requested from RightsLink, permission must be obtained from that source.

[BACK](#)

[CLOSE WINDOW](#)



Magic-Angle Stacking and Strong Intermolecular π - π Interaction in a Perylene Bisimide Crystal: An Approach for Efficient Near-Infrared (NIR) Emission and High Electron Mobility

Author: Jiadong Zhou, Wenqiang Zhang, Xiao-Fang Jiang, et al

Publication: Journal of Physical Chemistry Letters

Publisher: American Chemical Society

Date: Feb 1, 2018

Copyright © 2018, American Chemical Society

PERMISSION/LICENSE IS GRANTED FOR YOUR ORDER AT NO CHARGE

This type of permission/license, instead of the standard Terms and Conditions, is sent to you because no fee is being charged for your order. Please note the following:

- Permission is granted for your request in both print and electronic formats, and translations.
- If figures and/or tables were requested, they may be adapted or used in part.
- Please print this page for your records and send a copy of it to your publisher/graduate school.
- Appropriate credit for the requested material should be given as follows: "Reprinted (adapted) with permission from {COMPLETE REFERENCE CITATION}. Copyright {YEAR} American Chemical Society." Insert appropriate information in place of the capitalized words.
- One-time permission is granted only for the use specified in your RightsLink request. No additional uses are granted (such as derivative works or other editions). For any uses, please submit a new request.

If credit is given to another source for the material you requested from RightsLink, permission must be obtained from that source.

[BACK](#)

[CLOSE WINDOW](#)

Discrete π -Stacks of Perylene Bisimide Dyes within Folda-Dimers: Insight into Long- and Short-Range Exciton Coupling



Author: Christina Kaufmann, David Bialas, Matthias Stolte, et al

Publication: Journal of the American Chemical Society

Publisher: American Chemical Society

Date: Aug 1, 2018

Copyright © 2018, American Chemical Society

PERMISSION/LICENSE IS GRANTED FOR YOUR ORDER AT NO CHARGE

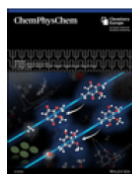
This type of permission/license, instead of the standard Terms and Conditions, is sent to you because no fee is being charged for your order. Please note the following:

- Permission is granted for your request in both print and electronic formats, and translations.
- If figures and/or tables were requested, they may be adapted or used in part.
- Please print this page for your records and send a copy of it to your publisher/graduate school.
- Appropriate credit for the requested material should be given as follows: "Reprinted (adapted) with permission from {COMPLETE REFERENCE CITATION}. Copyright {YEAR} American Chemical Society." Insert appropriate information in place of the capitalized words.
- One-time permission is granted only for the use specified in your RightsLink request. No additional uses are granted (such as derivative works or other editions). For any uses, please submit a new request.

If credit is given to another source for the material you requested from RightsLink, permission must be obtained from that source.

[BACK](#)

[CLOSE WINDOW](#)



Photoinduced Symmetry-Breaking Charge Separation

Author: Eric Vauthey
 Publication: ChemPhysChem
 Publisher: John Wiley and Sons
 Date: Mar 30, 2012

Copyright © 2012 WILEY-VCH Verlag GmbH & Co. KGaA, Weinheim

Order Completed

Thank you for your order.

This Agreement between IISER TVM -- Ebin Sebastian ("You") and John Wiley and Sons ("John Wiley and Sons") consists of your license details and the terms and conditions provided by John Wiley and Sons and Copyright Clearance Center.

Your confirmation email will contain your order number for future reference.

License Number 5335181172739

[Printable Details](#)

License date Jun 24, 2022

✓ Licensed Content

| | |
|------------------------------|--|
| Licensed Content Publisher | John Wiley and Sons |
| Licensed Content Publication | ChemPhysChem |
| Licensed Content Title | Photoinduced Symmetry-Breaking Charge Separation |
| Licensed Content Author | Eric Vauthey |
| Licensed Content Date | Mar 30, 2012 |
| Licensed Content Volume | 13 |
| Licensed Content Issue | 8 |
| Licensed Content Pages | 11 |

📄 Order Details

| | |
|--------------------------|----------------------|
| Type of use | Dissertation/Thesis |
| Requestor type | University/Academic |
| Format | Print and electronic |
| Portion | Figure/table |
| Number of figures/tables | 1 |
| Will you be translating? | No |

📄 About Your Work

| | |
|----------------------------|--|
| Title | Orthogonal Bichromophoric Systems: From Null Exciton Coupling to Symmetry-Breaking Charge Separation |
| Institution name | IISER TVM |
| Expected presentation date | Sep 2022 |

📄 Additional Data

| | |
|----------|----------|
| Portions | Figure 3 |
|----------|----------|